Dynamics of interfacial swimmers

Dolachai Boniface

▶ **To cite this version:**

Dolachai Boniface. Dynamics of interfacial swimmers. Fluids mechanics [physics.class-ph]. Université de Lyon, 2020. English. NNT : 2020LYSE1163 . tel-03281202

HAL Id: tel-03281202
https://theses.hal.science/tel-03281202

Submitted on 8 Jul 2021

HAL is a multi-disciplinary open access archive for the deposit and dissemination of scientific research documents, whether they are published or not. The documents may come from teaching and research institutions in France or abroad, or from public or private research centers.

L'archive ouverte pluridisciplinaire **HAL**, est destinée au dépôt et à la diffusion de documents scientifiques de niveau recherche, publiés ou non, émanant des établissements d'enseignement et de recherche français ou étrangers, des laboratoires publics ou privés.

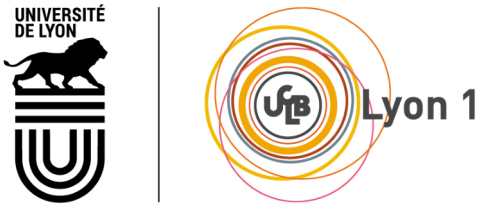

N° d'ordre NNT : 2020LYSE1163

THÈSE DE DOCTORAT DE L'UNIVERSITÉ DE LYON
opérée au sein de
l'Université Claude Bernard Lyon 1

École Doctorale ED52
Physique et Astrophysique de Lyon

Spécialité de doctorat : Physique

Soutenue publiquement 08/10/2020, par :
Dolachai Boniface

Dynamics of interfacial swimmers

Devant le jury composé de :

Biben Thierry, Professeur des Universités, Université Lyon 1	Examinateur
Bickel Thomas, Maître de Conférences, Université de Bordeaux	Rapporteur
Cantat Isabelle, Professeur des Universités, Université de Rennes 1	Examinatrice
Michelin Sébastien, Professeur, Ecole Polytechnique	Examinateur
Talini Laurence, Directrice de Recherche CNRS, CNRS Aubervilliers	Rapporteure
Cottin-Bizonne Cécile, Directrice de Recherche CNRS, Université Lyon 1	Directrice de thèse
Detcheverry François, Chargé de Recherche CNRS, Université Lyon 1	Co-directeur de thèse
Ybert Christophe, Directeur de Recherche CNRS, Université Lyon 1	Co-directeur de thèse

Acknowledgments - Remerciements

Cette thèse a commencé de manière anodine, comme tant d'autres, au milieu du printemps 2017, motivée par une envie de partir de Paris et de se confronter à la "matière active". Entre-temps trois années se sont écoulées à Lyon, riches en expériences et en découvertes. Une pandémie mondiale et un premier confinement pour cette dernière année de thèse, et c'est à Toulouse, durant ce second (deuxième ?) confinement que j'écris ces remerciements.

Naturellement, ceux-ci vont vers mes maîtres de thèse, Cécile Cottin-Bizonne, François Detcheverry et Christophe Ybert, les piliers indispensables à ce travail de recherche qui m'a passionné tout du long. Je les remercie pour m'avoir soutenu, formé et guidé au travers des méandres de la nage interfaciale, mais aussi pour m'avoir laissé cette liberté me permettant ainsi d'être l'artisan de ce travail de recherche.

Je remercie Cécile, le premier support dans toutes les situations, et la première au front pour m'aider à surmonter l'ensemble des problèmes inhérents à une thèse. Je remercie François, dont la porte a toujours été ouverte pour écouter mes hypothèses, et pour m'avoir aidé à élaborer des modèles, des plus invraisemblables à ceux qui ont structuré ma compréhension. Je remercie Christophe, dont les idées aux détours de conversations, gribouillées sur le coin d'un brouillon, ont débloqué des situations, et même, d'ouvrir et de progresser bien au-delà du problème initial.

Je remercie Thomas Bickel et Laurence Talini pour avoir rapporté ma thèse, et Thierry Biben, Isabelle Cantat ainsi que Sébastien Michelin pour l'avoir examinée. Je tiens particulièrement à remercier l'ensemble des membres de mon jury de thèse pour avoir assisté en personne à ma soutenance, acte anodin dans un contexte normal, mais au combien significatif et réconfortant dans ce contexte de pandémie mondiale.

De nombreuses autres personnes m'ont aidé tout au long de cette thèse et il est difficile de tous les remercier, particulièrement quand on est dans l'équipe "Liquide et interfaces". Mais je tiens à émettre une petite pensée pour l'ensemble de mes co-bureaux. Particulièrement ceux de la première heure qui m'ont accueilli les bras ouverts, Marie-Emeline, Teresa et Angélique, et ont fait l'ILM un endroit accueillant dès la première minute. J'ai aussi une pensée pour mes compagnons thésards qui ont rendu ce séjour sur Lyon particulièrement agréable, Antony, Leonel, Ong, Akash, Grégoire, Malèke, Justin, Victor ... Enfin, ces personnes que j'ai joint ou qui se sont joint dans cette quête vers la compréhension de la nage interfaciale, Ronan, Laurent, Maria et Clément.

Je remercie aussi mes compagnons nageurs du club de Villeurbanne et ma famille, qui ont été les supporters indirects de cette thèse. Mais aussi, une thèse c'est aussi parfois un temps passé loin de ses proches. Je m'excuse auprès de mon frère pour ne pas avoir été au premier rang de ses propres réussites, et auprès de ma très jeune nièce pour être un oncle si peu présent.

Finally, I want to thank Cecilia, who gave me a great support for the writing of the manuscript during the first lockdown. You made this last year much easier than it should have been. I hope to do the same for you.

Dynamics of interfacial swimmers

The self-propelled objects are systems using the energy from their environment or carrying their fuel, to transport themselves. They are ubiquitous since our environment is full of mechanical machines or even living beings. Medical issues such as the controlled delivery of medicine, or issues related to the active matter, such as the spontaneous organisation of different scales objects, have led to intense research activity to elaborate new strategies allowing the self-propelling for various sizes systems. Among these strategies, this thesis focuses on a specific class, the interfacial swimmers. The term "swimmer" refers here to the fluid environment in which the moving being operates, more accurately, to the interface between two fluids as underlined by the term "interfacial". This interface is characterised by surface energy, the surface tension, which can be considered as a linear force. To propel themself, the interfacial swimmer induces a surface tension gradient by releasing a chemical specie, a surfactant, or some heat. The classic case is a swimmer propelling at the water-air interface by discharging a surfactant. Even though this type of propulsion was described in 1686, the same century as the vapour machine, the understanding is still low, quantitatively but also qualitatively. Thus, the behaviour prediction as a function of the object characteristic - for instance, the shape - remain partial. Will we obtain a motion? Will it be a translation or a rotation? In which direction? This thesis tries to address those questions by considering the dynamics of a symmetrical object: a disk. To do so, we have developed a complete approach: experimental, theoretical and even numerical, through the elaboration of toy models and simulations implementation.

keywords: Marangoni, self-propelled, camphor, interface, hydrodynamics, surface tension, FEM simulation, interfacial swimmer

Résumé

Les objets autopropulsés, capables de se mouvoir en exploitant une source d'énergie embarquée ou présente dans leur milieu, sont courants dans notre environnement de par les machines mécaniques ou même les êtres vivants qui le peuplent. Pourtant, des problématiques médicales telle que la délivrance contrôlée de médicaments, ou liées à la matière active, telle que la structuration ou l'organisation spontanée d'objets à différentes échelles, ont amené une intense activité sur l'élaboration de nouvelles stratégies permettant l'auto-propulsion d'objets de taille variées. Parmi ces stratégies, cette thèse s'intéresse à une classe spécifique que sont les nageurs interfaciaux. Le terme "nageur" renvoie ici au milieu fluide dans lequel évolue le mobile, et plus exactement à l'interface entre deux fluides comme souligné par le terme "interfacial". Cette interface est caractérisée par une énergie surfacique, la tension de surface, qui peut aussi être considérée comme une force linéaire. Pour se propulser les nageurs interfaciaux génèrent un gradient de tension de surface par libération d'une espèce chimique, le tensioactif, ou de chaleur. Le cas classique étant un nageur se propulsant à l'interface eau-air en relarguant un tensioactif. Paradoxalement, bien que cette forme de propulsion ait été identifiée en 1686 [1], au même siècle que la machine à vapeur, ses caractéristiques n'en restent pas moins partiellement comprises quantitativement mais aussi qualitativement. Ainsi la simple prédiction du comportement d'un objet en fonction de ses caractéristiques - de forme par exemple - reste très partielle. Obtiendra-t-on un mouvement ? Sera-t-il essentiellement translationnel ou rotationnel ? Dans quelle direction ? Ce sont ces questions simples que cette thèse a tenté d'aborder en considérant la dynamique d'un objet parfaitement symétrique : un disque. Pour ce faire, nous avons développé une approche complète du problème en combinant des considérations aussi bien expérimentales que théoriques et même numériques via l'élaboration de modèles-jouets et l'implémentation de simulations.

Du point de vue expérimental, les disques sont constitués d'agarose (1- 15 mm de rayon) chargés en camphre[2]. Nous avons étudié leur dynamique qui se caractérise par une translation spontanée à des vitesses stationnaires. Nous avons ainsi exploré comment cette vitesse de nage dépend de paramètres tels que l'épaisseur d'eau, le temps de nage, etc ... Cette description offre pour la première fois une caractérisation complète et quantitative des propriétés de nage par brisure spontanée de symétrie, étape indispensable à l'établissement d'un cadre explicatif pour ces phénomènes.

Munis de ce corpus de propriétés expérimentales, nous avons élaboré un modèle-jouet générique[3], visant à fournir un cadre théorique à la nage interfacial par brisure spontanée de symétrie. Le principe clé est d'obtenir un découplage effectif entre les problèmes de transport - du tensioactif - et le calcul du champ hydrodynamique. Ceci est obtenu en assimilant le disque en translation stationnaire à un point source chimique dans un écoulement uniforme. Dans un premier temps, nous nous limitons au cas où seule la force capillaire, force de tension de surface sur le contour du nageur, est motrice. Dans ce cas la brisure spontanée de symétrie n'apparaît

[1] Antonio de Heide. Centuria observationum medicarum. Janssonio-Waesbergios, Apud, 1686

[2] Siowling Soh, Kyle J M Bishop, and Bartosz A. Grzybowski. Dynamic self-assembly in ensembles of camphor boats. Journal of Physical Chemistry B, 2008.

[3] Au-delà des nageurs interfaciaux le modèle-jouet générique peut être appliqué aux nageurs autophorétiques.

qu'au dessus d'un nombre Marangoni critique[4]. A haut Péclet[5], le modèle prédit que ce nombre devient proportionnel au nombre Marangoni à la puissance 2/3. De façon remarquable, les différents prédictions de ce modèle simpliste, quant à la vitesse de nage en fonction du la taille par exemple, mais aussi quant au effets de faibles asymétries sur celle-ci, sont en accord semi-quantitatif avec les mesures expérimentales.

En complément, nous discutons des différentes limitations liées aux simplifications sous-jacentes au modèle, en particulier concernant l'absence des effets Marangoni. Via le théorème réciproque de Lorentz, il est possible d'exprimer la force d'interaction visqueuse engendrée par les courants Marangoni, et d'inclure un ersatz de leur contribution dans le toy modèle. Pour ce modèle dit de Lorentz, il n'y a pas de nombre Marangoni critique, contrairement au modèle-jouet générique. Toutefois, la loi de puissance 2/3 est conservée à haut Péclet. Quantitativement, la vitesse de nage prédite est réduite de 60 %, cette abaissement donne une prédiction plus proches des résultats expérimentaux.

Même s'il est possible de proposer un cadre théorique relativement efficient pour décrire la nage spontanée de nos disques de camphre, celui-ci nécessite de nombreuses simplifications notamment sur le traitement de l'hydrodynamique du problème et sur les effets Marangoni. De ce fait, il est intéressant de compléter les approches précédentes par un volet numériques permettant d'explorer le rôle et l'influence des différents mécanismes physiques sur la réponse finale du système. Nous avons donc développé des simulations par éléments finis. Dans le modèle numérique le plus avancé, l'ensemble des couplages caractérisant la propulsion Marangoni sont implémentés. Le diagramme de nage[6] obtenu s'avère plus riche que ceux obtenus avec les modèles analytiques simples. Notamment, il apparaît un point critique défini par un Péclet critique et un nombre Marangoni critique, duquel émerge une branche stable et instable. Le système devient bistable sur une gamme de nombres Marangoni. Dans cette zone, il est nécessaire d'appliquer une perturbation d'amplitude finie pour activer la nage. A haut Péclet, la branche stable vérifie encore cette loi de puissance 2/3 avec une proximité notable avec le modèle-jouet de Lorentz.

De façon remarquable, et en cohérence avec le succès de l'approche analytique simpliste, le diagramme de nage et l'évolution de la vitesse loin du seuil de nage, semble extrêmement robuste au degré de détail de description de la physique utilisé, y compris l'incorporation ou non des effets Marangoni ! Plus en détail néanmoins, les simulations numériques ouvrent un certain nombre de questions à explorer dans le futur. Si la réponse en nage est peu affectée, le détail des champs de vitesse ou de concentration semble fortement influencé par les effets Marangoni, et une comparaison de ces aspects avec des données expérimentales ou des considérations théoriques seraient importantes pour aller plus loin dans la compréhension du système. De même, numériquement il apparaît que la taille de la zone d'émission du tensioactif a une influence notable sur le phénomène. Ainsi, la position du point critique s'éloigne rapidement de l'origine avec l'augmentation de la surface de relargage relative, de telle sorte que nous n'avons pas trouvé numériquement un point stable dans le cas où toute la surfaces du nageur relargue. Pour le moment il y a un hiatus entre la prédiction numérique et les observations expérimentales.

Enfin, l'approche numérique permet d'étudier finement les contributions des différents mécanismes physiques exerçant des forces sur le nageur, notamment par une utilisation judicieuse du théorème de Lorentz. Ainsi nous avons avons introduit dans ce travail le concept de nageur à concentration, pour lequel le relargage du tensioactif n'est pas basé sur un flux, mais une concentration constante sur sa surface. L'idée est fortement contre-intuitive sachant qu'une

[4]Quantifie les forces d'origine capillaire, via l'intensité de l'émission et la sensibilité de tension de surface à la concentration locale.

[5] Ratio entre le transport advectif moyen et diffusif.

[6]Diagramme exprimant le Péclet de nage pour un nombre de Marangoni donné.

concentration constante sur le pourtour indique une force capillaire nulle, c'est donc sur les écoulements Marangoni que doit se reposer la propulsion. Expérimentalement, ce type de nageurs paraît correspondre au cas de disques en camphre pur, qui de fait, nagent en l'absence a priori de force capillaire. Numériquement, nous trouvons bien que les effets Marangoni peuvent effectivement exercer une contribution motrice à distance via la friction visqueuse sur le nageur. Néanmoins, aucun point de nage n'a été trouvé du fait d'une force motrice trop faible par rapport à la force de traînée. Tout en restant prudent, à défaut d'engendrer le mouvement, cette force des courants Marangoni semble pouvoir contribuer à ce mouvement dans le cas de nageurs se dissolvant.

Contents

Preamble

In 1959, Richard Feynman laid the conceptual foundations for nanotechnology and he anticipated one of the most widely discussed applications for molecular machines: nano-robotic surgery and localised drug delivery [2]. Since this famous talk "There's plenty of room at the bottom", the research about nano-micro motor has bloomed, with the development of various strategies and mechanisms beyond classical mechanical motor. Using a chemical motor is one of those strategies. Typically, they have a size going from the molecular to the micro/millimetre scale and they can perform inspection, manipulation, and transport functions in the fields of medicine and engineering [6, 4]. Among them, interfacial swimmers are objects moving at the interface between two fluids. They generate and exploit a surface tension gradient to self-propel by releasing a surface-active quantity, generally a chemical species [5]. They have already been used as a mechanical power supply [3], and a race in performance for speed, duration and control is already engaged [7] to open new fields of application. Even if interfacial swimmers are known for more than three centuries [1] numerous questions remain open about: What is their self-propulsion mechanism? Does an isotropic object swim? How does velocity depend on their size? How do they interact with their environment?

This PhD will bring a contribution to some of those questions. After a first chapter describing the state of the art and introducing the key concepts, the second chapter will present the main experimental results about the individual swimming of a symmetric object. In the third and fourth chapters, we complete our study with respectively analytical models and simulations, starting from a toy model characterising the symmetry-breaking mechanism to simulations modelling the fully coupled problem. Finally, the last chapter gathers the conclusions from our different investigations, together with some perspectives for future work.

Bibliography

[1] Antonio de Heide. *Centuria observationum medicarum*. Janssonio-Waesbergios, Apud, 1686.

[2] Richard P Feynman. There's plenty of room at the bottom. *California Institute of Technology, Engineering and Science magazine*, 1960.

[3] Mark Frenkel, Alla Vilk, Irina Legchenkova, Shraga Shoval, and Edward Bormashenko. Mini-Generator of Electrical Power Exploiting the Marangoni Flow Inspired Self-Propulsion. *ACS Omega*, 4(12):15265–15268, 2019.

[4] Yiying Hong, Darrell Velegol, Neetu Chaturvedi, and Ayusman Sen. Biomimetic behavior of synthetic particles: From microscopic randomness to macroscopic control. *Physical Chemistry Chemical Physics*, 12(7):1423–1435, 2010.

[5] Satoshi Nakata, Yasutaka Iguchi, Sachie Ose, Makiko Kuboyama, Toshio Ishii, and Kenichi Yoshikawa. Self-Rotation of a Camphor Scraping on Water: New Insight into the Old Problem. *Langmuir*, 13(16):4454–4458, 1997.

[6] Walter F. Paxton, Shakuntala Sundararajan, Thomas E. Mallouk, and Ayusman Sen. Chemical locomotion. *Angewandte Chemie - International Edition*, 45(33):5420–5429, 2006.

[7] Abdon Pena-Francesch, Joshua Giltinan, and Metin Sitti. Multifunctional and biodegradable self-propelled protein motors. *Nature Communications*, 10(1):1–10, 2019.

Voilà donc le mouvement dans la matière ! un degré supérieur du mouvement amènerait la vie.
Here, then, is movement in matter. One degree more of movement might bring on life!

Bouvard et Pécuchet by Gustave Flaubert

Chapter 1

State-of-the-art: History and Modern Twists

Contents

1.1 Early steps: from biology to capillarity

1.1.1 Inspiration from the biology locomotion

Self-propelled objects are systems which use the energy from their local environment or carry their fuel, to transport themself. They are ubiquitous, since all biological systems which move by themselves, by definition, are self-propelled objects. More specifically for swimmers, or objects moving in a fluid medium, there is one main strategy to induce self-motion: using a deformable appendage, such as flagella, cilia, fins, wings, etc, and pushing on the surrounding fluid to induce motion. This simple method is used at all the biological scales from whales [26] to bacteria [55].

An alternative method to move is to alter the properties of the surrounding environment to generate a motor force. One property which can be used for this is the surface tension, a force per unit length characterising the property of the interface between two fluids, for example, air and water. This force cannot be exploited without a gradient, in an analogue way that a piston only moves if there is a difference of pressure. To create this gradient, some aquatic Coleoptera, including *velia* and *microvelia* [12], emit a chemical compound which lowers the surface tension. By releasing this product, the water-walkers induce a surface tension imbalance between the front and the rear. As a result, insects propel toward the high surface tension and move forward (see fig right 1.1). This locomotion method allows *microvelia* to have a short transient motion at 17 cm/s, which is twice their normal walking speed. However, creating a surface tension gradient is not a widespread displacement technique in the living kingdom. If a surface tension gradient can be used for propulsion, most of those insects have also to maintain surface tension high enough around them to support their weight and avoid sinking. Indeed, they also use this force against the gravity to maintain their bodies at the surface (see fig. left 1.1).

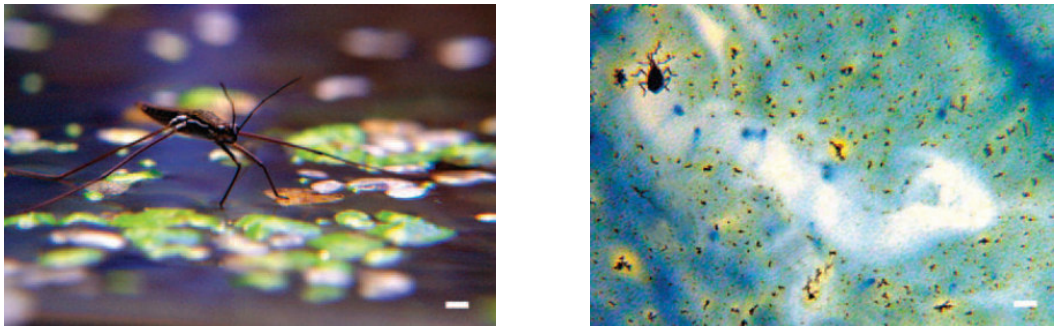

Figure 1.1: Use of surface tension by the insects. (Left) *Gerris* using the surface tension to maintain the body out of the water, only the legs touched the water surface. (Right) *Microvelia* using the surface tension for propulsion. To illustrate the insect motion, there is a blue dye upon the water surface, when the insect releases the surface active product and move, the dye is swept away by the flow created around the insect, which causes the white trail visible on the picture. Those two pictures are from [12]. Scale bars, 1mm.

This propulsion without deformation has inspired artificial self-propelled object design. Indeed, while conceiving an artificial flagellum is a complex task [23], producing an object with no moving part and releasing passively a surface active product (see 1.1.3) is simpler. Despite the rarity of the capillary driven motion in the animal kingdom, the physicists have often associated such artificial interfacial swimmer movement with biological motion. This statement dates back to more than 250 years with the French physicist Romieu alluding to “un mouvement qui ressemble à ceux des animaux” (an animal-like motion) to describe the gyration

movement of camphor grain upon water interface.

1.1.2 Artificial interfacial swimmers, a long history

From a biological point of view, the motion based on surface tension may be a million-year-old method [1]. What about the human-made interfacial swimmers?

The history of artificial interfacial swimmers is exceptionally long and old, compared to the other human-made self-propelled objects. Simple systems such as bark from aromatic tree [69] or a stick with a side coated with sap [2], dropped on a water surface can exhibit this motion based on surface tension propulsion. This facility to create interfacial swimmers makes them likely much older than the first written descriptions which have reached us. According to the introduction about interfacial swimmer by the English physicist Tomlinson [109], the first written observation relating capillary propulsion was made with camphor grain in 1686 by Dr Heide [20] (for more information about camphor see 2.2). Ironically, those camphor grains were not evolving upon water but olive oil, and they were not observed to the naked eye but with one of the early microscopes. However, there is older written testimony (1557) [22] by the botanist Rembert Dodoens, relating camphor thrown upon the water. But, instead of the expected motion, the author described a self-ignition. The different translations between the Latin original text and the final text in old French may explain this strange statement.

In 1748, the French physicist Romieu [95] rediscovered the fast motion of camphor grains upon water. The cause of motion was assumed to originate from the electricity. Since then, the motion of camphor grains have entered in the physics domain and numerous physicists have tried to explain this phenomenon. The electric propulsion was quickly refuted, and in 1787 the famous Italian physicist Volta [109, 69] explained the self-propulsion as a mechanical phenomenon due to vapour emanation from camphor. He also reproduced the same behaviour with little bodies loaded with ether or benzoic acid. In 1794, the Italian physicist Carradori de Prato proved that the existence of a force coming from the air-water interface and an energetic surface-attraction. He tried to explain the camphor grain motion with these new ideas. His views conflicted with those of the Genevan physicist P. Prevost, who stated that the interfacial motion is due to the releasing/creation of an elastic fluid which spreads on the water surface and pushes the swimmer away [21]. Research made during the 19th century and the understanding of the capillarity with Plateau [91], Rayleigh [93], Marangoni [64], etc. gave reason to Carradori. The motion of camphor grains and other similar systems was classified among the capillary phenomena.

During this same century, camphor-related phenomena left the scientific community to reach the popular culture. Through the promotion of the French chemist, physician and politician Raspail, camphor became a very common drug, considered as a cure-all [36]. In correlation, the motion of camphor scrap upon water surface became a well-known phenomenon portrayed in the famous French writer Flaubert's novel *Bouvard et Pécuchet* (1881): "ils l'émiettèrent [une cigarette Raspail] sur de l'eau et le camphre tourna" (they crumbled it [a Raspail cigarette] over some water, and the camphor moved about). At the same time, in popular science journals, they presented descriptions of experiments involving camphor grain or little boat moving with alcohol (see fig. 1.2).

During the 20th century, the curiosity about camphor movement seemed to fade away in Europe and in physics, with no major paper to report. In East Asia, where the natural camphor comes from, children are still playing with old toy [16] based on camphor, called "camphor fish" or "floating doll". Initiated by researchers in Japan, camphor swimmers were re-discovered in 1997 [78] as an interesting experimental system for various physical phenomena at the frontier

[1] Coleoptera have appeared 270 million years ago.

[2] https://www.youtube.com/watch?v=yH9CLwXrICg

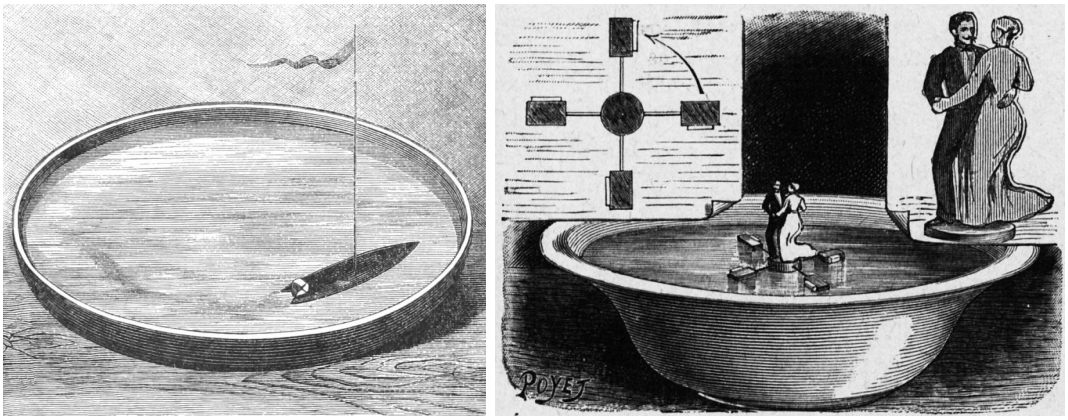

Figure 1.2: (Left) Engraving representing a boat powered by a camphor scrap from *The popular science Monthly Volume 35* (1889). (Right) Engraving made by Poyet representing "perpetual dancers", the rotating movement is maintained as along as camphor is not entirely evaporated, from *La Science amusante* (1894) by Arthur Good aka Tom Tit.

between capillarity, hydrodynamics, or non-linear physics.

1.1.3 Capillarity: Basic Concepts

The surface tension based propulsion is a capillary phenomenon, hence the necessity to introduce here some elements of the associated physics. In this section, we present basic concepts and tools that will be necessary to understand the various phenomena that control interfacial swimming. More elements on those concepts can be found in classical books [19, 1] or popular science articles [12].

a. Surface tension

The surface tension γ is the inherent *free energy per unit area*, associated with the interface creation between two immiscible media. Practically, this means that there is an energy cost, a work δW, needed to create a surface $\mathrm{d}S$ between two fluids, such that $\delta W = \gamma\ \mathrm{d}S$. At the microscopic level, the surface energy originates from the tendency of the molecules composing the fluid to be cohesive with each other and have mutual attraction energy. In the bulk, a molecule is fully surrounded by the fluid and the cohesion energy U is maximized. At the interface, a liquid molecule is only half surrounded by fluid molecules hence a decrease in the cohesion energy. Therefore, creating surface costs an amount of work corresponding to the energy gap between the molecules at the surface and their previous state in the bulk. This statement allows estimating the surface tension given by $\gamma \sim U/2S$, with S the molecule area. We can note that the more cohesive the fluid is, the higher the surface tension. For example, the liquid-air surface tension is typically around 20 $\mathrm{mJ/m^2}$ for an alkane whose cohesiveness arises from van der Waals interactions but rises to γ =72 $\mathrm{mJ/m^2}$ for water interface due to the stronger cohesion of hydrogen bondings and up to γ =1900 $\mathrm{mJ/m^2}$ for liquid iron.

A generic phenomenon arising from this surface tension is the surface minimisation. A system tends to evolve spontaneously toward its minimum energy. Therefore, a fluid would tend toward a state of minimal interface compatible with the constraints applied to the system. This phenomenon explains why the bubbles or the drops evolve spontaneously toward a spherical shape if no external stresses apply to them, the sphere being the shape minimizing the surface for a given volume.

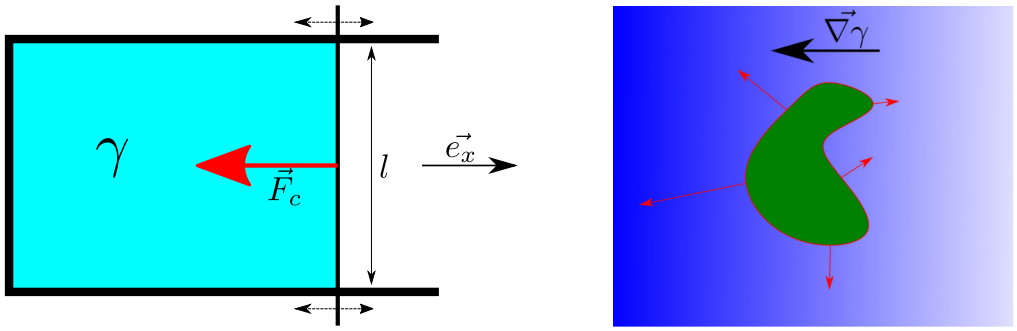

Figure 1.3: Surface tension. (Left) schematic of a famous experiment [19] illustrating capillary force with aqueous film bounded by a rectangle frame with a free moving side. (Right) sketch illustrating the net capillary force experienced by an object submitted to a surface tension gradient, the red arrows are the local quantity $\gamma \boldsymbol{n}$ with $\boldsymbol{n}$ the normal vector to contact line contour.

As stated before, surface tension can also be seen as a lineic force tangent to the interface and driving the system toward a minimum energy state. A classical and simple experiment to illustrate this surface minimisation is a liquid film supported by a rectangular frame composed of three fixed sides and a fourth one moving freely along the normal direction x (see fig. 1.3). Spontaneously, the free side moves toward the inside part of the frame, such that the film surface is reduced. If there is nothing to stop the free side motion, it moves until the liquid film disappears. On the contrary, if we want to extend the film length of the quantity $\mathrm{d}x$, the work needed is

$$\delta W = F \, \mathrm{d}x = 2\gamma l \, \mathrm{d}x, \tag{1.1}$$

with l the frame width, and F a force to produce the work δW. The capillary force exerted by the film on the moving side is $F_\mathrm{c} = 2\gamma l \ \boldsymbol{n}$ with $\boldsymbol{n}$ the normal to the contact line contour, the factor two accounting for the up and down interfaces. We can generalize the capillary force expression to more complex contours:

$$\boldsymbol{F}_\mathrm{c} = \int_{\partial\Omega} \gamma(l) \ \boldsymbol{n} \ \mathrm{d}l, \tag{1.2}$$

with $\partial\Omega$ so-called contact line where the interface is attached to the object. If the surface tension is constant along the contact line surrounding the object, then the net capillary force vanishes [3].

b. Wetting and triple contact line

Generally speaking, wetting describes how a liquid deposited on substrate, solid or liquid, behaves. When a liquid is in contact with a flat and clean substrate, we can observe, either a total wetting, with the fluid spreading as a molecular film on the substrate, or a partial wetting, with the fluid remaining confined into a drop. The spreading parameter S is used to foresee which behaviour occurs. S is the surface energy difference between a dry substrate γ_{SG} and wet substrate $\gamma_{LS} - \gamma$, with γ_{SG}, γ_{LS} and γ respectively the surface tension between the solid and the air, the liquid and the solid, and the liquid and air (see fig. 1.4). If $S > 0$ the affinity between the liquid and the substrate is high enough for a total wetting, if $S < 0$, only a partial wetting occurs. In this case, the liquid does not spread over the solid and forms a drop with an equilibrium angle θ_E.

[3] If γ=cst, then $\boldsymbol{F}_\mathrm{c} \propto \int_{\partial\Omega} \boldsymbol{n} \ \mathrm{d}l$.
Also $\int_{\partial\Omega} \boldsymbol{n} \ \mathrm{d}l = \int_{\partial\Omega} ((\boldsymbol{n}\cdot\boldsymbol{e}_x)\boldsymbol{e}_x + (\boldsymbol{n}\cdot\boldsymbol{e}_y)\boldsymbol{e}_y) \ \mathrm{d}l = \iint_\Omega ((\nabla_s \cdot \boldsymbol{e}_x)\boldsymbol{e}_x + (\nabla_s \cdot \boldsymbol{e}_y)\boldsymbol{e}_y) \ \mathrm{d}S = 0$.

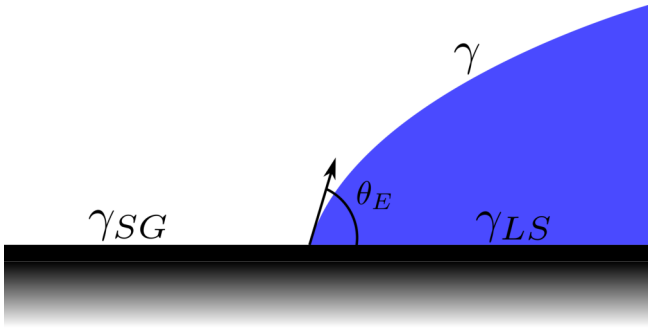

Figure 1.4: Schematic sketch of the triple line.

For the partial wetting, at the contact line between the solid and the fluid, three phases coexist, hence the name of "triple line". The stable contact angle is set by an energy consideration through a virtual work argument that yields to the Young-Dupré law:

$$\gamma_{SG} - \gamma_{LS} - \gamma \cos\theta_E = 0 \quad \Leftrightarrow \quad \cos\theta_E = \frac{\gamma_{SG} - \gamma_{LS}}{\gamma}. \tag{1.3}$$

c. Laplace pressure

The surface tension is also the cause of a pressure discontinuity across a curved surface, known as Laplace pressure:

$$P_{out} - P_{in} = -\gamma \left(\boldsymbol{\nabla} \cdot \boldsymbol{n}\right), \tag{1.4}$$

with $\boldsymbol{n}$ the outward pointing normal at the surface, and P_{out} and P_{in} respectively the outside pressure and the inside pressure accordingly to the definition of $\boldsymbol{n}$. We note H the total curvature, such as $2H = -\boldsymbol{\nabla} \cdot \boldsymbol{n}$, which can also be expressed as $2H = \frac{1}{R_1} + \frac{1}{R_2}$ with R_1 and R_2 the radii curvature in two orthogonal directions. For a spherical drop of radius R we have $R = R_1 = R_2$ thus resulting in $\Delta p = 2\gamma/R$. The pressure inside the drop is higher than the pressure in the surrounding environment. One consequence of Laplace pressure is foam coarsening: the biggest bubbles grow at the expense of the smallest due to the pressure imbalance.

Another well-known consequence of the Laplace pressure is the capillary imbibition where a liquid can rise or invade a porous solid against gravity. Considering a simple capillary tube, if the meniscus curvature inside the tube is negative, then the pressure discontinuity between air and water is negative. To compensate this pressure difference, the water rises into the tube until the hydrostatic pressure gradient eventually equilibrates the Laplace pressure.

d. Surface stress and Marangoni flow

So far, the Laplace pressure provides us with information about the normal stress discontinuity at the interface. What about the tangential stress? Whenever surface tension gradients are present at the interface, the previously explained lineic force reasoning, and the associated capillary force F_c (1.2) makes it clear that there exists a surface stress at the interface. This surface stress induces a boundary condition[4] of the form:

$$\bar{\boldsymbol{\sigma}} \cdot \boldsymbol{n} = \boldsymbol{\nabla}_s \gamma, \tag{1.5}$$

[4]We can generalise to a curved interface:

$$\bar{\boldsymbol{\sigma}} \cdot \boldsymbol{n} = \underbrace{-\gamma \boldsymbol{n} (\boldsymbol{\nabla}_s \cdot \boldsymbol{n})}_{\text{Laplace}} + \underbrace{\boldsymbol{\nabla}_s \gamma}_{\text{Marangoni}} .$$

with $\boldsymbol{n}$ the normal at the interface and $\boldsymbol{\nabla}_s$ is the surface gradient such that $\boldsymbol{\nabla}_s f = \boldsymbol{\nabla} f - (\boldsymbol{\nabla} f \cdot \boldsymbol{n})\,\boldsymbol{n}$, and $\bar{\boldsymbol{\sigma}}$ the stress tensor along the interface. In practice, surface tension inhomogeneity can result from a non-uniform temperature or interface composition. Because a fluid at rest cannot sustain a shear stress, this stress will induce a capillary flow known as Marangoni flow, named after Marangoni who has described it during his thesis [64] about *the tears of wine*[5]. In this phenomenon, a liquid mass transfer is created by an ethanol gradient. Note that the associated flow acts as a homogenising contribution that will tend to damp the temperature or composition heterogeneities.

e. Surfactant

As we just mentioned, different quantities can affect the surface tension such as the temperature[6] or chemical species present at the interface. In this last case, we name the chemical product a surfactant. Surfactant is a special (and majoritarian) class of surface molecules which lowers surface tension at an interface between two media. Because it is involved in many natural and industrial processes, it will be the situation of interest for interfacial swimming, we will hereafter implicitly consider the case of air-water interfaces and surfactants. However, most of the elements equally apply to other liquid-gas or liquid-liquid interfaces.

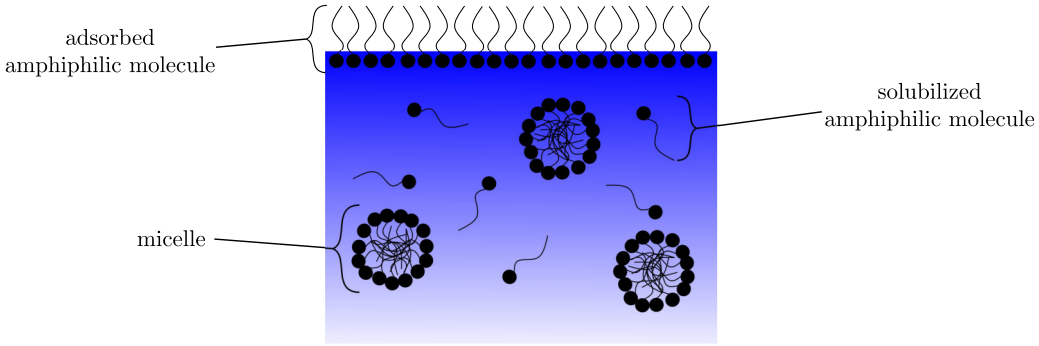

Figure 1.5: Schematic visualisation of amphiphilic surfactant organization.

Commonly, the term surfactant refers to an amphiphilic organic compound with a hydrophobic "tail" and hydrophilic "head". Because of this Janus nature, they organize at the interface, with the tail toward the air and the head toward the water (see fig. 1.5), thus forming an adsorbed monolayer between the polar and apolar surroundings that lowers the interfacial cost. Usual amphiphilic surfactants can be solubilized in the aqueous phase and therefore partition between the bulk and the adsorbed phase. Amphiphilic surfactants are generally associated with a CMC, "Critical Micelle Concentration". Above the CMC, amphiphilic surfactant self-organise into aggregates -spherical for the simplest case- the micelles. In practice, further increase of the solubilized amount of surfactant above CMC essentially modifies the concentration of micelles and no longer affects neither the concentration of free surfactants nor the surface concentration of the adsorbed phase and therefore the surface tension.

Considering the thermodynamic equilibrium, the surfactant bulk concentration, the surface concentration and surface tension are determined by a state function. A general formula to

[5]The name "Marangoni" is often associated with capillarity induced motion phenomena, this is why we refer sometimes to "Marangoni propulsion"

[6]For temperature, the capacity to modify the interface activity is due to the cohesive energy per molecule that depends on temperature, but also the entropic contribution to the free energy: $\gamma S = G = H - TS$ with S the area of the interface, G Gibbs free energy, H enthalpies and S the entropy.

link surfactant concentration to surface tension can be deduced from the Gibbs equation:

$$\Gamma = -\frac{a}{\mathcal{R}T}\left(\frac{\partial\gamma}{\partial a}\right)_{T,p}, \tag{1.6}$$

with Γ the surface concentration, a the activity of the solute, $\mathcal{R}$ is the gas constant, T is the absolute temperature and p is the pressure. For a solute concentration c far from the saturated concentration, we have $a \simeq c$. Then, by assuming that $\Gamma = K_H c$, with K_H the Henry isotherm coefficient, at low activity a we have:

$$\gamma = \gamma_0 - \mathcal{R}T\Gamma, \tag{1.7}$$

with γ_0 the surface tension at $\Gamma = 0$. This formula is only valid for low concentration but it indicates that increasing the surfactant concentration lowers the surface tension and increasing the temperature has the same effect. Analogously, the formula (1.7) can also be seen as the bidimensional equivalent of the perfect gas equation from which it comes that $\gamma - \gamma_0$ the "surface pressure" and Γ are linearly related.

Note that so far we considered soluble surfactants so that the surface tension relates to the bulk concentration. Note however that among the various surfactant molecules, some can be considered insoluble meaning that they are released at the interface by an external source, and hereafter remain confined in a two-dimensional adsorbed layer. As we will discuss in section 1.4, this will have consequences when considering surfactant transport in domains that may be three-dimensional or two-dimensional depending on the case.

1.2 Modern physics

Despite their long history and their appearance in popular and ludic science, interfacial swimmers have kept on being the object of scientific investigations. This section reviews the recent literature on the subject. Because of the rapidly growing literature around self-propulsion topics in the last fifteen years, the only concept of "interfacial swimmers or surfers" has become too broad, encompassing some situations or physical objects that are beyond the scope of this thesis. Therefore we deliberately restrict in this manuscript the meaning of the concept of "interfacial swimmers or surfers" to *self-propelled objects evolving at the interface between two fluids with a motion based on a surface tension gradient generated by surfactant concentration gradient or a temperature gradient.* Accordingly, this does not include several interesting, yet quite separate topics, such as the phoretic particles evolving at an interface [112, 24], oil droplets moving with surface waves or magnetocapillary swimmers [33].

1.2.1 Diversity of the interfacial swimmers

Inspired by Feynman's view in miniature autonomous motile objects [25], or motivated by the fascinating properties displayed by the so-called active matter, a huge recent literature explored possible routes for fabricating self-propelled artificial particles. For interfacial swimmers, this gave rise to several different designs or strategies that we now describe.

a. Materials and Chemistry

The vast majority of the interfacial swimmers bases their motion on generating surfactant concentration gradient. In general, every given chemical species could be surface active to some level, and can, in principle, all be used to generate interfacial propulsion. Hence, the long list of compound used is not very meaningful by itself. However, among all such practical realizations

it is possible to identify three different classes illustrated in figure 1.6, and for which we will give a more detailed description in the following: the "dissolving swimmers", the "loaded swimmers" and the "boats". Note that a review of the different experimental realizations of interfacial swimmers, together with their classification, is presented in table1.2.

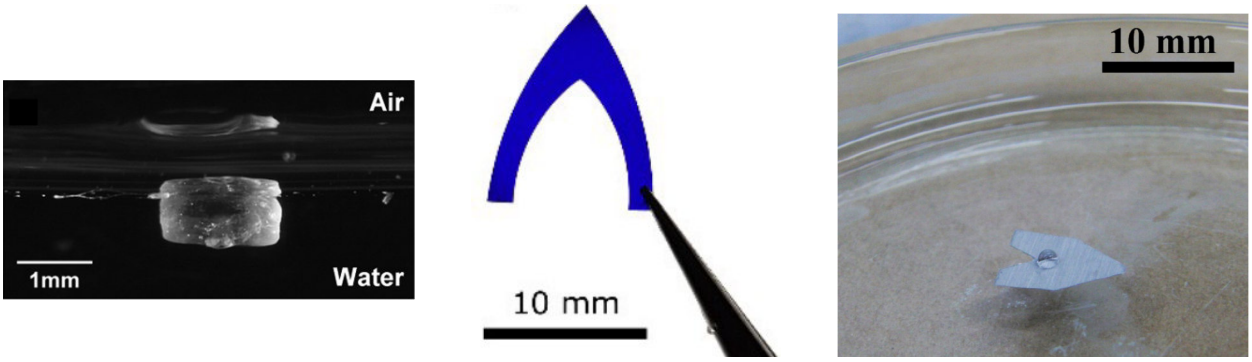

Figure 1.6: Exemples of the three types of interfacial swimmers, from left to right: aspirin [6] (dissolving swimmer), SRT protein - HFIP [88] (loaded swimmer), aluminium-ethanol [74] (boat).

- **Dissolving swimmer**

  The dissolving swimmers are the simplest among all swimmers since they are just made of surfactant. They can be droplet[7] such as aniline oil, pentanol and ethyl salicylate at the water-air interface or dichloromethane drop on a CTAB solution, or a piece of solid substance, such as camphor, benzoquinone, aspirin, etc. Those swimmers are easy to make, but the surfactant properties limit their application. In particular, their swimming is more complex because their size evolves in time while their component dissolves progressively.

- **Loaded swimmer**

  The loaded swimmers are made of a matrix which can be a gel/polymer or a MOF (Metal Organic Framework). The framework is used to hold the surfactant while providing some additional advantages over the previous dissolving swimmers. The gel-polymers give malleable and scalable solid which maintains processability. The matrix containing the surfactant defines the swimmer size and shape, which remain fixed over time. In addition, because the matrix maintains the swimmer's mechanical integrity, it allows for using a wider range of surfactants than the dissolving swimmers. Finally, let us stress that the framework can be used to regulate the release rate of surfactant, and improve the efficiency and durability of the swimmer. Among swimmers belonging to this class, we can quote the agar-gel/camphor system. In this case, the gel is made first and is loaded afterwards with camphor. For acrylamide gel/ ethanol swimmer, the matrix is crafted already loaded by integrating the ethanol in the hydrogel solution. Finally, we can also evoke the framework PCN-222 (MOF) which can be refuelled multiple times.

- **Boat**

  The third and last group are the boats. The boat is made of a passive hull and an active part where the surfactant is released, that for convenience we call "motor". This motor can be a bulk surfactant or a piece of loaded matrix. Another possibility is to carry a fuel tank containing a liquid surfactant and connected with the surrounding fluid by a channel.

[7] We are talking about self-moving floating drop, more explicitly drop moving at the interface between two fluids, generally air and water. They should not be mistaken with self-moving drop evolving in the fluid bulk [61] or on a solid substrate [13].

Generally, they are intrinsically anisotropic with a front and rear part. The most famous boat is certainly the camphor boat since it is not only a scientific object but also a toy[16]. Staying with popular and entertaining realizations, let us mention the so-called "cocktail boat", whose hull is made of edible gelatine containing an ethanol-based surfactant.

As illustrated in table 1.2 of the appendix p.41, the diversity of interfacial swimmers in recent literature is important. Different aspects have motivated the creation of so many new swimmers. An important one is the research of performance (faster, longer duration, ...) and functionality (trajectory control, drug carrier, biocompatibility ...), which can be reached with highly surface active product [88], specific matrix [40], chemical reactions (see following part) and so on. However, when it comes to studying the capillary propulsion in itself, it appears that the most classical camphor swimmer offers appealing characteristics, namely a robust and sustained activity over long durations. In particular, camphor sublimates at room temperature ($\sim$ 20°C). Because of this property, an interface contaminated by camphor self-cleans spontaneously. It allows the swimmers made of camphor to reach a quasi stationary-state even in a confined environment such as a pool. This explains why a huge part of the literature[8] makes use of camphor-derivated swimmers either for boats, loaded or dissolving swimmers. This PhD makes no exception as this old system presents the well-suited properties for the fundamental investigations we wish to carry on.

b. Non-linear behaviours: chemical reactions and molecular interactions

As already mentioned, the upsurge of studies around interfacial swimmers, and especially camphor ones, have been initiated by Japanese teams mostly from the non-linear physics community [83]. A significant part of this literature thus deals with using interfacial swimmers to generate transition towards oscillating dynamics, density waves, etc. Although far from our present interests, we briefly review here some aspects of these studies were non-linear responses are achieved by coupling the surfactant dynamics with a reaction with the liquid medium. In addition to being a significant part of recent studies, they are also a major source of information on the present system.

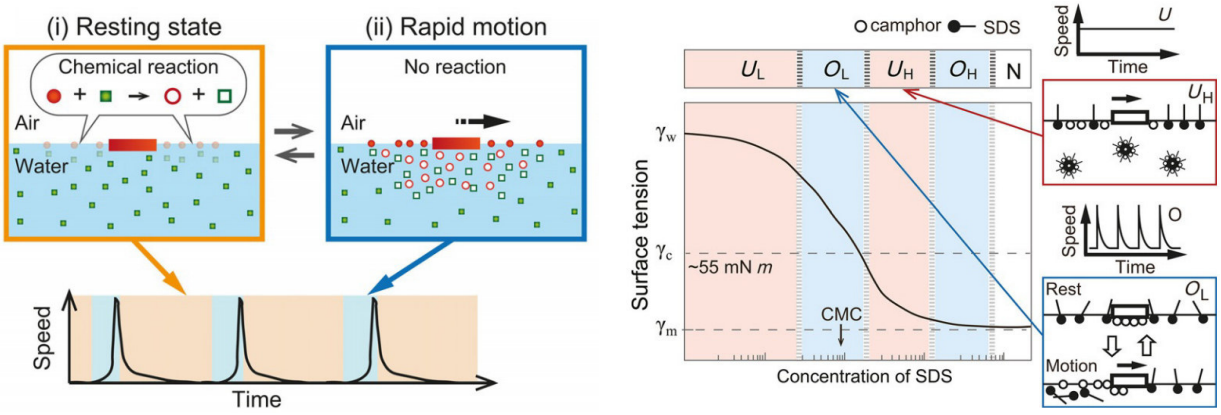

Figure 1.7: Non-linear-behaviour described in pictures from [101]. (Left) schematic illustration of the mechanism for oscillatory motion coupled with a chemical reaction. (Right) surface tension evolution as a function of the SDS concentration, the light red part correspond to the continuous regime, the blue part to the oscillation regime and the white part to the no motion regime. γ_w is the surface tension for pure water, γ_c is the surface tension for aqueous solution saturated in camphor, and finally, γ_m is the minimum surface tension for an aqueous solution of SDS.

[8] [43, 50, 76, 37, 53, 49, 81, 48, 35, 27, 99, 28, 85, 84, 109, 51, 32, 80, 14, 71, 42, 66], etc. (non-exhaustive list).

- **Chemical reaction**

  A first way to change the swimmer behaviours is to couple the surfactant transport with a chemical reaction in the bulk. This allows inducing a series of regime transition controlled by the reactant concentration in bulk. At low reactant concentration, the classical steady-state swimming is achieved, which changes to an oscillatory swimming dynamics at higher concentration and up to a motionless object above some reactant concentration (see left fig. 1.7). Qualitatively, the surfactant S reacts with the reactant R and turns into a new chemical specie S^* with no or a much lower surface activity. Consequently, a competition appears between the release rate of surfactant and the renewing of the reactant, driving to the different regimes. The phenomenon can be reproduced with different chemical reactions [101, 82] such as acid-base, redox and enzyme. An interesting variation appeared when the chemical specie S^* is associated with a surface activity high enough to induce capillary propulsion [101]. In this case, the continuous regime comes back at high concentration after the oscillation mode.

- **Molecular interaction with an anionic surfactant**

  A similar transition between swimming mode can be obtained when an anionic surfactant is used [81] to lower the average surface tension of the water (see right fig. 1.7). However, the mechanism is different, no chemical reaction is involved, and two stages have been distinguished: above or below the anionic surfactant CMC. Below the CMC, the continuous and oscillation modes, have been attributed to the competition between the fuel surfactant, inducing the propulsion, and the anionic surfactant in solution. In few words, if the average surface tension of the solution is too low, the capacity of the fuel surfactant to lower the surface tension becomes too weak to induce a continuous motion, hence the two modes observed. The second stage has been witnessed when the fuel surfactant is camphor and the solution surfactant is SDS. People have observed a "regeneration of continuous and oscillatory motion". This regeneration is attributed to a complex interaction between the camphor and the SDS micelles[43, 84].

In conclusion, the recent literature shows that the dynamics of interfacial swimmers can be much richer than a simple steady-state translation, especially whenever competing species are incorporated in the liquid bulk.

c. Shape

Even if literature reports complex patterns for the swimmers dynamics, we will hereafter focus onto instances of continuous motion. Even with this restriction, there is still a variety of behaviour reported. Irrespective of the swimmer's class considered, observed motions [89] includes: (i) a pure translation motion of the centre of mass, (ii) a pure rotational motion (spinning) or a combination of both yielding for instance to a gyration in circle loops or a spinning swimmer with a weak displacement of the centre of mass. To be more quantitative, the solid motion can be decomposed into a translation associated to velocity U, and a rotation associated with an angular velocity ω. Therefore we can compute the dimensionless number $\mathcal{K} = U/\omega l$ with l the typical size of the swimmer, such that $\mathcal{K} > 1$ corresponds to a swimmer and $\mathcal{K} < 1$ is a spinner. Experimentally, the motion is dominated either by (i) or (ii). Changing the shape of the swimmer allows targeting one of the two motion types.

For the dissolving and loaded swimmers, specific shapes seem to lead to steady translation, like the disk, the U-shape and the arrow shape, while the Y-shape leads to spinning. The elliptic swimmers are peculiar since both translation [37] and spinning [7] were observed. For the boats, the problem is slightly different since the behaviour is also controlled by the position of the

motor on the hull. We can distinguish boats designed for swimming, with one motor at the rear [60], from the boats designed for spinning with multiple motors organised to create a pure torque [70].

The idea that shape controls the motion behaviour is particularly well illustrated by liquid dissolving swimmers. Indeed, self-propelled surfactant drops change their shape according to the motion, contrary to the solid swimmers whose shape is imposed. A small drop of pentanol ($V < 0.1\mu L$) deposited upon water translates and keeps a circular shape, but for bigger drops ($V > 0.1\mu L$) it takes a U-shape with a translation motion. For the spinning regime, drops of PVDF-DMF form spontaneously an asymmetric shape, and they exhibit a self-rotation [116]. Finally, dichloromethane drops on a CTAB solution have two motion regimes [9] depending on CTAB concentration [90]. For the lowest concentration, the drop keeps a circular shape and translates slowly, while for concentration above the micellar concentration the drop becomes a rotator described as "an elongated structure with two sharp tips".

As can be seen from the recent literature, interfacial swimmers can perform both translational or rotational motions depending primarily on their shape, with complex responses being achieved for deformable liquid objects where a coupling exists between shape and dynamics. To date, however, it seems that there exists no clear and general framework that can foresee the response for a given shape. Indeed there exist little studies which compare the stability of different swimming modes. In the following, we will focus on a single mode -translation- to see that the simple description of it for symmetric objects is already challenging. Form effects will be considered shortly for elliptical swimmers, again only with respect to translational motion.

d. Thermal Effects

For the sake of completeness, it is important to finish this review on experimental realizations of interfacial swimmers by mentioning swimmers based on thermo-capillary rather than soluto-capillary effects. From an experimental point of view, this distinction is meaningful. Indeed, contrary to chemical swimmers which carry their "fuel", thermal swimmers get their power from an external source, a blue LED [62] or a halogen light [29] illuminating the set-up. Contrary to the chemical swimmers, such interfacial swimmers are not really autonomous. Coming back to the actual case of external heating thermocapillary swimmer are entirely or partially made of an effective light-absorbing matter. The absorbed light raises the swimmer temperature, and it becomes a heat source, the same way that a chemical swimmer is a surfactant source. As stated in 1.1.3, surface tension gradient can be obtained with a chemical gradient but also with a temperature gradient. From a theoretical point of view, these two groups can be treated the same way, since the heat transport verifies the same equation as the transport of a chemical specie. Although the remaining of the manuscript will focus on soluto-capillary swimmers, a direct extension can be made towards heat-driven systems.

1.2.2 Collective behaviour

So far, we have mostly described phenomena associated with single isolated swimmers, which will be also the configuration studied during this PhD. However part of our initial motivation for these systems was to use them in a many-body configuration as a macroscopic active matter system until we realized that more information would be needed on the single swimmer. Indeed, coupling many interfacial swimmers leads to complex and rich phenomena which have motivated the already mentioned non-linear physics approach to those systems, with the identification of various collective effects such as pattern formation, rhythmic behaviour or spatio-temporal pattern.

[9] There are two other regimes, pulsation and polygonal shape, but associated with a resting drop.

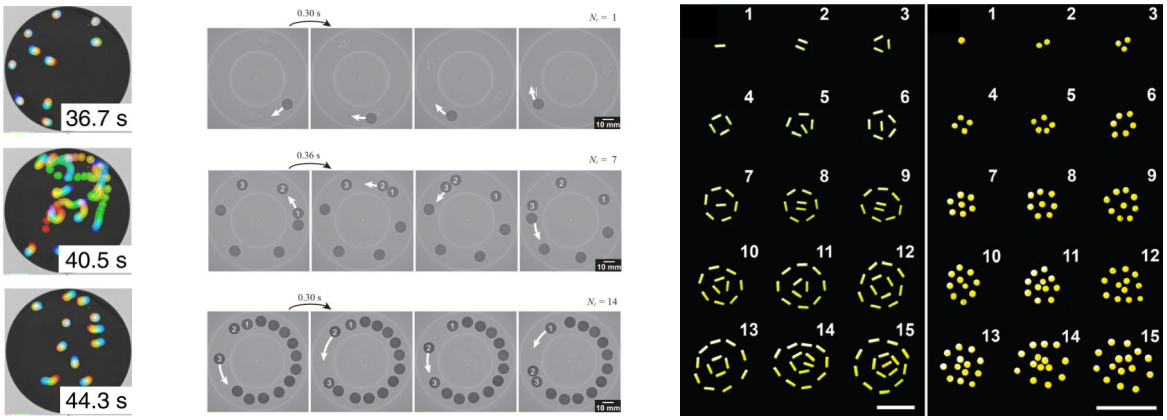

Figure 1.8: Collective behaviour for interfacial swimmers. (Left) three superimposed images of collective motion of 11 agar gel-camphor disks evolving in 40 mm pool at different times. The color indicates the time progress from red to blue. From [104]. (Middle) three regimes for camphor boat in annular channel, from top to bottom, *continuous*, *billard-type* and *catch and release-type*, from [42]. (Right) Pattern formation for camphor agar gel swimmers in shallow water [99]. Scale bar = 1 cm.

Overall, three types of collective behaviours have been observed so far with interfacial swimmers:

- **Intermittency**

  One swimmer displays continuous translational dynamics at a constant velocity. At low densities, this continuous individual motion is preserved. However, above a critical density, the swimmers display a rhythmic behaviour [104, 47]: starting from a near motionless state, a swimmer slowly destabilizes and triggers the motion of all others, thus provoking an activity burst in all the pool (see left fig. 1.8). This burst fades out to a new near motionless period, and the whole sequence starts again. This rhythmic behaviour is qualitatively close to the oscillatory motion mentioned previously 1.2.1, when rests alternate with motion burst. The main difference comes from the coordination of all the swimmers in the pool. At higher density, there is no more motion.

- **Spatio-temporal pattern**

  Spatio-temporal patterns have been observed in a circular narrow channel [101]. For symmetric swimmers[10], three behaviours have been identified, the continuous motion at low densities, then the "billiard-type" where just a few swimmers move creating a collision chain. Finally "catch and release-type", the swimmers form a circular chain cluster, where the head-swimmer detaches and reaches the tail, this action repeats, creating a global chain motion. For camphor boats, because of the intrinsic asymmetric, they move in just one direction. If two are placed in an annular channel they exhibit synchronized swimming [53]. If the number of camphor boats increases the continuous motion is replaced by oscillatory synchronization quantitatively comparable to a traffic flow [102].

- **Swarming and cluster formation**

  Finally, let us mention some recent studies more in line with active matter approaches that have looked for swarming dynamics or cluster formation in interfacial swimmers' assemblies. These collective dynamics were shown to occur in shallow water configurations. This is, for instance, the case for loaded agar gel/ camphor swimmer [99] which start

[10] disks of paper soaked with a methanol solution saturated in camphor, and then dried to remove the methanol.

exhibiting collective behaviours for water depth comparable with the swimmer thickness. Among those, the most impressive is arguably swarming, with a collection of small rod-like surfers self-organizing behind a single big V-shape swimmer to form a moving swarm.

When the swimmers have a similar shape [99], rods or disks, they form spontaneously a static cluster composed of regularly spaced elements, as illustrated in the fig. 1.8, where ones see how surfers organise in regular polygons. This last experiment has been reproduced in [85], but with swimmers from two different groups, loaded swimmers and dissolving swimmers. For agar gel-camphor swimmers (loaded swimmers), the results are the same, the swimmers self-organised in a cluster as described above. For dissolving swimmers the organization is distinct, the swimmers touched each-other and created a dendrite-like pattern. This capacity to interact with other swimmers and in particular to join and to create a new active structure has been reported for other dissolving swimmers, such as aspirin [6] and benzoquinone [97].

1.3 Physics of propulsion

In the previous sections, we went through the major aspects of recent works dealing with interfacial swimmers. For individual swimmers, we focused on the strategies to achieve motion and the means for controlling its dynamics. We then reviewed how complex non-linear or collective effects can arise from the interaction in assemblies of such objects. For all of the above-mentioned topics, a key underlying feature is the physical mechanism that propels the swimmer. We review here the state-of-the-art of the understanding and modelling of this surface tension propulsion. Note that the different attempts for addressing this question have mostly relied on some common simplifying assumptions that we summarize here:

- The interface is flat and the flow verifies the Stokes equations.
- The surfactant is insoluble, which means that its transport is limited to the interface.
- The surface tension γ varies linearly as a function of the surface active quantity $\mathcal{C}$, surfactant concentration or temperature. We introduce the linear factor κ that relates those two quantities.

Unless specifically stated, the following studies are done within the previous framework.

1.3.1 Asymmetric swimmers

As explained in section 1.1.1 and eq. (1.2) a net force on a floating object can arise from an asymmetry of surface tension along its perimeter. The most natural way of achieving this configuration is thus to encode the asymmetry in the design of the interfacial swimmer. This corresponds to the vast majority of the approaches reviewed in this section and thus also corresponds to the framework of most theoretical descriptions.

a. "Historical toy model"

The first model developed to understand the swimmer motility properties corresponds to the basic picture of a surface tension unbalance imposed between the front and the rear of a floater. It is best approached with boat-type because the hull prevents partially the surfactant from surrounding the swimmer. If we assume that the hull totally blocks the surfactant from reaching the top, then we can create a simple toy model allowing to estimate the velocity [74, 11]. We roughly evaluate the surface tension difference between the front and the rear of the boat

$\Delta\gamma$. For instance, the surface tension unbalance for camphor boats is about $\Delta\gamma \simeq 15$ mN/m[11]. The swimmer dynamics verifies an equilibrium of all the forces applying on the swimmer at the steady-state. For the "historical toy model", only two forces are considered the drag force and the capillary force. The capillary force is estimated with $\Delta\gamma$, such that $F_c = \alpha l \Delta\gamma$, with l a typical length of the swimmer and αl the characteristic length for the rear contact line. At this very schematic level, the drag force is assumed as $F_v = K l^p U^n, \quad n = 1, 3/2 \quad p = 1, 3/2$, with K a constant depending on the swimmer geometry and the characteristics of the fluid and U the steady-state velocity. The power n depends on the considered regime, $n = 1$ and $p = 1$ for Stokes flow, and $n = 3/2$ and $p = 3/2$ for the viscous drag boundary layer. Finally, the swimming velocity is given by:

$$U = \left(\frac{\Delta\gamma \ \alpha}{K l^{p-1}} \right)^{-1/n}, \quad n = 1, 3/2 \quad p = 1, 3/2 \ . \tag{1.8}$$

This toy model is the simplest approach and has the virtue of introducing motor and drag contributions on the swimmer. However, it does not address the physics behind each term - especially the capillary force- and can only be used to estimate of orders of magnitude.

b. Towards more realistic models: "Pure diffusion transport models"

The schematic toy model oversimplifies numerous aspects of the problem. For instance, it posits the difference in surface tension and the drag force and does not provide ways of connecting each of them with the details of any given interfacial swimmer. A step further was achieved by *Lauga et al.*[54] who considered the continuous distribution of surface tension and the impact of Marangoni flow on the drag. To do so, they considered a swimmer disk releasing an insoluble surfactant with a prescribed concentration $f(\Phi)$ along the perimeter. The advection is neglected and there are no couplings between the flow and the surfactant distribution. With those specific conditions, the surfactant distribution obeys a purely diffusive transport equation and thus decouples from the hydrodynamic problem. From the computed surfactant distribution, the capillary force can be calculated, together with the boundary conditions for flow problem. The latter is solved and the viscous drag force is calculated form this full hydrodynamic velocity field. The steady-state velocity is given by the equality between those two forces:

$$U = \frac{\kappa c_1 \pi}{4\mu a^2}, \tag{1.9}$$

with μ the viscosity, a the disk radius and c_1 the first term in the cosine series describing the prescribed concentration along the disk contour. If the Marangoni flow is neglected, the new speed is over-predicted by 50%, meaning that the Marangoni flow contribution lowers the steady-state speed and thus acts as a resistive contribution. *Massoud* [65] simplifies the computation by using the Lorentz reciprocal theorem and extends the swimmer geometry to the oblate or prolate shape.

Complementarily, *Würger* has conceived a model based on a closely related principle [115]. Unlike Lauga's treatment of an insoluble surfactant, heat is considered, therefore imposing a diffusive transport in 3D. The source is simpler than the previous model since it is a point source[12] shifted from the centre of a swimmer ball and the heat distribution around the ball swimmer is truncated at the second term in the multipole expansion. Finally, the velocity is given by :

$$U = \frac{\chi}{8} \frac{\kappa}{2\eta} \frac{\mathcal{J}}{2\pi D a}, \tag{1.10}$$

[11] water surface tension is 70 mN/m, the surface tension for a saturated solution of camphor is 55 mN/m.

[12] We call point source, an infinitesimally small source. Mathematically the point source is described by $\mathcal{J}\delta(\boldsymbol{x} - \boldsymbol{X}_s)$, with $\mathcal{J}$ the release rate, δ the Dirac function and $\boldsymbol{X}_s$ the source position.

with b the distance between the point source and the swimmer centre, $\chi = b/a$ a dimensionless number quantifying the geometric asymmetry, η the viscosity, D the diffusion rate and $\mathcal{J}$ the total heat release rate of the point source. We can point out that the velocity is proportional to the asymmetry.

Lauga model is a priori the first one to provide an exact approach for interfacial swimmers. Yet, the validity range is limited to a strict regime: Stokes flow and surfactant/heat transport dominated by diffusion. This last condition is the key in the resolution as it allows neglecting the advection transport. However, a symmetric source verifying a pure diffusion transport will necessarily lead to a symmetric surfactant distribution, and therefore to no driving forces nor motion. Therefore, none of those models can predict the propulsion of an isotropic swimmer.

1.3.2 Isotropic self-propelled object

The "pure diffusion transport models" are accurate but the transport regime used restricts their relevance to asymmetric swimmers. In this section, we focus on isotropic self-propelled objects and their motion, and more accurately, on the processes underlying the spontaneous symmetry breaking mechanism generating the self-propulsion.

a. Interfacial swimmers

The models presented previously have all in common to treat asymmetric swimmers. But what about symmetric swimmers? At first sight, the motion for a symmetric object is not obvious, since asymmetry is necessary to obtain capillary propulsion. However, numerous experiments with a disk-shaped swimmer demonstrated that the motion of a symmetric interfacial object is possible and easy to obtain [31, 35]. Contrary to an anisotropic swimmer, the motion of isotropic self-propelled objects relies on a spontaneous symmetry breaking. Qualitatively, for an interfacial swimmer, let us consider an initial velocity perturbation from the immobile state. Due to this velocity perturbation, the initial symmetry is broken and convective transport will polarize the system along the motion direction. In other words, if the disk moves, the surfactant distribution is no longer symmetric and therefore a net capillary force appears on the object. If the resulting motion enhances the initial perturbation, then there is positive feedback and the speed might increase. This qualitative mechanism underlines the key importance of an object motion to obtain a spontaneous symmetry breaking, which appears as the result of an instability due to convective transport.

Indeed all models on symmetric swimmers are build on this principle and therefore incorporate the motion of the emitting source particle in the surfactant transport equation. However, they share the same stringent simplification by assuming a homogeneous advective flow. De facto, this neglects excluded volume effects together with no-slip boundary conditions on the swimmers. Besides, Marangoni flows are neglected in such scheme and overall surfactant transport reduces to a diffusion equation with a moving source. The capillary force is evaluated from the surfactant distribution which is practically decoupled from the hydrodynamics problem except for being parametrized by the moving velocity U. Meantime, the whole hydrodynamic complexity is bypassed by considering a Stokes drag force $F_{\mathrm{v}} \propto U$. Finally, motor and resistive forces are connected through Newton's law applied to the swimmer and yield an implicit equation for the swimming velocity U. Mathematically, the spontaneous symmetry breaking mechanism for this type of problem has been rigorously proved [14] for a surfactant remaining at the interface and a surface source swimmer.

The older model which verifies this common base seems to have been proposed by *Mikhailov et al.* [68] and describes a disk with a central point source releasing a soluble surfactant, whose

velocity is found to be:

$$U = \frac{2D}{a}\left(1 - \frac{4C\eta D^2}{\kappa \mathcal{J}}\right), \tag{1.11}$$

with C the friction coefficient associated to the disk for the Stokes drag. Since $U \geq 0$, we can define a critical value for the parameters defining the system such as $\kappa\mathcal{J}/\eta D^2 > 4C$. Since the formula (1.11) is obtained with the assumption that the diffusion dominates the mean flow transport, this speed prediction is valid only if surfactant transport is dominated by diffusion.

Following Mikhailov work, some generalisations were proposed to a surface source, to different shapes or to the case of an evaporating surfactant. However, those models focus on the swimming behaviour and/or the spontaneous symmetric breaking itself [83]. To do so, they use a linear decomposition at low speed, such that all the terms in $O\left(U^4\right)$ are neglected. For a simple swimmer disk, they obtain a generic equation corresponding to a subcritical pitchfork bifurcation:

$$\frac{\mathrm{d}\tilde{U}}{\mathrm{d}\tilde{t}} = -(\alpha - \mu)\tilde{U} + \omega\tilde{U}^3 + o(\tilde{U}^3), \tag{1.12}$$

with a critical α value for $\alpha_c = \mu$. This model has numerous variations either simplified for the oldest[76] and/or with other couplings such as a chemical reaction [82]. Those different investigations are described in [83]. Finally, we can note advanced versions of those type of models explaining the particular motion of an elliptical swimmer [49, 37]. For the more complex variations, for instance, with a chemical reaction or elliptical swimmer, the solution is obtained numerically. The analytical solution is found with a linear decomposition at low speed, which means the prediction obtained are only valid at low speed, $U \ll \sqrt{Dk}$, with k the surfactant evaporating rate. Those models are valid in a system whose surfactant transport is dominated by diffusion or/and by the evaporation[13].

In conclusion, all studies to date on the symmetric swimmer motion are based on variations around the same idea and simplifications allowing to uncouple the hydrodynamic and the surfactant transport. Surprisingly enough, despite the model ideas are in principle quite generic, its use has been limited to studying the swimming instability threshold or to the prediction of the swimmer behaviour in a specific environment or condition. Unlike what was done for asymmetric swimmers, there exists no real study on the general steady-state velocity properties.

b. In the bulk: phoretic swimmers and swimming droplets

As we just saw, the modelling of the propulsion mechanism of symmetric interfacial swimmers is implemented with raw simplifications, especially concerning the neglect of the swimmer boundary condition or the Marangoni flow (see 1.4). However, very similar problems also exist in bulk where symmetric object embedded in a 3D medium can also exhibit spontaneous symmetry breaking to self-propel. Although the driving force is no longer a capillary force, the symmetry breaking proceeds from the same sort of instability induced by convective heat or solute transport. It is therefore relevant to review the recent achievement obtained for the description of such systems.

Swimming droplets are artificial microswimmers made of a liquid, self-propelling in bulk solution, and stabilized by an ionic surfactant[61]. The propulsion is based on a Marangoni stress over the drop interface. As is the case for our disk interfacial swimmers, there is no intrinsic anisotropy: the droplets which are initially spherical objects with homogeneous boundary condition for surfactant release at their surface. In the absence of motion, the surrounding surfactant environment is thus expected to be isotropic with no net driving force on the droplet.

[13] $U \ll \sqrt{Dk} \quad \Leftrightarrow \quad \frac{Ua}{D}\frac{U}{ak} \ll 1.$

Yet as for the camphor disks, these droplets are found to self-propel [110, 45] thus exhibiting swimming through a spontaneous symmetry breaking.

Aside from this experimental evidence of spontaneous swimming in bulk from spherical objects, theoretical proposals were put forward to understand this kind of swimmers. Before being extended to the previous case of droplets, they were initially thought around simpler solid objects responding to so-called phoretic mechanisms. These phoretic swimmers exploit the flow generated by the concentration gradient, also known as phoretic flow, to self-propel. Generally, they include two different sides, one is passive, the other is active, that is coated with a catalyser that induces a chemical reaction and therefore a concentration gradient [4]. As far as we are aware, in the case of a reactive isotropic particles, there is presently no experimental report of spontaneous swimming. Yet, it is tempting to explore whether these objects can in principle self-propel as observed for solid disks or liquid droplets.

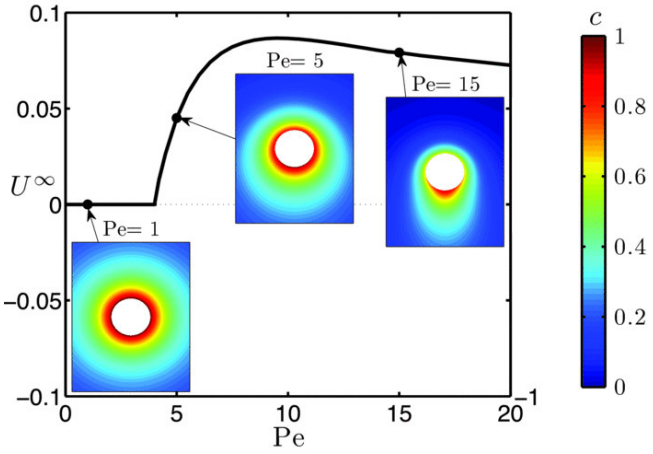

Figure 1.9: Swimming diagram for an isotropic phoretic particle, steady-state swimming speed as a function of the Peclet number, from [67]. The colour scaled figures show the concentration field around the phoretic swimmer at different Pe.

The phoretic swimmer and swimming droplet have a locomotion mechanism based on two different phenomena: phoretic and Marangoni stress. However, a concentration gradient is necessary for both to induce the self-propulsion. The mechanisms are similar enough to be treated both by a generalized chemical interaction approach. This was done by *Michelin and al* [67] who demonstrated theoretically that anisotropy is not necessary for locomotion, thus providing the first rigorous demonstration of a symmetry-breaking instability. In practice, they studied a spherical particle immersed in a Newtonian fluid. The particle has a chemical activity with a solute leading to an isotropic surface emission rate around the object. The gradient in solute concentration induces a slip velocity on the particle surface, such that the speed on the particle boundary is proportional to the concentration surface gradient. To solve the fluid flow, they use the Stokes equations. A trivial solution of this problem always exists in the form of an isotropic concentration field around the particle (see a near-isotropic concentration field at Pe=1, on the fig. 1.9), associated with the absence of flow in the bulk. However, an analytical stability analysis shows that this motionless state may become unstable to velocity fluctuations. This happens at a critical Péclet number $Pe_c = 3$, (this dimensionless number involves diffusion, emission rate and phoretic responsivity), above which velocity fluctuations will be amplified, and the particle will move spontaneously, with the concentration field being no longer isotropic. This prediction explains why self-propulsion has not been reported for isotropic colloids ($Pe_{col} \sim 0.1$ in this case), but indicates that it could be achieved in principle with larger objects. Since then, this first approach has been completed with other studies

to generalize it to the case of droplets and their Marangoni-dominated propulsion. We can note the paper [73] treating deformable self-propelled object, more adapted to the swimming droplets modelling. Other papers treat theoretically the swimming droplets [72, 18] which are the only experimental bulk objects involving in a motion based on a spontaneous symmetry breaking.

1.3.3 Summary of the interfacial swimmer models

We have roughly divided all the models dedicated to the description of the interfacial swimmers in three classes. The table 3.3 below sums up their main aspects and also recall the weaknesses and validity domain:

- The *historical toy models* are valuable to estimate an order of magnitude for the velocity, since they posit a driving and a drag force, but no means to derive them from the details of the problem.
- For the *pure diffusion transport models*, we have an analytical solution for interfacial swimmer[14] but only valid in specific conditions: pure diffusion transport for the surfactant/heat and Stokes flow for the hydrodynamics. Moreover, because there is no advection, the interfacial swimmer considered must be intrinsically anisotropic to achieve motion.
- For the *mobile source models*, the advection due to the excluded swimmer volume and the Marangoni flow are neglected. Since the resistive force is just the Stokes drag force and the motor force the capillary force, the Marangoni flow force applying on the swimmer is also neglected. The models belonging to this group are solved analytically for regimes in which the mean advection transport is negligible compared to the diffusion transport, or/and for systems dominated by the surfactant evaporation.

Models	**Hydrodynamic**	**Transport**	**Swimmer**	**Couplings**
Historical toy models [74, 11]	$F_{drag} \propto U^n$ n=1 ou 2	fixed boundary condition $\Delta\gamma = cst > 0$	Boat (asymmetric)	NC
Pure diffusion transport models [54, 65, 115]	Stokes flow	diffusion	asymmetrical source	$T \rightarrow H$
Mobile source models [83, 68, 76, 15] [37, 49, 50]	$F_{drag} \propto U$	diffusion moving source	unspecific	NC

Table 1.1: Interfacial swimmer analytical models. In "couplings" column, $T \rightarrow H$ means that there is a coupling from the transport on the hydrodynamic, and "NC" means no coupling.

1.4 Marangoni flows

For interfacial swimmers, the surface tension heterogeneity necessary to generate a driving capillary force on the swimmer will also induce a surface-stress that will impact the flow

[14] The solution takes into account the effect of the Marangoni flow in the viscous force applying on the swimmer.

field in the liquid. Even if those flow fields are a constitutive part of the interfacial swimmer problem, the complexity they induce is often not taken into account in the swimming models (see tab. 3.3). Aside from swimmers, these Marangoni flows are also present in a wide variety of situations, and they have an important role in natural or industrial processes. They have thus been the object of a rich literature. But, most of the time, those processes involve a drop of surfactant released atop a thin liquid film ($\sim$ 1 µm), such as for pulmonary surfactant replacement [114] or emulsion and foam stability [44]. Meanwhile, for interfacial swimmers, the Marangoni flow occurs in a thicker layer of water ($\sim$ 1-10 cm), with a moving surfactant source. We review in this section some configurations that involve Marangoni flows and share some similarities with our system.

1.4.1 Fixed source

Before it destabilizes and starts to move, an interfacial swimmer reduces to a fixed surfactant source lying on a liquid subphase, hence the interest for this configuration. The surfactant spreading from a fixed source has a crucial role in natural or industrial processes. As already stated, the shallow water configuration has received a lot of attention (see [34]). However, for interfacial swimmers, the Marangoni flow occurs in a thicker water subphase ($\sim$ 1-10 cm), with a moving surfactant source. Therefore, in this section, we restrict to theories or experiments involving a fixed surfactant source generating the so-called Marangoni convection, but in finite or deep-water configurations comparable with what is found for interfacial swimming experiments.

a. Modelling: steady-state in an infinite half-space liquid phase

The problem of convection induced by capillary stress generated by the spreading of heat has been solved by *Bratukhin et al.*[10]. More precisely, the authors solved analytically the steady-state of a heat point source upon a free surface delimiting a half-space. The flow verifies the Navier-Stokes equation. Because the surface active quantity is the temperature, the transport is not limited to the interface. Note that the results would be equivalent if a soluble surfactant is considered instead of the heat. With this study, the streamlines and the isotherms can be computed for different heat source powers (see fig. 1.10). For instance, the lower-right figure shows isotherms for a low power source: the temperature distribution is dominated by diffusive transport. When the heat source is stronger, a Marangoni flow appears (left), the divergent flow around the swimmer leads to a rising flow under the heat source. This flow "compresses" the isotherm lines, which explains why they are close just under the heat source (upper-right).

A further interesting theoretical study made by *Thess et al.* [107] deals with Marangoni flows. In this paper, the main aim is to describe the spreading of an interfacial active quantity (temperature or surfactant concentration) at high Peclet number (no diffusion transport only advection). The study is developed in [108], the canonical problem is generalized to the effect of finite depth, rotating fluid and to the influence of a magnetic field. A noteworthy aspect yielded by those papers is the "closure law" of the surface velocity induced by a steady surface tension field γ:

$$v(x) = -\frac{1}{2\eta}\mathcal{H}[\gamma](x), \quad \text{(1D)} \qquad v(\boldsymbol{x}) = \frac{1}{4\pi\eta}\int \frac{\boldsymbol{x}-\boldsymbol{x}'}{|\boldsymbol{x}-\boldsymbol{x}'|^3}\gamma(\boldsymbol{x}')\ \mathrm{d}\boldsymbol{x}', \quad \text{(2D)} \tag{1.13}$$

with $\mathcal{H}$ the Hilbert transform[15]. Roughly speaking, the Hilbert transform is like a "soft derivative operator" but non-local. However, Marangoni flow is not proportional to the gradient of

[15]The Hilbert transform is linear convolution with the function $f(t) = 1/\pi t$ [9].

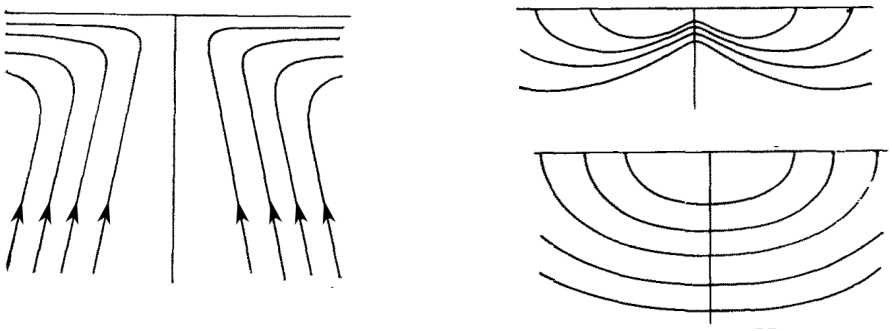

Figure 1.10: Flow and temperature field around a point source. (Left) streamlines $A = 2.24$, with A a parameter governing the source heat power. (Right) Isotherms for $A = 2.24$ and $A = 0.44$ (top and bottom respectively). All the figures are from [10] and illustrate a fixed heat source system over fluid half-space.

surface tension[16]. If we assume that the advection transport dominates the diffusion transport, then the surface velocity expression can be injected in the transport equation, which gives a relation depending exclusively on the surfactant concentration [17]. The one-dimensional problem can be solved analytically [106], and the extension of the surfactant with time is given by $\xi \sim t^n$ with $n = 1/2$ for an insoluble surfactant and $n = 1$ for a soluble surfactant. The paper [8] takes another look at Thess's approach and tries to define an effective diffusion spreading for the surfactant, which would take into account the advection due to the Marangoni flow. Independently, the paper [52] tries also to define properly an effective diffusion and support the experimental observations [103], which defends the idea that the Marangoni flow advection can be injected into the transport equation through an effective diffusion.

Those theoretical studies give us information about the expected behaviour around a fixed swimmer for the Marangoni flow but also the surfactant/temperature distribution. Notably, the closure law given by Thess 1.13, allows us to have a better intuition about surface velocity field. However two points differ from interfacial swimming experiments: first, those models consider a steady-state in an infinite half-space fluid and secondly, they give no information for a moving source.

b. Surfactant spreading in a pool: quasi steady-state

The models presented above involve an infinite half-space liquid phase, whereas the interfacial swimmer experimental conditions are quite different. For instance, the pool is finite, therefore, instead of a steady-state, we consider a quasi-steady state since the surfactant accumulates in the pool. In [94, 56, 5], the experimental conditions are close to the swimmer environment, i.e. Marangoni convection takes place in a pool tens centimetres in width and a few centimetres in depth. From a top view of the pool (see fig. 1.11), the capillary flow organises the space in two concentric areas. There is the inner area with radius R, where the Marangoni flow is fast and divergent. For the outer area, the Marangoni flow is less powerful and the surface fluid motions are characterised by a lower speed and chaotic flows. Our region of interest is the inner area.

References [94, 56] investigate the evolution of R and V_{max}, respectively the radius of the inner area and the maximum flow speed. R and V_{max} mainly depend on the chemical property

[16] A simple example is to take the surface tension $\gamma(x) = x/(x^2 + a^2)$, therefore, the surface flow is given by $v(x) = -a/2(x^2 + a^2)$, at some x position, the flow velocity is finite whereas the gradient of surface tension vanishes.

[17] In [108], the closure law for thin liquid films is also given. Notably, in one dimension, surface velocity verifies $v(x) = -1/4\nabla\gamma$.

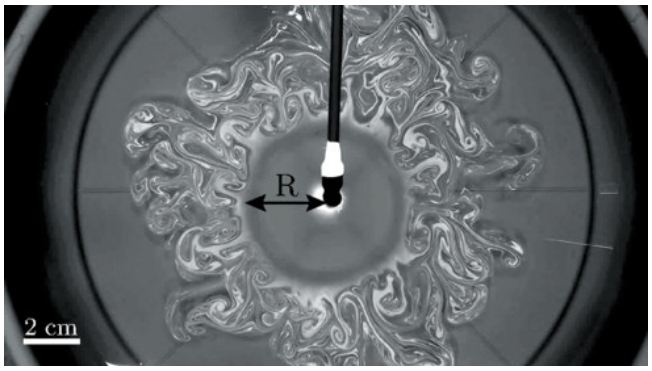

Figure 1.11: Picture representing the flow around a surfactant source (top view) from [56].

of the surfactant. For instance, R and V_{max} are correlated with the CMC, for amphiphile surfactant, or the limit solubility c_s for alcohol, such that $R \propto c^{*-3/4}$ and $V_{max} \propto c^{*1/4}$, with c^* being either the CMC or the limit solubility. Those experimental results support a model developed in [56]. The predicted scaling laws governing the interfacial and bulk flows can be deduced by considering the flows and the surfactant dynamic are coupled through two aspects. First, the Marangoni flow transports the surfactant on a larger distance from the source than the simple diffusion, which increases the surface exchange with the bulk. Secondly, the flow sweeps the subphase and increases the vertical concentration gradient leading to a more efficient diffusion process.

Beyond the evolution of R and V_{max}, an interesting aspect is to know how the surface velocity evolves around the source. The paper [5] treats this point, and verifies a quantitative agreement with the theoretical study made by *Mandre* [63]. They show that adsorbed and solubilized surfactants should exhibit different signatures. In particular, the surface velocity verifies $u(r, z = 0) \propto r^{-n_i}$, with n_i equal to 3/5 or 1 for adsorbed or solubilized surfactant respectively. The experiment uses two amphiphilic compounds[18] characterised whose CMC differ by a hundred. At low concentration[19] the amphiphilic surfactant is mainly adsorbed and can be considered practically insoluble, hence verifying the associated flow field exponent. At higher concentration, the solubility of the surfactant increases, and the dissolved surfactant signatures are verified. Reciprocally, checking the signatures allow characterising the surfactant dynamics [5]. This method is applied to the camphoric acid, a surfactant used to create interfacial swimmers (see tab. 1.2). Contrary to amphiphilic surfactants which are injected via capillary, the camphoric acid is contained in a matrix of agar gel in contact with the water surface. This injection reproduced what we can expect for a fixed loaded swimmer. According to the results, the Marangoni flow induced by the camphoric acid verifies the signatures for an adsorbed surfactant. However, the more widely used camphor has not been tested yet.

A distinct method to inject a surfactant in a solution is from evaporation. In [3], an ethanol drop is maintained above a water surface. The ethanol evaporates from the drop and it condensates at the interface, which generates a Marangoni flow with a velocity of a few centimetres per second. The same phenomenon can be reproduced with a disk of camphor maintained just above the water [51] to study the deep induced by Marangoni flow generated by such system.

In conclusion, the experimental results and the models provide the main scaling laws governing the Marangoni flow and the surfactant spreading for a fixed source. Moreover, those

[18] SDS and Tergitol.

[19] The notion of high and low concentration is relative to the CMC. Here low concentration is for $c < 20\%$CMC and high concentration for $c > 20\%$CMC.

scaling laws have been verified in conditions comparable to interfacial swimming experiments. A noteworthy point: the surfactant spreading is mostly governed by the surfactant CMC or limit solubility, but also by their dynamics, either adsorbed or solubilized.

1.4.2 Mobile source and interfacial swimmer

A legitimate evolution toward the complexity of the interfacial swimmers is to consider a moving source. The literature treating this subject is rather scarce, and we found only one paper [113]. The literature treating the Marangoni flow around a swimmer is more prominent although mostly qualitative. We review those works in this short section.

a. Surfactant spreading from a mobile source

As already mentioned, only one theoretical study [113] treats a moving surfactant source. More accurately, the studied system corresponds to an insoluble surfactant released from a constantly moving point source upon a thin liquid film coating a planar substrate. The main predictions obtained concern the wake created by the mobile source. Notably, at steady-state, the width y of the wake evolves as $y \sim x^{1/3}$ with x, the orthogonal distance from the source along the motion direction. For the surface concentration, we have the scaling law $\Gamma \sim x^{-1/3}$. Those scaling laws are not directly applicable to most of the interfacial swimmer situations since they describe a problem in shallow water conditions.

b. Marangoni flow around a swimmer

The Marangoni flow is one of the main elements missing in the "mobile source models" (see tab. 3.3) describing symmetric swimmer. However, for the models involving asymmetric swimmer, we can extract some prediction about the swimmer/Marangoni flow interaction. The outcome of such interaction is not straightforward as some theoretical studies predict a resistive contribution [54] (see 3.17), while other predicts a motor contribution [111]. In this last case, the swimmer does not evolve in a half-space liquid phase, but on a shallow liquid subphase, with a depth comparable to the swimmer thickness. Otherwise, both are based on Stokes flow and pure diffusion transport. On the experimental side, the reverse motion direction for a V-shape camphor gel swimmer on shallow liquid [99] seems to be closely related to the theoretical phenomena referred to the "Reverse Marangoni surfing" [111]. As a result, the direction of the motion is not the same for a V-shape swimmer in deep or shallow water.

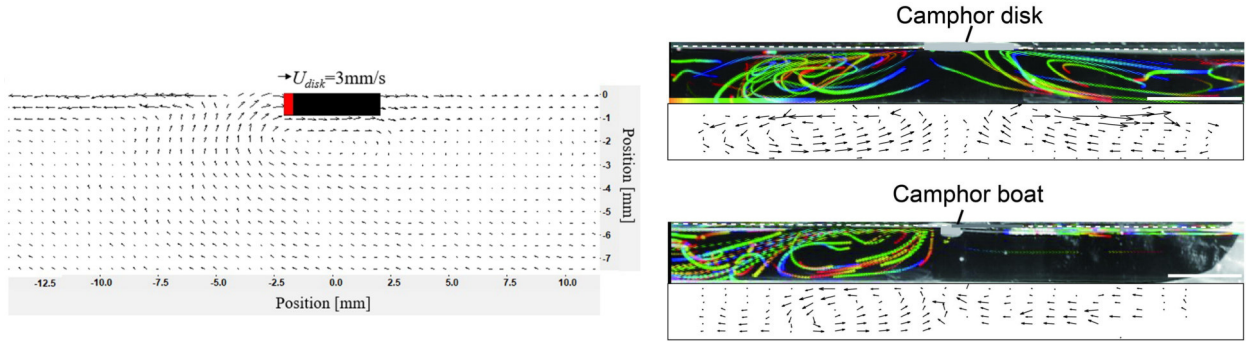

Figure 1.12: Marangoni flow generated around an interfacial swimmer. (Right) horizontal plan of the flow velocity field around boat powered by soap (Dawn), from [105]. (Left) profiles of Marangoni flow for a fixed camphor disk and camphor boat obtained by tracking the locations of visualization particles. The white scale bars are 10 mm long, from [66].

From a more experimental point of view, the existence of Marangoni flows around a camphor swimmer has been known for a long time [109], and has been evidenced during the 19th century with the motion of lycopodium-powder[20] coating an interface. Some experiments seem to underline the role played by the Marangoni flow on the swimmer dynamic. In [66], the effect of Marangoni flow is estimated indirectly by measuring the steady-state velocity of a free swimmer. When the flow is studied quantitatively, the swimmer is fixed. The purpose of the author was to show the difference between a camphor disk (dissolving swimmer), and a camphor boat, measuring the stable speed in different depth conditions: large (20 mm) and small (5 mm). Notably, it seems that the Marangoni flow has a motor contribution for the camphor disk and a resistive contribution for the camphor boat. Indeed, the speed of the camphor decreases in low water depth, because the Marangoni recirculation flow would be less powerful since the rolls can not develop properly (see fig. 1.12). The only experiment where the Marangoni flows are measured for a mobile swimmer is in a very recent contribution [105]. In this paper, the studied object is a PDMS boat with the rear coated with soap. The flow around the boat is quantitatively evaluated with PIV[21]. In the horizontal plane, a divergent flow is observed, it extends over a distance around ten times the swimmer size, and the maximal velocity is about the swimmer speed, with a velocity upstream 10% higher. Notably, the stagnation point is roughly one diameter behind the swimmer. This observation is confirmed in the horizontal plane (see fig. 1.12). The position of the stagnation point is attributed to the time needed for the soap compounds [22] to be adsorbed, and therefore to have a surface activity.

1.5 Summary and questions

In this state-of-the-art chapter, we introduced the interfacial swimmer, the different physical concepts associated with our work and reviewed the relevant research activities around the interfacial swimmer.

Experimentally, the many pieces of research to date have mostly aimed at identifying novel system motivated by the research of functionalities, leading to an important diversity of interfacial swimmers. To order the different kind of interfacial swimmers, we introduced three classes to group them according to their structure: *dissolving swimmer*, *loaded swimmer* and *boat*. Another part of this experimental literature is dedicated to the description of new phenomenologies. Indeed for individual swimmer, studies have explored a wide spectrum of configuration, from the shape of a swimmer or adding reactant or surfactant in the fluid bulk. Overall, those descriptions give qualitative information on the variety of swimmer behaviour: swimming or not, translating or spinning, continuous or intermittent, etc. Surprisingly, only a few studies try to characterise the swimming as a function of simple parameters such as the depth of water or the swimmer size.

On the theoretical side, proposing an analytical model taking into account all the coupling characterising the interfacial swimming is particularly challenging. For asymmetric swimmers, the problem has been solved analytically for Stokes flow and pure diffusion transport. However, because of this last assumption, the models fail to predict the motion for our case of interest: symmetric swimmer. Currently, the class of models treating this type of swimmers allows a spontaneous symmetry breaking by considering the source motion and a homogeneous advective mean flow in the transport equation, thus the Marangoni flow is neglected in those models. Despite this route being in principle quite generic, it has been limited so far to the onset of the swimming instability or to the prediction of the swimmer behaviour in the spectrum of configuration evoked above.

[20] Dry spores of clubmoss plants.
[21] Particule Image Velocimetry.
[22] In all likelihood, mainly amphiphilic molecules.

Despite a long history and a renewed research activity over the recent years, it thus appears that the properties of interfacial swimmers, especially those devoted to symmetric object, lack a clear and quantitative description. It is the objective of the present PhD to contribute to an improved understanding of these systems, focusing on some open questions that we identified in the literature.

(i) **Characteristics of the swimming of a symmetric interfacial swimmer**

Curiously, the velocity of symmetric interfacial swimmers has not been fully characterised yet, in particular, the dependence on size is missing. Similarly, the variations of the speed as a function of some elements inherent to an experiment, such as the depth of water or the time dependency, remain to be clarified. Such missing information limits our ability to understand the physics at stake. In the same line of ideas, only a few considerations have been devoted to the role of the releasing rate or conditions at the swimmer surface. Yet, these processes play a key role in the build-up of the forces driving motion.

(ii) **What is the propulsion mechanism for a symmetric swimmer? Can we predict the velocity of the swimmer?**

Unlike for asymmetric interfacial swimmers, there is currently no model which can predict the spontaneous swimming of a symmetric interfacial swimmer using controlled approximations of the full problem equations. We would like to develop a minimal framework and a simple model that supports the spontaneous propulsion of those symmetric interfacial swimmers. Beyond the propulsion mechanism, the elaboration of models is also motivated to predict and describe the experimental results. In the literature, the models have not been pushed up to experimentally relevant regimes, where it could be critically evaluated against observations.

(iii) **How important are the Marangoni flows?**

As evidenced in the literature review, the Marangoni effects can be quite difficult to model. In the specific case of symmetric interfacial swimmers, the contribution of the Marangoni effects on swimming is still an open question. Proposing developments to assess such contribution are therefore a major direction to explore for achieving a comprehensive description of these systems.

Accordingly, I have developed during this PhD a set of complementary investigations on the dynamics of a single symmetric interfacial swimmer, mostly a camphor disk. This includes the experimental characterizations of the swimming, the development of analytical models aiming at capturing the basic features of such systems and up to the implementation of numerical finite element studies to incorporate and discuss the relative importance of neglected contributions including Marangoni flows.

In more details now, the next chapter is dedicated to the experiments on the swimming of disks made of agarose gel loaded with precipitated camphor. The first part gives a detailed description of the protocol and the set up used to perform the experiments. We characterize the variation of the swimming velocity with the size of the swimmer, the time and the depth of water, but also the effect of a small asymmetry. In parallel to the velocity, we have also studied the dynamics of camphor -its release and the evaporation- which eventually constitutes the underlying driving force for the observed dynamics. Finally, the importance of camphor release mechanism is further revealed by complementing the experiments with camphor-loaded agarose swimmers by experiments with pure camphor swimmers.

In the third chapter, after a presentation of the full equations governing the Marangoni propulsion, we introduce a point-source toy model giving a simple framework for the spontaneous symmetry breaking mechanism by decoupling the transport and the hydrodynamics. In a

subsequent step, we refine the toy model by considering the interaction between the Marangoni flow and the swimmer. The idea is generalised to a spherical interfacial swimmer with a fixed concentration along its surface. Finally, the toy model approach is extended to predict the swimming orientation of elliptical swimmers. We finish by comparing the prediction and the experimental results.

In the fourth chapter, we describe a numerical implementation of the fully coupled problem. After checking its reliability, we display a bifurcation diagram characterising the steady-state. By implementing supplementary elements such as a surface source or a finite Reynolds regime, we study how they change this swimming diagram. We check the stability or instability of the branches composing the swimming diagram, with time dependant simulations. The last part is dedicated to the characterization of the concentration and velocity field around a swimmer, in particular the chemical and hydrodynamic wake.

The manuscript ends with a conclusion gathering the main elements of our investigation, together with some preliminary work and opening perspectives.

1.6 Appendices

1.6.1 Interfacial swimmer classification

Group	Characteristics		References
dissolving swimmer	**fuel**		
	camphor		[78] *
	benzoquinone		[97, 100]
	phenanthroline		[77, 38]
	aspirin		[6]
	coumarin		[79]
	azobenzene crystals		[86]
	aniline oil		[15]
	pentanol		[75]
	dichloromethane		[90]
	PVDF-DMF		[116]
	butyl salicylate		[96]
loaded swimmer	**matrix**	**fuel**	
	agar gel	camphor/ camphoric acid	[99] */[2]
	acrylamide gel / pNIPAAm	ethanol	[98] / [7]
	SRT protein	hexafluoroisopropanol	[88]
	cellulose acetate	peppermint essential oil	[57]
	Pa-co-PN hydrogel	SDS	[58]
	PSA gel	THF	[31]
	polysulfone	DMF	[117]
	P(VDF-co-HFP)	EMIM-TFSI	[30]
	PCN-222	BA/DMF/DEF/DBF	[87]
	CuJAST-1 / HKUST-1	DPA	[41, 39]/[40]
boat	**hull**	**motor**	
	polyester film / PVC tube	camphor	[80] */[28]
	paper	PVDF-DMF	[116]
	PDMS / SU-8	IPA	[59] / [60, 92]
	aerogel/gelatin/aluminium	alcohol	[46]/[11]/[74]

Table 1.2: Chemical interfacial swimmer classification. "*" indicates that numerous articles deal with this swimmer, only the oldest ones is put into the references. Note that the subdivision in a group such as solid and liquid swimmer for the fuel swimmer, or polymer/gel or MOF (Metal Organic Framework) are marked by a black line. Inspired from a table in [88].

1.6.2 Camphor

Camphor is arguably the most used surfactant to generate capillary propulsion. The camphor contribution in the artificial interfacial swimmer is major 1.1.2, and remains major in the current study about interfacial swimmers 1.2. Such a preference is explained by its physical properties. But what is camphor? To answer we base our response on [69].

Camphor is a white, waxy, volatile solid characterised by a strong aroma *Sui generis*. It belongs to the class of terpenoid, with the chemical formula $C_{10}H_{16}O$ (for the 3D structure, see fig. 2.2). Camphor is produced naturally by many plants, but mostly by some tree species, in particular, the camphor laurel, also known as the camphor tree *Cinnamomum camphora*. The camphor laurel is a large evergreen tree, which grows naturally in South East Asia, from Vietnam to Japan. It grows up to 20 -30 mhigh, and some specimens have a circumference above 20 m. An identified property of camphor is to repel the xylophagous[23], which explains why the wood from the camphor tree is acknowledged as resistant to the insects.

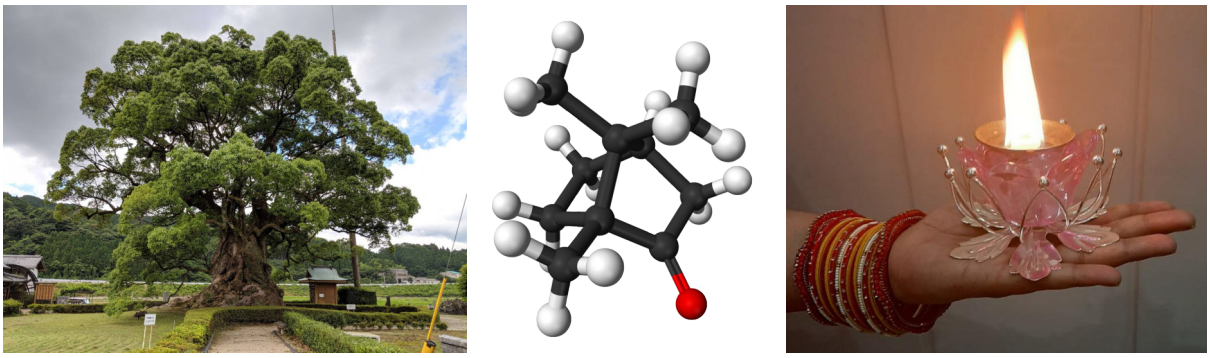

Figure 1.13: (Left) Picture of a camphor laurel. (Middle) Bidimensional structure of the camphor molecule. (Right) Burning camphor in a diya (oil lamp) for the *Aarti*, photo by R. Singh.

The etymology of the word "camphor" [17] is also quite interesting since it explains how camphor came in Europe during the Middle age. "Camphor" come from the medieval Latin "camphora" or "caphura". This word derives from the Arabs "kafur". The Arab merchant may have taken this word from the Sanskrit[24] word "karpuram", from Malay "kapur" which means camphor tree.

The natural camphor is extracted from pulverized wood with condensed vapour. In the native region of the camphor tree, camphor is mostly used as a perfume, in the medicine and as an insect repellent. In India, the camphor is used in the Hindu religious ceremony *Aarti* where it is burnt. Finally, at the beginning of plastic production, it has been used massively use to produce celluloid.

[23] Wood-boring insects.
[24] Liturgical language of Hinduism and Buddhism.

Bibliography

[1] a W Adamson and a P Gast. *Physical Chemistry of Surfaces Sixth Edition*. 1997.

[2] V S Akella, Dhiraj K Singh, Shreyas Mandre, and M M Bandi. Dynamics of a camphoric acid boat at the air–water interface. *Physics Letters, Section A: General, Atomic and Solid State Physics*, 382(17):1176–1180, 2018.

[3] M. Arangalage, X. Li, F. Lequeux, and L. Talini. Dual Marangoni effects and detection of traces of surfactants. *Soft Matter*, 14(17):3378–3386, 2018.

[4] A. Aubret, S. Ramananarivo, and J. Palacci. Eppur si muove, and yet it moves: Patchy (phoretic) swimmers. *Current Opinion in Colloid and Interface Science*, 30:81–89, 2017.

[5] M M Bandi, V S Akella, D. K. Singh, R S Singh, and S Mandre. Hydrodynamic Signatures of Stationary Marangoni-Driven Surfactant Transport. *Physical Review Letters*, 119(26), 2017.

[6] Tamás Bánsági, Magdalena M. Wrobel, Stephen K. Scott, and Annette F. Taylor. Motion and interaction of aspirin crystals at aqueous-air interfaces. *Journal of Physical Chemistry B*, 117(43):13572–13577, 2013.

[7] Noy Bassik, Beza T. Abebe, and David H. Gracias. Solvent driven motion of lithographically fabricated gels. *Langmuir*, 24(21):12158–12163, 2008.

[8] Thomas Bickel. Spreading dynamics of reactive surfactants driven by Marangoni convection. *Soft Matter*, 15(18):3644–3648, 2019.

[9] T. K. Boehme and Ron Bracewell. The Fourier Transform and its Applications. *The American Mathematical Monthly*, 1966.

[10] I. K. Bratukhin and L. N. Maurin. Convection inf a fluid-filling half space. *Pmm*, 31(3):577–580, 1967.

[11] Lisa J. Burton, Nadia Cheng, and John W.M. Bush. The cocktail boat. *Integrative and Comparative Biology*, 54(6):969–973, 2014.

[12] John W.M. Bush, David L. Hu, and Manu Prakash. *The Integument of Water-walking Arthropods: Form and Function*, volume 34. 2007.

[13] M. K. Chaudhury and G.M. Whitesides. How to make water run uphill. *Science*, 256(June):1539–1541, 1992.

[14] Xinfu Chen, Shin Ichiro Ei, and Masayasu Mimura. Self-motion of camphor discs. Model and analysis. *Networks and Heterogeneous Media*, 4(1):1–18, 2009.

[15] Yong Jun Chen, Yuko Nagamine, and Kenichi Yoshikawa. Self-propelled motion of a droplet induced by Marangoni-driven spreading. *Physical Review E - Statistical, Nonlinear, and Soft Matter Physics*, 80(1):1–25, 2009.

[16] M. Chujyo. *Edo Jidai Kodomo Asobi Daijiten*. Tokyodo Publishing, 2014.

[17] CNRTL (Centre National de Ressource Textuelles et Lexicales). Camphre.

[18] Charlotte De Blois, Mathilde Reyssat, Sébastien Michelin, and Olivier Dauchot. Flow field around a confined active droplet. *Physical Review Fluids*, 4(5):54001, 2019.

[19] David Quéré. De Gennes, Pierre-Gilles, Françoise Brochard-Wyart. *Capillarity and wetting phenomena: drops, bubbles, pearls, waves.* 2013.

[20] Antonio de Heide. *Centuria observationum medicarum*. Janssonio-Waesbergios, Apud, 1686.

[21] D.J. Carradori de Prato. Sur les expériences de cit. Prevost de Genève sur la force expansible des émanations odoriférantes, et du citoyen Venturi de Modène sur les mouvemens du camphre sur l'eau. *Annales de Chimie*, 37, 1801.

[22] Rembert Dodoens. *Histoire des plantes, en laquelle est contenue la description entière des herbes... non seulement de celles qui croissent en ce païs, mais aussi des autres estrangères qui viennent en usage de médecine , par Rembert Dodoens... traduite de bas aleman en fr.* 1557.

[23] Rémi Dreyfus, Jean Baudry, Marcus L. Roper, Marc Fermigier, Howard A. Stone, and Jérôme Bibette. Microscopic artificial swimmers. *Nature*, 2005.

[24] Wenjie Fei, Yang Gu, and Kyle J.M. Bishop. Active colloidal particles at fluid-fluid interfaces. *Current Opinion in Colloid and Interface Science*, 32:57–68, 2017.

[25] Richard P Feynman. There's plenty of room at the bottom. *California Institute of Technology, Engineering and Science magazine*, 1960.

[26] F.E. Fish and G.V. Lauder. Passive and Active Flow Control By Swimming Fishes and Mammals. *Annual Review of Fluid Mechanics*, 38(1):193–224, 2006.

[27] Mark Frenkel, Victor Multanen, Roman Grynyov, Albina Musin, Yelena Bormashenko, and Edward Bormashenko. Camphor-Engine-Driven Micro- Boat Guides Evolution of Chemical Gardens.

[28] Mark Frenkel, Victor Multanen, Roman Grynyov, Albina Musin, Yelena Bormashenko, and Edward Bormashenko. Camphor-Engine-Driven Micro-Boat Guides Evolution of Chemical Gardens. *Scientific Reports*, 2017.

[29] Valeri Frumkin, Khaled Gommed, and Moran Bercovici. Dipolar thermocapillary motor and swimmer. *Physical Review Fluids*, 4(7), 2019.

[30] Kazuaki Furukawa, Tetsuhiko Teshima, and Yuko Ueno. Self-propelled ion gel at air-water interface. *Scientific Reports*, 7(1):1–8, 2017.

[31] J. P. Gong, S. Matsumoto, M. Uchida, N. Isogai, and Y. Osada. Motion of polymer gels by spreading organic fluid on water. *Journal of Physical Chemistry*, 100(26):11092–11097, 1996.

[32] Jerzy Gorecki, Hiroyuki Kitahata, Nobuhiko J Suematsu, Yuki Koyano, Paulina Skrobanska, Marian Gryciuk, Maciej Malecki, Takahiro Tanabe, Hiroya Yamamoto, and Satoshi Nakata. Unidirectional motion of a camphor disk on water forced by interactions between surface camphor concentration and dynamically changing boundaries †. *Phys. Chem. Chem. Phys*, 19:18767, 2017.

[33] Galien Grosjean, Maxime Hubert, Ylona Collard, Salvatore Pillitteri, and Nicolas Vandewalle. Surface microswimmers, harnessing the interface to self-propel. (1):1–10, 2018.

[34] D. Halpern and J. B. Grotberg. Dynamics and transport of a localized soluble surfactant on a thin film. *Journal of Fluid Mechanics*, 237(1):1–11, 1992.

[35] Yuko Hayashima, Masaharu Nagayama, and Satoshi Nakata. A camphor grain oscillates while breaking symmetry. *Journal of Physical Chemistry B*, 105(22):5353–5357, 2001.

[36] Jean François Hutin. Raspail, Don Quichotte du camphre! *Histoire des sciences médicales*, 49(2):167–178, 2015.

[37] Keita Iida, Hiroyuki Kitahata, and Masaharu Nagayama. Theoretical study on the translation and rotation of an elliptic camphor particle. *Physica D: Nonlinear Phenomena*, 272:39–50, 2014.

[38] Keita Iida, Nobuhiko J. Suematsu, Yumi Miyahara, Hiroyuki Kitahata, Masaharu Nagayama, and Satoshi Nakata. Experimental and theoretical studies on the self-motion of a phenanthroline disk coupled with complex formation. *Physical Chemistry Chemical Physics*, 12(7):1557–1563, 2010.

[39] Yasuhiro Ikezoe, Justin Fang, Tomasz L. Wasik, Menglu Shi, Takashi Uemura, Susumu Kitagawa, and Hiroshi Matsui. Peptide-Metal Organic Framework Swimmers that Direct the Motion toward Chemical Targets. *Nano Letters*, 15(6):4019–4023, 2015.

[40] Yasuhiro Ikezoe, Justin Fang, Tomasz L. Wasik, Takashi Uemura, Yongtai Zheng, Susumu Kitagawa, and Hiroshi Matsui. Peptide assembly-driven Metal-Organic Framework (MOF) motors for micro electric generators. *Advanced Materials*, 27(2):288–291, 2015.

[41] Yasuhiro Ikezoe, Gosuke Washino, Takashi Uemura, Susumu Kitagawa, and Hiroshi Matsui. Autonomous motors of a metal-organic framework powered by reorganization of self-assembled peptides at interfaces. *Nature Materials*, 11(12):1081–1085, 2012.

[42] Yumihiko S. Ikura, Eric Heisler, Akinori Awazu, Hiraku Nishimori, and Satoshi Nakata. Collective motion of symmetric camphor papers in an annular water channel. *Physical Review E - Statistical, Nonlinear, and Soft Matter Physics*, 88(1):1–3, 2013.

[43] Yumihiko S. Ikura, Ryoichi Tenno, Hiroyuki Kitahata, Nobuhiko J. Suematsu, and Satoshi Nakata. Suppression and regeneration of camphor-driven Marangoni flow with the addition of sodium dodecyl sulfate. *Journal of Physical Chemistry B*, 116(3):992–996, 2012.

[44] Ivan B. Ivanov and Peter A. Kralchevsky. Stability of emulsions under equilibrium and dynamic conditions. *Colloids & Surfaces A 128*, 128:155–175, 1997.

[45] Ziane Izri, Marjolein N. Van Der Linden, Sébastien Michelin, Olivier Dauchot, Marjolein N Van Der Linden, and Olivier Dauchot. Self-propulsion of pure water droplets by spontaneous marangoni-stress-driven motion. *Physical Review Letters*, 113(24):1–5, 2014.

[46] Hua Jin, Abraham Marmur, Olli Ikkala, and Robin H.A. Ras. Vapour-driven Marangoni propulsion: Continuous, prolonged and tunable motion. *Chemical Science*, 3(8):2526–2529, 2012.

[47] Ronan Kervil. *Matière active et écoulements : jets de bactéries et nageurs interfaciaux*. PhD thesis, 2018.

[48] Hiroyuki Kitahata, Shin Ichi Hiromatsu, Yukie Doi, Satoshi Nakata, and Mohammed Rafiqul Islam. Self-motion of a camphor disk coupled with convection. *Physical Chemistry Chemical Physics*, 6(9):2409–2414, 2004.

[49] Hiroyuki Kitahata, Keita Iida, and Masaharu Nagayama. Spontaneous motion of an elliptic camphor particle. *Physical Review E - Statistical, Nonlinear, and Soft Matter Physics*, 87(1):1–4, 2013.

[50] Hiroyuki Kitahata and Yuki Koyano. Spontaneous motion of a camphor particle with a three-mode modification from a circle. 2020.

[51] Hiroyuki Kitahata, Hiroya Yamamoto, Misato Hata, Yumihiko S. Ikura, and Satoshi Nakata. Relaxation dynamics of the Marangoni convection roll structure induced by camphor concentration gradient. *Colloids and Surfaces A: Physicochemical and Engineering Aspects*, 520:436–441, 2017.

[52] Hiroyuki Kitahata and Natsuhiko Yoshinaga. Effective diffusion coefficient including the Marangoni effect. *Journal of Chemical Physics*, 148(13), 2018.

[53] Masahiro I. Kohira, Yuko Hayashima, Masaharu Nagayama, and Satoshi Nakata. Synchronized self-motion of two camphor boats. *Langmuir*, 17(22):7124–7129, 2001.

[54] Eric Lauga and Anthony M.J. Davis. Viscous Marangoni propulsion. *Journal of Fluid Mechanics*, 705:120–133, 2012.

[55] Eric Lauga and Thomas R. Powers. The hydrodynamics of swimming microorganisms. *Reports on Progress in Physics*, 72(9), 2009.

[56] Sébastien Le Roux, Matthieu Roché, Isabelle Cantat, and Arnaud Saint-Jalmes. Soluble surfactant spreading: How the amphiphilicity sets the Marangoni hydrodynamics. *Physical Review E*, 93(1):1–13, 2016.

[57] Ioannis L. Liakos, Pietro Salvagnini, Alice Scarpellini, Riccardo Carzino, Carlos Beltran, Elisa Mele, Vittorio Murino, and Athanassia Athanassiou. Biomimetic Locomotion on Water of a Porous Natural Polymeric Composite. *Advanced Materials Interfaces*, 3(11):1–8, 2016.

[58] Yuling Liang, Yibin Xu, Wei Ye, Dahua Yao, Yunhua Chen, and Chaoyang Wang. Multistage hydrogel rockets with stage dropping-off by thermal/light stimulation. *Journal of Materials Chemistry A*, 6(35):16838–16843, 2018.

[59] Xinchuan Liu, Hao Li, Lei Qiao, and Cheng Luo. Driving mechanisms of CM-scaled PDMS boats of respective close and open reservoirs. *Microsystem Technologies*, 17(5-7):875–889, 2011.

[60] Cheng Luo, Lei Qiao, and Hao Li. Dramatic squat and trim phenomena of mm-scaled

SU-8 boats induced by marangoni effect. *Microfluidics and Nanofluidics*, 9(2-3):573–577, 2010.

[61] Corinna C. Maass, Carsten Krüger, Stephan Herminghaus, and Christian Bahr. Swimming Droplets. *Annual Review of Condensed Matter Physics*, 7(1):171–193, 2016.

[62] Claudio Maggi, Filippo Saglimbeni, Michele Dipalo, Francesco De Angelis, and Roberto Di Leonardo. Micromotors with asymmetric shape that efficiently convert light into work by thermocapillary effects. *Nature Communications*, 6:6–10, 2015.

[63] Shreyas Mandre. Axisymmetric spreading of surfactant from a point source. *Journal of Fluid Mechanics*, 832:777–792, 2017.

[64] Carlo Marangoni. *Sull'espansione delle goccie d'un liquido galleggianti sulla superfice di altro liquido*. 1865.

[65] Hassan Masoud and Howard A. Stone. A reciprocal theorem for Marangoni propulsion. *Journal of Fluid Mechanics*, 741:1–7, 2014.

[66] Yui Matsuda, Nobuhiko J Suematsu, Hiroyuki Kitahata, Yumihiko S Ikura, and Satoshi Nakata. Acceleration or deceleration of self-motion by the Marangoni effect. *Chemical Physics Letters*, 654:92–96, 2016.

[67] Sébastien Michelin, Eric Lauga, and Denis Bartolo. Spontaneous autophoretic motion of isotropic particles. *Physics of Fluids*, 25(6), 2013.

[68] Alexander Mikhailov and D. Meinköhn. Self-Motion in Physico-Chemical Systems Far from Thermal Equilibrium. *Stochastic Dynamics*, 484:334–345, 1997.

[69] D.B.J.L. Millot. *Histoire pharmacologique du camphre*. PhD thesis, 1837.

[70] Tetsu Mitsumata, Jian Ping Gong, and Yoshihito Osada. Shape memory functions and motility of amphiphilic polymer gels. *Polymers for Advanced Technologies*, 12(1-2):136–150, 2001.

[71] Hiroaki Morohashi, Masayuki Imai, and Taro Toyota. Construction of a chemical motor-movable frame assembly based on camphor grains using water-floating 3D-printed models. *Chemical Physics Letters*, 721(November 2018):104–110, 2019.

[72] Matvey Morozov and Sébastien Michelin. Nonlinear dynamics of a chemically-active drop: From steady to chaotic self-propulsion. *Journal of Chemical Physics*, 150(4), 2019.

[73] Matvey Morozov and Sébastien Michelin. Self-propulsion near the onset of Marangoni instability of deformable active droplets. *Journal of Fluid Mechanics*, 860:711–738, 2019.

[74] Albina Musin, Roman Grynyov, Mark Frenkel, and Edward Bormashenko. Self-propulsion of a metallic superoleophobic micro-boat. *Journal of Colloid and Interface Science*, 479:182–188, 2016.

[75] Ken Nagai, Yutaka Sumino, Hiroyuki Kitahata, and Kenichi Yoshikawa. Mode selection in the spontaneous motion of an alcohol droplet. *Physical Review E - Statistical, Nonlinear, and Soft Matter Physics*, 71(6):1–4, 2005.

[76] Masaharu Nagayama, Satoshi Nakata, Yukie Doi, and Yuko Hayashima. A theoretical and experimental study on the unidirectional motion of a camphor disk. *Physica D: Nonlinear Phenomena*, 194(3-4):151–165, 2004.

[77] Satoshi Nakata and Yoshie Arima. Self-motion of a phenanthroline disk on divalent metal ion aqueous solutions coupled with complex formation. *Colloids and Surfaces A: Physicochemical and Engineering Aspects*, 324(1-3):222–227, 2008.

[78] Satoshi Nakata, Yasutaka Iguchi, Sachie Ose, Makiko Kuboyama, Toshio Ishii, and Kenichi Yoshikawa. Self-Rotation of a Camphor Scraping on Water: New Insight into the Old Problem. *Langmuir*, 13(16):4454–4458, 1997.

[79] Satoshi Nakata, Yasutaka Irie, and Nobuhiko J. Suematsu. Self-Propelled Motion of a Coumarin Disk Characteristically Changed in Couple with Hydrolysis on an Aqueous Phase. *Journal of Physical Chemistry B*, 123(19):4311–4317, 2019.

[80] Satoshi Nakata, Masahiro I. Kohira, and Yuko Hayashima. Mode selection of a camphor

boat in a dual-circle canal. *Chemical Physics Letters*, 322(5):419–423, 2000.

[81] Satoshi Nakata and Mai Murakami. Self-motion of a camphor disk on an aqueous phase depending on the alkyl chain length of sulfate surfactants. *Langmuir*, 26(4):2414–2417, 2010.

[82] Satoshi Nakata, Masaharu Nagayama, Hiroyuki Kitahata, Nobuhiko J. Suematsu, and Takeshi Hasegawa. Physicochemical design and analysis of self-propelled objects that are characteristically sensitive to environments. *Physical Chemistry Chemical Physics*, 17(16):10326–10338, 2015.

[83] Satoshi Nakata, Véronique Pimienta, István Lagzi, Hiroyuki Kitahata, and Nobuhiko J Suematsu, editors. *Self-organized Motion*. Theoretical and Computational Chemistry Series. The Royal Society of Chemistry, 2019.

[84] Satoshi Nakata, Ryoichi Tenno, Ayano Deguchi, Hiroya Yamamoto, Yoshikazu Hiraga, and Shunsuke Izumi. Marangoni flow around a camphor disk regenerated by the interaction between camphor and sodium dodecyl sulfate molecules. *Colloids and Surfaces A: Physicochemical and Engineering Aspects*, 466:40–44, 2015.

[85] Hiraku Nishimori, Nobuhiko J. Suematsu, and Satoshi Nakata. Collective behavior of camphor floats migrating on the water surface. *Journal of the Physical Society of Japan*, 86(10):1–9, 2017.

[86] Y. Norikane, S. Tanaka, and E. Uchida. Azobenzene crystals swim on water surface triggered by light. *CrystEngComm*, 18(38):7225–7228, 2016.

[87] Jun H. Park, Slawomir Lach, Konstantin Polev, Steve Granick, and Bartosz A. Grzybowski. Metal-Organic Framework "swimmers" with Energy-Efficient Autonomous Motility. *ACS Nano*, 11(11):10914–10923, 2017.

[88] Abdon Pena-Francesch, Joshua Giltinan, and Metin Sitti. Multifunctional and biodegradable self-propelled protein motors. *Nature Communications*, 10(1):1–10, 2019.

[89] Véronique Pimienta and Charles Antoine. Self-propulsion on liquid surfaces. *Current Opinion in Colloid and Interface Science*, 19(4):290–299, 2014.

[90] Véronique Pimienta, Michèle Brost, Nina Kovalchuk, Stefan Bresch, and Oliver Steinbock. Complex shapes and dynamics of dissolving drops of dichloromethane. *Angewandte Chemie - International Edition*, 50(45):10728–10731, 2011.

[91] J.A.F. Plateau. *Statique experimentale et theorique des liquids soumis aux seules forces moleculaires*. 1873.

[92] Lei Qiao, Di Xiao, Frank K. Lu, and Cheng Luo. Control of the radial motion of a self-propelled microboat through a side rudder. *Sensors and Actuators, A: Physical*, 188(ii):359–366, 2012.

[93] Lord Rayleigh. On the instability of jets. *Proceedings of the London Mathematical Society*, 1878.

[94] Matthieu Roché, Zhenzhen Li, Ian M Griffiths, Sébastien Le Roux, Isabelle Cantat, Arnaud Saint-Jalmes, and Howard A Stone. Marangoni flow of soluble amphiphiles. *Physical Review Letters*, 112(20):1–5, 2014.

[95] M. Romieu. Mémoire sur une nouvelle végétation chymique faite avec le camphre; et sur quelques propriétés de cette substance. *Histoire de l'académie royale des sciences*, page 443, 1756.

[96] Yusuke Satoh, Yoshimi Sogabe, Katsuhiko Kayahara, Shinpei Tanaka, Masaharu Nagayama, and Satoshi Nakata. Self-inverted reciprocation of an oil droplet on a surfactant solution. *Soft Matter*, 13(18):3422–3430, 2017.

[97] Jennifer E. Satterwhite-Warden, Dilip K. Kondepudi, James A. Dixon, and James F. Rusling. Co-operative motion of multiple benzoquinone disks at the air-water interface. *Physical Chemistry Chemical Physics*, 17(44):29891–29898, 2015.

[98] Rachita Sharma, Suk Tai Chang, and Orlin D. Velev. Gel-based self-propelling particles

get programmed to dance. *Langmuir*, 28(26):10128–10135, 2012.

[99] Siowling Soh, Kyle J M Bishop, and Bartosz A. Grzybowski. Dynamic self-assembly in ensembles of camphor boats. *Journal of Physical Chemistry B*, 2008.

[100] Nobuhiko J. Suematsu, Yumi Miyahara, Yui Matsuda, and Satoshi Nakata. Self-Motion of a benzoquinone disk coupled with a redox reaction. *Journal of Physical Chemistry C*, 114(31):13340–13343, 2010.

[101] Nobuhiko J. Suematsu and Satoshi Nakata. Evolution of Self-Propelled Objects: From the Viewpoint of Nonlinear Science. *Chemistry - A European Journal*, 24(24):6308–6324, 2018.

[102] Nobuhiko J. Suematsu, Satoshi Nakata, Akinori Awazu, and Hiraku Nishimori. Collective behavior of inanimate boats. *Physical Review E - Statistical, Nonlinear, and Soft Matter Physics*, 81(5):1–3, 2010.

[103] Nobuhiko J. Suematsu, Tomohiro Sasaki, Satoshi Nakata, and Hiroyuki Kitahata. Quantitative estimation of the parameters for self-motion driven by difference in surface tension. *Langmuir*, 30(27):8101–8108, 2014.

[104] Nobuhiko J. Suematsu, Kurina Tateno, Satoshi Nakata, and Hiraku Nishimori. Synchronized intermittent motion induced by the interaction between camphor disks. *Journal of the Physical Society of Japan*, 84(3):1–6, 2015.

[105] Samrat Sur, Hassan Masoud, and Jonathan P. Rothstein. Translational and rotational motion of disk-shaped Marangoni surfers. *Physics of Fluids*, 31(10):102101, 2019.

[106] A. Thess. Stokes flow at infinite Marangoni number: Exact solutions for the spreading and collapse of a surfactant. *Physica Scripta T*, 67:96–100, 1996.

[107] A. Thess, D. Spirn, and B. Jüttner. Viscous flow at infinite marangoni number. *Physical Review Letters*, 75(25):4614–4617, 1995.

[108] A. Thess, D. Spirn, and B. Jüttner. A two-dimensional model for slow convection at infinite Marangoni number. *Journal of Fluid Mechanics*, 331:283–312, 1997.

[109] Charles Tomlinson. XLVII. On the motions of camphor on the surface of water. *The London, Edinburgh, and Dublin Philosophical Magazine and Journal of Science*, 38(257):409–424, 1869.

[110] Taro Toyota, Naoto Maru, Martin M. Hanczyc, Takashi Ikegami, and Tadashi Sugawara. Self-propelled oil droplets consuming "Fuel" surfactant. *Journal of the American Chemical Society*, 131(14):5012–5013, 2009.

[111] Vahid Vandadi, Saeed Jafari Kang, and Hassan Masoud. Reverse Marangoni surfing. *Journal of Fluid Mechanics*, 811:612–621, 2017.

[112] Xiaolu Wang, Martin In, Christophe Blanc, Maurizio Nobili, and Antonio Stocco. Enhanced active motion of Janus colloids at the water surface. *Soft Matter*, 11(37):7376–7384, 2015.

[113] H. A.R. Williams and O. E. Jensen. Two-dimensional nonlinear advection-diffusion in a model of surfactant spreading on a thin liquid film. *IMA Journal of Applied Mathematics (Institute of Mathematics and Its Applications)*, 66(1):55–82, 2001.

[114] Alastair J.J. Wood and Alan H. Jobe. Pulmonary Surfactant Therapy, 1993.

[115] Alois Würger. Thermally driven Marangoni surfers. *Journal of Fluid Mechanics*, 752:589–601, 2014.

[116] Lidong Zhang, Yihui Yuan, Xiaxin Qiu, Ting Zhang, Qing Chen, and Xinhua Huang. Marangoni Effect-Driven Motion of Miniature Robots and Generation of Electricity on Water. *Langmuir*, 33(44):12609–12615, 2017.

[117] Guanjia Zhao, Tzu Hui Seah, and Martin Pumera. External-energy-independent polymer capsule motors and their cooperative behaviors. *Chemistry - A European Journal*, 17(43):12020–12026, 2011.

E pur si muove!
And yet it moves!

A phrase attributed to Galileo Galilei

Chapter 2

Experiments: spontaneous swimming of a symmetric object

Contents

Introduction

Interfacial swimmers are self-propelled objects which rely on capillary phenomena to move at the interface between two fluids. The simplest example might be the camphor boat: a plastic hull with a scrap of camphor attached at one extremity [11, 5, 9, 17, 8]. The dissolution of camphor locally decreases the surface tension at the rear of the boat, leading to a force unbalance that propels the boat forward. The camphor boat is an asymmetric system. One may wonder what happens in a symmetric system? To put it bluntly, *does a symmetric interfacial swimmer swim?* The question is simple but the answer is far from trivial. Indeed, the mechanism behind Marangoni propulsion requires an asymmetric distribution of surfactant. When the release of surfactant is symmetric, is spontaneous motion possible?

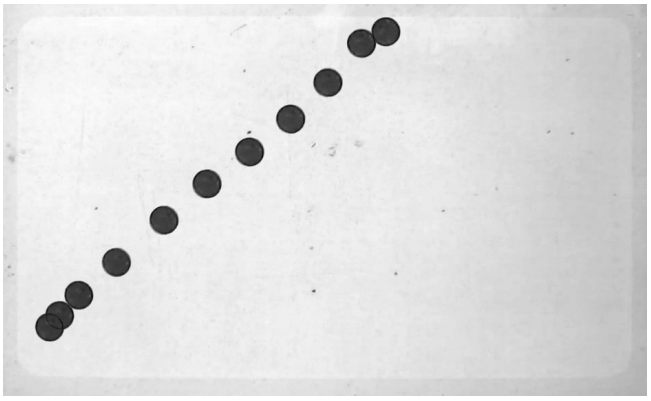

Figure 2.1: Spontaneous motion of a symmetric swimmer. Images superimposition of a disk of agar gel loaded with camphor ($\varnothing = 1$cm) evolving in a pool filled with water. Each picture is separated by 0.3 s.

"And yet it moves", Experiences demonstrate that a symmetric, disk-shaped, interfacial swimmer can move [6]. Following the reference [17], we crafted a disk of agar gel loaded with precipitated camphor. When deposited at the air-water interface, we observe a clear and uninterrupted movement. Thus, a symmetric interfacial swimmer can swim. The propulsion is spontaneous and does not even need to be triggered. The question is no more whether a symmetric swimmer can swim, but how does it swim?

In this chapter, we present our experimental results on the motion of a symmetric interfacial swimmer. We focus primarily on the agarose gel-camphor swimmers, which belong to the class of *loaded swimmers*. We first explain how the swimmers are made, the experimental set-up and analysis tool used. We characterize as much as possible our experimental system, in particular the surfactant release. After discussing the influence of various parameters on the velocity, we focus on its dependence on swimmer size and asymmetry. Finally, we extend our experimental study to the case of pure camphor swimmers, which belong to the class of *dissolving swimmers*.

2.1 Swimmer crafting, set-up and tracking tools

In this section, we describe the preparation protocols for our swimmers, such as those shown in figure 2.1. We also explain our set-up and the method for the measurement of velocity.

2.1.1 Swimmer crafting

All the interfacial swimmers used in this thesis are based on the surface activity of camphor. Either the camphor is infused in a gel matrix, the agarose-gel-camphor disks, or the camphor

is directly used to make the swimmer, the pure camphor disks. We now describe in detail the protocol followed to obtain those different swimmers used throughout this PhD.

a. Camphor

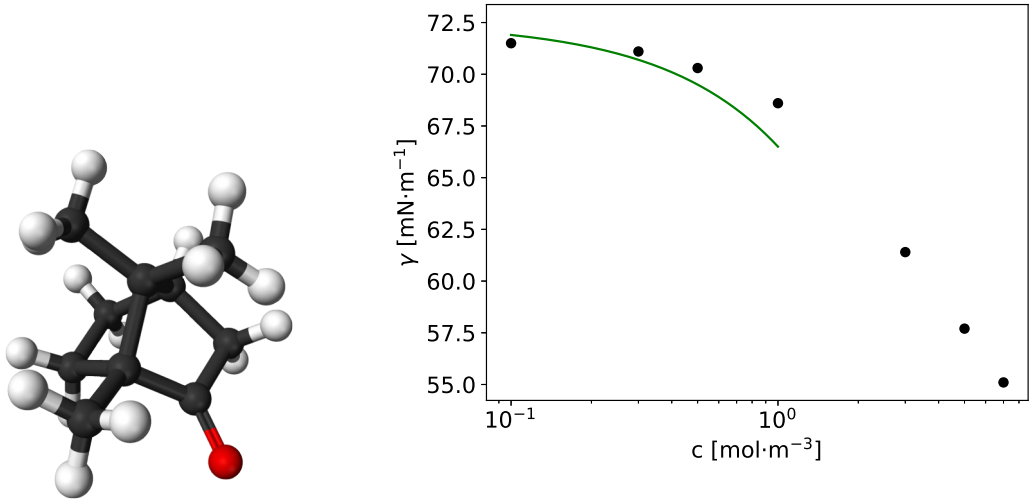

Figure 2.2: Camphor molecule and surface activity. (Left) schematic representation. (Right) surface tension as a function of the camphor concentration. Data from [7]. The green curve is the linear estimation for the low concentration.

Camphor is a compound that belongs to the class of terpenoid, with the chemical formula $C_{10}H_{16}O$. Even though camphor is not an amphiphilic molecule, it can lower the surface tension at the air-water interface (see fig.2.2). At low concentration, the surface tension depends linearly on the camphor concentration $\gamma = \gamma_0 - \kappa c$, with $\kappa = 6\times10^{-3}$ $(\mathrm{N\,m^{-1}})/(\mathrm{mol\,m^{-3}})$ [19]. The choice of camphor as a "fuel" surfactant relies on its ability to evaporate at room temperature ($\sim 21°\mathrm{C}$), which means that an interface contaminated with camphor spontaneously self-cleans with time. As a result, in contrast to most other surfactants, camphor can be released continuously in a solution without saturating the interface. The camphor solubility is high in methanol and ethanol (around 1 g/mL) but low in water (around 1 g/L) [15]. As a consequence, a piece of gel can be loaded with camphor by being soaked in an alcohol-camphor bath. Then the camphor is precipitated into the gel with a second bath of water.

b. Agarose gel-camphor disk

The *loaded swimmers* used for the experiments are disks made of agarose gel loaded with precipitated camphor [17]. This agarose gel is initially a solution of agarose (*ref. 3810 Roth*) -5% in weight- and millipore water.

- The first step is to obtain a melted agarose gel by using a microwave. Next, the bubbles formed are eliminated by maintaining the gel in a liquid state during 20-30 minutes with a hot (T>80°C) water bath. During this process, the gel is contained in a close container to avoid the loss of water by evaporation. The bubbles go up and accumulate at the surface. Eventually, the surface foam can be eliminated manually by removing the top layer of the melted gel.
- The second step is to create a sheet of agarose gel. To do so, the melted gel is poured on a plate and quickly spread with a metal bar. The plate and the metal bar are specifically designed to obtain a sheet of agarose gel with the desired thickness. The small

irregularities, such as bubbles or bumps, and the borders of the sheet are cut out. Before being loaded with camphor, the agarose gel sheet is soaked during at least two hours in methanol or ethanol bath[1]. This allows to remove the unfixed water in the agarose gel and replace it with alcohol, such that water does not interfere during the next step.

- The third step is to load the agarose gel with camphor. The sheet is immersed into a solution of methanol[2] saturated with camphor (*ref. 148075 Aldrich* or *ref. A10936 Alfa Aesar*), around 1.1 g/mL of camphor for methanol at 20°C[3], during at least 12 hours, typically one night. The loaded agarose gel sheets can be conserved in this state during weeks.

- The fourth step is to remove the methanol and to precipitate the camphor inside the agarose gel sheet. The sheet is soaked in two baths of millipore water solution saturated with camphor, 30 seconds each bath. Whereas it was initially transparent, the sheet turns white during the process because of the camphor precipitation. A camphor-saturated aqueous solution is used instead of millipore water to avoid a released of camphor into the bath and then preventing any early ageing phenomena. The second bath is used to remove the camphor crystals formed over the sheet during the first bath. Then, the loaded agarose gel sheet is conserved during the experiments day in a hermetic container filled with camphor-saturated water.

- The fifth and last step is to punch the disks with a circular puncher (Biopsy Punch). The swimmers are ready to use immediately. The final objects are swimmers with a radius a that varies from 1 mm to 11 mm and a thickness $e = 0.5$ mm.

For disks too big to be punched (a >11 mm), or swimmers with non-circular shapes (ellipse, band, rectangle, etc.), the protocol is slightly different. Instead of the punchers, a cutting plotter (*Graphtec CE5000*) is used. Because this step is too long and the cutting board too dirty to be used directly on loaded sheets, the cutting is performed right after the second step on simple agarose gel sheets. The piece of agarose gel produced can be cleaned without risking early ageing or contamination. Then, the production protocol follows the same steps.

c. Pure camphor disk

The pure camphor disks are made of compacted camphor grains. To do so, we use pellet die set, normally dedicated to solid spectroscopy [18]. Camphor, as commercialized, comes in centimetric scraps made of aggregated camphor grains. The first step is to crunch the camphor until the grains separate. Then, we insert the powder in a cylindrical mould [4] sandwiched between two anvils. To control the swimmer thickness, we measure precisely the quantity of powder inserted in the pellet die set, typically 0.025 g for a 4-mm radius disk with a thickness $e = 0.5$ mm. A hydraulic press is used to exert the pressure 300 MPa during at least 10 s. The camphor is easy to compact but it attaches to the anvils, hence the use of disks of parchment paper to protect them and to avoid sticking. The final product is a translucent disk of pure camphor, which is conserved in a hermetic container.

[1] Methanol seems to be a better choice to replace the water in the hydrogel, since this loading step uses a solution of camphor-methanol. However, ethanol bath does not seem to affect the quality of the crafted swimmer. Moreover, during this bath, the system is easier to handle, since ethanol requires less precaution than methanol.

[2] An interesting attempt to report is to substitute methanol with ethanol during the loading process. Indeed both chemicals dissolve the same quantity of camphor, and the ethanol has the advantage to be easier to manipulate since it does not require a fume hood. However, at the precipitation step, the sheet obtained was not homogeneously white, and irregularities were visible. We observe that such irregularities do not affect the ability to swim.

[3] The real criteria is to observe undissolved camphor grains in the solution.

[4] For us the possible diameters were 8 mm and 13 mm.

d. Partially loaded swimmer and floating agarose gel

To get information on the separate contributions between the swimmer hydrodynamic size and the surface releasing the surfactant (see 2.2.3), we use what we call "partially loaded swimmers". Those swimmers are disks of agarose gel with two concentric parts, the core and the crown. "Core swimmers" have their core loaded in camphor and the crown made of bare gel. For "crown swimmer", it is the opposite.

Because the bare gel sinks in water and detaches from the loaded part. To solve this issue, we have conceived "floating agarose gel". We modify the agarose gel buoyancy by adding glass bubbles. The weight proportions are 94% of millipore water, 5% of agarose and 1% of glass bubbles (*3M Glass Bubbles-K20 Series*, whose density is 0.2 g/cc). The glass bubbles increase the gel buoyancy and make it float. Then, we prepare gel sheets as described above[5].

Because we want our partially loaded swimmers to be as symmetric as possible, the agarose gel is not cut out manually but with a cutting plotter. The piece of agarose gel obtained is loaded following the protocol described above[6]. The loaded and unloaded pieces are assembled into one swimmer just before use.

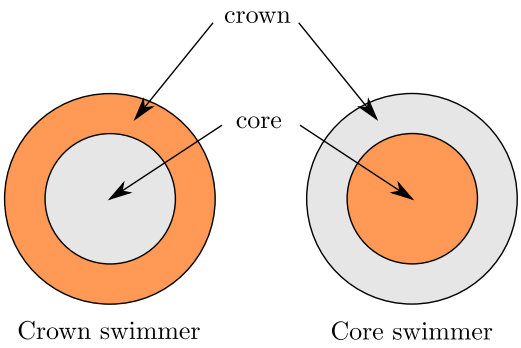

Figure 2.3: Partially loaded swimmers, the orange part is loaded with camphor while the grey part corresponds to agarose gel lightened with glass bubbles.

2.1.2 Experimental set-up

Once the swimmer is prepared, it is laid upon water contained in a pool. We observe that the motion can be very sensitive to surface contamination. It is necessary to protect the setup and to follow a cleaning protocol. To extract quantitative information, the motion is recorded with a camera, then analysed with a tracking program. Because tracking requires a well-contrasted image, special care is given to the lightning. In this section, we describe the set up used to respect all this constrains.

Camera To record the motion of the camphor swimmers, the camera is placed above the swimming pool (see fig. 2.4). We use a Canon PowerShot S110, taking either 30 frames (1280×720 pixels) per second or 24 frames (1920×1080 pixels) per second. The first configuration is the "default" one. When the tracking program requires a better image quality, we use the second setting.

[5]Note that the melted floating gel has to be agitated before crafting the sheet gel. Then, the glass bubbles are homogeneously dispersed in the gel. Air bubbles are not a problem as long as the surface sheet remains flat.

[6]When a thin agarose gel structure has to be loaded, such as a crown, it should be with the complementary surrounding agarose gel sheet in which it has been cut it out. Indeed the agarose gel is deformable, and during the loading process, the thin structure can deform. But when the camphor precipitates within the gel, it gets stiffer and the deformed shape is fixed.

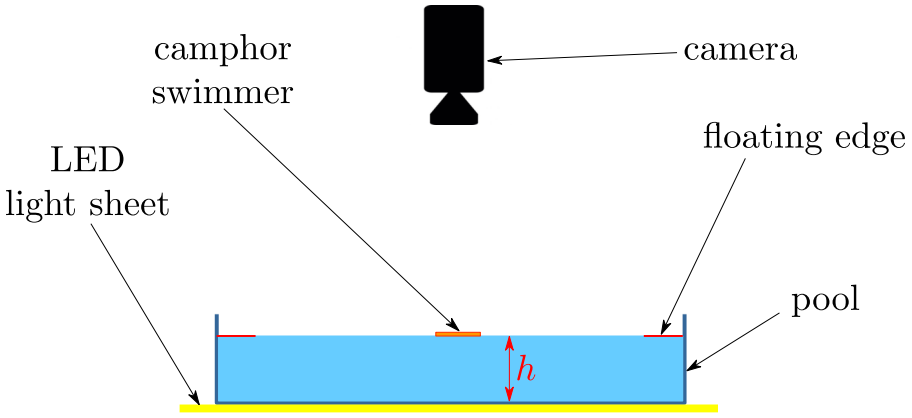

Figure 2.4: Experiemental set-up.

Pools and lightning Three pools have been used in this thesis.

- If not mentioned otherwise, we use a plexiglass rectangular pool ($17 \times 27 \times 1$ cm) with a capacity of 459 mL. It has been specifically designed to be used at full capacity of water. Indeed, the border is a two steps stair, such that for one-centimetre water depth, the water contact line is at the top of the first step. Thus, the water surface is nearly flat.
- The second pool is a glass cylindrical water tank ($\varnothing = 23$ cm), used for higher water depth, up to 8 cm depth.
- The third pool is specifically used for "big" swimmers, with a typical radius higher than 12 mm. This pool is made of white plastic, with the dimension 540×385×80 mm, and it is not transparent.

The first plexiglass and glass pools are both transparent. The set up is backlighted with a LED light sheet, as illustrated in fig 2.4. Because the third pool is made of opaque plastic, backlighting is not possible, the lighting comes from multiple spots around the pool. All pools are filled with millipore water, whose depth h is obtained indirectly from the volume of water poured.

Figure 2.5: Floating edges for the circular pool($\varnothing = 22.5$ cm).

Floating edges To prevent the swimmer from getting stuck at the pool border, we use a floating edge [7]. Indeed, a general behaviour observed for agarose gel-camphor swimmers is the tendency to follow the pool edges, in particular in circular pools. [13, 10]. A solution is to use a

[7] The two steps border for the rectangular pool allows to have a flat water surface, but the same effect can be obtained by using a floating edge .

reinjecting system, typically a "flower" shape floating edge (see fig 2.5), inspired from [5]. The principle is simple, by following the petal contour the swimmer is reinjected toward the pool centre because of the sharp petal ends. In practice, the floating edge is cut from a thin film of plastic (polyester) and it surrounds the free surface. For the cylindrical pool, the floating edge is always used, for the rectangular pools, except for exceptions[8] the floating edge is useless.

Environment and cleaning process The experiments are performed in an air-conditioned room with temperature in the range 22-23°C. The swimmer motion is sensitive to the contamination by any exterior agent. We have taken several precautions to minimize such contamination. First, the whole set-up is covered by a plexiglass box ($53 \times 66 \times 37$ cm) which mostly prevents the dust from reaching the interface. Second, we organise our experimental sessions in "runs", that is the recording of one swimmer evolving in the pool, for a typical duration of 15-30 mn. Between each run, the water surface is partially sucked ($\sim$ 30mL over $\sim$ 500mL) and replaced by clean water. Every hour, after about three runs, the pool is drained and refilled with millipore water. Though we followed this protocol systematically, it might not have been strictly necessary. Indeed, as described in appendix 2.5.1, three swimmers in three successive runs without cleaning process in between, reproduce the same behaviour. For long runs ($\sim 1-3$ h) the dust contamination rests upon the protection box and the experimentalist care since there are neither cleaning process nor water renewal during the run.

2.1.3 Tracking tools

We now explain how the swimmer motion is extracted from the video recording. The swimmer position is identified in each frame, giving a list of positions that are used to reconstruct the trajectory.

Tracking target The tracking program gives the position on each frame of a "tracking target". To be efficient the target must appear well contrasted on the video frame, such that it is much whiter or darker than the uniform background. In most cases, it is the swimmer itself. Indeed, with backlighting, the agarose-gel disk appears as a dark grey circle over a light grey background (see fig. 2.1). However, in some conditions, the swimmer can not be used as a target because of an insufficient contrast. For instance, this is the case, with an agarose-gel swimmer evolving over the white background of the big pool, or when the light goes through the pure camphor swimmer or the floating agarose gel. We use then as the tracking target a thin black plastic disk ($\varnothing = 2$mm) laid on the swimmer upper face. Note that the target weight (0.428 mg) remains small compared to the swimmer mass (around 1% of a 4-mm pure camphor swimmer mass).

Tracking program The tracking program is mostly based on the python libraries *Trackpy* and *opencv*. The first step is to treat the image by removing the background, determined by averaging 100 frames randomly picked in the video. Then, a tracking function based on the Crocker–Grier algorithm [3], is applied to the image. Briefly, the image is first submitted to a convolution with a Gaussian characterized by a width comparable to the target size. The position of the particle centre is then identified as the maximum in the convoluted image. Other features such as the "mass" (= surface $\times$ brightness) or the surface eccentricity[9] as also determined, which can be used to discriminate potential failures.

[8] For strip swimmers (3×30 mm), we use a specific floating edge constituted of multiple peaks preventing the strips to get close to the pool wall, otherwise, they tend to stop translating and spin close to the wall.

[9] Zero for a circle and one for a line.

The Crocker–Grier algorithm is efficient as long as the tracking target is just a few pixels wide (< 15 pixels), but the computational efficiency decreases quickly for wider targets. Indeed, convoluting with a wide Gaussian is numerically expensive. Accordingly, for large targets, we divide the tracking process into two steps. First, the number of pixels in the image is lowered, and we apply the Crocker–Grier algorithm on this pixelated image, which yields a first approximation for the swimmer position, the image is then cropped in the vicinity of the estimated position and the exact position is obtained using a circle Hough transform [22]. To link the swimmer positions from one frame to the next, the algorithm uses prediction from velocity. In our case, since there is only one swimmer, this step is mostly used to remove the tracking errors.

By tracking the swimmer position $(x_i,\ y_i)$ as a function of frame time t_i, we obtain the trajectory. The instantaneous velocities are computed through simple discretization.

$$u(t_i) = \frac{x_{i+1} - x_i}{t_{i+1} - t_i}, \quad v(t_i) = \frac{y_{i+1} - y_i}{t_{i+1} - t_i}, \quad U(t_i) = \sqrt{u(t_i)^2 + v(t_i)^2}, \tag{2.1}$$

with u and v the velocity components in direction x and y, U the speed modulus and i the frame number.

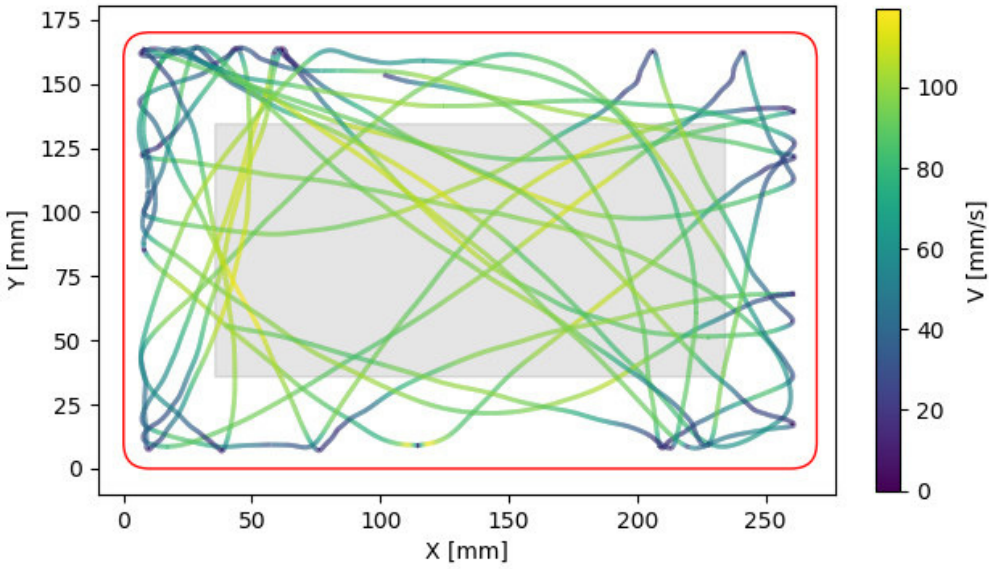

Figure 2.6: Trajectory of an individual swimmer. The swimmer is a 6-mm radius agarose gel swimmer in the rectangular pool (border in red), h=0.5cm, the trajectories extend from 180 s to 280 s, the speed is represented by a colour scale. Only points in the light grey rectangle are considered when computing the velocity (see 2.1.4). Note that to obtain a continuous trajectory from discrete data, we use a spline interpolation function. Example of trajectory data without interpolation can be seen in figure2.26 shows data less treated (just a conversion from pixel to millimetre)

2.1.4 Exclusion area

We are interested in the steady motion of swimmers. However, the swimmer motion is interrupted by the borders of the pool. We can note on figure 2.6, that the swimmer speed changes along the trajectory. In particular, the velocity is not constant in the vicinity of the wall: the swimmer first stops upon hitting the wall, then it accelerates to reach a plateau until it touches a border again. To discard the velocity variation near the borders, we have defined an exclusion area, which includes all space located at a distance d_p or less from an edge (see

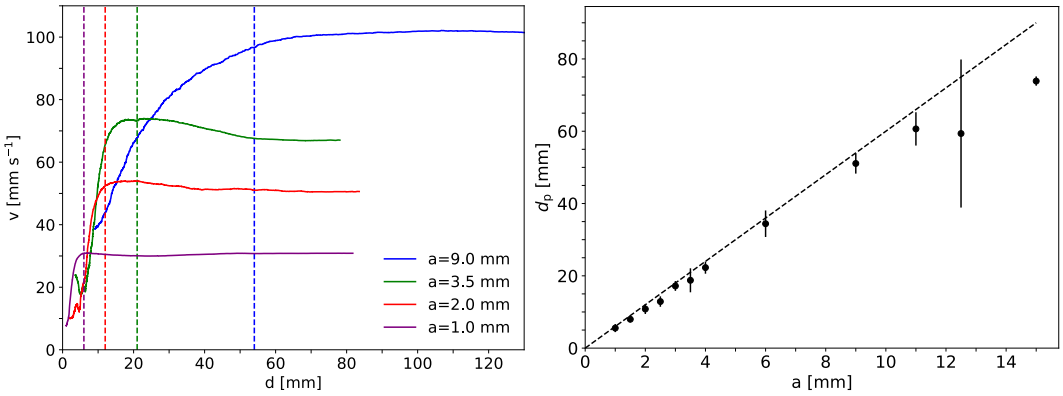

Figure 2.7: Effect of walls on the swimmer average velocity. (Left) the continuous lines show the average velocity over time for arbitrary runs as a function of distance from the wall. The vertical dashed lines the 6-radii exclusion zone. (Right) characteristic length as a function of swimmer radius. The dashed line corresponds to $d_p = 6a$.

fig. 2.6). All data presented in this chapter were obtained from the central area of the pool, outside the exclusion area.

Figure 2.7 (left) shows how the swimmer average velocity depends on the distance to the wall. When the swimmer is in contact with the border, the velocity is minimal. It then increases until it reaches a plateau, at a value that depends on the swimmer size. Defining d_p as the largest distance at which the deviation of the speed exceeds 5% of the plateau magnitude, we find that to a good approximation $d_p = 6a$ (see right fig. 2.7). The extent of our exclusion area is thus proportional to the swimmer size.

Note that our definition of exclusion length is sufficient to avoid boundary effects but it is not sufficient to characterize how the swimmer interacts with the wall. In particular, we do not distinguish between swimmers going toward or away from the wall, whereas the behaviour is not symmetric: a sudden slow down in the former, and a smooth acceleration for the latter (see figure 2.6).

2.2 Individual motion of a symmetric swimmer: agarose-gel swimmer

Now that we have presented the preparation protocol for crafting swimmers and the experimental set-up, we can now focus on the main system of our study, the disk of agarose gel loaded with precipitated camphor or in brief "the agarose gel swimmer". Our first task is to characterize how much camphor is released by the swimmer, a key quantity of our system. We then explore the dependence of the swimmer velocity on various controlling parameters.

A preliminary remark is in order, that applies to all this chapter. Most of the results are graphs displaying dots with an error bar. Unless specifically stated, the dot is the mean value over time if the results are extracted from a specific run or an average over several swimmers if the experiment has been reproduced multiple times. The error bars correspond to a P confidence interval obtained from Student's law, generally $P = 0.95\%$. When there is no error bar, the dots correspond to the raw measurements on a single swimmer.

2.2.1 Camphor dynamics: released and evaporation

A key process underlying the swimmer motion is the release of camphor in the liquid. Here we provide a quantitative characterization and a simple picture for it. Independently, we also

provide an order of magnitude for the evaporation rate k.

a. Experimental observations

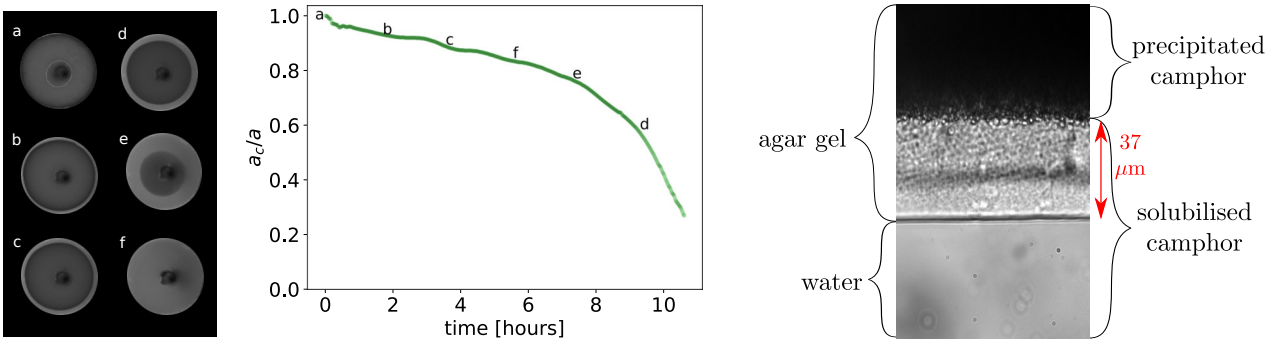

Figure 2.8: Time evolution of the agarose swimmer aspect. (Right) time evolution of the radius of loaded core radius a_c over the swimmer radius a for an immobile disk. Pictures from a top view of the swimmer illustrate this evolution through time. We observed three decreasing phases, the early fast regime (t< 1 h), followed by a long 7-hours linear decreasing, and finally an acceleration with a concave decreasing during the three last hours. The swimmer is kept fixed, by being impaled on pin (darker spot in the middle). $a = 2.5$ mm. (Left) Picture of the depletion layer for a 15-min old swimmer. Note the expected thickness for the depletion layer is 33 µm, according to (2.5).

The visual aspect of our swimmers changes with time. While uniformly white initially, two concentric regions appear after approximately one hour, from a top view: a transparent crown surrounding an opaque core[10]. The radius of the core a_c is plotted in figure 2.8, showing a decrease that is constant at first, then accelerating. Another phenomenon is revealed by closer examination with a microscope: looking at a vertical cross-section of the swimmer (see right fig. 2.8), two identifiable domains appear, separated by a distinct interface. A thin layer of transparent gel - that we call "boundary layer", can be seen which grows with time, thus reducing the volume occupied by the precipitated camphor. The transparent layer presumably corresponds to a region where camphor is solubilised. Note that those observations are consistent with those made in [1] in closely related system (swimmer based on camphoric acid).

In the following, we propose a simple interpretation for the boundary layer, based on a one-dimensional model and a diffusion process of the camphor. An understanding of the transparent crown long time behaviour is more complex, as it involves a two-dimensional problem. A minimal model is discussed in appendix 2.5.2.

b. The growing diffusion layer model

Inspired by those qualitative observations, we now elaborate a simple model describing the camphor release dynamics, from which we can determine $\mathcal{J}$ the total release rate. This model is based on the idea that the camphor flux is controlled by the growing depleted layer around the loaded core described above. Inside this hydrogel layer, the camphor is no more precipitated but solubilised into the water (see fig. 2.9). If we consider only the central part of the swimmer, far from the edges, the problem becomes one-dimensional. As illustrated in figure 2.9, we distinguish two layers in the swimmer. First, there is the loaded core, in which the camphor is precipitated and characterised by the uniform concentration C_{sol}. Second, there is the diffusion layer, characterised by a thickness $\delta(t)$. Within this layer, transport is

[10]The backlighting makes the transparent crown look white and the white core look grey for figure 2.8.

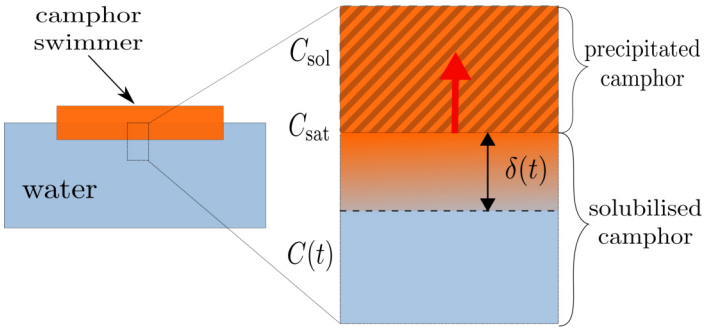

Figure 2.9: Growing diffusive layer model. The transport of camphor is governed by diffusion in the gel layer and an advancing front that moves in the solid domain. Notations are introduced in the text.

controlled by the steady diffusion transport between two Dirichlet boundary conditions. At the interface between the precipitated and the solubilised camphor, we impose C_{sat}, the saturation camphor concentration in water. At the other interface between the gel and water, we assume a perfectly mixed solution with a uniform concentration $C(t)$ everywhere in the outside solution. The interface between precipitated and solubilized camphor recedes upon dissolution of the former. Therefore, assuming a quasi-steady state dynamic, the diffusion flux of camphor must be equal to the flux from precipitated camphor dissolution, such that

$$\frac{\mathcal{J}(t)}{\mathcal{A}} = (C_{sol} - C_{sat})\dot{\delta}(t) = D_g \frac{C_{sat} - C(t)}{\delta(t)}, \tag{2.2}$$

with $\mathcal{A}$ the swimmer surface in contact with water, D_g the diffusion rate of camphor into the agarose gel and the dot $\dot{}$ indicates the derivative as a function of the time. Note that $C_{sat} \ll Csol$ (see tab. 2.1), then the term $(C_{sol} - C_{sat})$ can be approximated by C_{sol}. Moreover, if we consider that the swimmer release in a hermetic volume of fluid, without any leak, then the evolution of the concentration is given by

$$\mathcal{J} = V\dot{C}(t), \tag{2.3}$$

with V the solution volume. Solving these equations, one gets

$$\frac{C(t)}{C_{sat}} = 1 + W\left[-e^{\frac{-t}{\tau}-1}\right], \tag{2.4}$$

with W the Lambert function[11], and $\tau = V^2 C_{sat}/\mathcal{A}D_g C_{sol}$ is a characteristic time.

It is worthy to consider the simplifying assumption $C \ll C_{sat}$ which holds at an early time, with a large reservoir or when the water is permanently renewed close to the surface thanks to the swimmer motion, in those cases

$$\delta(t) = \sqrt{\frac{2D_g C_{sat}}{C_{sol}}t}, \tag{2.5}$$

$$J(t) = \sqrt{\frac{D_g C_{sol} C_{sat}}{2t}}. \tag{2.6}$$

The formula of the flux rate gives some interesting information about the dynamics of camphor release. Notably, this flux rate decreases with time following a power law with exponent $-1/2$. Because the swimmer velocity is presumably an increasing function of flux, we can guess that the swimmer speed decreases with time. Also, this formula allows us to estimate an order of magnitude for the total release rate. By assuming that the diffusion rate of camphor into

[11] The Lambert function is solution of $W(x)e^{W(x)} = x$.

agarose gel is the same order of magnitude as in water, i.e. $D_g \sim 1 \times 10^{-9}\mathrm{m}^2/\mathrm{s}$, and with the measurement of C_{sol} (see tab. 2.1), we can estimate from (2.6) that $\mathcal{J} \sim 1 \times 10^{-9}\mathrm{mol/s}$ for a 4-mm radius swimmer after 800 s[12]. We now confront this model to test with experimental measurement involving agarose gel swimmers releasing camphor in water, this method allows better estimation of the total flux rate.

c. Spectroscopy experiments: measurement of the concentration of precipitated camphor in agarose gel C_{sol} and the camphor release rate $\mathcal{J}$

As regards the camphor emitted by a swimmer, there are two essential quantities: the total release rate $\mathcal{J}(t)$, and the total amount of camphor loaded. The latter is determined by C_{sol}, which is a quantity appearing in eq.(2.6) describing the camphor flux through the swimmer surface. Those quantities can be determined indirectly with spectroscopy experiments [13] based on the measurement of the camphor concentration in a solution [19]. Indeed, camphor has an absorption peak for the wavelength 290 nm in ethanol [21] and 285 nm in water. This absorption varies as a function of the camphor concentration, thus, with a calibration curve (see fig. 2.10), we can measure the concentration in an unknown solution.

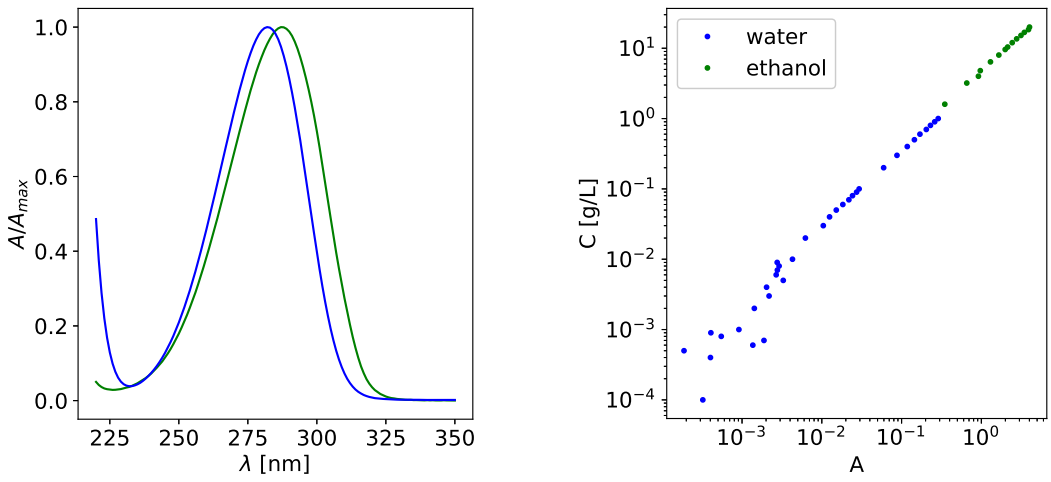

Figure 2.10: Spectroscopic properties of a camphor solution of water or ethanol (blue and green respectively). (Left) Absorption spectra of camphor for wavelength λ= 220 to 350 nm. The data is normalized by the maximal absorption A_{max}. (Right) Calibration curve relating the peak absorption to the camphor concentration.

- **C_{sol}, the concentration of camphor trapped in the agarose gel** To measure this quantity, we immerse 40 swimmers with a radius $a = 4$ mm and a thickness $e = 0.5$mm in a hermetic bottle containing 50 mL ethanol until they release all their camphor in the solution. For more precaution, we wait for 12 hours, the duration of the loading process (see p. 51). The solution is stirred meanwhile. Ethanol is used instead of water because of the higher solubility of camphor into an alcohol solution. Then, the concentration of camphor is measured, and we obtain $C_{sol} = 5200\ \mathrm{mol/m}^3$, which means that an agarose gel camphor swimmer is made of 80% of camphor in volume.

[12] 800 s corresponds to the intermediate time for the range 700 s- 900 s used to determine the average velocity for a run, see 2.2.2.

[13] We use a Perkin Elmer Lambda 900 apparatus.

- **J, the total flux rate** We immerse 25 swimmers with a radius $a = 4$ mm and a thickness $e = 0.5$ mm in a hermetic bottle containing 500 mL of stirred water. A small amount of solution (less than 10 mL) is taken every four minutes – the time required to obtain a spectrum from 350 to 220 nm–, then poured back in the bottle, so that, the volume of the solution remains constant. To prevent any leakage, the bottle remained closed between the samplings, and the opening is partially sealed with parafilm, only a small hole remains, large enough to insert a needle for sampling.

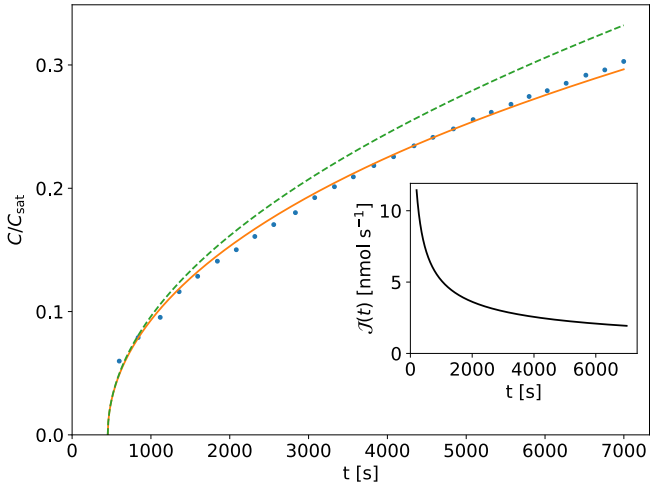

Figure 2.11: Measurement of camphor release by 25 fully immersed camphor disks. $C(t)$ is the concentration in the solution at time t. The continuous line is a fit to Eq. (2.4) including a time shift $t_0 = 450$ s. The dashed line is the concentration predicted if $C(t) \ll C_{sat}$, $C(t)/C_{sat} = \sqrt{2t/\tau}$ (Inset) Expected flux for a single half-immersed swimmer as a function of time.

Figure 2.11 shows the evolution of the concentration as a function of time. The growing diffusive layer model gives a satisfactory description of the concentration in the release experiment, as long as a time shift is introduced for the fit, approximately $t_0 = 450$s. Several factors might be suggested as an explanation for such a shift. First, the model is only approximate at the earliest time, where the flux diverges. Second, a time of about 2 min is needed to prepare the 25 camphor disks, which are not immersed simultaneously and may lose some camphor by sublimation. Also, the early release might be influenced by the initial state of the surface. In any case, the time shift remains small compared to the characteristic time. From the latter, one can deduce a diffusion coefficient in the gel $D_g = 0.4 \times 10^{-9}$ m^2/s, which is close and below the value in free water. Finally, we deduce from the variation of the concentration a flux $\mathcal{J}(t)$ equal to 5×10^{-9} mol/s for an half-immersed disk at the time $t = 800$ s[14].

d. Spectroscopy experiment: measurement of the evaporation rate k

We have just estimated the camphor released by a swimmer in the liquid. Yet camphor also leaves the solution by evaporation in the air. Here we evaluate the magnitude of this effect. The evaporation of camphor is also a key element in the transport dynamics of this surfactant, which has made it one of the most used "fuel" to power Marangoni propulsion. Here we extend our use of the spectroscopy measurement to evaluate the evaporation k.

We measure the camphor concentration in a pool from which camphor evaporates. The rectangular pool ($17 \times 27 \times 1$ cm) is fulfilled with 459 mL of an aqueous solution of camphor

[14] 800 s corresponds to the intermediate time for the range 700 s- 900 s used to determine the average velocity for a run, see 2.2.2.

(1g/L) with no stirring[15]. The pool is placed in the same experimental condition as a run: the usual protection box covers the pool, and the temperature of the experimental room is 24 °C. The evolution of the concentration in the pool is displayed in figure 2.12. As expected, the camphor concentration decreases in time because of the evaporation.

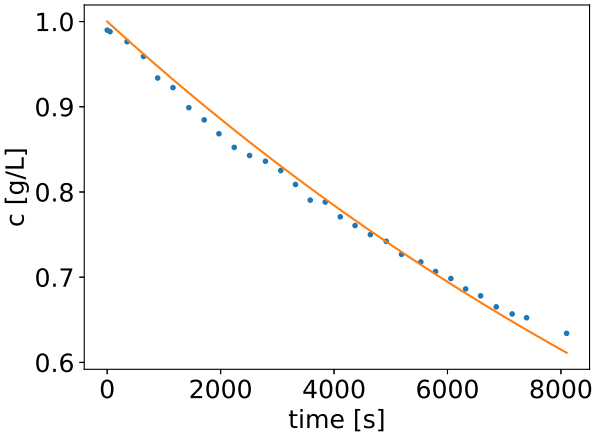

Figure 2.12: Time evolution of the concentration for an aqueous solution of camphor (1g/L) resting in an open pool. The blue dots are the measured concentration and the orange line is a fit to the eq.2.8.

This data can be rationalized with a simple model, where the camphor concentration is assumed to be the same throughout the liquid, and the evaporation rate proportional to the concentration

$$\dot{C} = -\frac{k}{h}C, \quad C(0) = C_0, \tag{2.7}$$

with the water depth h.Then the solution concentration is just a decreasing exponential

$$\frac{C(t)}{C_0} = \exp\left(-\frac{k}{h}t\right). \tag{2.8}$$

By adjusting the experimental data with this expression (fig. 2.12), with just one free parameter, we can extract the evaporation rate $k = 6 \times 10^{-7}$ m/s.

From the evaluation of k we can compute the typical concentration at the equilibrium $c^*_{eq} = \mathcal{J}/k\mathcal{A}_{pool}$. For the rectangular pool ($\mathcal{A}_{pool} = 459$ cm^2), we have $c^*_{eq} = 0.2$ mol/m^3 with the flux rate determined above, then $c^*_{eq} \ll C_{sat}$. Therefore, the evaporation prevents the camphor saturation in the rectangular pool for a total flux rate equivalent to the one generated by 4mm swimmer[16].

We have not found in the literature measurement of the evaporation k[17], except for a rough estimate based on the swimmer lifetime [17].

[15] It is not sure that the solution is at rest, evaporation might induce motion.

[16] As computed earlier, even the quantity of camphor contained in a 4-mm radius swimmer is not enough to saturate the rectangular pool.

[17] However, a relaxation rate k_r has been introduced in [19] for a model treating the camphor as an insoluble surfactant. This relaxation rate is the sum of the evaporation rate into the air and a dissolution rate into the bulk. It has been estimated at $k_r = 4.3 \times 10^{-8}$ m/s. In [19] the authors use the surface concentration since they consider just the surface dynamics of camphor, and the relaxation rate introduced $\bar{k}_r$ is adapted to a surface concentration. However, in the same paper, they also introduced the Henry isotherm K_H, which link linearly the surface concentration Γ with the bulk concentration at the surface c_0, such that $\Gamma = K_H\, c_0$. Then we deduced that $k_r = \bar{k}_r K_H$. which is one order below our measured evaporation rate. Since k_r include also the dissolution into the bulk, we would expect on the contrary a higher value for this relaxation rate.

e. Table of the quantities

Finally, with our estimates of the total release rate $\mathcal{J}$, the concentration of camphor inside the loaded core C_{sol} and the evaporation rate k, we can gather in table 2.1 the basic parameters that characterize our swimmers.

Quantity	Symbol	Value	Source
density	-	0.992	[15]
molar mass	-	$152.23\ \mathrm{g\cdot mol^{-1}}$	-
concentration saturation in water	C_{sat}	$7.9\ \mathrm{mol\cdot m^{-3}}$ (=$1.2\ \mathrm{g\cdot L^{-1}}$)	[15]
concentration saturation in ethanol/methanol	-	$1\ \mathrm{g\cdot mL^{-1}}$	[15]
evaporation rate	k	$6\times10^{-7}\mathrm{m\cdot s^{-1}}$	p.62
absorption peak spectroscopy	-	290 nm (ethanol) / 285 nm (water)	[21]/p.60
linear concentration dependence of surface tension	κ	$6\times10^{-3}\mathrm{N\,m^2\,mol^{-1}}$ (at 297 K)	[19]
precipitated camphor concentration in agar gel	C_{sol}	$5200\ \mathrm{mol\,m^{-3}}$	p.60
release rate for a single agar gel swimmer [18]	$\mathcal{J}$	$5\times10^{-9}\ \mathrm{mol\,s^{-1}}$	p.61
diffusion rate of camphor into agar gel	D_g	$D_g = 0.4\times10^{-9}\ \mathrm{m^2\,s^{-1}}$	p.61

Table 2.1: Properties of camphor and characteristic of agar gel swimmer. the "p.#" indicates the page number in the case the measurement was carried out during this thesis.

2.2.2 Main experimental results: swimmers velocity

So far, we have presented an experimental characterization of the camphor processes that fuels the swimmer motion: release rate and dynamics, self-cleaning process, etc. These elements will be necessary to build a basic modelling of the propulsion dynamics. We now address the main experimental characterization which focuses on the swimmer velocity and the various parameter that control it.

a. General observation

We first provide a general description of the individual swimming. The motion starts as soon as the swimmer is in contact with water. If one focuses on the central zone of the pool (without the excluded area), this motion is in a first approximation, ballistic with constant velocity. The distance travelled by a swimmer in one second is several times its diameter, from 15 times for the smallest $a = 1$ mm to three times for the biggest $a = 15$ mm. In the following, we will characterize this steady-state velocity and its dependence on several parameters which make it change.

Before doing so, let us be more specific on the displacement. Figure 2.6 shows typical trajectories for intermediate radius size. We note that even in the central part of the pool, trajectories are not perfectly straight. A quantitative measure is provided by the radius of curvature r_c, shown in figure 2.13. The average radius of curvature is at least 20 times the swimmer radius. Also, only the swimmers with a equals to 1 mm gyrate since the curvature radius is below half the rectangular pool width. Otherwise, the pool is too small for the swimmer to close the loop, and we obtain partially curved trajectories. Besides, there is a significant increase of the average curvature radius with the swimmer size. One possible interpretation is related to the intrinsic default made during production. Those defaults may have a typical size independent of the swimmer radius, then their effect is stronger on the smallest swimmers than on the biggest ones. In the following, we will not consider further the curvature but focus on the velocity modulus.

[18] $\mathcal{J}$ is the total release rate for a 4-mm radius swimmer half-immersed and estimated from the inset of fig. 2.11 at time t = 800 s.

There are several aspects that we will not address in the following. First, the swimmer may exhibit reorientation events occurring in the vicinity of the walls. Second, we can also note the tendency to follow the wall, which is clearly seen in a circular pool. In a rectangular pool, trajectories tend to remain close to the wall after a contact. Characterizing the interaction between swimmer and wall would require much further development.

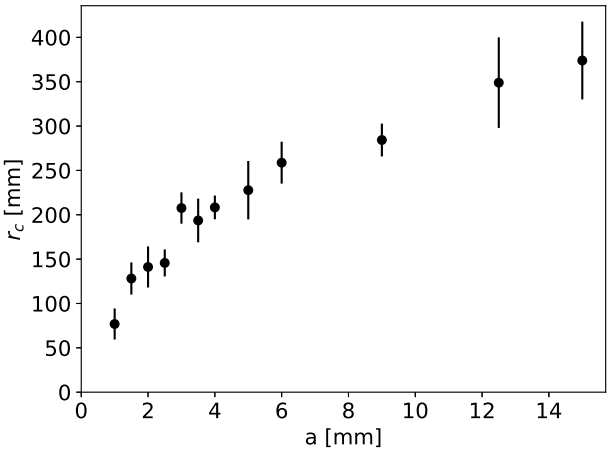

Figure 2.13: Evolution of the average curvature radius r_c as a function of the swimmer radius. An average is taken over all the values measured between different runs and the error bars correspond to a 95% confidence interval obtained from Student's t-distribution.

b. Time and water depth dependence

Time evolution An agarose gel swimmer swims continuously all along the 15 min run. Actually, it can swim during hours. However, the velocity is not constant over time and decreases slowly, as shown in figure 2.14[19]. The speed drop is only 10% over a 15-min run and 66 % over one hour. Several factors may be thought as possible causes: saturation of the pool in camphor, contamination or/and decreasing flux.

The saturation argument can be refuted because even in the worst condition, the concentration of camphor dissolved in the pool is far from saturation concentration [20]. Despite all the precautions, the accumulation of an exterior contaminating agent, such as dust, may also explain this behaviour (see 2.1.2). To test this hypothesis, we performed an experiment detailed in the appendix 2.5.1. We performed three successive runs without the cleaning process and found that the velocity time evolution of the three swimmers is the same, in the limit of a few $mm/$s difference. It means that the camphor and the dust accumulated during one run, do not affect the next run. Therefore, those two quantities have no visible effect on the time evolution of the swimmer speed. Finally, only the hypothesis involving the decreasing of the flux remains. And indeed, this speed decreasing is qualitatively consistent with the camphor released rate reduction described earlier (see 2.2.1).

The time-dependence of the velocity may be a problem to compare velocities between swimmers. In the following, we will consider that the velocity for an agarose gel swimmer is the average value over the time range 700-900 s. This choice results from a compromise. We want to avoid the first few minutes where the velocity changes most rapidly. On the other hand,

[19]The time evolution is a concave shape function and we can expect a velocity null in a finite time.

[20]If we assume that all the camphor contained in 4-mm radius swimmer dissolved instantaneously into the rectangular pool, then the concentration would be 3.6% of C_{sat}. This configuration is impossible given the low flux rate of camphor and the evaporation rate occurring all along the run.

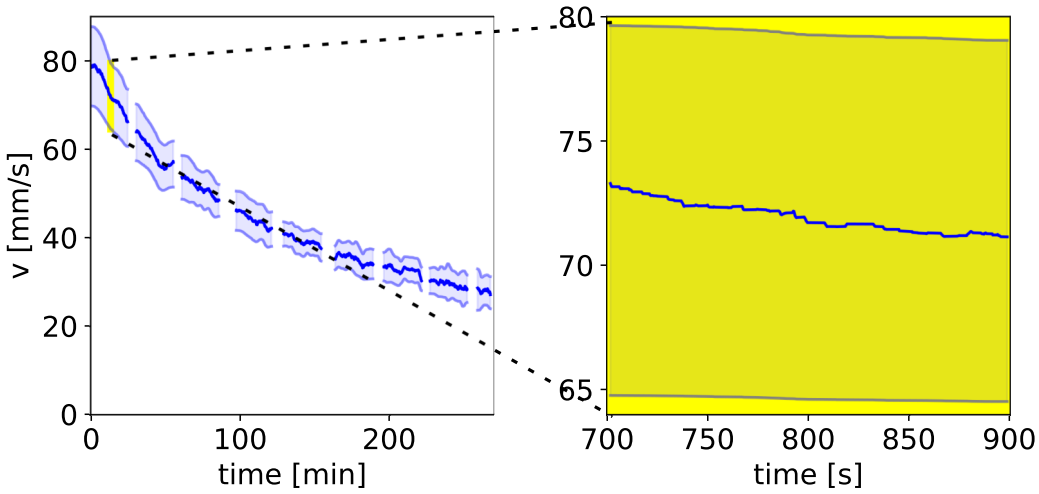

Figure 2.14: Time dependence of the velocity, for a swimmer of a radius $a = 4$ mm. (Left) the line is the data averaged over a 1-min sliding window and the blue area around corresponds to one standard deviation. (Right) close-up on the 700 to 900 s interval over which the velocity is computed. Note that the average value decreases by only a few percent.

the chosen time should be sufficiently short, so that the experiment can be repeated multiple times. Finally, one can note that the variation in velocity is quite small (only 3%) much below the standard deviation (see fig. 2.14).

Water depth The time evolution of the velocity reflects the decrease in the strength of the chemical motor through the release rate. As a natural counterpart, one can expect to change the velocity by modifying the dissipative forces. In this respect, changing the liquid height is likely to increase the dissipation in the flow between the no-slip surfaces of the bottom wall and the swimmer, hence reducing its velocity. This expectation is borne out in figure 2.15, which shows the velocity of swimmer 4 mm in radius as a function of the water depth. The velocity is independent of pool depth for h above about 10 mm with a plateau around 75 mm/s. Below $h = 7.5$ mm, the velocity decreases, with a drop at h= 2.5 mm to a value 40% lower than the plateau. We note that for 4-mm swimmer, the change of regime occurs when the depth gets lower than the swimmer radius $h/a \simeq 0.6$. Therefore, a velocity measured in a one-centimetre depth pool is a reasonable approximation of the infinite-depth velocity. This is not true for a 15-mm swimmer in a pool 10 mm in depth if we assume that the ratio h/a is the key quantity in the criterion. Note in the Stokes regime, the drag of a disk moving at the interface is increased by 10% as soon as $h = 5a$ [4]. The dependence we observe appears to be weaker, which suggests that the flow departs significantly from Stokes solution and/or that the pool depth may affect factors other than the drag, through Marangoni flows for instance.

c. Size dependency

In addition to time and pool depth, the disk parameter is certainly the most natural parameter to look at. In terms of its effect on the velocity, things are a priori more entangled as we expect it to increase both the chemical motor and the friction. If one naively assume that the release rate increases as a^2 and the drag as aU, a balance of force[21] yields a velocity varying as $\sqrt{a}$. Figure 2.16 displays the experimentally measured sized dependency of velocity. It increases from 25 mm/s for a 1-mm radius swimmer to 110 mm/s for a 15-mm radius. As

[21] Roughly, without diffusion, the typical surface concentration is $\mathcal{J}/U$. Therefore the typical capillary force is $\kappa J a^2/U$, which equilibrate with a Stokes drag force $F_v \sim aU$. Then we deduce that $U \propto a^{-1/2}$.

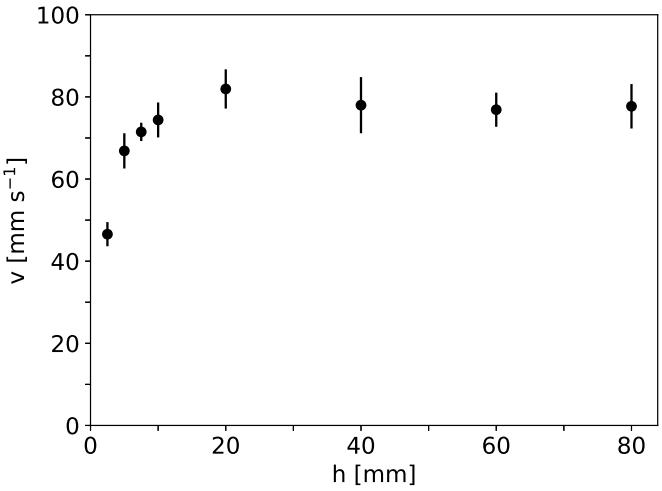

Figure 2.15: Depth dependence of the velocity. The swimmers are 4 mm in radius.

suggested by our simple arguments, the increase in velocity is sub-linearly. A power-law with exponent 1/3 gives a reasonable description of the data for swimmer down to 2.5 mm, but not below this size, even when considering error bars. This overfitting for the smallest swimmer may be attributed to the swimmer shape. Since the thickness is always the same (e=0.5 mm), the smallest swimmers are closer to the cylinder than the disk compared to the largest swimmers.

The error bars are quite important, as they can represent up to 20% of the averaged value. This may be explained by our choice of encompassing the expected mean value with a high probability, P=0.99, assuming a Student's t-distribution. The relative largest error bar, for a=12.5 mm, is associated to the size with the less performed runs, only four, and unfortunately, one run is much slower than the other[22]. But beyond, some statistical particularity the experiment is well reproducible in the limits of a variety of few millimetres per second[23].

In the following chapter *Modelling*, we try to understand this behaviour, in particular, we elaborate a simple toy model explaining where the 1/3 power law may come from.

2.2.3 Side experiments: more on the role of the chemical source

In the previous section, we have characterized the different parameters – time/release rate, pool depth and swimmer size – which control the spontaneous velocity of our basic swimmers. We complement this exploration with experiments on different swimmers to gain some additional insights into the underlying mechanisms. We focus here on the role of the chemical source.

a. Symmetry breaking: influence of asymmetry

The disks of agarose gel-camphor are symmetric self-propelled objects which suggest that their swimming mechanism is based on a spontaneous symmetry breaking. Yet, despite the experimental care taken to fabricate the disks, one can always be argued that residual asymmetries will unavoidably remain. Accordingly, we present here results where a finite asymmetry is

[22]The list of the four velocities measured is respectively 82,107,110,107 mm/s. A bubble of air trapped below the swimmer slows down its speed. It may explain why certain runs involve much slower swimmer.

[23]The figure2.24 illustrate also well this reproducibility, not only on the measured speed but also for the whole time evolution along a run.

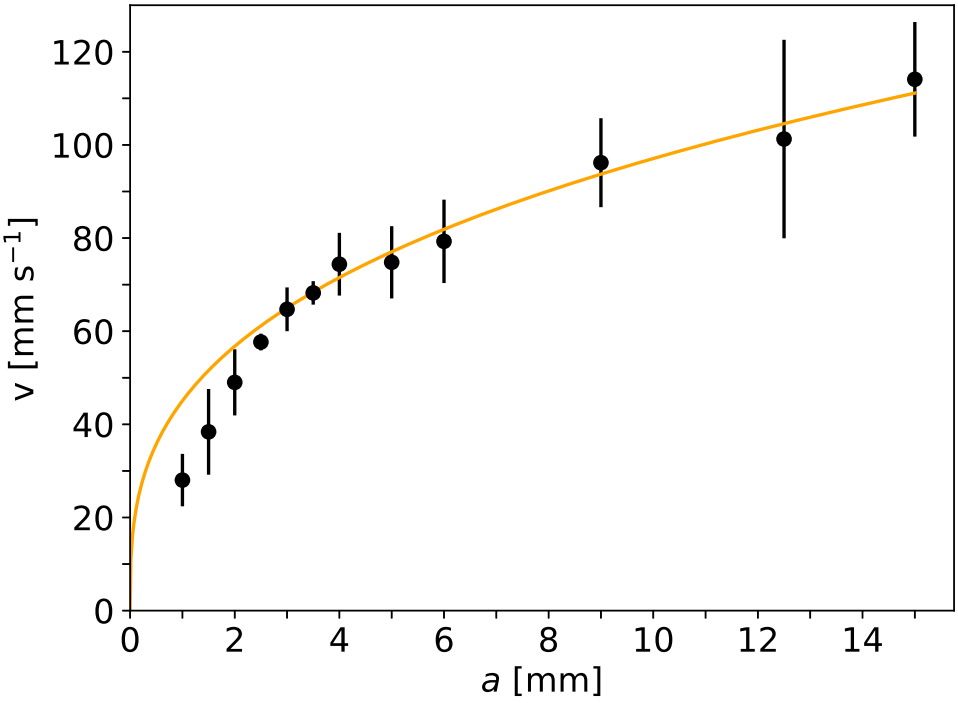

Figure 2.16: Size dependence of the swimming velocity. The pool depth is $h = 10$ mm. The continuous line is a fit $v = c\,a^{1/3}$, with $c = 45 \pm 0.5$. The probability that the average is within the error bar for a Student's t-distribution is $P = 0.99$.

purposely imposed on the swimmer, to see how it impacts the swimming velocity. Experimentally, the radial symmetry of the swimmer is broken by punching in the inner part of the disk, a small hole with radius a_h at a distance b_h from the centre (see left fig.3.17). For an uniform flux of camphor over swimmer surface, the barycentre of camphor released is thus shifted by a distance $b' = b_h(a_h/a)^2$ and we use $\chi' = |b'/a|$ to quantify this geometric asymmetry. The measured velocity is normalized by $\bar{v}$ the average velocity over all the runs involving a swimmer with the same hole size[24]. The idea is to focus on the velocity change induced by the controlled asymmetry [25].

The figure 3.17 presents the velocity measured for swimmers. The influence of the hole position on the swimming velocity is not detectable, considering the standard deviation (error bars). The velocity is thus independent of asymmetry. Those results support the idea that the swimming velocity is a reproducible observable. While hidden asymmetries and defaults may facilitate the transition from motionless to swimming particle and possibly break the degeneracy of swimming orientation concerning the disk orientation, their influence of the steady velocity appears to be negligible. We will discuss further in the next chapter the possibility of symmetry-breaking mechanism.

Two remarks are in order. First, we note that the asymmetry independence of velocity is fully consistent with previous observations on camphor boats [18]. In those experiments, a camphor disk is attached below a rectangular plastic plate, at a fixed distance d behind the plate centre. There is a significant range of d where propulsion is steady and the velocity remains constant, suggesting that the symmetric version of those camphor boats have a motion

[24]Note that $\bar{v}(a_h = 0.5 \text{ mm}) = 77$ mm/s and $\bar{v}(a_h = 1.5 \text{ mm}) = 56$ mm/s.

[25] The hole in the swimmer also modifies the total flux rate, but, we assume, in a manner independent of the hole position. We are thus comparing swimmers with equal fluxes.

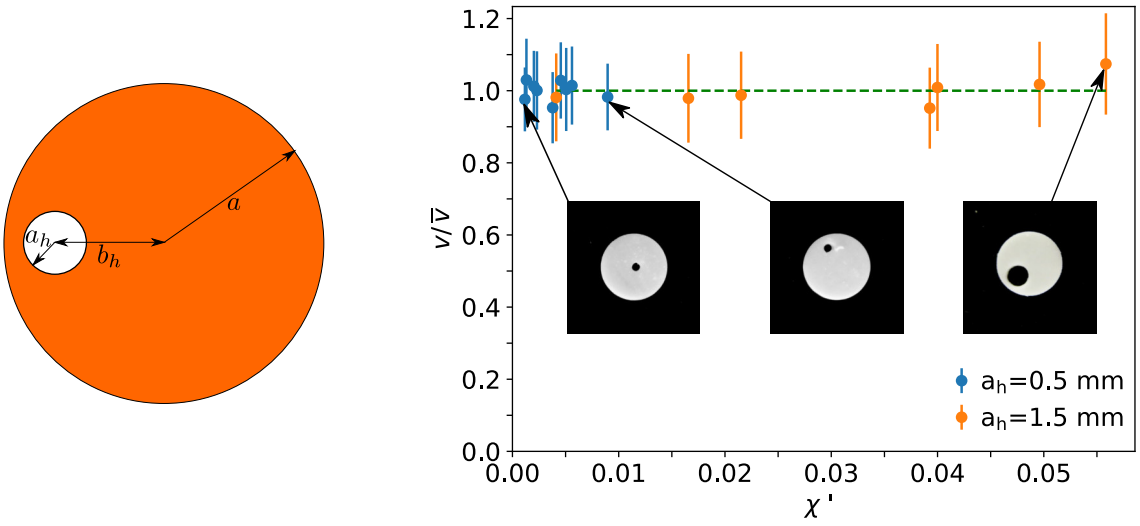

Figure 2.17: Velocity of swimmers made asymmetric with a hole. (Left) schematic représentation of a holed swimmer. (Right) swimming velocity of camphor disks with controlled asymmetry. Since the size of the hole can vary for each χ', the velocity is normalized by the average velocity $\bar{v}$ for each hole size a_h over all the χ'. A few swimmers are shown as insets. The dashed line corresponds to a unit ratio $v/\bar{v} = 1$. In all cases, $a = 4$ mm and $h = 10$ mm.

also based on a symmetry-breaking mechanism. The second remark is that the asymmetry induced by the hole may be more complex than that suggested by the χ' formula [26]. However, our main observation – a small asymmetry likely leaves the velocity unchanged – remains valid.

b. Swimmer surface contribution: crown and core swimmers

The influence of the release rate on the swimmer velocity was hinted with the time evolution, where the velocity decrease was attributed to a reduction in release rate. Yet, the link remained quite indirect. We now try to modulate in a controlled manner the strength of the chemical source. This can be done while keeping the swimmer size fixed by preparing swimmers composed of two parts, either "active" by being loaded with camphor or "passive", without camphor. If the outer area contains camphor, it is a "crown swimmers", otherwise it is "core swimmers" (see fig. 2.3). The detail of the crafting is presented in 2.1 p.53.

Most theoretical treatments to date [12] consider a homogeneous release from the whole surface. Yet there are some indications in the literature that the swimmer contour controls the dynamics. The rhythmic behaviour observed for a group of camphor disks [20] appears to be controlled by the total contour length, and not by the total surface of swimmers, which suggests a more important role for the periphery.

To get some insight, we measure the velocity of the crown and core swimmers, all of size $a = 10$ mm, and with crown thickness as small as 1-mm[27].

Figure 2.18 presents the variation of the swimmer velocity as a function of the ratio between active and total area. For core swimmers, the velocity increases steadily with the active area. For crown swimmers, the velocity increases up to the surface ratio of about 60%, then apparently reaching a plateau [28]. Motion is thus possible irrespective of whether the camphor is released,

[26] Indeed χ' only takes into account the asymmetry generated by a shift of the barycentre release for a disk, but the hole also modifies the drag and creates a new releasing surface if we take into account the thickness of the swimmer.

[27] Because of a technical constraint, the crown must be at least 1-mm thick. Otherwise, the ring is too fragile to be manipulated. Therefore, the maximum active part for a core swimmer is 64% and the minimum active part for a crown swimmer is 36%.

[28] This plateau below one may be a result of the fabrication process. The crown and core swimmers are more manipu-

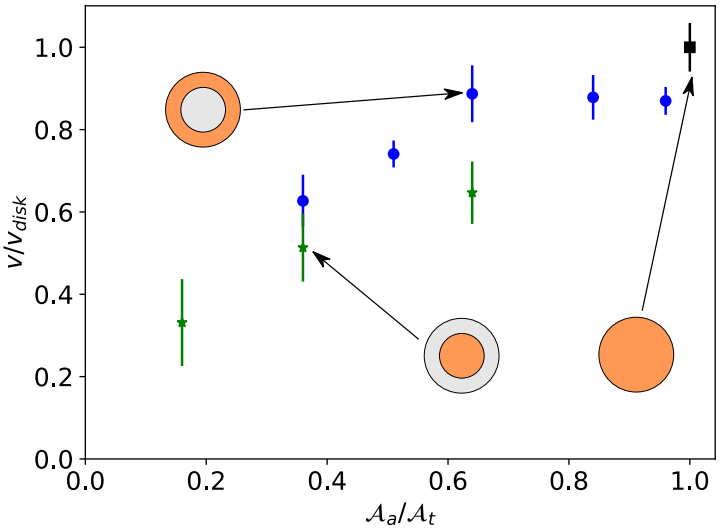

Figure 2.18: Swimming velocity of symmetric swimmers made of an active part loaded with camphor (orange) and a passive part without camphor(light grey): disk (black square - active), crown (blue circle - exterior part active), core (green star - inner part active). The velocity evolution is normalised by the total active disk velocity and expressed as a function of the area of the active part $\mathcal{A}_a$ normalized by the total area $\mathcal{A}_t$. In all the case $a = 5$ mm and $h = 10$ mm.

from the core or the crown of the swimmer, and the release rate is a key parameter affecting the swimming velocity. Yet, the comparison between core and crown swimmers reveals that the swimming velocity is not determined only by the total release rate of camphor. It also depends on where the camphor is released. Releasing at the periphery leads to a faster motion, while the contribution from the central 40% seems marginal. Qualitatively, this difference may be interpreted as follows. The capillary force driving the motion arises from an unbalance in perimeter surface tension. One can imagine that a release far from the contour may induce a weaker response. Indeed, because of the diffusion, a surfactant emitted in the centre may be too diluted to have a significant contribution to the surface concentration. Then, for a 5-mm radius swimmer, the 40% marginal inner area corresponds to the inner surface 4 mm away from the swimmer contour.

2.3 Individual motion of symmetric swimmer: pure camphor swimmer

In the last experimental section of this chapter, we explore a second type of camphor disks. Whereas we have focused above on agarose gel swimmers, which belong to the class of *loaded swimmers*, we now consider the pure camphor swimmers, which belong to the class of *dissolving swimmers*. Despite their intrinsic difference, the two types are rarely distinguished in the literature and are often designed by the generic name "camphor disks", except in specific cases [29]. Beyond the structure, the main difference lies in the type of boundary condition imposed at the swimmer surface. The growing layer model that we discussed above for the gel swimmers essentially imposes a fixed flux boundary condition. On the contrary, as we discuss

lated than simple disks. However, this explanation is not totally satisfying since the supplementary handling is just the assembly of the active and passive parts.

[29] In [14], agarose gel swimmers and pure camphor swimmers placed in the same condition, shallow water, form two different patterns, respectively regularly spaced or dendritic.

below, the natural assumption for pure camphor swimmers is that the solution is saturated at the solid camphor boundary, thus setting a fixed concentration.

2.3.1 Size evolution and release of camphor

In contrast with the *loaded swimmers* which keep their shape along the run, the *dissolving swimmers* shrink with time. Therefore, it is important to first properly describe the size evolution before measuring and analysing the swimming dynamics. Two methods were used to measure the swimmer size. The first simply uses the video recording to estimate it [30]. However, the precision is low (1 mm corresponds to 5 pixels) and needs to be compensated with multiple measurements to give a reliable evolution. For the second method, we remove the swimmer from the water pool and we take a large magnification picture. The precision is much better (1 mm corresponds to 35 pixels). However, the measurement requires more manipulation than the first method. Nevertheless, those two measurement methods give results both reproducible and mutually consistent. The figure 2.19 shows how the radius of the swimmer decreases as a function of time for the two initial sizes, 4 mm and 6.5 mm radii. The curve starts with a linear regime before concavity sets in. Quantitatively, the 4-mm swimmers lose 50% of their initial size in 6000 s, while the 6.5 mm swimmers need 9000 s to shrink in the same proportion.

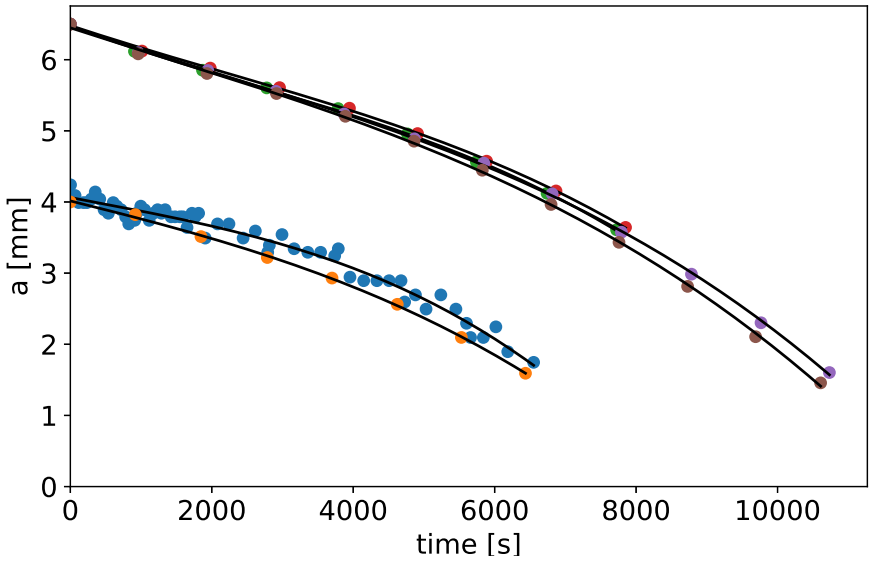

Figure 2.19: Time Evolution of the radius a of a pure camphor swimmer. The results of six runs are shown; two starting with a 4 mm radius swimmer and four with a 6.5 mm radius swimmer. The colour dots are the measurement and the black lines are the interpolation function (spline curve) used in the analysis. Note that only the data illustrated with the blue dots have been done with the video recording. Otherwise, all the other curves were obtained with the second method. Note that neither a rescaling $a/a_{t=0}$, nor a shift with the final time $t = 6600$ s on the smallest swimmer leads to collapse on a master curve.

The evolution of the thickness is more difficult to measure quantitatively. We have evidenced that the swimmers get thinner with time. Some measurements with binocular indicate that the 0.5 mm initial thickness is about 40% lower after 2000 s. This suggests that the radial shrinking proceeds at a faster pace than the disk thinning, and hints at an edge effect. Since we

[30] Since pure camphor swimmers are transparent, the swimmer size is measured from selected frames in which the swimmer passes above a fine mesh placed below the pool.

do not know how the thickness of those swimmers evolves precisely, we do not have access to the total release rate of camphor for the pure camphor swimmers. However, we can state that the quantity released is much higher for the pure camphor swimmers. Indeed, if we compare only the size of pure camphor swimmers with the size of a loaded core for an agarose gel swimmer, we notice that a 4-mm camphor disk shrinks by half in less than 2 hours, while a 2.5-mm radius core containing precipitated camphor needs 9 hours to do so (see fig. 2.8).

The shrinking of camphor swimmers is due to the dissolution of solid camphor in the surrounding fluid. Thus, the release mechanism is different from the growing layer proposed for gels swimmers. Here, the crystals of camphor are in contact with the solution. In the absence of further indication, it seems natural to assume that the camphor concentration is at saturation at the interface because there is a coexistence there between crystallized and solubilized camphor. To conclude, compared to the gel swimmers, pure camphor swimmers involve a different boundary condition and a release rate which is certainly higher.

2.3.2 Experimental measurements: evolution of the velocity

The pure camphor swimmers shrink with time. We take advantage of this peculiarity to explore different sizes with a single run. Thus, in contrast to gel swimmers, where we repeated multiple runs with swimmers of various sizes, here we follow only a few swimmers, but during a very long run.

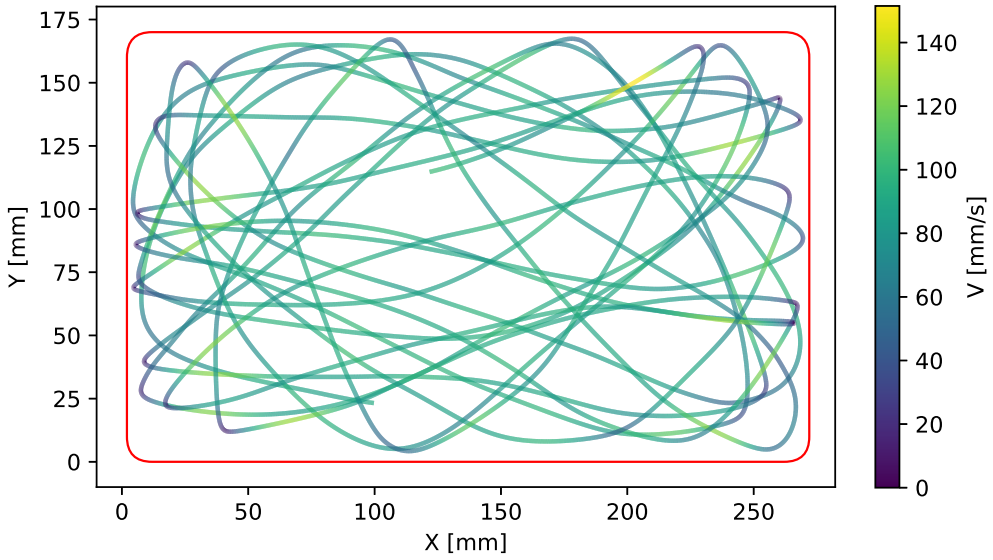

Figure 2.20: Trajectory for a pure camphor swimmer. Its radius is a=2.7 mm. The pool is rectangular (border in red), with depth $h = 1$ cm, The trajectory extends from 9100 s to 9200 s. The colour indicates the velocity magnitude.

a. General observation

We first summarize generic features of pure camphor swimmer, to help the reader visualize the global behaviour. As the gel swimmer, the pure camphor swimmer moves instantaneously after being laid upon water. Beyond the spontaneous symmetry breaking already discussed, this may be quite surprising observation. Indeed, because the surface tension is constant along the contour, the resulting capillary force vanishes, implying that motion is driven by a different force, presumably viscous entrainment from Marangoni flows. To our knowledge, a propulsion mechanism with a capillary force null has never been reported so far. On the quantitative side,

the pure camphor swimmer swims faster than their gel counterpart. Their velocity is typically 10 times their diameter per second for the 5-mm radius swimmer, and up to 15 for the 2-mm radius swimmer. Besides, the velocity also decreases with time over a few hours. For instance, the swimmer velocity is roughly divided by two after 180-min run for an initial 6.5-mm radius swimmer.

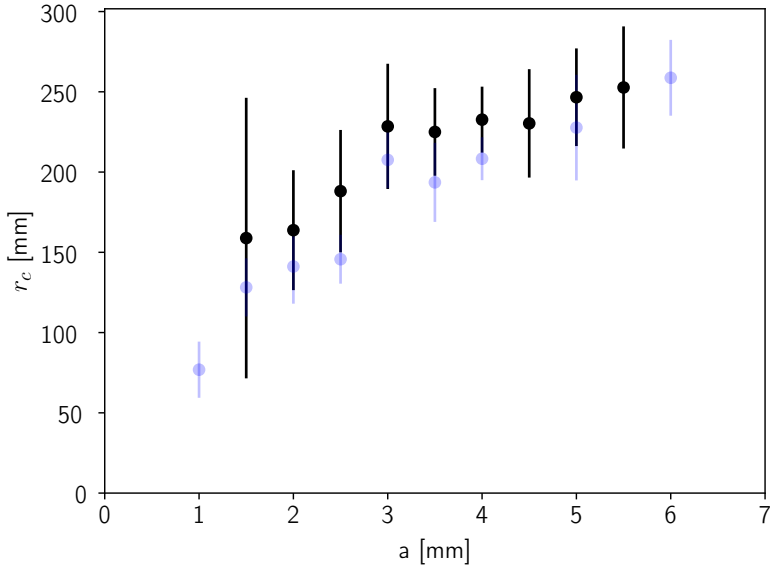

Figure 2.21: Evolution of the curvature radius r_c as a function of the swimmer radius. The results from the agarose gel swimmers are in blue (for the complete curve see fig. 2.13, and the results for the pure camphor swimmers are dark.

Just like the gel swimmers, the pure camphor swimmers exhibit non-straight trajectories. The change of the curvature radius with size is very similar (see fig. 2.21), leading to the same conclusion: the larger the swimmers, the straighter the trajectories. However, pure camphor swimmers can have behaviours quite different. In contrast to gel swimmers, they can exhibit a change of concavity while crossing the pool. Moreover, a cusp may occur in the middle of the pool[31]. Those two phenomena are illustrated in appendix 2.5.3.

Finally, the last new feature of pure camphor swimmer is the interaction with the wall. Direct observation reveals that this interaction is much more symmetric, i.e. the ongoing angle is almost the same as the outgoing angle. This observation is well illustrated by comparing the figure 2.20 and 2.6. Contrary to gel swimmers that tend to follow the wall, the camphor disks explore much more the inner surface of the pool. Despite this quasi-specular interaction, the "bounce" is oriented. The swimmer decelerates when approaching the wall, but reaccelerates on leaving it, reaching a maximum value that is above the velocity in the middle of the pool. As an example, we have recorded speeds around 140 mm/s while the expected average speed is around 80 mm/s. In the remainder of this work, we will focus most of the time on gel swimmers but the new features seen in pure camphor swimmers are noteworthy and call for further exploration.

[31]Those two particularities appear more specifically for small swimmer, $a < 2.5$mm, and the cusp is quite rare, but they are new features never observed with agarose swimmer.

b. Time dependence

For the gel swimmers, we found that the time dependence of the speed is mostly correlated with the reduction in release flux of camphor. For pure camphor swimmers, the release of camphor is based on a direct dissolution of crystal in the fluid bulk, which suggests that the boundary condition remains constant in time. Thus, the reason for the time dependence of velocity may be sought in another factor. Since the size and thickness of the pure camphor also evolve with time, those parameters seem to be good candidates to explain $U(t)$.

Figure 2.22 shows the velocity time evolution of the velocity for two swimmers with different initial size, respectively 6.5 mm and 4 mm for the radius. Those two examples are representative of all the performed runs. The speed increases shortly up to a maximum around 30 min after which it continuously decreases, until the end of the run. Because the radius was shown to monotonously decreasing with time (see fig. 2.19), the change in velocity cannot be described by this sole variable. In a tentative scenario, we propose that two phenomena compete in time to set the swimming velocity. The first is the reduction in size, that dominates at a long time and leads to a reduction in velocity. The second involves profiling of the disk cross-section and/or its thickness decrease, which would lower the drag coefficient. At early time, shape adjustment over the thickness would occur quickly as compared to radius relative evolution, thus yielding a velocity increase. At larger time, the evolution is dominated by radius and the velocity weakens.

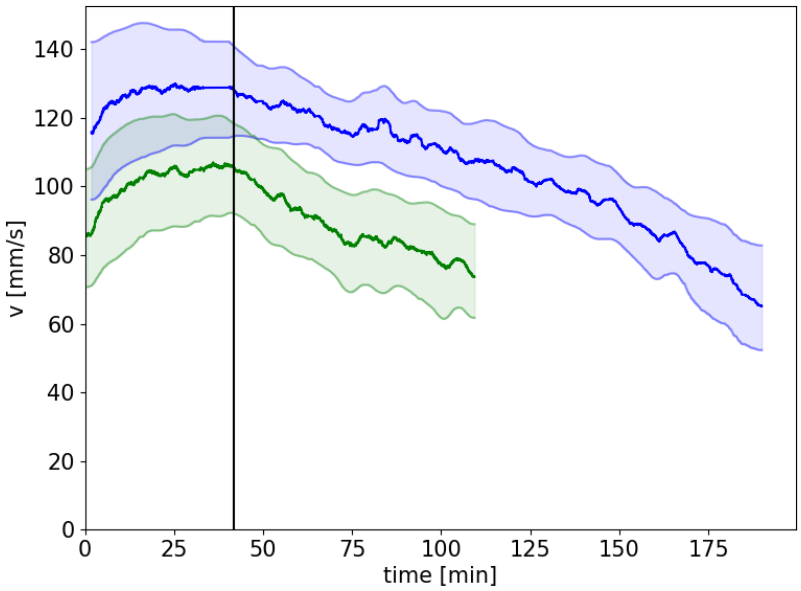

Figure 2.22: Time dependence of the velocity. The swimmer has a initial radius $a = 6.5$ mm (blue) or $a = 4$ mm (green). The colour lines are the data averaged over a 1-min sliding window and the coloured area around corresponds to one standard deviation. The vertical black line indicates the arbitrary limit $t = 2500$ s chosen as the mark the starting point for the study on the size dependence.

c. Size dependence

As discussed above, defining a size-velocity relationship for the pure camphor swimmer is not straightforward, because there is no one-to-one correspondence. We have chosen to consider the data points where the velocity decreases with time (see figure 2.22). We thus discard the first 2500 s of each run, that includes the increasing and plateau portions of the curve. One

can now extract the velocity for a given radius of a given swimmer [32]. Finally, we obtain our final value for the velocity $U(a)$ by taking an average over all swimmers having this radius a.

Following this protocol, we obtain the figure 2.23 displaying the velocity as a function of the radius. The velocity increases from 70 mm/s for 1.5-mm radius swimmers to 120 mm/s for a 6-mm radius. Pure camphor swimmers move faster than the gel swimmer of the same size with an almost twofold increase for the smaller swimmers. The curve $U(a)$ is also concave but a tentative power-law fit yields a higher exponent: around $1/2$ as compared to $1/3$ for gel swimmer. This suggests that pure camphor swimmer of large size could reach very high velocities [33]. Two remarks are in order. (i) It must be remembered that our method to obtain $U(a)$ leads to comparing swimmers with different thicknesses. In all cases, the thickness remains negligible compared to the radius, even for the smallest swimmer. (ii) Compared to the gel swimmer, the error bars are wider. The likely explanation is the small number of measurements done, only four for each point.

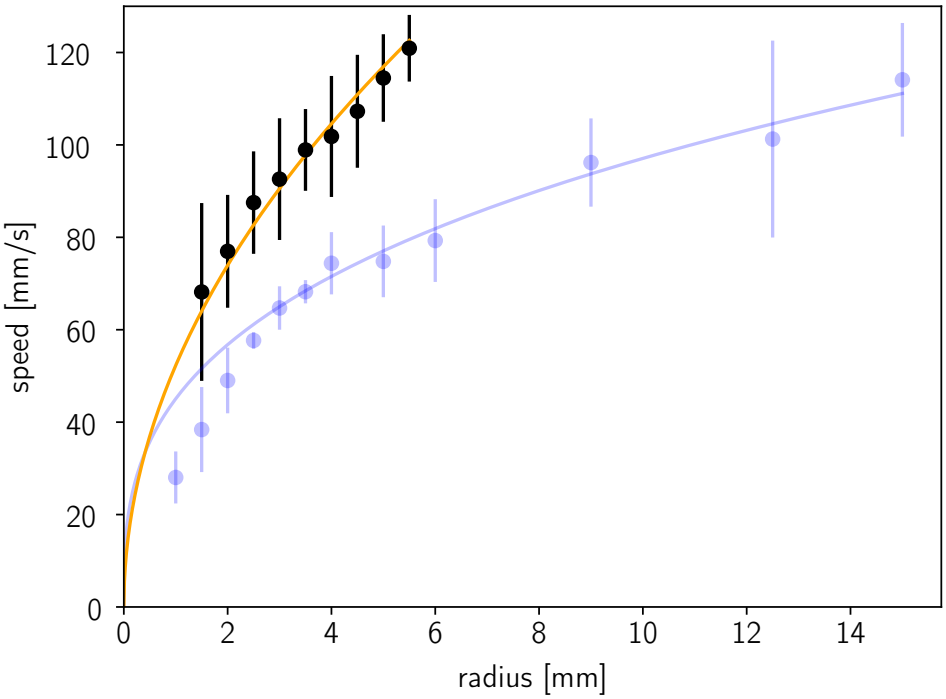

Figure 2.23: Size dependence of velocity for pure camphor and gel swimmers (black and blue points respectively). The latter is the same as in figure 2.16. For both, the pool depth is $h = 10$ mm. The continuous orange line is a fit $v = ka^{1/2}$ with $k = 52.4 \pm 0.6$. $P = 0.99$, the probability that the average is within the error bar for a Student's t-distribution.

Even though in the following, the focus is primarily on gel swimmers, we will also investigate the principle by which the pure camphor swimmer can swim. A very simple model will be presented in the next chapter. Some insight about the possible mechanism will also be given when discussing the various contributions to the forces acting on the swimmer.

[32] In practice, the velocity at radius a' is obtained as the average over the time interval $[t(a = 0.99\,a'), t(a = 1.01\,a')]$. In this time range, the swimmer radius is less than 1% away from the nominal radius a'. In this process, we used the interpolation of experimental points, the black curves displayed on figure 2.19. Because of the acceleration in size reduction, this time range varies from approximatively 300 s for the biggest size to only 30 s for the smallest.

[33] Bigger swimmer has not been tested because of crafting constraint. The largest mould used only allows to craft 6.5-mmradius disk (see 2.1 p. 52).

2.4 Summary

In this chapter we characterized experimentally some key properties of gel swimmers: the flux, the size dependency of the velocity $U(a)$ and the effect of the asymmetry. We also considered pure camphor swimmers, whose features are more complicated. This ensemble of observations calls for a better understanding of several points.

Using controlled defects, we show that a small asymmetry has no visible effect on the velocity. This result is consistent with previous results on camphor boat [18], which concluded that asymmetry matters only when exceeding an "asymmetric threshold".

We found that for both types of swimmers, the velocity increases sub-linearly with the size, albeit in a different manner. Perhaps surprisingly, in view of the experiments already done, we found no framework that could rationalize those observations. For instance, in [16] treating asymmetric shaped swimmers, the smaller swimmers are predicted to swim faster than large ones.

The idea that the swimmer release camphor through a given flux is quite common in the literature [12]. On the contrary, to the best of our knowledge, the idea of a swimmer with fixed concentration everywhere on its surface has not been considered so far.

There is currently no framework that could rationalize those observations satisfactorily. In the two following chapters, we will explain our steps in this direction. We will first develop simple models that focus on predicting the velocity, before turning to simulation to get a more complete view of the phenomena at work.

2.5 Appendices

2.5.1 Three runs in raw, no cleaning protocol

In this experiment, we performed three successive 30-min runs without any cleaning process or water change. Also, there is no rest time between the runs allowing the camphor to evaporate. The purpose is to show that the cleaning protocol (see 2.1.2 p.55) is just supplementary security and to put in in evidence that the decreasing swimming velocity with time is not mainly due to the accumulation of camphor in the pool (see p.64).

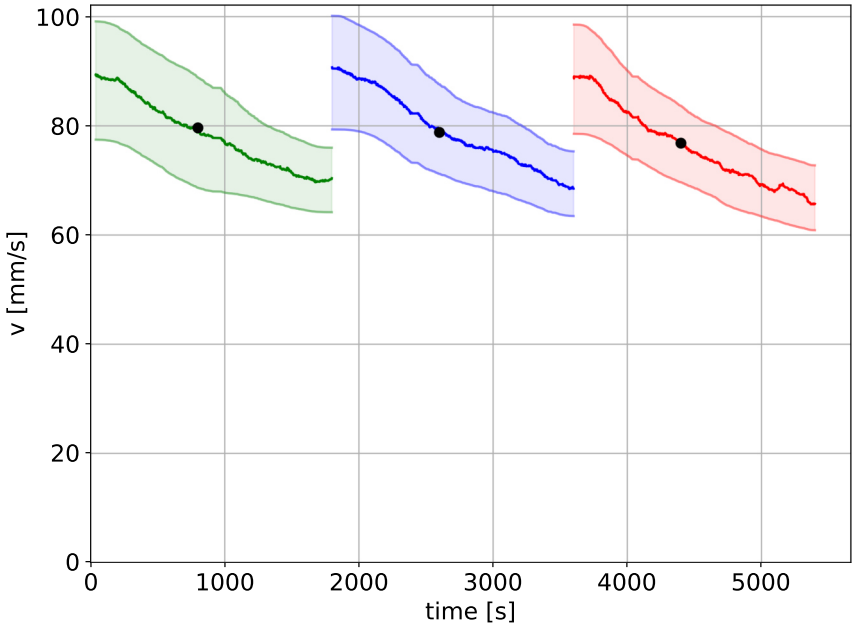

Figure 2.24: Time dependence of the velocity for three swimmers released subsequently in the same pool without cleaning. The line is the data averaged over a one-minute sliding window, while the coloured area corresponds to one standard deviation. The black dot is the computed velocity as defined in the main text. The swimmer radius is $a = 4$ mm.

Figure 2.24 shows the time evolution of this experiment. Despite the continuous release of camphor and the probable surface contamination with dust, the three swimmers have a quantitative comparable behaviour. Therefore, the time dependency of the velocity for camphor swimmers is not due to those factors. It comes rather from an internal dynamics intrinsic to the agarose gel-camphor swimmers described in 2.2.1.

2.5.2 Extended growing diffusion layer model: time evolution of the crown for agarose gel- camphor swimmer

The growing layer model considered in 2.2.1 was purely one-dimensional, here we extend this model to the extremity of the core of precipitated camphor (in orange for the left fig. 2.25). At the extremity the shrinking dynamics is much faster, than the 1D growing layer model prediction[34], whence the necessity to designed a model adapted to the edge effect. However, the growing layer model capture with much more simplicity the total flux for the range time considered ($\sim$ 15 min). Therefore we propose it here just as a curiosity which described qualitatively quite well the evolution of the precipitated camphor core for a long experiment ($\sim$ 10 h).

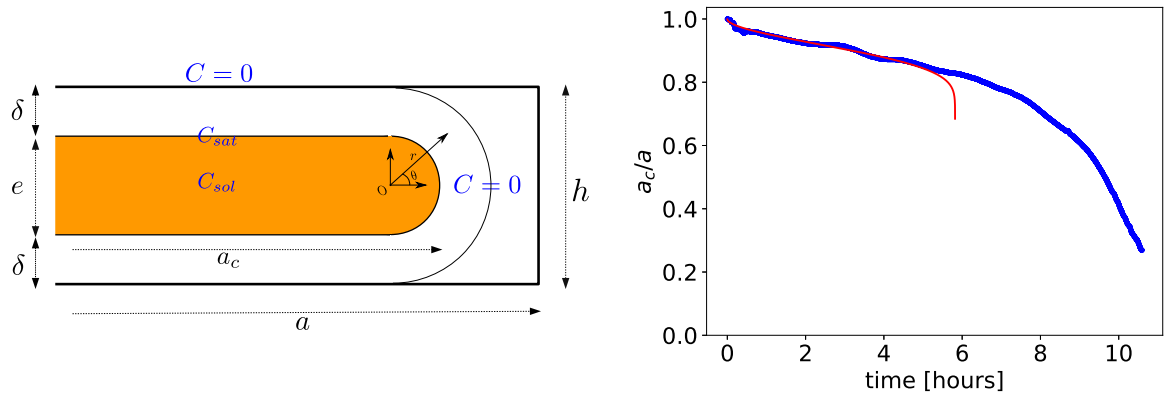

Figure 2.25: (Left) Schematic illustration of the extended growing layer model, with the introduction of the different parameters. (Right) Time evolution of the camphor loaded core radius a_c over the swimmer radius a. The blue dots are the experimental data and the red curve is an experimental fit using the formula prediction (2.13) with D_g the diffusion of camphor in the gel as a fitting parameter.

In this model, we focus specifically on the edge of the inner loaded core. We impose a circular profile at this extremity with diameter e governed by the depletion layer thickness δ defined previously in the growing layer model (2.5). We have $2\delta + e = h$, with h the swimmer thickness (see fig. 2.25 (left)). At the interface between precipitated camphor and solubilized camphor, we impose the concentration C_{sat}. The iso-concentration $C = 0$ surround this extremity at the constant distance δ. Between those two Dirichlet conditions, the camphor is transported by diffusion. Since $h/a \ll 1$, we neglect the curvature of the swimmer and we consider a bidimensional problem with cylindrical symmetry.

As a reminder $\delta = \sqrt{2D_g C_{sat}/C_{sol} t}$, with D_g the diffusion coefficient of camphor in agarose gel. Because of the cylindrical geometry and symmetry [2], we have at the extremity:

$$C(r) = \frac{C_{sat}}{\ln\left(1 - \frac{2\delta}{h}\right)} \ln\left(\frac{r}{h/2}\right), \tag{2.9}$$

with r the distance from the centre of the round extremity. As in the growing layer model, we assume that inside the gel the camphor distribution is always in a the steady-state such that the radial diffusion flux

$$\bar{j} = \frac{D_g}{\pi} \int_{\theta=-\pi/2}^{\pi/2} r\, \boldsymbol{e}_r \cdot \boldsymbol{\nabla} C \, \mathrm{d}\theta = -D_g \frac{C_{sat}}{\ln\left(1 - \frac{2\delta}{h}\right)}, \tag{2.10}$$

[34]It the core was shrinking as fast by its face as its extremity, it would be totally consumed in only 3 hours according to experimental result for a 2.5-mm radius swimmer. However, we note that the core lasts much longer.

is equal to the radial dissolution flux

$$\bar{j} = -\frac{\mathrm{d}a_c}{\mathrm{d}t} C_{sol} \frac{(h - 2\delta)}{2}, \tag{2.11}$$

the factor $1/2$ come from that $e = h - 2\delta$ is the diameter of the core extremity and not the radius. Then by equalising the radial diffusion flux from the concentration distribution with the radial flux from the dissolution of camphor, we obtain a differential equation for a_c the radius of the loaded core.

$$\frac{\mathrm{d}a_c}{\mathrm{d}t} = \frac{h}{2\tau} \frac{1}{\left(1 - \sqrt{t/\tau}\right) \ln\left(1 - \sqrt{t/\tau}\right)}, \quad 1/\tau = 8 \frac{D_g}{h^2} \frac{C_{sat}}{C_{sol}}. \tag{2.12}$$

τ is the time to consume all the loaded core. Close to this time the core is extremely thin, that is why $\dot{a_c}$ diverges. Therefore,

$$\frac{a_c}{a} = 1 - \frac{h}{2a} \left[\ln|t^*| - (E_i(t^*) - \gamma)\right], \quad t^* = \ln\left(1 - \sqrt{t/\tau}\right). \tag{2.13}$$

with E_i the exponential integral, defined by $E_i(x) = \int_x^\infty e^{-t}/t \, \mathrm{d}t$, and γ the Euler–Mascheroni constant.

The extended growing layer model captures the short convex decrease at the beginning, the fast collapse at the end, and in the middle the concavity inversion which looks a linear decreasing. Those three phases are indeed presented in the experimental results (see fig. 2.8). Moreover, it can fit the first 5 hours results by just letting the diffusion D_g as a free parameter, for the other parameter see tab. 2.1). We obtain $D = 1 \times 10^{-9} \mathrm{m}^2/\mathrm{s}$ which is the the good order of magnitude. However, it fails to describe the duration of the core lifetime and predicted a total consumption of 40 % earlier than the one observed experimentally.

In conclusion, despite its simplicity, this extension of the growing diffusion layer model gives qualitatively the expected behaviour. It is consistent with the hypothesis that the dynamics at the extremity of the loaded core is due to an edge effect. However, it fails to predict the lifetime of the loaded core. This aspect may be solved by taking into account the evaporation of camphor for one face of the swimmer instead of using a Dirichlet boundary condition. We could expect a core which would last longer and then a better description for the long time behaviour.

2.5.3 Example of particular trajectories observed for pure camphor swimmers

We present two examples of particular trajectories observed for the pure camphor swimmers. They are particular since "S" trajectory (up) or the cusp (down) have never been observed for the agarose-camphor swimmer.

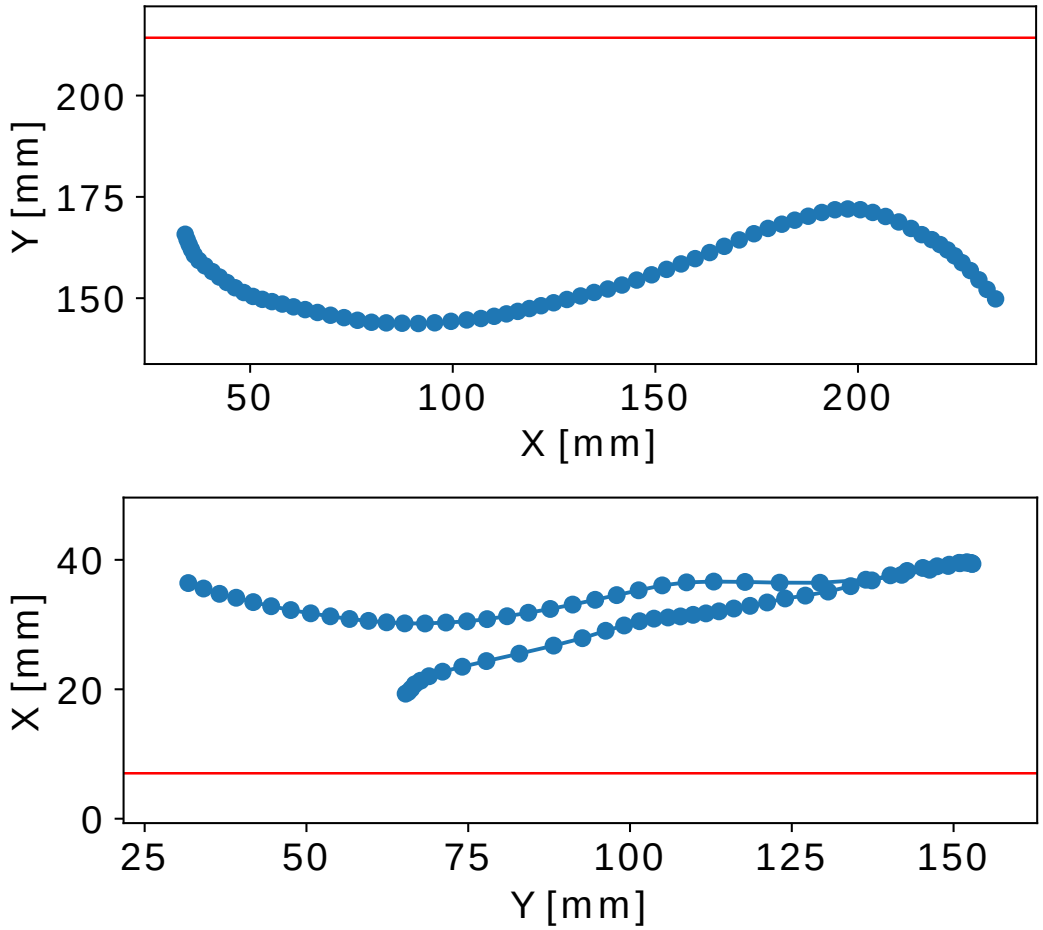

Figure 2.26: Two particular trajectories observed for the pure camphor swimmers. The closest pool wall is represented with a red line. (Up) "S" trajectory for a 2.2-mm radius swimmer, the trajectory concavity changes during a pool crossing, $t \in [9950, 9953]$ s. (Down) cusp in the middle of the pool without the help of a wall for a 2-mm radius swimmer, $t \in [10247, 10250]$ s. Note that in both cases we consider an "old" swimmer that has been moving for almost 3 hours before observing the trajectories. The swimmer is small and particularly thin, which means that their mass is low, and they have less inertia.

Bibliography

[1] V S Akella, Dhiraj K Singh, Shreyas Mandre, and M M Bandi. Dynamics of a camphoric acid boat at the air–water interface. *Physics Letters, Section A: General, Atomic and Solid State Physics*, 382(17):1176–1180, 2018.

[2] J Crank. Mathematics of Diffusion 2.ed. *Oxford University Press*, 1957.

[3] John C Crocker and David G Grier. Methods of digital video microscopy for colloidal studies. *Journal of Colloid and Interface Science*, 179(1):298–310, 1996.

[4] A. M.J. Davis. Slow viscous flow due to motion of an annular disk; pressure-driven extrusion through an annular hole in a wall. *Journal of Fluid Mechanics*, 1991.

[5] Julien Deseigne, Olivier Dauchot, and Hugues Chaté. Collective motion of vibrated polar disks. *Physical Review Letters*, 105(9):1–4, 2010.

[6] J. P. Gong, S. Matsumoto, M. Uchida, N. Isogai, and Y. Osada. Motion of polymer gels by spreading organic fluid on water. *Journal of Physical Chemistry*, 100(26):11092–11097, 1996.

[7] Yumihiko S. Ikura, Ryoichi Tenno, Hiroyuki Kitahata, Nobuhiko J. Suematsu, and Satoshi Nakata. Suppression and regeneration of camphor-driven Marangoni flow with the addition of sodium dodecyl sulfate. *Journal of Physical Chemistry B*, 116(3):992–996, 2012.

[8] Yuichiro Karasawa, Shogo Oshima, Tomonori Nomoto, Taro Toyota, and Masanori Fujinami. Simultaneous measurement of surface tension and its gradient around moving camphor boat on water surface. *Chemistry Letters*, 43(7):1002–1004, 2014.

[9] Masahiro I. Kohira, Yuko Hayashima, Masaharu Nagayama, and Satoshi Nakata. Synchronized self-motion of two camphor boats. *Langmuir*, 17(22):7124–7129, 2001.

[10] Yuki Koyano, Nobuhiko J. Suematsu, and Hiroyuki Kitahata. Rotational motion of a camphor disk in a circular region. *Physical Review E*, 99(2):1–13, 2019.

[11] Satoshi Nakata, Masahiro I. Kohira, and Yuko Hayashima. Mode selection of a camphor boat in a dual-circle canal. *Chemical Physics Letters*, 322(5):419–423, 2000.

[12] Satoshi Nakata, Véronique Pimienta, István Lagzi, Hiroyuki Kitahata, and Nobuhiko J Suematsu, editors. *Self-organized Motion*. Theoretical and Computational Chemistry Series. The Royal Society of Chemistry, 2019.

[13] Satoshi Nakata, Hiroya Yamamoto, Yuki Koyano, Osamu Yamanaka, Yutaka Sumino, Nobuhiko J. Suematsu, Hiroyuki Kitahata, Paulina Skrobanska, and Jerzy Gorecki. Selection of the Rotation Direction for a Camphor Disk Resulting from Chiral Asymmetry of a Water Chamber. *Journal of Physical Chemistry B*, 120(34):9166–9172, 2016.

[14] Hiraku Nishimori, Nobuhiko J. Suematsu, and Satoshi Nakata. Collective behavior of camphor floats migrating on the water surface. *Journal of the Physical Society of Japan*, 86(10):1–9, 2017.

[15] O'Neil MJ. The Merck Index - An Encyclopedia of Chemicals, Drugs and Biologicals. Cambridge, UK: Royal Society of Chemistry, 2013.

[16] Abdon Pena-Francesch, Joshua Giltinan, and Metin Sitti. Multifunctional and biodegradable self-propelled protein motors. *Nature Communications*, 10(1):1–10, 2019.

[17] Siowling Soh, Kyle J M Bishop, and Bartosz A. Grzybowski. Dynamic self-assembly in ensembles of camphor boats. *Journal of Physical Chemistry B*, 2008.

[18] Nobuhiko J. Suematsu, Yumihiko Ikura, Masaharu Nagayama, Hiroyuki Kitahata, Nao Kawagishi, Mai Murakami, and Satoshi Nakata. Mode-switching of the self-motion of a camphor boat depending on the diffusion distance of camphor molecules. *Journal of Physical Chemistry C*, 114(21):9876–9882, 2010.

[19] Nobuhiko J. Suematsu, Tomohiro Sasaki, Satoshi Nakata, and Hiroyuki Kitahata. Quantitative estimation of the parameters for self-motion driven by difference in surface tension. *Langmuir*, 30(27):8101–8108, 2014.

[20] Nobuhiko J. Suematsu, Kurina Tateno, Satoshi Nakata, and Hiraku Nishimori. Synchronized intermittent motion induced by the interaction between camphor disks. *Journal of the Physical Society of Japan*, 84(3):1–6, 2015.
[21] R.C. Weast. *Handbook of Chemistry and Physics. 64th ed.* CRC Press Inc, 1983.
[22] HK Yuen, J. Princen, J. Illingworth, and J. Kittler. Comparative study of Hough Transform methods for circle finding. *Image and Vision Computing*, 8(1):71–77, 1990.

via the magic of the reciprocal theorem

Hassan Masoud and Howard A. Stone [25]

Chapter 3

Modelling of interfacial swimmers

Contents

Introduction

The previous chapter presented the experimental results about the individual swimming of symmetric interfacial swimmers. Most of them were obtained with the agarose gel-camphor "loaded swimmer". Notably, the velocity increases as a power-law of the size and a small asymmetry does not affect significantly the swimmer velocity. In this chapter, the goal is to understand the mechanism underlying the propulsion of those interfacial swimmers. To do so, we first introduce the equations governing the Marangoni propulsion. We take care to describe the problem in its most general formulation first, although a few assumptions will be already presented. This allows to identify and discuss more clearly the simplifying hypothesis - some quite usual- on which the subsequent modelling is built on. The Marangoni propulsion problem is a complex one since the two main physical phenomena, hydrodynamics and surfactant transport, are coupled by the advection transport, but also by the Marangoni flows.

Confronted with such a complex problem, we propose a toy model in the spirit of the *mobile source models* presented in the chapter *State of the art*. The main idea is to decouple the flow and surfactant distribution, by evaluating both in two simple independent situations. The first toy model allows understanding the spontaneous symmetry breaking mechanism, and the expected effect if an asymmetry is introduced. Contrary to the other existing *mobile source models*, its prediction is not limited to the low Péclet regime. We will also introduce a modified version of our basic toy model which relies on the Lorentz reciprocal theorem to take into account the Marangoni contribution into the total viscous force. This approach opens the possibility to introduce the new concept of concentration swimmer.

3.1 Problem formulation and dimensionless equations

The swimming of camphor swimmer is a complex problem which involves a two-way coupled process including hydrodynamics, diffusion and advection... In this section, we gather all the equations describing an object moving at a fluid interface because of Marangoni propulsion. Then we present their dimensionless version expressed with only four dimensionless number Pe, M, Sc and N. The idea is to show the problem in its full complexity before proposing simplified but tractable models.

3.1.1 Governing equations

The system under study is an object moving at the interface between two fluids and which releases a surfactant which is transported by advection and diffusion. The surfactant concentration modulates locally the surface tension, which acts directly on the swimmer through a capillary force on the perimeters and on the fluid through capillary stress. The reference system propels upon water via the surface effect of camphor, that is why we consider in this chapter a surfactant, but Marangoni propulsion could also be obtained with heat instead. We can distinguish two main physical phenomena: hydrodynamics and surfactant transport. We define $\boldsymbol{r} = (x, y, z)$ the position in the bulk, $\boldsymbol{\rho} = (x, y)$ the position at the surface, $\boldsymbol{u}(\boldsymbol{r}, t)$ the fluid speed, $\boldsymbol{U}(t)$ the interfacial swimmer velocity, $c(\boldsymbol{r}, t)$ the camphor concentration in the bulk and $\Gamma(\boldsymbol{\rho}, t)$ the camphor concentration at the surface.

For the hydrodynamics, a vast majority of the models neglect the effect of the upper fluid, generally air, and consider the interfacial swimmer as a floating object upon an infinite half-space fluid. The fluid underneath is generally water. The flow around the swimmer is governed

by the Navier-Stokes equation for a Newtonian incompressible fluid.

$$\rho\left(\frac{\partial \boldsymbol{u}}{\partial t}+\boldsymbol{\nabla u}\cdot\boldsymbol{u}\right)=\boldsymbol{\nabla}p+\boldsymbol{\nabla}.\bar{\boldsymbol{\tau}}=\boldsymbol{\nabla}\cdot\bar{\boldsymbol{\sigma}},\qquad \boldsymbol{\nabla}\cdot\boldsymbol{u}=0, \tag{3.1}$$

$$\bar{\boldsymbol{\tau}}=\eta(\boldsymbol{\nabla u}+\boldsymbol{\nabla u}^T),\qquad \bar{\boldsymbol{\sigma}}=-p\bar{\mathbb{1}}+\bar{\boldsymbol{\tau}}\ , \tag{3.2}$$

with $\boldsymbol{u}$ the flow velocity, p the pressure, $\bar{\boldsymbol{\sigma}}$ stress tensor and $\bar{\boldsymbol{\tau}}$ the viscous stress tensor. The fluid is characterised by a density ρ and a viscosity η. As regards boundary condition, we assume no-slip on the swimmer surface and the velocity is supposed null at the infinity.

$$\begin{aligned}&\boldsymbol{u}=\boldsymbol{0}, && (r\to\infty)\\ &\boldsymbol{u}=\boldsymbol{U}, && \text{(at the swimmer surface)}\end{aligned}$$

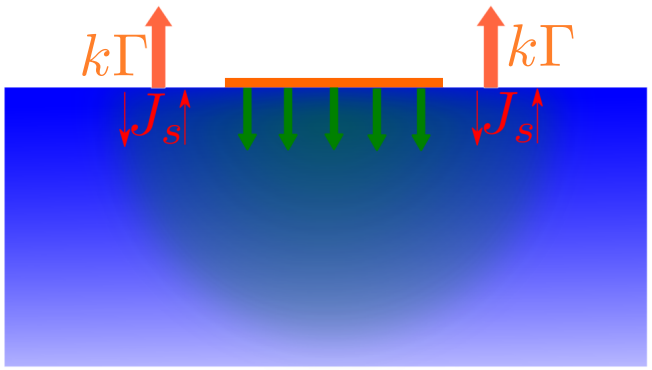

Figure 3.1: Scheme of the camphor exchanges.

Surfactant transport is governed by the equation of advection-diffusion. The bulk concentration c and the surface concentration Γ follow two distinct equations coupled through an interface exchange rate J_s[1]. Since camphor evaporates at room temperature[2], the phenomenon is also taken into account in the surfactant dynamics with an evaporation rate k.

$$\frac{\partial c}{\partial t}+\boldsymbol{\nabla}\cdot(\boldsymbol{u}c)=D_b\Delta c-J_s\delta(z), \tag{3.3}$$

$$\frac{\partial \Gamma}{\partial t}+\boldsymbol{\nabla}_s\cdot(\boldsymbol{u}\Gamma)=D_s\Delta_s\Gamma+J_s-k\Gamma, \tag{3.4}$$

with D_b and D_s respectively the diffusion coefficient in the bulk and at the interface and δ the Dirac function. We also introduce the notation ∇_s, $\boldsymbol{\nabla}_s$ and Δ_s, respectively the surface divergence, surface gradient and surface scalar Laplacian, such that for the scalar w and the vector $\boldsymbol{w}$:

$$\boldsymbol{\nabla}_s w=\boldsymbol{\nabla}w-\boldsymbol{n}(\boldsymbol{n}\cdot\boldsymbol{\nabla}w),\quad \boldsymbol{\nabla}_s\cdot\boldsymbol{w}=\sum_{i=1}^{3}\partial_i w_i\,(1-\boldsymbol{e}_i\cdot\boldsymbol{n}),\quad \Delta_s w=\boldsymbol{\nabla}_s\cdot\boldsymbol{\nabla}_s w, \tag{3.5}$$

with $\boldsymbol{n}$ the normal to the surface and i referring to x, y or z. The exchange term J_s is used to describe the complex exchange dynamics at the interface. In its simplest form, it can be written as:

$$J_s=r_{b\to s}c_s(\Gamma_{sat}-\Gamma)-r_{s\to b}\Gamma(C_{sat}-c_s), \tag{3.6}$$

[1]For heat, there is no distinction between surface and bulk.

[2]Rigorously the vapour of surfactant can condensate back in the fluid medium. Experiments have demonstrated that scraps of camphor close to the water surface induce Marangoni flow without being in contact with the fluid medium [17]. Moreover, interfacial swimmers based on alcool vapour have been designed [15].

with $r_{b\to s}$ and $r_{s\to b}$ respectively the rate of exchange of camphor from the bulk to the surface and inversely, C_{sat} and Γ_{sat} the saturation concentration, and c_s is the bulk concentration at the surface.

The source of surfactant is implemented through a boundary condition at the swimmer surface. Here again, we already reduce the complexity by considering one of two extreme situations, either a Neumann boundary condition by imposing a surfactant flux at the surface [13] or a Dirichlet boundary condition by prescribing concentration along the disk contour [20].

All the previous equations describe an advection-diffusion transport with coupling from the hydrodynamics with the specie transport via the advection. However, when the transported solute is a surfactant, the distribution acts on the flow dynamics through the capillary stress

$$\bar{\boldsymbol{\sigma}} \cdot \boldsymbol{n} = \underbrace{-\gamma(\Gamma)\boldsymbol{n}\left(\boldsymbol{\nabla}_{\boldsymbol{s}} \cdot \boldsymbol{n}\right)}_{\text{Laplace}} + \underbrace{\boldsymbol{\nabla}_s \gamma(\Gamma)}_{\text{Marangoni}}, \tag{3.7}$$

with γ the surface tension. The Laplace term in the stress tensor expression involves the pressure difference between the inside and the outside of a curved surface which delimits two different media. The Marangoni term is due to the surface tension gradient.

The dependence of γ and Γ is a decreasing function $\gamma = f(\Gamma)$. The simplest assumption, quite standard, is to approximate f with an ideal gas equation relation at low concentration or by a Langmuir isotherm:

$$\gamma = \gamma_0 + \mathcal{R}T\Gamma_{sat} \log\left(1 - \frac{\Gamma}{\Gamma_{sat}}\right), \qquad \text{(Langmuir isotherm)} \tag{3.8}$$

$$\simeq \gamma_0 - \mathcal{R}T\Gamma, \quad \Gamma \ll \Gamma_{sat} \qquad \text{(ideal gaz equation)} \tag{3.9}$$

with T the temperature, $\mathcal{R}$ the gas constant and γ_0 the surface tension at $\Gamma = 0$.

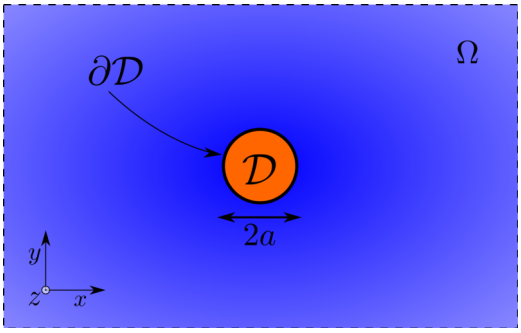

Figure 3.2: Sketch of the interface, with $\mathcal{D}$ the interfacial swimmer surface (orange), $\partial\mathcal{D}$ its contour and Ω the free surface.

Finally, the swimmer dynamics is described by Newton's second law

$$m\frac{\mathrm{d}\boldsymbol{U}}{\mathrm{d}t} = \boldsymbol{F}_\mathrm{c} + \boldsymbol{F}_\mathrm{v}, \tag{3.10}$$

$$\boldsymbol{F}_\mathrm{c} = \oint_{\partial\mathcal{D}} \gamma \boldsymbol{n}_{\partial\mathcal{D}} \,\mathrm{d}l, \tag{3.11}$$

$$\boldsymbol{F}_\mathrm{v} = \iint_{\mathcal{D}} \boldsymbol{n}_{\mathcal{D}} \cdot \bar{\boldsymbol{\sigma}} \,\mathrm{d}S, \tag{3.12}$$

with m the mass of the swimmer, $\boldsymbol{n}_{\partial\mathcal{D}}$ the normal to the contact line along the interface, $\boldsymbol{n}_{\mathcal{D}}$ the normal to the swimmer surface and, $\boldsymbol{F}_\mathrm{c}$ and $\boldsymbol{F}_\mathrm{v}$ the two forces which apply on the swimmer,

respectively the capillary force and the viscous flow force. The capillary force is the integral of surface tension over the swimmer contour and drives the object toward high tension surface[3].

To conclude this section, we see the Marangoni propulsion for an interfacial swimmer, is a complex and fully coupled problem, involving several couple phenomena.

3.1.2 Simplifying assumptions, dimensionless equation and dimensionless number

The complete problem presented above is too complex to be amenable for an analytical model, hence, the need to reduce complexity by introducing some common simplification. Next, the resulting equations are written in a dimensionless form which would be the base for our models.

a. Simplifying assumptions and considered problem

Some simplifications are widespread in the literature. In this part, we present the most common ones[4], and we specify in which specific conditions they are not relevant. We introduce a hierarchy from the most to the less relevant simplification in the context of experiments with camphor disks:

(i) **A flat swimmer** In most of the models, the swimmer has infinite buoyancy (negligible mass or zero thickness) so that it lies at the top of the surface with no immersed volume. Note that "the Reverse Marangoni surfing" [24] is a theoretical phenomenon for which the thickness of the swimmer compared to the depth of water is a key parameter[5].

(ii) **the complex exchange between surface and bulk** Generally, most of the model describing the interfacial swimmer consider either a surfactant exclusively lying at the interface (insoluble limit) [20], or a soluble surfactant or heat [39], transport in the bulk. Those two particular cases are useful to make the model tractable but should be seen as the two limiting cases of a more general phenomenon. The full description of the two coupled dynamics as described by the equations (3.3)(3.4)(3.6) has never been taken into account into a model as far as we know. Some 2D transport model[6] introduce the parameter k which describes a negative flux $k\Gamma$ taking into account the evaporation and the dissolution in the bulk of the surfactant [36].

(iii) **Linear dependency between surface tension and concentration** Most models [24] use a simplified and more convenient expression with a linear relation between γ and c via the coefficient κ with:

$$\gamma = \gamma_0 - \kappa c. \tag{3.13}$$

This implies that the concentration remains very far from saturation everywhere in the system, even in the vicinity of the source[7]. Likewise, the possibility of locally saturating

[3] A mistake is to consider a flat interface, but still taking into account the meniscus trough a contact angle for the computation of the capillary force but not for the stress force. This mistake is more widely discussed in appendix 3.7.5

[4] To make this list of the most common assumptions we considered the models of interfacial swimmer [20, 39, 13, 29, 36].

[5] It may explain some odd experimental observations in shallow water[35] where the swimmer seems to move toward the high surface gradient. Either the swimmer moves toward other swimmers or it reverses its motion direction compared to deep water.

[6] The transport of the surfactant is restricted to the free surface.

[7] Note, that respecting to the Gibbs equation $\kappa = K_H \mathcal{R} T$, with T the temperature, $\mathcal{R}$ the gas constant and K_H the Henry length such that $\Gamma = K_H\, c$. Using the Henry length means that we assume an instantaneous equilibrium between bulk and surface such that:

$$K_H = \frac{r_{s\to b}}{r_{b\to s}} \frac{C_{sat}}{\Gamma_{sat}}. \tag{3.14}$$

This formula is only valid respecting $\Gamma \ll \Gamma_m$ and $C_{sat} \ll c$.

the camphor solution has not been considered.

(iv) **A flat interface** This simplification is the most widely used. It simplifies the geometry of the problem and allows to neglect the Laplace pressure in the surface boundary condition (3.7). The criteria to quantify the legitimacy of this assumption is a low capillary number $Ca = \eta U/\gamma \ll 1$ [8], Ca being the relative effect of viscous drag forces versus surface tension forces. Experiments have shown that interfacial swimmers may create a depression around them due to the divergent Marangoni flow. According to [17], this hollow is only few micrometre depths compared to the average level of water. For the moment, its effects on the swimmer dynamics have not been studied.

b. Dimensionless numbers and dimensionless equations

We can now define a set of dimensionless equations which will be used in the future models. Note that for the swimmer, we consider a disk with the radius a releasing a soluble surfactant. In the following part of this chapter, the dimensionless quantities are noted with a tilde ($\tilde{}$) and the typical quantities with an asterisk (*).

Dimensionless number The set of dimensionless equations is based on the dimensionless numbers:

$$Pe = \frac{Ua}{D}, \tag{3.15}$$

$$M = \frac{\kappa c^* a}{\eta D}, \tag{3.16}$$

$$Re = \frac{Ua}{\nu}, \tag{3.17}$$

$$Sc = \frac{Pe}{Re} = \frac{\nu}{D}, \tag{3.18}$$

$$N = \frac{a^3 \rho}{m}, \tag{3.19}$$

with $\nu = \eta/\rho$ and c^* a typical concentration. Note that Sc is not an independent dimensionless number, then for the steady-state motion we use two numbers, Pe and M and we need four for a time-dependant system by adding N and Re or Sc. The expression for c^* changes with the surfactant injection method, either by using a Neumann or a Dirichlet boundary condition over the swimmer surface.

Pe is the Péclet number, it compares the transport from the mean advection to the transport from diffusion. M is the Marangoni number, it compares the Marangoni-stress induced flow transport to the diffusion transport. M can be seen as a Péclet number for the typical Marangoni flow speed $u^* = MD/a = \kappa c^*/\eta$. Note that M describes the intrinsic properties of the system, whereas Pe is a variable of the system. The Reynolds number Re is the ratio of inertial flow forces over the viscous forces. The Schmidt number Sc compare the Péclet and Reynolds number, or in other words, Sc is the ratio between the momentum diffusivity and the solute diffusivity. Finally, N is the ratio between the water density and the swimmer density, up to a geometric factor.

Dimensionless equations "$U = 1$" A first natural mean to adimensionalize is to use a, the particle radius as the length scale, and its velocity U. A natural scale for stress and pressure in the viscous regime ($Re \ll 1$) is the one based on the viscous stress.

$$r = a\tilde{r}, \quad \boldsymbol{u} = U\tilde{\boldsymbol{u}}, \quad p = \frac{\eta U}{a}\tilde{p}, \quad \bar{\boldsymbol{\tau}} = \frac{\eta U}{a}\tilde{\bar{\boldsymbol{\tau}}}, \quad t = \frac{a}{U}\tilde{t}$$

[8] For camphor swimmers, $Ca \sim 0.1$.

Using such scales, the Navier-Stokes equation reduces to:

$$Re \left[\frac{\mathrm{d}\tilde{\boldsymbol{u}}}{\mathrm{d}\tilde{t}} + (\tilde{\boldsymbol{u}}.\tilde{\nabla})\tilde{\boldsymbol{u}} \right] = -\tilde{\boldsymbol{\nabla}}\tilde{p} + \tilde{\boldsymbol{\nabla}}.\tilde{\tilde{\boldsymbol{\tau}}}, \tag{3.20}$$

For transport, we introduce a typical concentration depending on the release source type. For a constant Dirichlet boundary condition, the typical concentration is the concentration prescribed at the swimmer surface, $c^* = C_{sat}$ for a dissolution dynamics. For a Neumann boundary condition characterised by a source releasing a total rate $\mathcal{J}$, it is possible to build a typical concentration through a balance between injected flux and a typical diffusive flux $J_D = Dc^*/a$[9]

$$c = c^*\tilde{c}, \quad \text{with} \quad c^* = \frac{\mathcal{J}}{Da} \quad \text{(Neumann-3D)} \quad \text{or} \quad c^* = C_{sat} \quad \text{(Dirichlet)}.$$

Then we obtain the dimensionless equation for the transport

$$Pe \left[\frac{\mathrm{d}\tilde{c}}{\mathrm{d}\tilde{t}} + \tilde{\boldsymbol{u}}.\tilde{\boldsymbol{\nabla}}\tilde{c} \right] = -\tilde{\Delta}\tilde{c}, \tag{3.21}$$

and for the Marangoni stress:

$$\tilde{\tilde{\tau}}.\boldsymbol{n} = -\frac{M}{Pe}\tilde{\nabla}_s\tilde{c}. \tag{3.22}$$

Finally, the dimensionless equation for the dynamics of the swimmer is given by:

$$\frac{Re}{N}\frac{\mathrm{d}\tilde{\boldsymbol{U}}}{\mathrm{d}\tilde{t}} = \frac{M}{Pe}\tilde{\boldsymbol{F}}_{\mathrm{c}} + \tilde{\boldsymbol{F}}_{\mathrm{v}} \tag{3.23}$$

For this chapter about modelling an interfacial swimmer, we use exclusively th non-dimensionalizing choice called "$U = 1$". For simulation with the Marangoni stress implemented, it appears not to be the most convenient choice, another adimensionlization will be used in some specific situation (see next chapter).

3.2 The ge toy model

Even when adopting all the previous simplifying assumptions, for the geometry and the surfactant properties, the interfacial swimmer motion remains a complex problem. The simpler transport problem and flow around a fixed source of surfactant is by itself already challenging [7, 21]. The coupling between the hydrodynamics and the advection-diffusion phenomena make an analytical treatment difficult. Because of this complexity, we propose a toy model, belonging to the class of *moving source* (see chapter 1).

Although this kind of approach has already been proposed in various situations (chemical reaction, elliptic shape, etc.)[29] it has been limited so far to low Pe regime, and have in general provided prediction for time dependence behaviour, orientation, etc. but not for velocity. The purpose of the following model is to give velocity prediction even for high Pe, and also give some precious information about the symmetry-breaking mechanism characterising this kind of swimmer.

[9] For a problem treating exclusively a surface transport, the flux equality is $\mathcal{J}/a = D\Gamma^*$, which gives $\Gamma^* = \mathcal{J}/Da$.

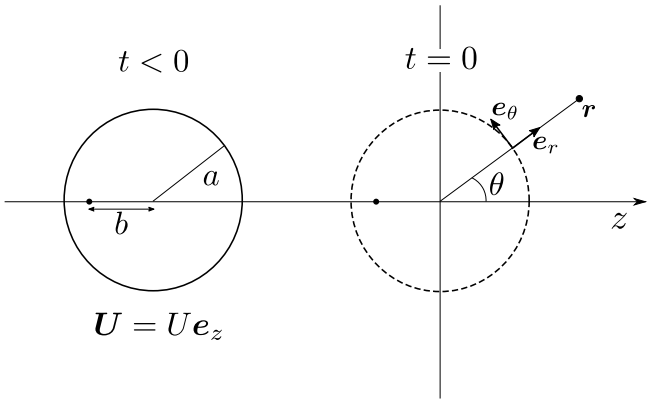

Figure 3.3: Schematic of the swimmer investigated. The motion is steady with velocity U. The point source is shifted by a distance b behind the centre and has position $R(t) = (Ut - b)\boldsymbol{e}_z$. At time $t = 0$, the swimmer center coincides with the origin.

3.2.1 The principle

The principles of the toy model are very simple and thus constitute a very generic approach to look at the self-motion by spontaneous symmetry breaking of reactive objects, including the interfacial swimmers but also the phoretic swimmers. Note that reactive means it acts as a source or a sink of a field (chemical, thermal) that has impacts on interfacial stresses. For interfacial swimmers, the coupling from the solute/heat transport to the hydrodynamics is due to the capillary stress at the interface. For phoretic swimmers, it is the advection generated by a solute/heat gradient that is described by the local slip velocity on the swimmer surface.

The basic idea is to practically decouple transport and hydrodynamic equation. In the swimmer frame of reference, the flow field can be expressed as

$$u = U + \delta u, \tag{3.24}$$

with U the mean flow or the undisturbed flow at the infinity and δu is the perturbation induced by the boundary condition on the swimmer surface. A proposal is to oversimplify the convection by keeping only U. Then, convection is thus preserved in transport equation but now appears through the source motion which parametrizes the equation of concentration/temperature field (3.25). We thus consider the steady motion of a point source moving at constant velocity U and releasing at total rate $\mathcal{J}$ a quantity ϕ that may be a solute or heat. The swimmer is assumed to be a sphere, if phoretic, or a disk, if interfacial, with radius a. The point source is shifted a distance $b < a$ behind the centre, with $b \geq 0$, so that the swimmer moves forward (see fig. 3.3). The swimmer is symmetric only if $b = 0$. We introduce another dimensionless parameter $\chi = b/a$ which is just the dimensionless expression of the length b. The distribution of surfactant is governed by a diffusion process, with a moving point source. Following the no-dimensioning method for "$U = 1$" (see p.88), we have

$$Pe\frac{\partial \phi}{\partial t} = \Delta\phi + \delta(\boldsymbol{r} - \boldsymbol{R}(t)), \qquad \text{(laboratory frame of reference)} \tag{3.25}$$

$$-Pe\ \boldsymbol{e}_z \cdot \boldsymbol{\nabla}\phi = \Delta\phi + \delta(\boldsymbol{r} - \boldsymbol{R}(0)), \qquad \text{(swimmer frame of reference)} \tag{3.26}$$

with $\boldsymbol{R}(t) = (t - \chi)\boldsymbol{e}_z$ the position of the source and δ the Dirac function. Note that the equations are expressed in the swimmer frame of reference, the swimmer is fixed and the fluid velocity far from the swimmer is thus $-U$. The spreading of surfactant is controlled by a linear equation with Green function $G(r, t)$,

$$\phi(\boldsymbol{r}) = \frac{1}{Pe}\int_{-\infty}^{0} G(\boldsymbol{r} - \boldsymbol{R}(t), -t)\ \mathrm{d}t. \tag{3.27}$$

In the case of pure diffusion, the Green function in dimension d is then

$$G(\boldsymbol{r}, t) = \left(\frac{Pe}{4\pi t}\right)^{d/2} \exp\left(-Pe\frac{r^2}{4t}\right). \tag{3.28}$$

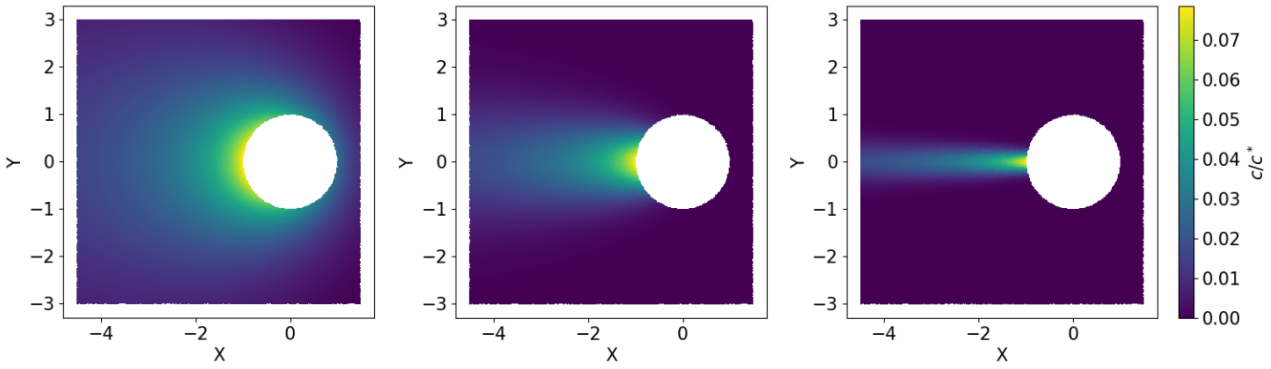

Figure 3.4: Solute for a sphere moving toward the positive x at different Péclet number (see eq. 3.30), from left to right, Pe=1, 10 ,100. $c^* = \mathcal{J}/Da$. The swimmer is the empty white part.

Contrary to numerous problems involving the Péclet number, Pe does not "quantify" the non-linearity in the transport equation from the advection term. Indeed, in the toy model, the advection flow is homogeneous, and the equation transport is linear. Instead, $1/Pe$ could be seen more as a geometric ratio which gives information about the width of the solute/heat wake compared to the swimmer size. As illustrated by the figures 3.4, the typical width of the wake behind the swimmer decreases with Pe. Since the source is punctual, the wake approaches a line when $Pe \to \infty$.

3.2.2 Application to the test case of a phoretic swimmer

Because of its very generic principle, the toy model applies to different situations of spontaneous swimming, notably to a parent problem of the interfacial swimmers: the autophoretic swimmers. Interestingly, some exact results are available on this system [27]. This will be an opportunity to examine whether the rough simplification assumed can indeed succeed in capturing the system response.

The isotropic phoretic swimmer is a sphere evolving in the fluid bulk, thus, the field ϕ is 3D. The gradient around the sphere induces on the surface of the swimmer a slip velocity,

$$\boldsymbol{u}_s = \frac{\mathcal{M}}{a}\left.\frac{\partial \phi}{\partial \theta}\right|_{r=a} \boldsymbol{e}_\theta, \quad \mathcal{M} = \frac{k_B T \lambda^2}{\eta}, \tag{3.29}$$

with $\mathcal{M}$ the mobility for a diffusiophoretic swimmer, k_B the Boltzmann constant and λ an effective interaction length that depends on liquid-solid interaction potential. Now for a symmetric swimmer, combining (3.27) - (3.28) gives

$$\phi(r, \theta) = \frac{1}{4\pi r} \exp\left(-\frac{Pe\ r}{2}(1 + \cos\theta)\right). \tag{3.30}$$

Then we inject this parametrisation of ϕ in 3.29 to determine the slip velocity. Finally, the swimmer velocity is obtained from an average of the slip velocity over the surface $\mathcal{S}$ of the swimmer [2].

$$U = -\frac{\mathcal{M}}{2a}\int_0^\pi \phi(a, \theta)\sin(2\theta)\ \mathrm{d}\theta, \tag{3.31}$$

thus leading to a closed equation for the velocity

$$\frac{1}{8}\frac{Pe^3}{M} = e^{-Pe/2}\left(\frac{Pe}{2}\cosh\frac{Pe}{2} - \sinh\frac{Pe}{2}\right), \qquad M = \frac{\mathcal{M}\mathcal{J}}{4\pi a D^2}. \tag{3.32}$$

The above calculation can be extended to an asymmetric swimmer. With the notation $\Lambda = \sqrt{Pe/4\chi}$, the result is

$$\frac{\chi Pe^2}{M} = e^{-(1+\chi)Pe} - 1 + 2\chi + \sqrt{\frac{\pi}{\chi Pe}}\left(\chi - \frac{Pe}{2}\right)e^{-\Lambda^2}\left[\mathrm{erf}(\Lambda) - \mathrm{erf}\left((1+2\chi)\Lambda\right)\right], \tag{3.33}$$

with erf the error function[10] We have now an equation involving Pe, M and χ. The analytical solution can not be given in the general case but we can investigate the limits of small and large Péclet. At low Pe we have

$$0 = -\chi + \left(\frac{3}{M} - 1 + \frac{3\chi^2}{5}\right)\frac{Pe}{2} + \left(1 + \frac{6\chi}{5} - \frac{2\chi^3}{7}\right)\left(\frac{Pe}{2}\right)^2 + \mathcal{O}(Pe^3),$$

then, at the lowest order

$$\chi = 0, \quad \frac{Pe}{2} = \frac{M}{3} - 1, \quad \text{for } M > M_c \quad M_c = 3, \tag{3.34}$$

$$\chi > 0, \quad Pe = \frac{2\chi M}{3}. \tag{3.35}$$

On the other hand, at high Pe

$$0 = \frac{1}{2}\frac{Pe}{M} - \frac{1}{Pe} + \frac{2}{Pe^2} + \mathcal{O}\left(\frac{1}{Pe}\right)e^{-(1+\chi)Pe},$$

a large-Pe expansion yields, irrespective of χ,

$$Pe = \sqrt{2M} - 1 + \frac{3}{2}\frac{1}{\sqrt{2M}} + \mathcal{O}\left(M^{-3/2}\right). \tag{3.36}$$

As in [27], we have a spontaneous symmetry breaking occurring only at a critical M (see the red curves fig. 3.5). Quantitatively, the exact threshold is $M_c = 4$, we find 3, which is only 25% away from the exact value. Also, the paper treating the exact solution evaluates numerically the function Pe/M, characterised by a maximum followed by a decay. The toy model yields similar behaviour. The maximum occurs at $M \simeq 9$ with magnitude $Pe/M \simeq 0.08$, we find $M \simeq 9.6$ and $Pe/M \simeq 0.28$. The toy model overestimates the velocity magnitude by a factor of three but captures the velocity threshold and maximum. The overestimation is attributed to the neglect of the swimmer excluded volume. A simple extension of the point-source model (see Appendix 3.7.1) that partially takes into account this effect leads to much better predictions for the velocity. As anticipated, at low Pe, the instability threshold disappears for an asymmetric swimmer: as soon as the point source is slightly shifted from the swimmer centre, there is no more critical M, and the slope at the origin gets steeper with χ. At large Pe, we observed that the Pe associated with the steady motion increases sub-linearly, and all the curves computed with different χ collapse on the same master curve (3.36) independently of χ.

Despite the simplification made, the toy model describes to some extent the main features of the autophoretic swimmer.

[10] $\mathrm{erf}(x) = \frac{2}{\sqrt{\pi}}\int_0^x e^{-t^2}\,\mathrm{d}t$.

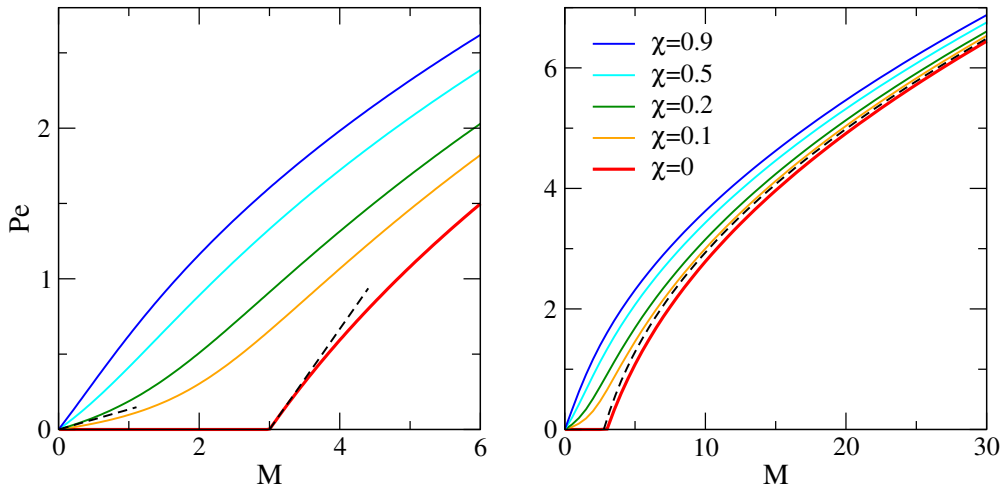

Figure 3.5: $Pe(M)$ relation in the point-source model in the small and large Pe regimes (left and right, respectively) for 3D autophoretic swimmers. Full lines give the solution computed numerically for asymmetry parameter $\chi = 0$, 0.1, 0.2, 0.5, and 0.9, from bottom to top. Approximations are shown in dashed lines, respectively from left to right equations (3.35), (3.34) and (3.36).

3.2.3 Interfacial swimmer

Our toy model has proved its capacity to capture the autophoretic system response on a semi-quantitative basis. In this part, we adapt the toy model to the interfacial swimmer. But as we pointed out in 3.1.2, we can distinguish two possibilities, either the surfactant spreads within the fluid bulk (3D) or lays at the interface (2D). We treat the two cases in turn.

a. 3D interfacial swimmer: soluble surfactant

We now consider an interfacial swimmer, releasing through a point source a soluble surfactant spreading into the fluid bulk. In the same spirit, we decouple the concentration and flow problems. For the transport part, with (3.27),(3.28) and $\chi = 0$, we obtain,

$$\phi(r,\theta) = \frac{1}{2\pi r} \exp\left(-\frac{Pe}{2} r(1+\cos\theta)\right), \tag{3.37}$$

which is the formula (3.30) with a factor two coming from the half-space geometry.

In the steady-state, the velocity verifies the swimmer dynamic equation (3.23) with the inertia term null i.e the velocity is fixed by the balance between the capillary force (3.11) and the drag force (3.12).

$$F_c = -2\kappa a \int_0^\pi \phi(a,\theta)\cos\theta \, \mathrm{d}\theta = \hat{F}_d. \tag{3.38}$$

All the hydrodynamics complexity (exclusion volume, Marangoni flow, etc.) is bypassed by assuming that the flow force $\hat{F}_d$ is the Stokes drag experienced by a disk moving at the speed U. Then, the drag is given explicitly by $\hat{F}_d = C\eta a U$, with C a numerical prefactor that depends only on the swimmer shape, $C = 16/3$ for a disk swimming along a flat surface. This simplification allows solving analytically the problem.

For a chemical or a temperature distribution within a 3D half-space, we obtain the following

equation, involving Pe, M and χ

$$\frac{Pe}{M} = -C \int_0^\pi \frac{\cos\theta}{2\pi\hat{r}} \exp\left[-Pe(\hat{r} + \cos\theta + \chi)\right] \, \mathrm{d}\theta, \quad \hat{r} = \sqrt{1 + 2\chi\cos\theta + \chi^2}, \quad M = \frac{\kappa\mathcal{J}}{\eta D^2}. \tag{3.39}$$

For a symmetric swimmer, this simplifies into

$$\frac{Pe}{M/C} = e^{-Pe/2} I_1\left(\frac{Pe}{2}\right), \tag{3.40}$$

with I_1 is the modified Bessel function of the first kind and order one. If the source is shifted from the disk centre, there is no closed form as presented above but $Pe(M)$ can be investigated analytically in the limiting case. In the regime of small Péclet number, we find at the lowest order,

$$\chi = 0, \quad \frac{Pe}{2} = \frac{1}{C}\frac{M}{4} - 1, \quad \text{for } \frac{M}{C} > 4, \tag{3.41}$$

$$\chi > 0, \quad Pe = \frac{\chi M}{2C}. \tag{3.42}$$

For large Pe, the integral in (3.39) can be evaluated[11], with the result

$$Pe = \frac{(M/C)^{2/3}}{[\pi(1-\chi)]^{1/3}}. \tag{3.43}$$

Let us point the various features of the swimming curves $Pe(M)$. At low Pe, there is an instability threshold as in the case of the autophoretic swimmer. Spontaneous symmetry breaking occurs only below a critical Marangoni number $M_c = 4C$. When $\chi > 0$, there is no critical value, and the swimmer starts to swim for M as small as we want. We also note that the slope at the origin depends on the χ such the higher χ, the steeper the slope. Far above the threshold, $Pe(M)$ is a concave increasing function, such that $Pe \propto M^{2/3}$. However contrary to autophoretic swimmers, in the presence of a tiny intrinsic asymmetry of the chemical, we still have a dependence on χ at high Pe.

b. 2D interfacial swimmer: insoluble surfactant

After considering a 3D transport of surfactant, we treat a surfactant caught at the interface. Since the interface is flat, the problem is purely two dimensional. Then surface concentration field at $\chi = 0$ is given by

$$\Gamma(r,\theta) = \frac{1}{2\pi} \exp\left(-\frac{Pe}{2} r\cos\theta\right) K_0\left(\frac{Pe}{2} r\right), \tag{3.44}$$

with K_0 the modified Bessel function of the second kind. Following the same approach as above, one obtains

$$\frac{Pe}{M} = -C \int_0^\pi \frac{\cos\theta}{\pi} e^{-\frac{Pe}{2}(\cos\theta+\chi)} K_0\left(\hat{r}\frac{Pe}{2}\right) \, \mathrm{d}\theta, \quad M = \frac{\kappa\mathcal{J}a}{\eta D^2}, \tag{3.45}$$

with $\hat{r}$ defined as in (3.39). The behaviour at small Pe is now

$$\chi = 0, \quad Pe = 4e^{-4C/M - \gamma_{EM}}, \tag{3.46}$$

$$\chi > 0, \quad Pe = \frac{\chi M}{2C}, \tag{3.47}$$

[11] We use the Laplace method, which works only because $\hat{r} + \cos\theta$ has a unique maximum over $[0, \pi]$.

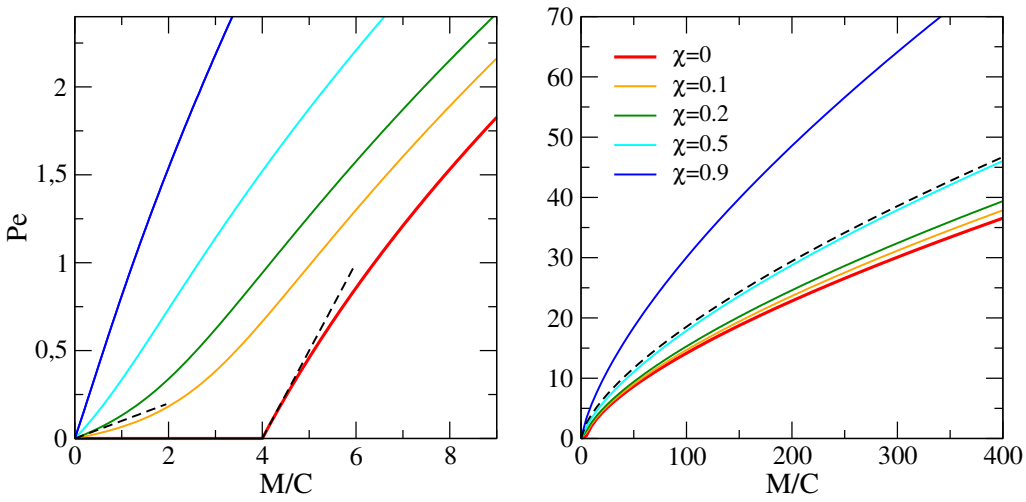

Figure 3.6: $Pe(M)$ relation in the toy model with point-source in the small and large Pe regimes (left and right, respectively) for 3D interfacial swimmers. Full lines give the solution computed numerically for asymmetry parameter $\chi = 0$, 0.1, 0.2, 0.5, and 0.9, from bottom to top. Approximations are shown in dashed lines, respectively from left to right equations (3.42), (3.41) and (3.43) with $\chi = 0.5$.

with γ_{EM} the Euler-Mascheroni constant. For large Pe, the Laplace method yields

$$Pe = \sqrt{M/C} - \frac{1}{2} + \mathcal{O}(M^{-1/2}). \tag{3.48}$$

The 2D interfacial swimmer exhibits the same global features as the 3D interfacial swimmer and phoretic swimmer. At low Pe, the asymmetric swimmer again differs from the symmetric swimmer. But for the latter, there is no true instability threshold and the slope at the origin is zero. At large Pe, the curve $Pe(M)$ increases sub-linearly according to a 1/2 power law, whatever χ (see fig. 3.7).

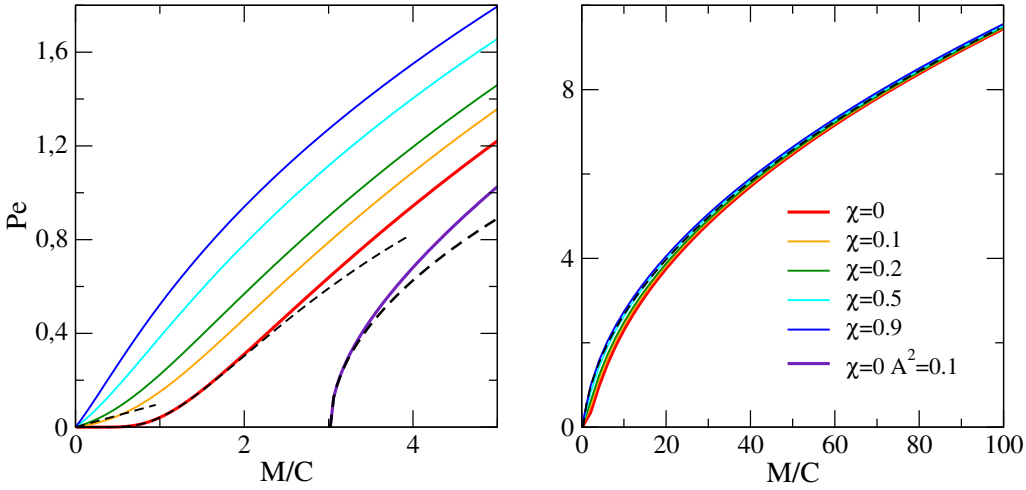

Figure 3.7: $Pe(M)$ relation in the point-source model in the small and large Pe regimes (left and right, respectively) for 2D interfacial swimmer. Full lines give the solution computed numerically for asymmetry parameter $\chi = 0$, 0.1, 0.2, 0.5, and 0.9, from bottom to top. Approximations are shown in dashed, respectively from left to right (3.47), (3.46), 3.51 and (3.48).

Finally, inspired by the experimental situation with camphor, we extend the model to

evaporating surfactant. Then, if the insoluble surfactant disappears from the surface at rate k, the concentration equation becomes

$$Pe\frac{\partial\phi}{\partial t} = \Delta\phi - A\phi + \delta(\boldsymbol{r} - \boldsymbol{R}(t)). \tag{3.49}$$

The solution now includes a factor e^{-At}. Considering the symmetric swimmer only, we have

$$\frac{Pe}{M/C} = e^{-\chi\frac{Pe}{2}} I_1\left(\frac{Pe}{2}\right) K_0\left(\sqrt{\frac{Pe^2}{4} + A^2}\right). \tag{3.50}$$

The behaviour at small velocities is qualitatively changed,

$$Pe = 2\sqrt{M/C - \frac{1}{K_0(A)}}, \quad \text{for} \quad M/C > \frac{1}{K_0(A)}. \tag{3.51}$$

The large-Pe behaviour is not modified at lowest order: The term $-1/2$ in (3.48) is replaced with $-(1 + A^2)/2$. Compared to the stable surfactant, at low Pe, there is critical M if the evaporation is non-zero. Knowing that K_0 is a decreasing function, we see that the critical value increase with the evaporation rate.

3.2.4 Summary

From the velocity equation at low and large Pe, we can deduce a formula for the velocity U. As we already mentioned, a major experimental control parameter at hand is the disk radius, so that it would be desirable to obtain an explicit radius dependency. To do so, we assume $\mathcal{J} = \mathcal{S}\pi(2a)^{d'-1}J$ with J is a lineic or surfacic flux, for the transport dimension $d' = 2$ or 3, and $\mathcal{S}$ is a constant depending on the swimmer and transport dimension, respectively $\mathcal{S} = 1$ for the phoretic sphere and the interfacial disk with a 2D transport, and $\mathcal{S} = 1/4$ for the interfacial disk with the 3D transport.

Type of swimmer	Low Pe		High Pe
	$\chi > 0$	$\chi = 0$	
Phoretic	$\frac{4\chi\mathcal{M}J}{3D}$	$\frac{2\mathcal{M}J}{3D} - \frac{2D}{a}$	$\sqrt{8\frac{\mathcal{M}J}{Da}}$
3D interfacial	$\frac{\chi\kappa\pi Ja}{2C\eta D}$	$\frac{\kappa\pi Ja}{2C\eta D} - \frac{2D}{a}$	$\left(\frac{\pi a}{D(1-\chi)}\right)^{1/3}\left(\frac{\kappa J}{C\eta}\right)^{2/3}$
2D interfacial	$\frac{\chi\kappa J\pi a}{C\eta D}$	$\frac{4D}{a}e^{-4\frac{C\eta D^2}{2\pi\kappa Ja^2}-\gamma_{EM}}$	$\sqrt{\frac{2\pi\kappa J}{C\eta}}$

Table 3.1: Swimmer velocity U for three types of swimmer considered in the low and high Pe regimes.

3.3 Reciprocal theorem: Marangoni contribution and the Lorentz toy model

So far, one basic assumption is that the fluid flow has uniform velocity. Such a simplification is a drastic one, as it neglects Marangoni flows whose origin is the same as the capillary driving.

Then, the Marangoni flow affects neither the surfactant transport since the advective flow is assumed uniform nor the swimmer dynamics since we assume a simple Stokes drag. This restriction can be partially relieved for the force exerted by the fluid on the swimmer. "Via the magic of the reciprocal theorem" [25], the flow force can be written as the sum of two forces: a viscous force without Marangoni flow $\hat{F}_\mathrm{d}$, and a second contribution due to the Marangoni flow $F_{\mathrm{v}\mathcal{M}}$. The magic is that we can calculate that contribution without actually knowing the Marangoni flow themselves, only knowing the Marangoni stress at the surface.

3.3.1 Lorentz Reciprocal theorem: Marangoni force and Marangoni flow contribution

The idea of "reciprocity" is usually associated with the acoustic or waves where the focus is on the scalar wave equation: the response measured at a location B from a source A is the same as the response measured at A from the source B, which can be linked with Green's second identity:

$$\int_V \left(\psi\,\nabla^2\varphi - \varphi\,\nabla^2\psi\right)\ \mathrm{d}V = \oint_{\partial V} \left(\psi\boldsymbol{\nabla}\varphi\cdot\boldsymbol{n} - \varphi\boldsymbol{\nabla}\psi\cdot\boldsymbol{n}\right)\ \mathrm{d}S,$$

with ψ and φ two scalar field, V a volume and ∂V the surface delimiting the volume V and $\boldsymbol{n}$ the normal to the surface element $\mathrm{d}S$. This identity applies to other scalar fields beyond acoustic equation, such as the Navier–Stokes equations and advection–diffusion–reaction equations [25]. The main interest of the reciprocal theorem is to bypass the computation of integral quantities such as the viscous flow force (3.12), which is particularly interesting in the case of the interfacial swimmer to compute the forces applying on the swimmer [24].

To use the reciprocal Lorentz theorem for our interfacial swimmer, we introduced two systems. The first is the Marangoni propulsion problem: an object moving at the surface of a half-space fluid, releasing a surfactant and thus generating a Marangoni flow but also a capillary and a viscous forces which applies on it. The second system is the purely hydrodynamics dual problem: the same object moving upon the surface of the same fluid, but without surfactant. Both verify the Stokes equation for an incompressible fluid[12]. To distinguish the Marangoni propulsion problem from the dual problem we add a hat for the quantities of the dual problem. As demonstrated in the appendix 3.7.3, we can obtain

$$\underbrace{\int_\Omega (\boldsymbol{n}\cdot\hat{\bar{\boldsymbol{\sigma}}})\cdot\boldsymbol{u}\ \mathrm{d}S}_{A} + \underbrace{\int_\mathcal{D} (\boldsymbol{n}\cdot\hat{\bar{\boldsymbol{\sigma}}})\cdot\boldsymbol{u}\ \mathrm{d}S}_{B} = \underbrace{\int_\Omega (\boldsymbol{n}\cdot\bar{\boldsymbol{\sigma}})\cdot\hat{\boldsymbol{u}}\ \mathrm{d}S}_{C} + \underbrace{\int_\mathcal{D} (\boldsymbol{n}\cdot\bar{\boldsymbol{\sigma}})\cdot\hat{\boldsymbol{u}}\ \mathrm{d}S}_{D}. \tag{3.52}$$

As a reminder, Ω refers to the free surface and $\mathcal{D}$ corresponds to the disk surface.

By using the no-slip boundary condition and the Marangoni stress, we can rewrite the four integrals A, B, C and D

$$A = 0 \quad \text{because} \quad \boldsymbol{n}\cdot\hat{\bar{\boldsymbol{\sigma}}} = 0, \qquad B = \int_\mathcal{D} (\boldsymbol{n}\cdot\hat{\bar{\boldsymbol{\sigma}}})\cdot U\boldsymbol{e}_\mathrm{x}\ \mathrm{d}S = U\hat{\boldsymbol{F}}_\mathrm{d}\cdot\boldsymbol{e}_\mathrm{x},$$

$$D = \hat{U}\boldsymbol{F}_\mathrm{v}\cdot\boldsymbol{e}_\mathrm{x}, \qquad C = -\int_\Omega \hat{\boldsymbol{u}}\ \cdot\boldsymbol{\nabla}_s\gamma\ \mathrm{d}S.$$

Finally, with the reciprocal theorem, the flow force reads as

$$\boldsymbol{F}_\mathrm{v}\cdot\boldsymbol{e}_\mathrm{x} = \frac{\hat{\boldsymbol{F}}_\mathrm{d}}{\hat{U}}U\boldsymbol{e}_\mathrm{x} + \int_\Omega \boldsymbol{\nabla}_s\gamma\cdot\frac{\hat{\boldsymbol{u}}}{\hat{U}}\ \mathrm{d}S, \tag{3.53}$$

$$\boldsymbol{F}_\mathrm{v} = \hat{\boldsymbol{F}}_\mathrm{d} + \boldsymbol{F}_{\mathrm{v}\mathcal{M}}. \tag{3.54}$$

[12]For the dual problem it is better to choose a system with an analytic solution, as moving disk or a sphere (see solutions in the appendix 3.7.4).

We have split the F_{v} into two contributions. The first contribution $\hat{\boldsymbol{F}}_{\mathrm{d}}$ (3.55), which is the Stokes drag for a moving object without any surfactant and Marangoni flow.

$$\hat{\boldsymbol{F}}_{\mathrm{d}} = -C\eta a U \boldsymbol{e}_{\mathrm{x}}, \tag{3.55}$$

The second contribution is the force $F_{\mathrm{v}\mathcal{M}}$ induced by the Marangoni flows (3.56). This Marangoni flow force is the integral over the free surface of the surface concentration gradient multiplied by the dual velocity field. Then, by using the linear relation between the surface tension and the concentration, $\gamma = \gamma_0 - \kappa c$, the force can be written as

$$\boldsymbol{F}_{\mathrm{v}\mathcal{M}} = -\kappa \int_{\Omega} \boldsymbol{\nabla}_s c \cdot \frac{\hat{\boldsymbol{u}}}{\hat{U}} \, \mathrm{d}S. \tag{3.56}$$

By using the divergent theorem[13], we can propose an alternative expression for $F_{\mathrm{v}\mathcal{M}}$

$$\boldsymbol{F}_{\mathrm{v}\mathcal{M}} = -\boldsymbol{F}_{\mathrm{c}} + \boldsymbol{F}_{\mathrm{m}\mathcal{M}}, \tag{3.57}$$

such that:

$$\boldsymbol{F}_{\mathrm{m}\mathcal{M}} = -\int_{\Omega} \gamma \boldsymbol{\nabla}_s \cdot \frac{\hat{\boldsymbol{u}}}{\hat{U}} \, \mathrm{d}S, \tag{3.58}$$

$$= \kappa \int_{\Omega} c \boldsymbol{\nabla}_s \cdot \frac{\hat{\boldsymbol{u}}}{\hat{U}} \, \mathrm{d}S, \tag{3.59}$$

$$= \boldsymbol{F}_{\mathrm{c}} + \boldsymbol{F}_{\mathrm{v}\mathcal{M}}. \tag{3.60}$$

We have thus decomposed the force originating in surfactant as a direct effect acting on swimmer contour and an indirect effect, mediated by Marangoni flow. That is why we call $F_{\mathrm{m}\mathcal{M}}$ the Marangoni force. We emphasize that $F_{\mathrm{m}\mathcal{M}}$ involves no other quantity than the concentration field at the surface.

A question which arises from this Marangoni flow force is the motor or resistive contribution in the swimming. This aspect will be discussed further in the next model. As regards to the Marangoni force $F_{\mathrm{m}\mathcal{M}}$, it is necessariliy a motor force as soon as there is a motion since the steady-state is reached when $\boldsymbol{F}_{\mathrm{m}\mathcal{M}} + \hat{\boldsymbol{F}}_{\mathrm{d}} = \boldsymbol{0}$ and $\hat{\boldsymbol{F}}_{\mathrm{d}}$ is a drag force.

The introduction of Marangoni force offers several advantages. First, $F_{\mathrm{m}\mathcal{M}}$ allows rewriting with an equivalent expression the swimmer dynamics 3.10, such that we do not compare anymore, a capillary force with a complex viscous flow force, but a drag force and a motor force induced by the surface tension inhomogeneity, which simplifies the analysis and the understanding of the problem.

Secondly, if we consider the expression of $F_{\mathrm{m}\mathcal{M}}$ itself (3.59), the key element to induce Marangoni propulsion is not correlated to the surfactant distribution along the swimmer contour, but instead, the surfactant distribution all around the swimmer. The idea simplifies the understanding of the Marangoni propulsion for a symmetric object in Stokes flow [14], such that,

[13] Demonstration:

$$\begin{aligned}
\boldsymbol{F}_{\mathrm{v}\mathcal{M}} \cdot \boldsymbol{e}_x = \int_{\Omega} \boldsymbol{\nabla}_s \gamma \cdot \frac{\hat{\boldsymbol{u}}}{\hat{U}} \, \mathrm{d}S &= \int_{\Omega} \left[\boldsymbol{\nabla}_s \cdot \left(\gamma \frac{\hat{\boldsymbol{u}}}{\hat{U}} \right) - \gamma \boldsymbol{\nabla}_s \cdot \frac{\hat{\boldsymbol{u}}}{\hat{U}} \right] \, \mathrm{d}S, \\
&= -\oint_{\partial \mathcal{D}} \gamma \underbrace{\frac{\hat{\boldsymbol{u}}}{\hat{U}}}_{=\boldsymbol{e}_{\mathrm{x}}} \cdot \boldsymbol{n} \, \mathrm{d}l - \int_{\Omega} \gamma \boldsymbol{\nabla}_s \cdot \frac{\hat{\boldsymbol{u}}}{\hat{U}} \, \mathrm{d}S, \\
&= -\boldsymbol{F}_{\mathrm{c}} \cdot \boldsymbol{e}_{\mathrm{x}} - \int_{\Omega} \gamma(c) \boldsymbol{\nabla}_s \cdot \frac{\hat{\boldsymbol{u}}}{\hat{U}} \, \mathrm{d}S.
\end{aligned}$$

[14] For a symmetric object moving upon a fluid verifying the Stokes equation the terms $\boldsymbol{\nabla}_s \cdot \frac{\hat{\boldsymbol{u}}}{\hat{U}}$ in (3.59) is an odd function of x, such that the rear or the front distribution can be compared evenly.

we have the simple statement: *"For a symmetric object, if there is more surfactant at the rear than the front, the capillary phenomena induce a motor force."*.

The expression of $F_{\mathrm{m}\mathcal{M}}$ can also be interpreted in terms of energy through the dual problem terms $\boldsymbol{\nabla}_s \cdot \frac{\hat{\boldsymbol{u}}}{\hat{U}}$ in (3.59). Physically, this term corresponds to the surface creation/destruction at the interface for the dual problem. If we consider the formula for $F_{\mathrm{m}\mathcal{M}}$, we note that it is very close to the rate of change of surface energy [37],

$$\mathcal{D}_s = \int_\Omega \gamma \boldsymbol{\nabla}_s \cdot \boldsymbol{u} \, \mathrm{d}S. \tag{3.61}$$

As illustrated by the figure 3.8, for a disk moving at the speed $\hat{U}\boldsymbol{e}_x$ upon a fluid verifying the Stokes equation, surface is destroyed at the swimmer front (energy gain) while surface is created at the swimmer rear (energy cost). Therefore, the Marangoni force is related to the energy generated in an imaginary system characterized by the flow of the dual problem and the surface tension of the capillary problem.

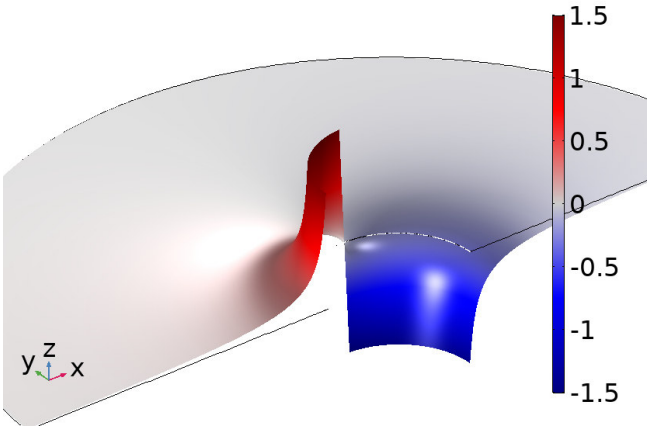

Figure 3.8: 3D representation of the surface divergence of the flow at the free surface normalized by the swimmer speed, $\boldsymbol{\nabla}_s \cdot \hat{\boldsymbol{u}}/\hat{U}$ (3.94) for a disk moving at the speed $\hat{U}\boldsymbol{e}_x$ upon a fluid verifying the Stokes equation. The z position (scale 1:1) and the color bar represent the local value of $\boldsymbol{\nabla}_s \cdot \hat{\boldsymbol{u}}/\hat{U}$, up to a magnitude 1.5 ($\boldsymbol{\nabla}_s \cdot \hat{\boldsymbol{u}}/\hat{U}$ diverges along the swimmer contour). Only the $y > 0$ are represented since the plan $(y = 0)$ is a plan of asymmetry.

We managed via the reciprocal theorem, to find a formula giving the expression of the Marangoni flow force as function of the surfactant distribution and the flow field for a dual problem, which the solution is already known analytically (see 3.7.4).

3.3.2 Lorentz toy model

A basic assumption of the toy model is to neglect the Marangoni flow for the transport and also in the viscous force applying on the swimmer. Using the results described just above, we proposed an improved model including an ersatz of the Marangoni flow force. In the spirit of the basic toy model, we uncouple hydrodynamics and transport by computing a surfactant surface field for a homogeneous flow field and then injecting this distribution in the formula of the forces. By doing so, we slightly improve the basic toy model by taking into account the Marangoni flow field generated by the surfactant distribution into the force applying on the swimmer. Note, that for this problem we limit our analysis to a soluble surfactant, creating the surfactant distribution around the swimmer. The insoluble case will no be treated.

a. Lorentz toy model

The Lorentz toy model is in the continuity of the basic toy model, except we now consider the force $F_{v\mathcal{M}}$, such that the speed steady state is reached when $\mathbf{0} = \boldsymbol{F}_c + \boldsymbol{F}_{v\mathcal{M}} + \hat{\boldsymbol{F}}_d$[15], which gives

$$\mathrm{MG}\left(\frac{Pe^2}{4}\right) = \frac{\sqrt{2\pi}C}{\xi}\frac{Pe}{M}, \quad M = \frac{\kappa\mathcal{J}}{\eta D^2}, \tag{3.62}$$
$$\mathrm{MG}(x) = \mathrm{MeijerG}\left(\left\{\left\{\frac{1}{4},\frac{3}{4}\right\},\{\}\right\},\left\{\left\{\frac{1}{2},\frac{1}{2}\right\},\left\{-\frac{1}{2},0\right\}\right\}\middle| x\right),$$

with $\xi = 2/3\pi$, a geometric factor from the dual problem, and MeijerG the Meijer G-function[16]. The behaviour at small and large Pe is now

$$Pe \ll 1, \quad Pe = 2\exp\left(\frac{8\sqrt{2}\,\pi}{\Gamma\left(\frac{1}{4}\right)\Gamma\left(-\frac{1}{4}\right)}\frac{C}{\xi}\frac{1}{M}\right), \tag{3.63}$$

$$Pe \gg 1, \quad Pe = M^{2/3}\Omega^{2/3}, \quad \Omega = -\frac{\xi}{C}\frac{\Gamma\left(-\frac{1}{4}\right)}{\Gamma\left(\frac{1}{4}\right)}. \tag{3.64}$$

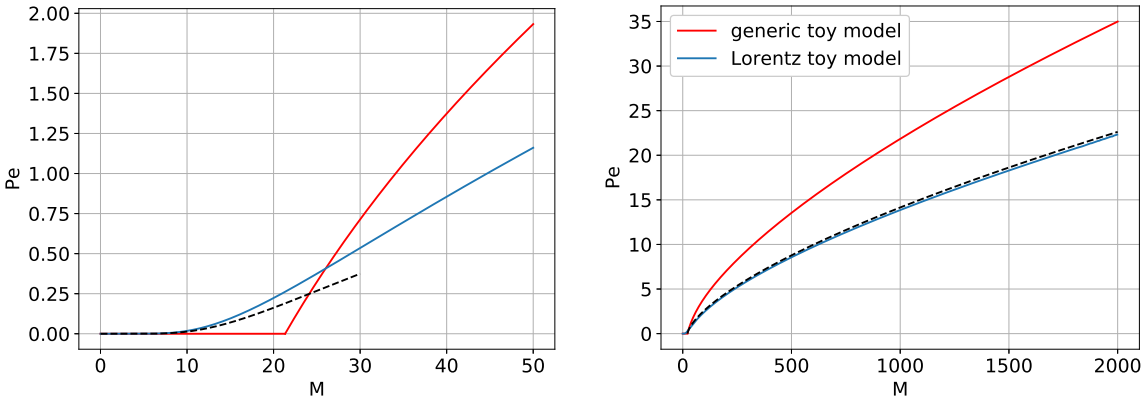

Figure 3.9: $Pe(M)$ relation in the basic toy model (red) and Lorentz toy model (blue) in the small and large Pe regimes (left and right, respectively) for 3D interfacial swimmers. Full lines give the solution computed numerically. Approximations are shown in dashed, respectively from left to right (3.63) and (3.64).

Compared to the simple basic toy model, the behaviour at low Pe is very different. There is no more a finite threshold: spontaneous motion is predicted in all situation. The predicted velocity is higher for the Lorentz toy model than for the basic toy model. The curves cross for $Pe \simeq 0.407$ corresponding to $F_{v\mathcal{M}}(Pe) = 0$. We will discuss this behaviour in the following part.

[15] Actually, the computation are easier to manage by replacing $\boldsymbol{F}_c + \boldsymbol{F}_{v\mathcal{M}}$ by $\boldsymbol{F}_{m\mathcal{M}}$ as stated in (3.60)

[16]
$$\mathrm{MeijerG}[\{\{a_1,\ldots,a_n\},\{a_{n+1},\ldots,a_p\}\},$$
$$\{\{b_1,\ldots,b_m\},\{b_{m+1},\ldots,b_q\}\},z] = \frac{1}{2\pi i}\int_L \frac{\prod_{j=1}^{m}\Gamma(b_j-s)\prod_{j=1}^{n}\Gamma(1-a_j+s)}{\prod_{j=m+1}^{q}\Gamma(1-b_j+s)\prod_{j=n+1}^{p}\Gamma(a_j-s)}z^s\,ds,$$

with Γ the gamma function [19].

At large Pe the behaviour predicted by the Lorentz toy model is very similar to the basic toy model (see fig.3.9): a sub-linear increasing verifying a 2/3 power law. However the prefactor is different, and the Lorentz toy model predicts a lower speed than the basic toy model. By comparing the models expansion, the factor between them is $(\Omega C\sqrt{\pi})^{2/3} \sim 1.57$, i.e. the basic toy model predicts a velocity 57% higher than the Lorentz toy model. Note this ratio is reminiscent of the +50 % in [20], which compares also a model with and without this Marangoni flow force but for an asymmetric swimmer at low Pe. This power-law relation between M and Pe, lead to the speed prediction at large Pe:

$$U = \left(\frac{a}{D}\right)^{1/3} \left(\frac{\Omega\kappa J}{\eta}\right)^{2/3}. \tag{3.65}$$

b. Marangoni flow force

As we just saw, incorporating part of the Marangoni flow consequences in the spontaneous swimming problem modifies some aspects of the basic toy model prediction. To explain them we have to focus on the element added: the Marangoni flow force.

$$\boldsymbol{F}_{\mathrm{v}\mathcal{M}} = \underbrace{\frac{\kappa\mathcal{J}\xi}{\sqrt{2\pi}D}\ \mathrm{MG}\left(\left(\frac{Pe}{2}\right)^2\right)\boldsymbol{e}_x}_{\boldsymbol{F}_{\mathrm{m}\mathcal{M}}} - \underbrace{\frac{\kappa\mathcal{J}}{D}e^{-\frac{Pe}{2}}I_1(\frac{Pe}{2})\boldsymbol{e}_x}_{\boldsymbol{F}_{\mathrm{c}}}, \tag{3.66}$$

$$= -\frac{\kappa\mathcal{J}}{D}\left(\xi\frac{\Gamma(-1/4)}{\Gamma(1/4)} + \frac{1}{\sqrt{\pi}}\right)\frac{1}{\sqrt{Pe}} + \mathcal{O}\left(\frac{1}{Pe^{3/2}}\right), \quad Pe \gg 1. \tag{3.67}$$

At low Pe the Marangoni flow force is positive, and the Marangoni flow favours the swimmer motion. In contrast, at large Pe, $F_{\mathrm{v}\mathcal{M}}$ is negative and it becomes a resistive contribution.

To explain this phenomenon, we remind that in the Marangoni flow force, the key element is the gradient of surface tension in the close swimmer neighbourhood. A surface tension gradient generates a parallel flow which drags the swimmer in the same direction. Therefore, if the strongest gradients are at the swimmer front, the contribution is motor. Respectively the contribution is resistive if the strongest gradients are behind the swimmer.

For Lorentz toy model, at low Pe, the initial isotropic distribution at $Pe = 0$ is compressed in front of the swimmer (see left fig. 3.10) creating a gradient generating a motor flow. But at high Pe, the mean advection is too important and it sweeps the surfactant toward the negative x, which generates a strong gradient at the swimmer rear (see right fig. 3.10 and fig. 3.4), and a resistive Marangoni flow. The tipping point between the two trends is reached when $Pe_r \simeq 0.407$ (determined numerically), as illustrated on the fig. 3.11. Pe_r is also the Péclet magnitude associated with the crossing between the Lorentz and the basic toy model. Finally, the vertical slope at $Pe = 0$ for the Marangoni flow force, explains why there is no critical M for the Lorentz toy model[17]: graphically, whatever the slope of $|\hat{F}_{\mathrm{d}}|$, there would be a crossing point at the origin with $F_{\mathrm{v}\mathcal{M}}$ at low Pe.

As regards the large Pe behaviour, the basic and the Lorentz toy model lead to the same power-law but with a different prefactor. The capillary force and the Marangoni flow force magnitude, and therefore $F_{\mathrm{m}\mathcal{M}}$, all decrease as $1/\sqrt{Pe}$ (see (3.67)). When the velocity equation at large Pe (3.64) is verified, we have $F_{\mathrm{v}\mathcal{M}}/\hat{F}_{\mathrm{d}} = (\Omega C\sqrt{\pi}) - 1 \simeq 0.97$. Therefore, at a swimming point, the resistive force from the Marangoni flow is almost equal to the Stokes drag force. It is as if the drag force in the basic toy model has been doubled.

[17] $Pe \ll 1, \quad F_{\mathrm{v}\mathcal{M}} \propto \log(Pe)Pe.$

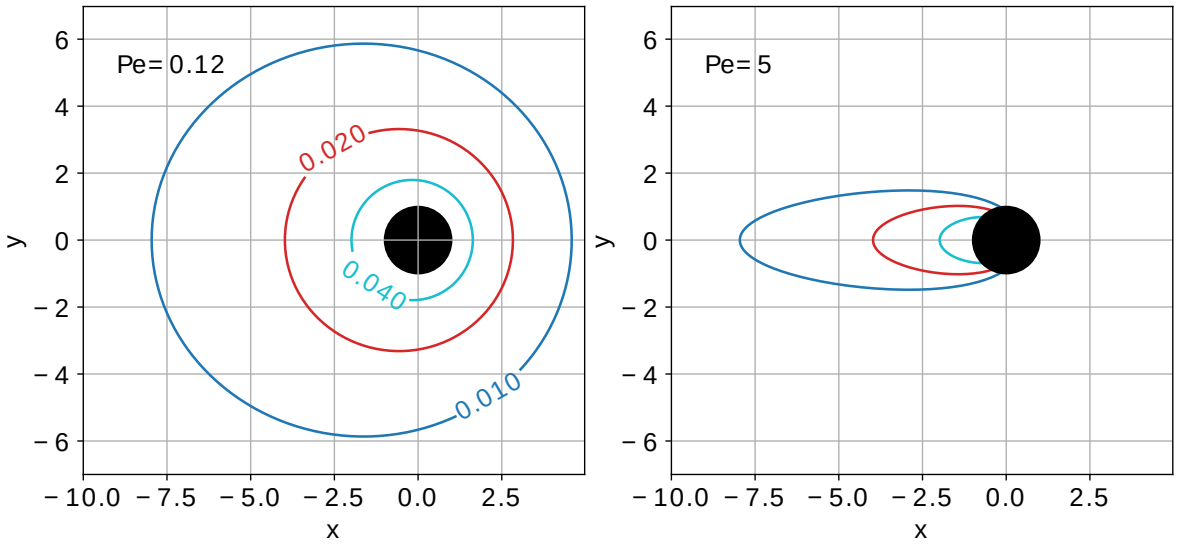

Figure 3.10: Solute iso-concentration [0.01,0.02,0.04] for the Lorentz toy model with $Pe = 0.12$ (left) and $Pe = 5$ (right), the swimmer (black disk) move toward the x positive. The concentrations are normalised by $c^* = \mathcal{J}/Da$.

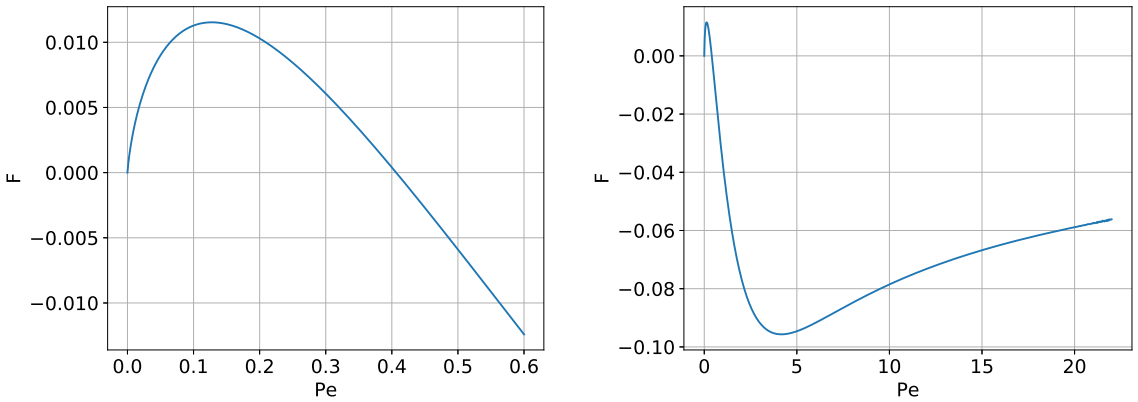

Figure 3.11: $F = F_{v\mathcal{M}}/F^*$ evolution as a function of Pe, with $F^* = \kappa\mathcal{J}/D$, in the small and large Pe regimes (left and right, respectively) for 3D interfacial swimmer. The force is oriented such that the positive value corresponds to a motor contribution for the swimmer motion.

In the literature, the idea that the Marangoni flow can act as a resistive force has already been evoked analytically in [20]. The idea that the Marangoni flow can have a motor contribution is less common. We can quote the phenomenon called "the reverse Marangoni surfing"[38], probably correlated to the experimental observation in [35]. In a few words, in shallow water, the interfacial swimmer can move toward a high surface tension spot, which is incompatible if the capillary force is the only motor force. But it becomes possible if this surface tension spot generates a Marangoni flow driving the swimmer to move toward it. The idea of a motor Marangoni flow has also been evoked in [26], to explain the variation of speed for camphor disk, between large and low water depth.

To conclude, the motor contribution of the Marangoni flow force at low Pe is generated by a stronger surface tension gradient at the swimmer front than the rear. At large Pe, the configuration is inverted, the stronger gradient is at the rear leading to a resistive contribution.

3.4 Concentration swimmer: model concept and toy model

We have focused so far on swimmers with a fixed surface flux, we now investigate the possibility of another class of swimmers with a fixed surfactant concentration. In the second chapter, we have characterised the motion of two types of interfacial swimmers, the agarose-camphor disks belonging to the class of "loaded swimmers", and the pure camphor disks belonging to the class of "dissolving swimmers". Considering the releasing mechanism at the first order, the former has been associated with a homogeneous release flux J, while, the latter is associated with the concentration C_{sat}[18]. We link the structure class of "loaded swimmers" with the theoretical concept of "flux swimmer", i.e. a swimmer with a homogeneous flux along the swimmer surface, while the "dissolving swimmers" are closer to the concept of "concentration swimmer", with a fixed concentration. This last aspect suggests that the capillary force should vanish, thus a priori eliminating the driving contribution to motion. Yet it moves. We will investigate theoretically the possibility of swimming for such concentration swimmers.

3.4.1 The concentration swimmer toy model

To explain how the concentration swimmer may move, we designed a simple model based on the same spirit than the Lorentz toy model presented in section 3.3.2. However, since we consider a Dirichlet condition along the swimmer surface, we can not use any more the computation of the concentration filed made for the point source. It seems that the surfactant distribution from a disk at fixed concentration is not available analytically. But, there is a geometry where much more results are available in the literature: a spherical swimmer, which we now consider.

a. Transport flow: low Péclet and low Reynolds

At low Pe, according to *Acrivos et al.* [1], the concentration field in the space around the sphere is given by:

$$c(r,\theta) = \frac{1}{r}\exp\left(-\frac{Pe}{2}r(1+\cos\theta)\right). \tag{3.68}$$

This outer expansions verifies the condition $c(r \to \infty) = 0$, it matches at some arbitrary distance with the inner expansion $c(r,\theta) = 1/r$ which satisfies the boundary condition $c(1,\theta) = 1$. We also note that the expression is very close to the point source toy models (3.37). To obtain the swimming equation, we inject directly the expression of c in the Marangoni flow force (3.56) [19]

$$Pe \ll 1, \quad Pe = \frac{4}{e^{1+\gamma_{EM}}}\exp\left(-\frac{8}{M}\right) \tag{3.69}$$

As the Lorentz toy model, there is no critical M (see fig. 3.12) with $Pe \propto \exp(-k_i/M)$, with k_i a positive constant depending on the considered model. Surprisingly the constant k_i is more than 6 times higher for basic 3D toy model leading to a lower Pe for the same M despite a lower drag coefficient.

[18] The camphor saturation concentration into water

[19] Because of the radial symmetry of the inner expansion $c(r,\theta) = 1/r$, its contribution in the computation of the Marangoni flow force (3.56) is zero. Moreover, we assume the match between the inner and the outer expansion is at an arbitrary short distance ϵ from the swimmer contour at low Pe. Because of those two aspects, we neglect the error made by directly assuming that the outer expansion is valid over all the free surface in the evaluation of the Marangoni flow force.

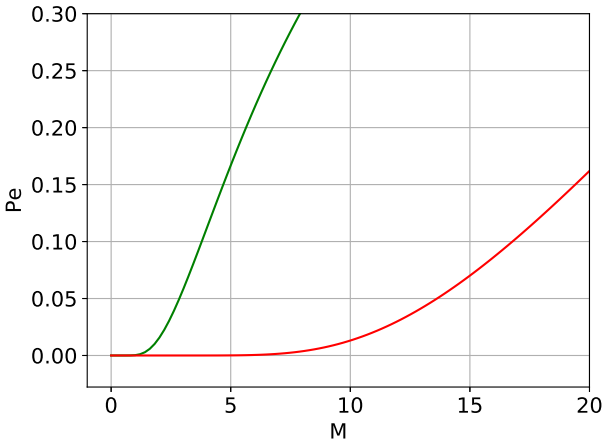

Figure 3.12: $Pe(M)$ relation in the toy model approach for a point-source disk (red line) and a spherical concentration swimmer (green line) at low Pe.

b. Transport flow: large Péclet and large Reynolds

At large Pe, the previous formula (3.68) is no more valid. In [22, 11], a formula is proposed for a sphere in a potential flow (large Reynolds), with a pure radial diffusion, only valid at large Pe,

$$c(r,\theta) = \operatorname{erfc}\left(\sqrt{\frac{Pe}{2}}\frac{(r^3-1)(1+\cos\theta)}{2r(2+\cos\theta)}\right), \tag{3.70}$$

with erfc $= 1 -$ erf and erf the error function[20]. From the concentration field formula (3.70), we determine the velocity equation and the dimensionless formula for $F_{\mathrm{v}\mathcal{M}}$:

$$\tilde{F}_{v\mathcal{M}}(Pe) = \frac{Pe}{M}C_s, \quad M = \frac{\kappa C_{sat} a}{\eta D}, \tag{3.71}$$

$$\tilde{F}_{v\mathcal{M}}(Pe) = \frac{3}{2}\int_{\theta=0}^{\pi}\int_{r=1}^{\infty} \operatorname{erfc}\left(\sqrt{\frac{Pe}{2}}\frac{(r^3-1)(1+\cos\theta)}{2r(2+\cos\theta)}\right)\frac{1-r^2}{r^3}\cos\theta\ \mathrm{d}\theta\ \mathrm{d}r, \tag{3.72}$$

with $C_s = 3\pi$ the drag factor adapted for a sphere half immersed. We tried without success to evaluate analytically the integral (3.72), then we compute it numerically (see fig. 3.13). From the evolution of $\tilde{F}_{v\mathcal{M}}$, we assume that at large Pe the Marangoni flow force tend toward a power law, $\tilde{F}_{v\mathcal{M}}(Pe) \simeq \beta\, Pe^{\alpha}$, such that

$$Pe \gg 1, \quad Pe = \left(\frac{\beta}{C_s}M\right)^{\frac{1}{1-\alpha}}. \tag{3.73}$$

Since α is almost equal to -1, the equation for the velocity at large Pe is very close to $Pe \propto M^{1/2}$ which is a different feature compared to the basic (3.43) and Lorentz toy model (3.64) with

[20] We detail the calculus to obtain the formula (3.70). We simply follow the method detailed in [11]. The concentration around a sphere in a potential flow in a cylindrical coordinate system is given by

$$\frac{c}{C_{sat}} = \operatorname{erfc}\left(\frac{\psi}{2\sqrt{\phi}}\right), \qquad \psi = \frac{U}{2}\left(r^2 - \frac{a^3}{r}\right)\sin^2\theta, \quad \text{(stream function for a sphere)}$$

$$\phi = D\int_0^{\theta} v_{\theta 0}(\theta')\, a^2 \sin^2\theta'\, a\ \mathrm{d}\theta', \qquad v_{\theta 0} = \frac{3U}{2}\sin\theta. \quad \text{(tangential velocity at the sphere surface)}$$

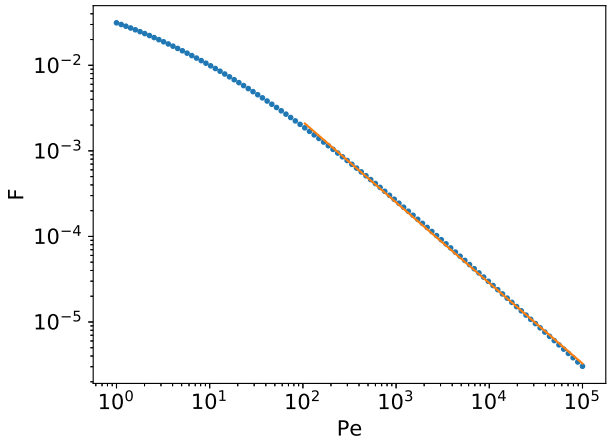

Figure 3.13: $\tilde{F}_{v\mathcal{M}}(Pe)$ the Marangoni force as a function of the Péclet number, the blue dots are the computed value for $\tilde{F}_{v\mathcal{M}}$. The orange line is a linear regression over $Pe \in [10^2, 10^5]$, leading to the power $\beta\, Pe^{\alpha}$ with $\alpha = -0.94$, $\beta = 0.16$, $R^2 = 0.999$.

respectively $Pe \propto M^{2/3}$. Considering (3.71), the prediction for the size dependence of the steady velocity is $U \propto a^{\frac{\alpha}{1-\alpha}}$. The power-law exponent is thus very close to -1/2, indicating that the velocity of concentration swimmers decrease with their size.

c. Qualitative understanding of the motor force for the concentration swimmer

With this toy model, we have shown that the concentration swimmer has surprisingly a behaviour quite close to point source toy models, despite a new release mechanism, a different shape - we have considered a sphere and not a disk- and an advective flow different at large Pe. However, so far we have not explained qualitatively the mechanism allowing the motion of the concentration despite a vanishing capillary force. From the concentration formula (3.70), we now explain this mechanism for our model system and more generally for the whole concept of concentration swimmer.

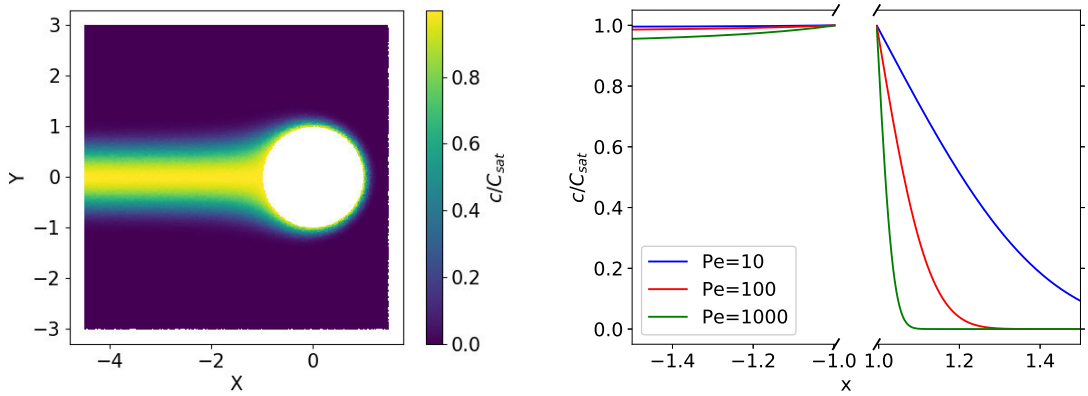

Figure 3.14: Distribution (3.70) of a surfactant around a sphere in potential flow with Dirichlet boundary condition. (Left) Colour field representation, computed with $Pe = 100$. (Right) concentration along the x-axis, with a y-shift 0.1, for Pe=10, 100 and 1000. Because the diffusion is purely radial, the concentration along the x-axis for $x < 0$ is always at the C_{sat}, we introduce a shift in y, to illustrate that Pe has also an effect for the negative x.

By observing the surfactant distribution around the sphere (see fig. 3.14), we can understand qualitatively why $F_{\mathrm{v}\mathcal{M}}$ is a motor force. Indeed, the concentration gradients are much stronger in front of the disk than behind. Then, the induced Marangoni flow at the front is much stronger than at the rear. Those divergent flows interact with the swimmer through viscous interaction and drag the swimmer along their motion leading to a motor Marangoni flow force. More generally, in the swimmer frame reference, the mean flow induced by the swimmer motion sweeps the surfactant toward the rear. For the flux swimmer, at large Pe, it leads to a stronger concentration gradient at the rear than at the front leading to a resistive Marangoni force (see fig. 3.4). At the contrary, for concentration swimmers, the surfactant swept combined with the Dirichlet boundary condition induces strong gradient at the swimmer front: the concentration goes from C_{sat} to zero within a short distance. As a result, the Marangoni flow force is motor.

In conclusion, qualitatively, the Marangoni flows induce a motor contribution for the concentration swimmer.

3.4.2 The concentration swimmer: literature

The concept of Marangoni propulsion with a zero capillary force is very counter-intuitive. To our knowledge, this mechanism of Marangoni propulsion has never been considered yet. However, the "dissolving swimmers" (see chapter *State-of-the-art*) could be modelled by concentration swimmer. When examining some of the phenomena reported in the literature, they question the relevance of the assumed capillary force propulsion and may suggest that the indirect Marangoni flow mechanism is indeed dominant.

A first piece of evidence may be found for swimmers interactions reported for concentration swimmers. In [34, 8] disks exclusively made of benzoquinone form pair and swim while staying in contact. The pair stability suggests that the capillary force is null or negligible since it is a repelling force[21]. Moreover, the motion of the pair supports the idea that, despite a capillary force probably weak, there is motion. The pair-swimming has also been observed for aspirin swimmers [4], also dissolving swimmers, but never for loaded swimmers to the best of our knowledge.

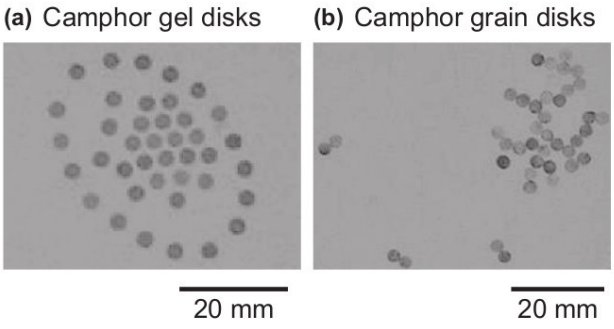

Figure 3.15: Spatial pattern of collective disks made of (a) agar gel - camphor and (b) pure camphor (more accurately, agglomerated grains of camphor), in shallow water, from [30].

Analogously, the concentration swimmer mechanism may explain a phenomenon observed in shallow water (see fig. 3.15). When disks of agarose gel-camphor swimmer are placed in low depth water, they tend to create a regularly spaced pattern, while disks of pure camphor create a dendritic pattern [30]. This experiment confronting the two swimmer types illustrates

[21]The capillary force is intrinsically a repelling force between two flux swimmers. Indeed, when they are close enough, the surfactant cloud around them increases locally the surfactant concentration along the swimmer contour, driving the swimmer to avoid the proximity with other swimmers.

well the dichotomy between the two classes. In one case the capillary force makes the swimmer staying away from each other, while in the second, a capillary force null or weak is consistent with swimmers touching each other.

References [28, 14] show that the motion of a pure camphor disk is a capillary phenomenon strongly correlated with the Marangoni flow. By using a solution of a surfactant (SDS) instead of pure water, the swimmer motion can be modified by lowering the surface activity of camphor: first lowering the speed at low concentration, then an oscillation behaviour and eventually no motion. Surprisingly, above a concentration threshold, the Marangoni flow and swimmer motion are regenerated. Then if we assume that the capillary force vanishes, the only remaining candidate to explain the motion is the Marangoni flow force.

In conclusion, the interaction between "dissolving swimmers" could be explained by a weak or zero capillary force. Meanwhile, the propulsion for "dissolving swimmers" is identified as a capillary phenomenon correlated with the Marangoni flow. Those two elements seem more consistent with a concentration swimmer than a flux swimmer model.

3.5 Back to the experiments

By decoupling surfactant transport and hydrodynamics, we have proposed several toy models, all focused on predicting the swimming velocity. Of course, to make the problem tractable, we introduced some simplifying assumptions. We now compare the predictions of our model to the experimental data and point out the limitations of our modelling. As an aside, we also show that toy models are easily extended to other situations and in conjunction with experiments, we investigate swimmers with various shapes. In particular, we address specifically the orientation of elliptic swimmers.

3.5.1 Comparison with the experiments results

As a reminder, the experiments giving information about the swimming of an individual symmetric swimmer involve a centimetre disk propelling upon a water surface. The surfactant "fuel" allowing the propulsion is camphor. Through this chapter, we introduced different quantities. We remind in the following table 3.2 those quantities their symbol and their experimental value. Then, we can also evaluate the dimensionless numbers for a 4-mm radius swimmer for

quantity	**symbol**	**value**	**source**
Swimmer radius and thickness	a, e	1-15, 0.5 mm	-
Typical speed 4-mm radius swimmer	U	75, 100 $\mathrm{mm\,s^{-1}}$	see fig. 3.16
Mass 4-mm radius swimmer agarose gel and pure camphor	m	31.6/24.9 mg	T
Release rate for a 4-mm radius swimmer	$\mathcal{J}$	5×10^{-9} $\mathrm{mol\,s^{-1}}$	T
Drag factor for a disk/sphere moving at the interface	C, C_s	16/3, 3π	[12]
Camphor concentration at saturation	C_{sat}	7.9 $\mathrm{mol\,m^{-3}}$	[31]
Diffusion coefficient of camphor in water	D	0.72×10^{-9} $\mathrm{m^2\,s^{-1}}$	[10]
Dynamic viscosity of water	η	1×10^{-3} Pa s	-
Density of water	ρ	1×10^{3} $\mathrm{kg\,m^3}$	-
Concentration dependence of surface tension [Eq (4.8)]	κ	6×10^{-3} $\mathrm{N\,m^2\,mol^{-1}}$	[36]

Table 3.2: Numerical value of parameters used in this study. Quantity. "T" means that the value has been evaluated during this thesis.

an agarose gel / pure camphor swimmer:

Dimensionless number	Pe	M	Re	Sc	N (3.19)
Value for agarose gel swimmer	4×10^5	6×10^{10}	3×10^2	1×10^3	2
Value for pure camphor swimmer	6×10^5	3×10^8	4×10^2	1×10^3	3

We observed that all the dimensionless numbers are comparable for the two types of swimmers, except for the Marangoni number with two orders difference between the pure camphor and the agarose gel swimmer. However, for both swimmers, the experimental regime is high Pe and high M.

a. Radius dependence of velocity

As a first approach, we can compare the evolution of the speed as a function of the radius between the 3D basic toy model prediction and the experimental results (see fig. 3.16). For the agarose gel swimmer, qualitatively $U(a)$ has a sublinear dependence. More quantitatively the bigger swimmers ($a > 2.5$ mm) data can be fitted with a 1/3 power law, which is consistent with the 3D basic toy and the Lorentz toy model, since, in both cases, the prediction is $U \propto a^{1/3}$ if $\mathcal{J} \propto a^2$. We note also that the 1/3 power law fails to describe the velocity for the smallest swimmers.

Beyond the radius dependence, the predicted velocity for 4-mm radius swimmer is over-estimated by a factor of 8 for the basic toy model (see tab. 3.1) and a factor of 5 for the Lorentz toy model (3.65). Considering the drastic assumptions involved the discrepancy is not unexpected, and we note that adding more features such as the Marangoni flow force, decreases the difference between the experimental results and the theoretical prediction. Moreover, the neglected physical ingredients in the model, such as the effect of the Marangoni flow on the surfactant distribution or the swimmer thickness are phenomena which may also tend to reduce the speed.

Because it is not clear whether camphor is closer to the soluble or insoluble limit [22], the predictions of the 2D basic toy model have also to be confronted to the experimental results[23]. Following the growing diffusive layer model[24] we assume a constant flux over the swimmer surface, the total release rate is then proportional to the swimmer area, $\mathcal{J} \sim a^2$ [25] and the speed would be

$$U = \sqrt{\frac{\pi a J \kappa}{C\eta}}, \tag{3.74}$$

with $J = \mathcal{J}/\pi a^2$ the surface flux[26]. Then, the velocity increases as the square root of the swimmer size, which is qualitatively consistent with the sublinear increasing observed experimentally. For the velocity magnitude, we obtain an over-prediction of factor 11 between the computed and the experimental value. The predictions of insoluble and soluble models are quite close to each other, and there is no ground to completely discard one of them.

As regards the size dependence of velocity for pure camphor swimmers, comparing the toy model and the results of the experiment is a difficult task since the shapes are different (a sphere instead of a disk). However, we may expect that the concentration toy model to give an order of magnitude no so far from the experimental result, since in both cases the typical

[22] It might also stand in between, making the situation even more complicated.

[23] $M_{2D} = 2 \times 10^{13}$ which is three orders of magnitude above the M associated to the 3D case.

[24] As a reminder we observed for the agarose-camphor swimmer that the precipitated camphor contained in core as to diffuse through a layer of agarose to reach the surrounding fluid, hence a diffusive flux over the swimmer surface.

[25] Note the difference with the assumption made in the 3.1. We simply assume that all camphor released eventually lies at the interface even for the 2D case

[26] note that for insoluble surfactant $\kappa = \mathcal{R}T$ [36].

length is a. Then, by using numeric relation between (3.73) valid at large Pe regime , the concentration toy model predicts a velocity $U = 0.5$ mm/s[27] for a 4-mm radius sphere, which is two orders of magnitude below the measured velocity for the same radius disk.

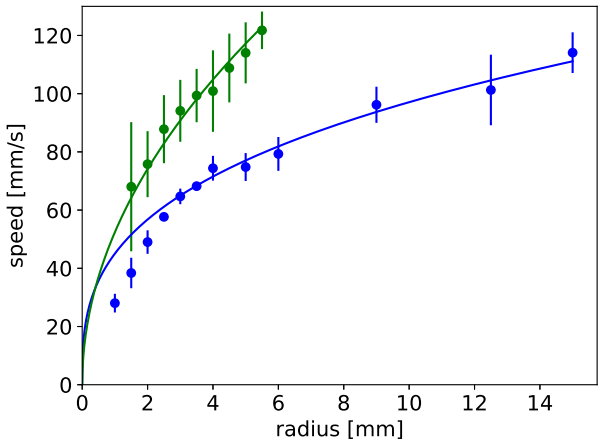

Figure 3.16: Experimental measurements for the evolution of the speed as a function of the radius for gel and pure camphor swimmers (blue and green dots respectively). The lines are two power-law fits respectively $U \propto a^{1/3}$ for the blue curve with a fit for $a > 2.5$ mm, and $a \propto a^{1/2}$ for the green curve.

b. Effect of a small asymmetry

An important question which has been raised in the previous chapter is the asymmetry effect on the swimmer speed. Indeed, an experimental swimmer has always some hardly reproducible defects. To introduce a controlled asymmetry in our swimmer, we punched a hole inside. By assuming a homogeneous flux over the swimmer surface, we expect to shift the barycentre of the total release rate, such that $\chi' = b'/a$, with $b' = b_h(a_h/a)^2$ with a_h and b_h respectively the radius of the hole and b_h its distance to the disk centre. As shown in chapter 2, we have observed that for those pierced swimmers, the position of the hole does not affect significantly the steady-state velocity. Considering the large Pe regime, this observation is consistent with the 2D and 3D basic toy model. Indeed, for the former, we expect no influence at all (3.48), while for the latter the expected modification is only 2% (3.43) for the maximal asymmetry ($\chi' = 0.06$) compared to the symmetric version of the swimmer (see tab. 3.1). Such a variation is smaller than our experimental error bars.

3.5.2 Limitation of the toy models

As we see, the predictions of the toy models are mostly semi-quantitative. Despite its success to capture experimental trends and magnitudes, it is interesting to re-examine the most important simplifying assumptions and how they may impact the theoretical outcome. We order them from what we consider the most important to the less important.

(i) *Neglect of Marangoni flows.* Inhomogeneity in the surfactant distribution around the swimmer generates Marangoni flows that are totally discarded in the toy model, and whose effect on the swimmer is partially taken into account in the Lorentz model. Although the case of a moving source is hardly considered, various works [33, 21, 3] from the literature,

[27] In the swimming equation (3.73), we use $\alpha = -0.94$ and $\beta = 0.16$ in agreement with the linear regression presented in the figure 3.73.

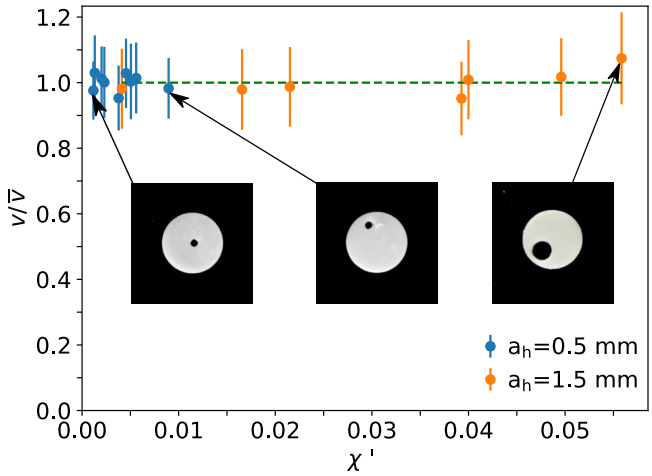

Figure 3.17: Swimming velocity of camphor disks with controlled asymmetry. The asymmetry is a hole with a radius a_h punched in the inner part of the disk. Since the size of the hole can vary for each χ', the velocity is normalized by $\bar{v}$ the average speed for each hole size a_h over all the χ'. A few swimmers are shown as insets. The dashed line corresponds to a unit ratio $v/\bar{v} = 1$. In all cases, $a = 4$ mm and $h = 10$ mm.

have tackled the case of a fixed chemical source as a motor for Marangoni flows. It is natural to use this case to get an estimate of the possible magnitude of such flows in our system. In [23], a fixed point source releasing a surfactant at a constant release rate induces divergent Marangoni flow around it, with velocity is given by $[\kappa\mathcal{J}/(2\pi\eta)]2\nu/r^3)^{1/5}$, with r the distance from the source and ν the kinematic viscosity, the insoluble surfactant is assumed. Now if we imagine the same for a fixed 4-mm radius agarose gel swimmer, it predicts 140 mm/s, which is comparable with the swimmer speed. However, we can expect that the presence of the swimmer reduces the effect compared to a simple point source.

Qualitatively, we can see the Marangoni flow as a homogenising phenomenon for the surfactant distribution by generating advection flow from toward the high concentration gradient. This point of view is compatible with the overprediction made by the 3D basic toy model and the Lorentz toy model. Indeed if we consider the Marangoni force (3.59) as the motor force, the "weight" function $\boldsymbol{\nabla}_s \cdot \frac{\hat{\boldsymbol{u}}}{\hat{U}}$ in the integral of the surfactant distribution, this function diverges over the swimmer contour then quickly decreased in $1/r^2$ (see (3.94)). Therefore a divergent flow sweeping the surfactant away from the swimmer reduces the motor force.

To date, taking into account the Marangoni flow in the transport problem is challenging. However, some papers suggest the idea of treating the Marangoni advection in some specific condition as an effective diffusion transport [6, 18]. Introducing this effective diffusion in our system would allow accounting for Marangoni advection within the point-source framework.

(ii) *Stokes flow and Stokes drag.* In all the models we assume a Stokes flow. For the basic toy models, this assumption permits a unified treatment of phoretic and interfacial swimmer, but, the Stokes flow assumption is no more accurate for the large interfacial swimmers since their Reynolds number can be well above unity ($Re \sim 100$). The Stokes flow is also a key assumption for Lorentz reciprocal theorem, thus, the formula for the Marangoni flow force (3.56) and the Marangoni force (3.59) are different if we include the inertia terms

for the hydrodynamics equation (see the demonstration in appendix 3.7.2)[28].

Numerical simulation involving a 4-mm radius disk swimming generating a Navier-Stokes flow shows that the drag force applying on it is five-time higher than the expected Stokes value at the same speed. This result is consistent with the overestimation of the speed. We can also expect a stronger drag force, if the deformation of the interface, relevant for largest swimmer, and the swimmer thickness, relevant for the smallest swimmer, are also taken into account in the problem.

In [32], experiments involving a disk sliding upon water, with a size and velocities comparable with the agarose gel swimmer suggest that a skin friction $F_v \sim (aU)^{3/2}$ is more adapted than Stokes drag, with $F_v \sim aU$. Assuming a viscous boundary layer under the disk, yield different predictions for the size dependence of the velocity: $U \sim a^\beta$ with β respectively equal to 0 for the 3D basic toy model and the Lorentz toy model, $1/5$ for the 2D basic toy model, and $-1/2$ for the concentration toy model. Those power-law factors are consistently weaker than those observed experimentally. Why the Stokes drag leads to better prediction remains to be understood.

(iii) *Absence of excluded volume.* The model assumes free flow within the swimmer or below the swimmer, which is clearly nonphysical since experimentally, interfacial swimmer and phoretic particle [29] are non-slipping particles. For the interfacial swimmer, the free-flow assumption is less drastic: Since the fluid remains mostly below the swimmer, the advection-diffusion of the chemical is less affected by excluded volume. Note that for the concentration toy model the free-flow is replaced by a potential flow, which allows taking into account the excluded volume of the sphere.

(iv) *Pure 2D/3D case.*

Taking into account the surface exchange kinetics between solubilized and adsorbed surfactant is complex. Actually, the 2D and 3D basic toy model treat the two extremal cases: either the surfactant lies exclusively at the interface (insoluble limit), either in the bulk (instantaneous surface-bulk equilibration). As mentioned in the section 3.1, two fields must be considered, the bulk concentration c and the interface concentration Γ. Note that in a recent study, for steady Marangoni flows induced by a point source [23, 3], the case of camphoric acid is better described by the 2D model, suggesting that such a limiting case could be appropriate for our experimental system.

(v) *Constant flux and constant concentration.*

Since the growing diffusion layer presented in the previous chapter, we assume that the flux rate of camphor for agarose gel swimmer is uniform along the surface, hence the assumption that the total release rate is proportional to the flux rate times the surface. However, this assumption of constant flux is valid only if we assume that the concentration is always far from the saturation. If this is not the case, we may expect that the total release rate increases with the swimmer speed, because the water under the swimmer is more thoroughly renewed. It implies that big swimmers may swim faster than predicted with the constant flux assumption.

The constant concentration assumption for the pure camphor swimmer is just based on the observation that solubilised camphor and solid camphor coexist at the same inter-

[28] It is possible to apply the reciprocal theorem for Navier-Stokes equation, but the dual problem for a disk or a sphere is no more solvable analytically and an integral over the volume appear. Thus, the reciprocal theorem loses most of its interest without the Stokes flow assumption (see appendix 3.7.3).

[29] In the case of phoretic swimmers, the basic toy model can be improved by using a dipole instead of a point source (see appendix 3.7.1).

face. Therefore, the concentration at this interface is the saturation concentration if an equilibrium is maintained. This is true only if the kinetics of exchange is sufficiently fast.

(vi) *Punctual release.* The camphor release occurs all over the immersed surface of the experimental swimmer, and not only at its centre as assumed in the model. As shown in Appendix 3.7.2, there are some conditions in which this assumption may be inconsequential.

3.5.3 Swimmers with elliptic and more complex shapes: orientation

So far, we have been exclusively concerned with the translation velocity of swimmers. We now turn our attention to the orientation of motion. For symmetric swimmers, the main motivation was to check whether the orientation is isotropic. But unexpected results drove us to prolongate our investigation to other shapes, with the hope of finding an explanation. It turns out that the toy model approach can rationalize some of the experimental results, in particular the case of elliptic swimmers.

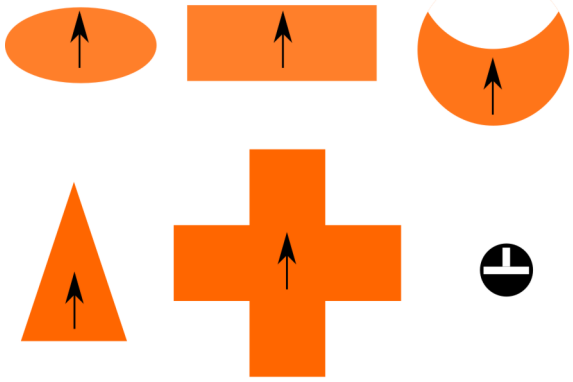

Figure 3.18: Shape of the swimmer used for the orientation experiment (orange - from left to right and up to down: ellipse, rectangle, lunula, triangle and cross) and the black target with a "T", used by the tracking programs to determine the position and the orientation. The black arrow represents the arbitrary orientation given to the swimmer. Scale: the ellipse is 1 cm wide and 2 cm long.

a. Experiments

The orientation experiments tested first the isotropy of the disk. Then we decided to extend our study to other shapes, which has required some changes in the set-up to determine the swimmer orientation. We present this new protocol and then the experimental observations from the run performed.

Set-up The set-up is similar to the one used to measure the swimmer velocity. There are only a few differences, that we detail here. The experiments involve agarose gel swimmers loaded, with different shapes (see fig. 3.18) evolving upon a one-centimetre layer of millipore water. One difference is the "tracking target". It is a thin disk of dark plastic ($\varnothing$=7 mm) with a "T" cut inside, which indicates the swimmer orientation.

Orientation probability distribution function (PDF) The swimmer absolute orientation (= orientation of the swimmer according to the pool) is evaluated by correlating a virtual "T" with the target "T". Note that this method leads to a typical orientation mistake characterised by $\pm 90°$ or $+180°$ compared to the correct orientation, those three values being the angular

positions of the correlation local maxima. Knowing the local velocity, we can determine the angular difference between the absolute orientation and the velocity vector, which gives the relative orientation of the motion or simply the swimmer orientation.

To characterise the orientation we display the PDF for each shape of swimmer tested. We observe two main behaviours. The first is the isotropic behaviour, only observed for the disk, for which the absolute orientation and the motion direction are independent, the PDF is flat (see up figure 3.19). The second behaviour is the nematic one, with two main peaks 180 °apart, corresponding to a movement along an axis. As evidenced by the ellipse and the rectangle, both move along their short axis [30]. The lunula also has a nematic behaviour. However, because it is a polarised shape with the two tips pointing in the same direction, we would expect a dominant orientation, but both peaks are comparable in size. Even so, other re-orientation events uncorrelated with the swimmer shape are present, contrary to the ellipse or rectangle. The nematic behaviour was observed for another class of particles that we call "deformed disks". They are swimmers which look isotropic to the eyes, but still have two nematic peaks emerging from a flat PDF [31].

Beyond the isotropic and nematic behaviours, we also observed a multi-orientation case for two shapes. For the isosceles triangles, there are numerous peaks in the orientation PDF with two mains ones (see down left fig. 3.19). The angular difference between those two peaks is $\Delta\theta = 200 \pm 20°$, above the 180 °of the nematic behaviour. This observation would need more data to be confirmed. Another particularity of the isosceles triangle is to gyrate, with a typical 9 cm radius of curvature, the tip pointing out. Finally, for the cross, we observed multiple peaks but neither their number nor their positions are reproducible.

In conclusion, a variety of behaviours is observed depending on the swimmer shape and symmetry. A clear observation is that elliptic and rectangular swimmers move preferentially along their short axis. This observation is consistent with previous reports [5, 16, 13] [32].

b. Toy model for the ellipse orientation

For the elliptic swimmer, we observe repeatedly the nematic behaviour with motion along the short axis. We now use the toy model approach to rationalize this behaviour. The angle formed between the short axis and the velocity vector $U\boldsymbol{e}_x$ is denoted as θ. The elliptic swimmer releases over its whole surface an insoluble surfactant through a homogeneous flux rate J, such that the transport is restricted to the liquid surface. Besides, we assume the effect of diffusion is negligible ($Pe = \infty$)[33] and we neglect the effect of the Marangoni flows. In those very particular conditions, the local surfactant concentration only depends linearly on the length l of swimmer upstream, such that the surface concentration $\Gamma = l(y)J/U$ (see fig. 3.20). The problem is now tractable because it is only geometric. The torque exerted by capillary force on the swimmer is

$$\boldsymbol{T} = -\kappa \int_{\delta\mathcal{E}} \Gamma\, \boldsymbol{p} \times \boldsymbol{n}\, \mathrm{d}l, \tag{3.75}$$

[30] In the PDFs gives in examples, for rare events the rectangle and the ellipse move along their long axis, the angular position $\pm 90°$. After checking those events on the video, it seems much more probable that they correspond to the typical mistake made by the program as explained above.

[31] Those disks mostly come from old puncher. During the crafting process, the swimmers are cut out from agarose gel sheet loaded in camphor, probably those punchers slightly deformed with times giving to the swimmer an elliptical shape.

[32] It seems that the interfacial swimmers move preferentially along their short axis when such axis can be defined. This observation may be independent of the surfactant and gel used since it has already been described for rectangular swimmer made with PNIPAm gel loaded with ethanol [5]. The class of swimmer also seems to not affect this behaviour, since this nematic motion has been observed for pure camphor ellipse [16, 13].

[33] Experimmentally $Pe \gg 1$, see 3.5.1.

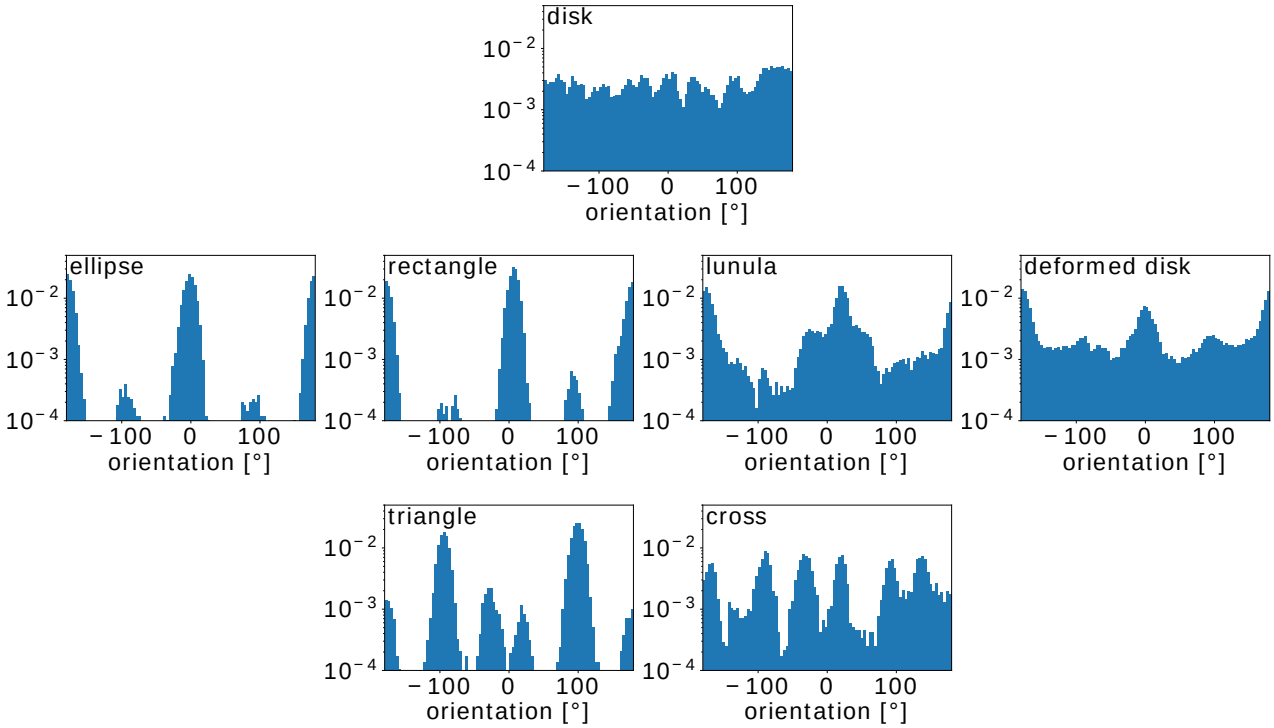

Figure 3.19: Example of typical probability distribution function for the swimmer orientation motion. The angle zero corresponding to a movement along the black arrow defines in the figure 3.18. The distributions are classified according to the behaviour, from up to down: (isotropic) disk a=9 mm/ (nematic) ellipse, rectangle, lunula and deformed disk / (multi-orientation) cross and triangle.

with $\delta\mathcal{E}$ the ellipse contour, $\boldsymbol{p}$ the vector linking the ellipse centre to the ellipse contour and $\boldsymbol{n}$ normal to the ellipse contour[34]. Then, by computing $\boldsymbol{T}(\theta)$, we can determine if an ellipse orientation is stable or unstable. With all the simplifications introduced the concentration is given by:

$$\begin{aligned}\Gamma(y,\theta) &= \frac{Ja}{U}\frac{\sqrt{2}b\sqrt{a^2+b^2-2y^2+(b^2-a^2)\cos(2\theta)}}{b^2\cos(\theta)^2+a^2\sin(\theta)^2}, && \text{if } l>0, \\ &= 0, && \text{otherwise,}\end{aligned} \tag{3.76}$$

with $2a$ and $2b$ respectively the length of the short and long axis of the ellipse. Finally, by injecting, this formula in the torque expression we get

$$\frac{T}{T^*} = -\frac{\tilde{a}^2(1-\tilde{a}^2)\sin(2\theta)\left((1-3\tilde{a}^2)\cos(2\theta)-4\tilde{a}^2\sin(\theta)+3\tilde{a}^2+1\right)\sqrt{\tilde{a}^2\sin(\theta)+\cos^2(\theta)}}{3\left(\tilde{a}^2\sin^2(\theta)+\cos^2(\theta)\right)^3}, \tag{3.77}$$

with $T^* = \kappa J b^3/U$ and $\tilde{a} = a/b$. Because of the ellipse symmetry, the torque vanishes when the motion is along its long and short axis. At the first order, the torque close to this angular position is given by:

$$\frac{T}{T^*} = -\frac{4}{3}(1-\tilde{a}^2)\tilde{a}^2\theta + \mathcal{O}(\theta^2), \tag{3.78}$$

$$= \frac{4}{3}\frac{(1-\tilde{a}^2)}{\tilde{a}}(\theta-\pi/2) + \mathcal{O}((\theta-\pi/2)^2). \tag{3.79}$$

[34]Note that in the capillary torque formula, we implicitly assume the linear dependency between the surface tension and the surface concentration (4.8).

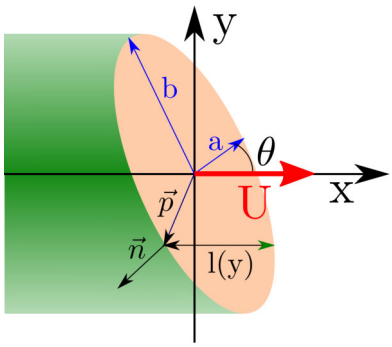

Figure 3.20: Schematic of the ellipse investigated.

This simple model predicts that the motion along the short axis ($\theta = 0°$) is stable ($\partial T/\partial\theta < 0$), while the motion along the long axis ($\theta = 90°$) is unstable ($\partial T/\partial\theta > 0$) (see fig. 3.21). For ellipse close to the disk ($\tilde{a} = 1$), the capillary torque magnitude is low, which is consistent with the idea of "deformed" disk presented introduced previously: the torque is not strong enough to prevent the exploration of unstable orientation when the swimmer, for instance, hits a wall, but the motion stability along the short axis remains marked by the slight deformation. For swimmer close to the other extreme case, the line $a = 0$, the $T(\theta)$ slope around the position $\theta = 90°$ is much steeper than for $\theta = 0°$, then the nematic behaviour would be mostly due to the instability to move along the long axis than the stability for the motion along the short axis.

In the literature, the specific motion of an ellipse has already been modelled analytically for slightly deformed disk [16] and numerically [13], but the computations developments are quite complex. The idea here is to propose a model simpler and more intuitive. We have discussed the limitation of the models but they can offer some insight beyond the velocity prediction.

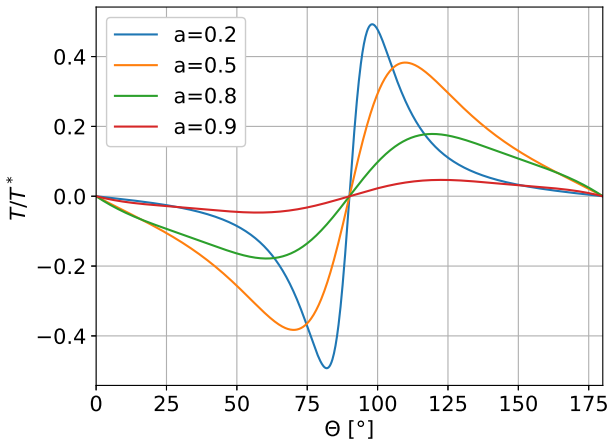

Figure 3.21: Evolution of the torque as a function of the orientation θ, with $\theta = 0$ being a motion along the short axis, for different a with $b = 1$.

3.6 Summary

We have proposed in this chapter a class of model for interfacial swimmers based on the idea of decoupling the transport and hydrodynamic problems. The approach is simple, versatile and amenable to several variations that we have explored. The main features of swimming are

summarized in table 3.3. While the basic toy model provides a minimal framework for the spontaneous symmetry breaking mechanism, the Lorentz model partially accounts for some of the Marangoni effects. We also explored the concentration swimmer, a possibility which has received little attention so far in the literature.

While the behaviours in the low Pe regime can be different between the basic and the Lorentz toy model, a basic prediction stands out in the high Pe regime: $Pe \propto M^{2/3}$. We propose in the next chapter an explanation for such behaviour based on the idea that the transport is dominated by advection.

Toy model	**Characteristic**			**Features**		
	Shape	Source	Driving force	Velocity equation	Low Pe	High Pe
Basic - 3D	disk	point source $\mathcal{J}$	F_{c}	(3.39)	$Pe \propto M$ $M_c = 4C$	$Pe \propto M^{2/3}$
Lorentz	disk	point source $\mathcal{J}$	$F_{\mathrm{m}\mathcal{M}}$	(3.62)	$\log Pe \propto -\frac{1}{M}$ $M_c = 0$ $F_{\mathrm{v}\mathcal{M}}$ motor	$Pe \propto M^{2/3}$ $F_{\mathrm{v}\mathcal{M}}$ resistive
Concentration	sphere	surface concentration C_{sat}	$F_{\mathrm{m}\mathcal{M}}$ $F_{\mathrm{c}} = 0$	(3.69) (3.71)	$M_c = 32\pi/5$ $F_{\mathrm{v}\mathcal{M}}$ motor	$Pe \propto M^{2/3}$ [35] $F_{\mathrm{v}\mathcal{M}}$ motor

Table 3.3: Summary of all the toy model involving a interfacial swimmer releasing soluble surfactant

Experimentally, the agarose-camphor swimmer and the pure camphor swimmer are described by high Péclet ($Pe \sim 10^5$) and high Marangoni number ($M \sim 10^{11}$ for gel swimmer and $M \sim 10^8$ for pure camphor swimmer). For these regimes, if we assume $\mathcal{J} \propto a^2$, the toys models predict a sublinear dependency, between the swimmer velocity and its size, which is indeed what we observed experimentally. However, for the velocity magnitude, the Lorentz toy model fairs better than the basic one, but still overestimates the velocity magnitude by a factor 5.

The evolution of the Marangoni flow force as a function of Pe is characterized by a switch from a resistive contribution at high Pe to a motor contribution at low Pe. This capacity to use the generated Marangoni flow to induce a motion may be achieved by swimmers with a fixed concentration at their surface. We finally introduced a model called the concentration toy model to support this idea, with a velocity equation at large Pe very close to the other toy models involving soluble surfactant. The velocity prediction for this toy model is just one order of magnitude below the experimental velocity, which is not so far since we compare disk-shaped swimmer with a sphere.

If toy models offer a simple but already rich view of possible swimming behaviours, they rely on a key assumption – the decoupling of transport and hydrodynamics – which can not be justified rigorously. The consequences of such an approximation remain unclear. Given the complexity, only numerical simulations can provide a complete view of the problem and capture the interplay between swimmer motion, surfactant transport and Marangoni flows. We now turn to such a numerical exploration to reach a more refined level of description and understanding.

[35] Potential flow for the transport and numerical evaluation of the power law.

3.7 Appendices

3.7.1 Extension toy model for phoretic particle

The toy model gives a correct description of the far-field concentration but only a rough approximation in the vicinity of the swimmer. Here we show that some improvements are possible with a relatively simple refinement. In particular, the phoretic sphere is a ghost shell for the point source, such that:

- Advection transport occurs within the phoretic particle leading to an anisotropic radial flux on the particle surface. This is in contrast with the isotropic flux imposed in [27].
- The advection velocity at the particle surface differs from the tangential one obtained from the slipping boundary condition in [27]

To improve the first point, an idea is to add a dipolar term, which can enforce a constant (to $\mathcal{O}(Pe^2)$) radial flux at the particle surface. Quantitatively, the radial flux is $J_r = -D\partial_r\phi + U\cos\theta\phi$. By injecting the solution for the point source solution (3.30), and developing at first order in Pe, we have:

$$\frac{J_r}{\mathcal{J}/4\pi a^2} = 1 - \frac{Pe}{2}\cos\theta + \mathcal{O}(Pe^2). \tag{3.80}$$

Now, for a dipolar source term of strength μ_1 at the origin, the distribution is given by:

$$\phi_1(r,\theta) = \frac{1}{4\pi D r}\frac{\mu_1\cos\theta}{r}\exp\left(-\frac{Ur}{2D}(1+\cos\theta)\right). \tag{3.81}$$

Then at the order zero, the radial flux is given by $2\mu_1\cos\theta/a$. To balance the angular modulation from the point source dipole, the dipole strength is chosen to be $\mu_1 = aPe\mathcal{J}/4$. The resulting concentration field at the surface is

$$\phi(a,\theta) = \frac{\mathcal{J}}{4\pi D a}\left(1+\frac{Pe}{4}\cos\theta\right)\exp\left(-\frac{Pe}{2}(1+\cos\theta\right). \tag{3.82}$$

Note that the formula above is unphysical for $Pe > 4$, but this value is never reached in the vicinity of the threshold. Then, the velocity equation is given by :

$$\frac{Pe^3}{M} = 4e^{Pe/2}\left(2Pe\cosh\frac{Pe}{2} - (4+(Pe/2)^2)\sinh\frac{Pe}{2}\right). \tag{3.83}$$

Such a correction shifts the threshold value from $M_c = 3$ to 6, instead of 4 in [27]. The maximum of Pe/M occurs at $M^* \simeq 15$ instead of $M^* = 9$ but the magnitude of the maximum is much closer to the point source model with $Pe^*/M^* = 0.11$ instead of the expected 0.085. To conclude, the missing excluded-volume effects in the point-source model lead to an overestimation of velocities but using a dipolar correction to impose at first order in Pe the isotropy of the solute release at the particle leads to improved estimates.

3.7.2 Non punctual release

In most of the toy model considered, the source is punctual. But what would happen if we consider a distributed source, possibly in an inhomogeneous way? If we consider only advection (infinite Pe) and a 2D interfacial swimmer, we can obtain a precise answer. We retain the radial symmetry of the source, with a local flux $J(\boldsymbol{r}) = \mathcal{J}/(\pi a^2) f(r/a)$ that leads to the velocity

$$U^2 = \check{\beta} \frac{\mathcal{J}\kappa}{C\eta a}. \tag{3.84}$$

where the prefactor is

$$\check{\beta} = \frac{2}{\pi} \int_0^1 \breve{f}(p)\ \mathrm{d}p, \quad \breve{f}(p) = 2 \int_{|p|}^{\infty} \frac{f(u)u}{\sqrt{u^2 - p^2}}\ \mathrm{d}u, \tag{3.85}$$

with $\breve{f}$ is the Abel transform of f. Combining the two above equations show that $\check{\beta} = 1$, whatever the function f. The velocity is independent of the release profile. Such a result arises in part because we have assumed a linear dependence of γ on concentration (see (4.8)). As a consequence, what matters is only the total amount of chemical behind the swimmer, not its spatial distribution. This conclusion would not hold for nonlinear relations $\gamma(\phi)$ (3.8).

3.7.3 Demonstration of the reciprocal theorem

In this section, we demonstrate the formula (3.52). We consider two problems. The former is the complete problem of a swimmer releasing a surfactant. The latter is a dual problem, with a swimmer in motion, but without any surfactant released. In both cases, we consider an incompressible Stokes flow, in the steady-state. The quantities associated with the dual problem are indicated with a hat $\hat{}$.

$$\boldsymbol{\nabla}\cdot\boldsymbol{u}=\boldsymbol{\nabla}\cdot\hat{\boldsymbol{u}}=0,\quad(\textbf{incompressibility})\qquad\boldsymbol{\nabla}\cdot\bar{\boldsymbol{\sigma}}=\boldsymbol{\nabla}\cdot\hat{\bar{\boldsymbol{\sigma}}}=\mathbf{0},\quad(\textbf{Stokes})\tag{3.86}$$

with $\boldsymbol{u}$ the flow velocity and $\bar{\boldsymbol{\sigma}}$ stress tensor. In this demonstration, we use the Einstein notation for the tensor, such that

$$[\bar{\boldsymbol{\sigma}}]_{ij}=-p\delta_{ij}+\tau_{ij},\tag{3.87}$$

$$[\bar{\boldsymbol{\tau}}]_{ij}=\eta(\partial_i u_j+\partial_j u_i),\tag{3.88}$$

with $\bar{\boldsymbol{\tau}}$ the viscous stress tensor. Then, by using the symmetry of the stress tensor and the Stokes equation,

$$\sigma_{ij}\hat{\tau}_{ij}=\sigma_{ij}\partial_j\hat{u}_i+\underbrace{\sigma_{ij}}_{=\sigma_{ji}}\partial_i\hat{u}_j=2\sigma_{ij}\partial_j\hat{u}_i=2(\partial_j(\sigma_{ij}\hat{u}_i)-\hat{u}_i\underbrace{\partial_j\sigma_{ij}}_{\boldsymbol{\nabla}\cdot\bar{\boldsymbol{\sigma}}=\mathbf{0}})=2\partial_j(\sigma_{ij}\hat{u}_i).$$

In the same manner,

$$\hat{\sigma}_{ij}\tau_{ij}=2\partial_j(\hat{\sigma}_{ij}u_i).$$

Then, by using the incompressibility of the flow, we obtain the equality

$$\sigma_{ij}\hat{\tau}_{ij}=-p\delta_{ij}\hat{\tau}_{ij}+\eta\hat{\tau}_{ij}\tau_{ij},=\hat{\sigma}_{ij}\tau_{ij},$$

where we have used $\tau_{ii}=2\nabla\cdot\hat{\boldsymbol{u}}=0$. We can therefore write

$$\boldsymbol{\nabla}\cdot(\hat{\bar{\boldsymbol{\sigma}}}\cdot\boldsymbol{u})=\boldsymbol{\nabla}\cdot(\bar{\boldsymbol{\sigma}}\cdot\hat{\boldsymbol{u}}),\tag{3.89}$$

$$\int_{\mathcal{V}}\nabla\cdot(\hat{\bar{\boldsymbol{\sigma}}}\cdot\boldsymbol{u})\,\mathrm{d}V=\int_{\mathcal{V}}\boldsymbol{\nabla}\cdot(\bar{\boldsymbol{\sigma}}\cdot\hat{\boldsymbol{u}})\,\mathrm{d}V,$$

$$\oint_{\mathcal{S}}\boldsymbol{n}\cdot(\hat{\bar{\boldsymbol{\sigma}}}\cdot\boldsymbol{u})\,\mathrm{d}S=\oint_{\mathcal{S}}\boldsymbol{n}\cdot(\bar{\boldsymbol{\sigma}}\cdot\hat{\boldsymbol{u}})\,\mathrm{d}S,$$

with $\mathcal{V}$ the fluid bulk and $\mathcal{S}$ the free surface. We use Green-Ostrogradski formula to obtain the last equality. For $\boldsymbol{n}\cdot\bar{\boldsymbol{\sigma}}\underset{r\to+\infty}{\longrightarrow}\mathbf{0}$ and $\boldsymbol{u}\underset{r\to\infty}{\longrightarrow}0$, we have:

$$\int_{\Omega}(\boldsymbol{n}\cdot\hat{\bar{\boldsymbol{\sigma}}})\cdot\boldsymbol{u}\,\mathrm{d}S+\int_{\mathcal{D}}(\boldsymbol{n}\cdot\hat{\bar{\boldsymbol{\sigma}}})\cdot\boldsymbol{u}\,\mathrm{d}S=\int_{\Omega}(\boldsymbol{n}\cdot\bar{\boldsymbol{\sigma}})\cdot\hat{\boldsymbol{u}}\,\mathrm{d}S+\int_{\mathcal{D}}(\boldsymbol{n}\cdot\bar{\boldsymbol{\sigma}})\cdot\hat{\boldsymbol{u}}\,\mathrm{d}S,\tag{3.90}$$

with Ω the free surface and $\mathcal{D}$ the particle surface. QED.

If instead of Stokes equation we consider that the capillary and the dual problems verify the Navier Stokes equation, $\boldsymbol{\nabla}\cdot\bar{\boldsymbol{\sigma}}=\rho(\boldsymbol{u}\cdot\boldsymbol{\nabla})\boldsymbol{u}\neq0$, then two volumic integrals appear in the final equality 3.90. The right hand side now includes a term

$$-\int_{\mathcal{V}}\hat{\boldsymbol{u}}\cdot\boldsymbol{\nabla}\cdot\bar{\boldsymbol{\sigma}}\,\mathrm{d}V,\tag{3.91}$$

and the dual equivalent for the left-hand side.

3.7.4 Exact Stokes flow around a moving disk and sphere

In this appendix we gather all the analytical solutions, which are used in this chapter for a disk or a sphere with a no-slip condition at their surface, generating Stokes flows around them, in a fluid characterised by the viscosity η. We note $\hat{\boldsymbol{u}}$ the flow field and u, v and w the velocity respectively along $\boldsymbol{e}_x$, $\boldsymbol{e}_y$ and $\boldsymbol{e}_z$.

a. Disk moving at the surface

We consider disk of unit size moving at the constant speed $\hat{U}$ upon an infinite half-space liquid. We introduce $\xi = 2/3\pi$. In a cylindrical coordinate (r, θ, z) centred on the swimmer [24], the velocity field on the liquid surface is:

$$\frac{\hat{u_r}}{\hat{U}}(r, \theta, z = 0) = \xi \cos\theta \left[\frac{\sqrt{r^2 - 1}}{r^2} + 3 \arcsin(1/r) \right], \tag{3.92}$$

$$\frac{\hat{u_\theta}}{\hat{U}}(r, \theta, z = 0) = \xi \sin\theta \left[\frac{\sqrt{r^2 - 1}}{r^2} - 3 \arcsin(1/r) \right], \tag{3.93}$$

$$\boldsymbol{\nabla}_s \cdot \frac{\hat{\boldsymbol{u}}}{\hat{U}}(r, \theta) = \xi \cos\theta \left[-\frac{3\sqrt{1 - 1/r^2}}{r^2 - 1} + \frac{1}{r\sqrt{r^2 - 1}} \right]. \tag{3.94}$$

In cartesian coordinate (x, y, z) [12]:

$$\mathcal{E} = -1 + x^2 + y^2 + z^2, \quad \mathcal{D} = \sqrt{4z^2 + \mathcal{E}^2}, \quad \lambda = \frac{1}{2}(\mathcal{D} + \mathcal{E}),$$

$$\frac{\hat{u}}{\hat{U}} = \xi \left(\frac{2x^2\lambda^{3/2}}{\mathcal{D}(\lambda + 1)^2} - \frac{\sqrt{\lambda}}{\lambda + 1} + 3 \arctan\left(\frac{1}{\sqrt{\lambda}} \right) \right), \tag{3.95}$$

$$\frac{\hat{v}}{\hat{U}} = \xi \frac{2xy\lambda^{3/2}}{\mathcal{D}(\lambda + 1)^2}, \quad \frac{\hat{w}}{\hat{U}} = \xi \frac{2xz\sqrt{\lambda}}{\mathcal{D}(\lambda + 1)}, \quad \frac{\hat{p}}{\eta\hat{U}} = -\xi \frac{4x\sqrt{\lambda}}{\mathcal{D}(\lambda + 1)} + \text{cst}. \tag{3.96}$$

b. Sphere moving at the surface

We consider a sphere of unit sized half-immersed in liquid and moving with constant speed $\hat{U}$. In a spherical coordinate (r, θ, ϕ) centred on the swimmer [12]:

$$\frac{\hat{u_r}}{\hat{U}}(r, \theta) = -\frac{1}{2}\cos\theta \left[\frac{1}{r^3} - \frac{3}{r} \right], \quad \frac{\hat{u_\theta}}{\hat{U}}(r, \theta) = -\frac{1}{4}\sin\theta \left[\frac{1}{r^3} + \frac{3}{r} \right], \tag{3.97}$$

$$\frac{p}{\eta\hat{U}}(r, \theta) = \frac{3}{2}\frac{\cos\theta}{r^2}, \quad \boldsymbol{\nabla}_s \cdot \frac{\hat{\boldsymbol{u}}}{\hat{U}}(r, \theta) = -frac3(1 - r^2)\cos\theta 4r^4. \tag{3.98}$$

3.7.5 About the contact angle and perpetual swimmer

The objective is to comment an assumption consisting in taking into account the angle created by the triple line along the swimmer contour despite the assumption of a flat free interface. Here, using a simple thought experiment, we show that such an assumption leads to nonphysical consequences. We consider a swimmer having two different sides, characterised by distinct contact angles. For simplicity we assume that contact angle for the right side is 90° (see fig.3.22). By taking into account those contact angles, we deduce that the linear capillary force projected along the x-axis is $\gamma(1-\sin\theta_E)$. Then a driving force applies on the swimmer and the two-sides swimmer should move indefinitely. Of course, this result is nonphysical: we obtain a perpetual motion from a passive object. But where is the mistake?

The issue comes from the neglect of the meniscus. Indeed, if the contact angle is not 90°then the free surface is not flat, then the Laplace pressure is not null (3.7), yielding a force on the swimmer. When accounting for this contribution, it turns out the forces exerted on the left and right side of swimmer are opposite to each other. The swimmer remains at rest, as expected [36].

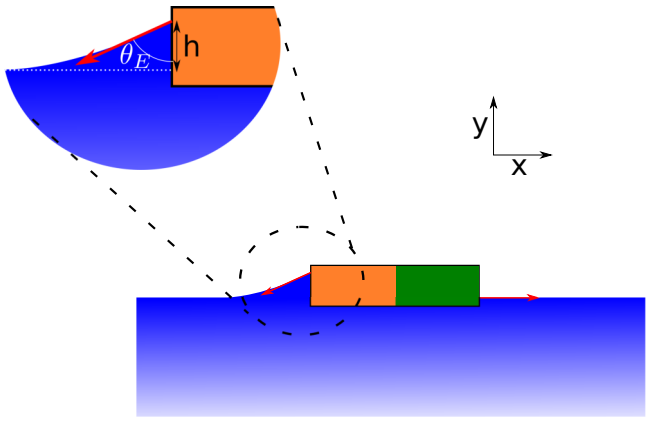

Figure 3.22: Schematic representation of a two-side swimmer, the left side is associated with contact angle $\theta_E \neq 90°$, the right side is associated with the contact angle $\theta_E = 90°$

The mistake is to consider the curvature induced by the meniscus just for the computation of the capillary force and not the Laplace pressure. Also, this little thought experiment shows that the capillary force and the Laplace pressure contribution applying on a swimmer side is equivalent for a flat interface or an interface curved by the swimmer meniscus.

[36] According to [9], the height h reached by the meniscus is given by:

$$h = \sqrt{\frac{2\gamma}{\rho g}}\,(1-\sin\theta_E)\,,$$

with ρ the liquid density and g the gravitational acceleration. By combining this expression with the hydrostatic pressure, we can compute the force pressure induced by the meniscus.

Bibliography

[1] Andreas Acrivos and Thomas D Taylor. Heat and Mass Transfer from Single Spheres in Stokes Flow. *Phys Fluids*, 5(4):387–389, 1962.

[2] J. Anderson. Colloid Transport By Interfacial Forces. *Annual Review of Fluid Mechanics*, 21(1):61–99, 1989.

[3] M M Bandi, V S Akella, D. K. Singh, R S Singh, and S Mandre. Hydrodynamic Signatures of Stationary Marangoni-Driven Surfactant Transport. *Physical Review Letters*, 119(26), 2017.

[4] Tamás Bánsági, Magdalena M. Wrobel, Stephen K. Scott, and Annette F. Taylor. Motion and interaction of aspirin crystals at aqueous-air interfaces. *Journal of Physical Chemistry B*, 117(43):13572–13577, 2013.

[5] Noy Bassik, Beza T. Abebe, and David H. Gracias. Solvent driven motion of lithographically fabricated gels. *Langmuir*, 24(21):12158–12163, 2008.

[6] Thomas Bickel. Spreading dynamics of reactive surfactants driven by Marangoni convection. *Soft Matter*, 15(18):3644–3648, 2019.

[7] I. K. Bratukhin and L. N. Maurin. Convection inf a fluid-filling half space. *Pmm*, 31(3):577–580, 1967.

[8] Tianqi Chen, Dilip K. Kondepudi, James A. Dixon, and James F. Rusling. Particle Flock Motion at Air–Water Interface Driven by Interfacial Free Energy Foraging. *Langmuir*, 35(34):11066–11070, 2019.

[9] David Quéré. De Gennes, Pierre-Gilles, Françoise Brochard-Wyart. *Capillarity and wetting phenomena: drops, bubbles, pearls, waves.* 2013.

[10] J. M.P.Q. Delgado. Molecular diffusion coefficients of organic compounds in water at different temperatures. *Journal of Phase Equilibria and Diffusion*, 28(5):427–432, 2007.

[11] Moshe Favelukis and Cam Hung Ly. Unsteady mass transfer around spheroidal drops in potential flow. *Chemical Engineering Science*, 60(24):7011–7021, 2005.

[12] J. Happel and H. Brenner. 1983_Book_LowReynoldsNumberHydrodynamics. 1963.

[13] Keita Iida, Hiroyuki Kitahata, and Masaharu Nagayama. Theoretical study on the translation and rotation of an elliptic camphor particle. *Physica D: Nonlinear Phenomena*, 272:39–50, 2014.

[14] Yumihiko S. Ikura, Ryoichi Tenno, Hiroyuki Kitahata, Nobuhiko J. Suematsu, and Satoshi Nakata. Suppression and regeneration of camphor-driven Marangoni flow with the addition of sodium dodecyl sulfate. *Journal of Physical Chemistry B*, 116(3):992–996, 2012.

[15] Hua Jin, Abraham Marmur, Olli Ikkala, and Robin H.A. Ras. Vapour-driven Marangoni propulsion: Continuous, prolonged and tunable motion. *Chemical Science*, 3(8):2526–2529, 2012.

[16] Hiroyuki Kitahata, Keita Iida, and Masaharu Nagayama. Spontaneous motion of an elliptic camphor particle. *Physical Review E - Statistical, Nonlinear, and Soft Matter Physics*, 87(1):1–4, 2013.

[17] Hiroyuki Kitahata, Hiroya Yamamoto, Misato Hata, Yumihiko S. Ikura, and Satoshi Nakata. Relaxation dynamics of the Marangoni convection roll structure induced by camphor concentration gradient. *Colloids and Surfaces A: Physicochemical and Engineering Aspects*, 520:436–441, 2017.

[18] Hiroyuki Kitahata and Natsuhiko Yoshinaga. Effective diffusion coefficient including the Marangoni effect. *Journal of Chemical Physics*, 148(13), 2018.

[19] Y. L., I. S. Gradshteyn, and I. M. Ryzhik. Table of Integrals, Series and Products. *Mathematics of Computation*, 1981.

[20] Eric Lauga and Anthony M.J. Davis. Viscous Marangoni propulsion. *Journal of Fluid Mechanics*, 705:120–133, 2012.

[21] Sébastien Le Roux, Matthieu Roché, Isabelle Cantat, and Arnaud Saint-Jalmes. Soluble surfactant spreading: How the amphiphilicity sets the Marangoni hydrodynamics. *Physical Review E*, 93(1):1–13, 2016.

[22] A. C. Lochiel and P. H. Calderbank. Mass transfer in the continuous phase around axisymmetric bodies of revolution. *Chemical Engineering Science*, 19(7):471–484, 1964.

[23] Shreyas Mandre. Axisymmetric spreading of surfactant from a point source. *Journal of Fluid Mechanics*, 832:777–792, 2017.

[24] Hassan Masoud and Howard A. Stone. A reciprocal theorem for Marangoni propulsion. *Journal of Fluid Mechanics*, 741:1–7, 2014.

[25] Hassan Masoud and Howard A. Stone. The reciprocal theorem in fluid dynamics and transport phenomena. *Journal of Fluid Mechanics*, 879:P1, nov 2019.

[26] Yui Matsuda, Nobuhiko J Suematsu, Hiroyuki Kitahata, Yumihiko S Ikura, and Satoshi Nakata. Acceleration or deceleration of self-motion by the Marangoni effect. *Chemical Physics Letters*, 654:92–96, 2016.

[27] Sébastien Michelin, Eric Lauga, and Denis Bartolo. Spontaneous autophoretic motion of isotropic particles. *Physics of Fluids*, 25(6), 2013.

[28] Satoshi Nakata and Mai Murakami. Self-motion of a camphor disk on an aqueous phase depending on the alkyl chain length of sulfate surfactants. *Langmuir*, 26(4):2414–2417, 2010.

[29] Satoshi Nakata, Véronique Pimienta, István Lagzi, Hiroyuki Kitahata, and Nobuhiko J Suematsu, editors. *Self-organized Motion*. Theoretical and Computational Chemistry Series. The Royal Society of Chemistry, 2019.

[30] Hiraku Nishimori, Nobuhiko J. Suematsu, and Satoshi Nakata. Collective behavior of camphor floats migrating on the water surface. *Journal of the Physical Society of Japan*, 86(10):1–9, 2017.

[31] O'Neil MJ. The Merck Index - An Encyclopedia of Chemicals, Drugs and Biologicals. Cambridge, UK: Royal Society of Chemistry, 2013.

[32] Giuseppe Pucci, Ian Ho, and Daniel M Harris. Friction on water sliders. *Scientific Reports*, 9(1):1–7, 2019.

[33] Matthieu Roché, Zhenzhen Li, Ian M Griffiths, Sébastien Le Roux, Isabelle Cantat, Arnaud Saint-Jalmes, and Howard A Stone. Marangoni flow of soluble amphiphiles. *Physical Review Letters*, 112(20):1–5, 2014.

[34] Jennifer E. Satterwhite-Warden, Dilip K. Kondepudi, James A. Dixon, and James F. Rusling. Co-operative motion of multiple benzoquinone disks at the air-water interface. *Physical Chemistry Chemical Physics*, 17(44):29891–29898, 2015.

[35] Siowling Soh, Kyle J M Bishop, and Bartosz A. Grzybowski. Dynamic self-assembly in ensembles of camphor boats. *Journal of Physical Chemistry B*, 2008.

[36] Nobuhiko J. Suematsu, Tomohiro Sasaki, Satoshi Nakata, and Hiroyuki Kitahata. Quantitative estimation of the parameters for self-motion driven by difference in surface tension. *Langmuir*, 30(27):8101–8108, 2014.

[37] A. Titta, M. Le Merrer, F. Detcheverry, P. D.M. Spelt, and A. L. Biance. Level-set simulations of a 2D topological rearrangement in a bubble assembly: Effects of surfactant properties. *Journal of Fluid Mechanics*, 838:222–247, 2018.

[38] Vahid Vandadi, Saeed Jafari Kang, and Hassan Masoud. Reverse Marangoni surfing. *Journal of Fluid Mechanics*, 811:612–621, 2017.

[39] Alois Würger. Thermally driven Marangoni surfers. *Journal of Fluid Mechanics*, 752:589–601, 2014.

Mobilis in mobile
Moving in the moving element

Vingt Mille Lieues sous les mers by Jules Verne

Chapter 4

Numerical approach of the full problem

Contents

Introduction

The propulsion of an interfacial swimmer is a phenomenon characterized by a two-way coupling between hydrodynamics and transport due to the advection and the Marangoni flows. To obtain analytically tractable models, we uncoupled those physical phenomena, by assuming a simple fluid flow, unaffected by the surfactant distribution. It is time to give back its mobility to the fluid and consider the motion of the swimmer in the "moving element". Given the complexity of the problem, it appears that numerical simulations are the only approach to do so.

There is a host of reasons that motivate a simulation approach for our problem. First, the analytical models are based on drastic assumptions, such as homogeneous flow or no Marangoni flows. Because simulations allow to include or not the various physical ingredients at play, one can investigate to which extent they affect the swimming velocity and the flow and concentration field. Second, the comparison between models and experiments is limited to the range accessible in the latter, namely the regime of large Péclet number. It is interesting to check whether the features predicted by simple models at low Pe, such as the critical Marangoni number, are indeed borne out. Finally, the experiments presented in chapter 2 focus almost exclusively on a single quantity, the swimmer velocity, whereas the mechanism underlying the Marangoni propulsion involves also the flow field and the surfactant distribution. In our experiments, those quantities are not accessible so far and would require some specific method to be measured, such as PIV for the flow field [12] or analysis with a thermic camera [13]. In contrast, numerical simulations give access to all quantities.

To understand the effect of each physical ingredient, we add them one by one in successive steps, starting from toy models of the previous chapter and moving toward a more realistic description. Our first step is to simulate the toys model, which allows verifying our numerical method. Then, we relax our simplifying assumptions, one at a time, to assess their influence on the swimming dynamics. First, we reintroduce the proper no-slip boundary condition below the swimmer surface, a situation we call model A. Second, Marangoni flows, artificially switched off so far, are reintroduced, a situation called model B. This allows assessing how much Marangoni stresses influence the surfactant distribution and the force exerted by the fluid on the swimmer. The model B already takes full account of the coupling between transport and hydrodynamics. It is used as a base for further extensions such as including Navier-Stokes equation for the hydrodynamics, time-dependent swimming or even the concentration swimmer.

The simulations are performed with the software *Comsol*, a multiphysics commercial platform based on the Finite Element Method (FEM)[1]. In the whole chapter, we consider a soluble surfactant, thus, the toy model always refers to the 3D version. First, we present the implementation of the simulations and check their reliability. Then, we determine the swimming diagrams for models A and B, and discuss their features. Finally, we give a more local view of the swimming phenomenon by investigating the surfactant and concentration fields.

4.1 Simulations: method and implementation

In this section, after a short introduction on FEM method, we go through a quick reminder of the physical equations. Those equations have been treated in dimensionless forms, and we recall and discuss the possible choices for non-dimensionalization. Next, we describe in details the numerical implementation as developed in *Comsol*. Some precautions are needed for this non-linear problem, without which the simulation may not converge or give unphysical results. We discuss in particular the choice of mesh and the finite-size effects.

[1]For the sake of simplicity, int he following we will call "simulation" the resolution of the different models using FEM.

4.1.1 Introduction to the Finite Element Method (FEM)

The FEM is a numerical method used for solving partial differential equations (PDE) and ordinary differential equations (ODE). Historically, FEM has been introduced as a useful tool of the applied mathematics by Richard Courant [2] in the 1940s. But several decades were necessary before it was fully developed in the different engineering disciplines and put on a rigorous mathematical basis in the 70s. The result of a FEM calculation is not the exact solution, but an approximation based on the discretization of the problem. FEM subdivides the studied system into smaller and simpler parts, the finite elements, hence the name. The approximation of the PDEs can be solved using numerical methods.

The FEM has several advantages. First, the discretization does not need to be uniform and can be tailored to match local features. Typically a large gradient or a delicate geometry can be resolved with a locally finer mesh. As a result, FEM can tackle complex geometries and multicomponent systems. Moreover, FEM can treat a large variety of physical problems such as structural analysis, heat transfer, fluid flow, mass transport, and electromagnetic potential, etc. In this thesis, we exploit the ability of the FEM method to address coupled problems, namely mass transport and fluid flow. Finally, FEM is a well-developed method, with a theory providing an error estimation for the resulting solution.

FEM is commonly introduced as a special case of the Galerkin method, a class of methods converting a continuous problem described by differential equations into a discrete problem. For this class of approximation method, the PDEs have to be formulated into their weak or variational forms. In *Comsol*, most of the equations are already pre-implemented, but all the manual modifications in the equations must be translated into the variational formulation, hence the necessity to know how to obtain this formulation from the usual PDE formulation. We give an example showing how to obtain the weak formulation from the classical one-dimensional diffusion-advection PDE:

$$\begin{cases} U\dfrac{\mathrm{d}c}{\mathrm{d}x} = D\dfrac{\mathrm{d}^2c}{\mathrm{d}x^2} + J, \quad \forall x \in]0,1[, \\ c(0) = c(1) = 0. \end{cases} \tag{4.1}$$

To obtain the weak formulation, the first equation of 4.1 has to be multiplied by a function v often refereed as "test function", also defined on the interval $]0,1[$ and verifying the same boundary condition as c. Then the equation is integrated,

$$-D\int_0^1 c''(x)v(x)\ \mathrm{d}x + U\int_0^1 c'(x)v(x)\ \mathrm{d}x = J\int_0^1 v(x)\ \mathrm{d}x.$$

The first equation of the left hand side can be integrated by parts[2] to lower the order of the spatial derivation, and boundary part can be simplified since $v(0) = v(1) = 0$ [3]. Then by defining the Hilbert space[4] $\mathcal{V} = \mathcal{H}^1(]0,1[)$, we have

$$\begin{cases} c \in \mathcal{V}, \\ a(c,v) = L(v), \quad \forall v \in \mathcal{V}, \end{cases} \tag{4.2}$$

[2]For higher dimension, the integration by part is replaced by Green's identities.

[3]To simplify the computation we use Dirichlet boundary condition, but the computation can be adapted to any boundaries condition.

[4]A Hilbert space is a vector space with an inner product $< f, g >$ such that the norm is defined by $|f| = \sqrt{< f, f >}$.

with

$$a(c,v) = D\int_0^1 c'(x)v'(x) + U\int_0^1 c'(x)v(x)\ \mathrm{d}x, \tag{4.3}$$

$$L(v) = J\int_0^1 v(x)\ \mathrm{d}x. \tag{4.4}$$

Equation (4.2) is the weak formulation of the one-dimensional transport problem. More generally, the weak formulation of a PDE can be obtained in two steps: first, multiplying by a "test" function and integrating, then eventually lowering the degree of derivation by using either the integration by part in 1D or the Green's identities in space of higher dimension.

4.1.2 Physical framework

As discussed in the previous chapter, the full general problem involves a large number of complex couplings, making it out of reach for the analytical problem but also possible for numerical approaches, at least at the level performed here. Therefore, compared to the previous analytical developments, we will release only the assumptions associated with what we think are a priori most significant mechanisms at stake. To simplify the simulations, we apply most of the widely used simplifications: flat surface, no distinction between surface and bulk for the surfactant transport, flat swimmer, etc. For more details and the discussion about those common simplifications, we refer to the previous chapter.

a. The physics: governing equation at steady-state.

We consider the following idealized system: a disk moving at a constant velocity on a flat surface of an infinitely wide and deep pool. In line with the toy model, and to avoid difficulties associated with high Pe numbers, we consider for now only low Re numbers. The flow is thus governed by the Stokes equation for a Newtonian incompressible fluid:

$$\begin{aligned} 0 &= \boldsymbol{\nabla} p + \boldsymbol{\nabla}.\bar{\boldsymbol{\tau}} = \boldsymbol{\nabla}\cdot\bar{\boldsymbol{\sigma}}, \qquad \boldsymbol{\nabla}\cdot\boldsymbol{u} = 0, \\ \bar{\boldsymbol{\tau}} &= \eta(\boldsymbol{\nabla}\boldsymbol{u} + \boldsymbol{\nabla}\boldsymbol{u}^T), \qquad \bar{\boldsymbol{\sigma}} = -p\bar{\mathbb{1}} + \bar{\boldsymbol{\tau}}\ , \end{aligned} \tag{4.5}$$

with $\boldsymbol{u}$ the fluid velocity, p the pressure and η the dynamic viscosity. Assuming the swimmer velocity has direction $-\boldsymbol{e}_x$ and modulus U, the no-slip boundary condition imposes $\boldsymbol{u} = -U\boldsymbol{e}_x$ on the swimmer surface. The swimmer releases a surfactant, transported by diffusion and advection in the bulk:

$$\boldsymbol{\nabla}\cdot(\boldsymbol{u}c) - D\Delta c = J(r'), \qquad r' = \sqrt{(x+Ut)^2 + y^2 + z^2}, \tag{4.6}$$

with c the concentration field and D the diffusion coefficient. The right-hand side of the equation corresponds to the source term $J(r')$. For a surface source, the released flux is $J(r') = J\Pi(r' - a_\mathrm{s})\delta(z)$ with $J = \mathcal{J}/\pi a_\mathrm{s}^2$, Π and δ are respectively the Heaviside and Dirac functions. a_s is the radius of the source area, which can vary from the disk radius a to zero. In this case, the source term is $\mathcal{J}\delta(r')$, with $\mathcal{J}$ the total release rate.

The set of equations (4.5)-(4.6) correspond to the traditional advection-diffusion problem with a solution species transported by the fluid flow. However, the species in our case are surfactants whose presence modifies the surface tension γ and induces Marangoni stress at the fluid surface:

$$\bar{\boldsymbol{\tau}}\cdot\boldsymbol{n} = \boldsymbol{\nabla}_s\gamma = -\kappa\boldsymbol{\nabla}_s c, \tag{4.7}$$

with γ the surface tension, and $\boldsymbol{\nabla}_s$ the surface divergence $\boldsymbol{\nabla}_s\gamma = \boldsymbol{\nabla}\gamma - \boldsymbol{n}(\boldsymbol{n}\cdot\boldsymbol{\nabla}\gamma)$, $\boldsymbol{n}$ being the normal pointing out of the fluid surface. As before, we assume a linear dependence between surface tension and surfactant concentration

$$\gamma = \gamma_0 - \kappa c. \tag{4.8}$$

Since the swimmer moves at a constant velocity, the total force acting on it is zero

$$\sum_{swimmer} \boldsymbol{F} = \boldsymbol{0}. \tag{4.9}$$

We have thus defined our idealized problem, where the swimmer motion, concentration field and fluid flow are all coupled to one another. Note that in the previous chapter we presented a more general view of the interfacial swimmer equations, without the implicit simplifications made here.

b. Dimensionless numbers and equations

We now present two sets of dimensionless equations, that for convenience, are called "$U = 1$" and "$\kappa = 1$". The first set has already been presented in detail in the previous chapter, the second has been designed specifically for simulation with Marangoni stresses. They are both analytically equivalent, but numerically, each one has its advantages and drawbacks. Depending on the context, the first or the second scheme is used. Whatever the case, we need the following two dimensionless numbers:

$$Pe = \frac{Ua}{D}, \qquad M = \frac{\kappa\mathcal{J}}{\eta D^2}. \tag{4.10}$$

Pe is the Péclet number, which compares the transport from the mean advection to the transport from diffusion. M is the Marangoni number, which compares the Marangoni flows advection to the diffusion (it can be seen as a kind of Péclet number associated with Marangoni flows). Note that M involves quantities that are generally fixed in an experimental system: fluid viscosity, diffusion rate, and so on. On the other hand, Pe involves the swimmer speed U which is not controlled by the experimentalist. For both sets of dimensionless equations, the reference size is the swimmer radius; from now on, all sizes are expressed in this unit.

Non-dimensionalization: "$U = 1$"

A natural way to adimensionalize the equations is to use the swimmer characteristics as reference: the radius for the lengths and the swimmer speed for the velocities. For the stress and the pressure, we base their dimensionless definitions on the viscous stress. The characteristic concentration is obtained by equalizing the flux from the source with the flux from the diffusion transport. Doing so, we obtain the following dimensionless definitions:

$$\boldsymbol{r} = a\tilde{\boldsymbol{r}}, \quad \boldsymbol{u} = U\tilde{\boldsymbol{u}}, \quad p = \frac{\eta U}{a}\tilde{p}, \quad \bar{\boldsymbol{\tau}} = \frac{\eta U}{a}\tilde{\bar{\boldsymbol{\tau}}}, \quad c = \frac{\mathcal{J}}{Da}\tilde{c}\ ,$$

Where the tilde indicates dimensionless quantities. The main equations (4.5) and (4.6) can then be rewritten as:

$$\boldsymbol{0} = -\tilde{\boldsymbol{\nabla}}\tilde{p} + \tilde{\boldsymbol{\nabla}}.\tilde{\bar{\boldsymbol{\tau}}}, \qquad Pe\ \tilde{\boldsymbol{u}}.\tilde{\boldsymbol{\nabla}}\tilde{c} = \tilde{\Delta}\tilde{c} + \tilde{\delta}(\tilde{\boldsymbol{r}}), \qquad \tilde{\bar{\tau}}.\boldsymbol{n} = -\frac{M}{Pe}\tilde{\nabla}_s\tilde{c}. \tag{4.11}$$

This set of equations is more convenient in the absence of Marangoni stress, that is for the toy models and the model A. Indeed the solution for the hydrodynamic flow remains the same for all Pe. Thus, if ones explore a range of Pe to pinpoint the swimming velocity, only the concentration field must be recomputed, which is advantageous for computation time. For numerical studies, this set of equations is more adapted when there is no Marangoni flow.

Non-dimensionalization: "$\kappa = 1$"

We keep the swimmer radius as characteristic size but now we choose for the characteristic velocity the one associated to Marangoni flows[5] $U^* = MD/a$.

$$\boldsymbol{r} = a\tilde{\boldsymbol{r}}, \quad \boldsymbol{u} = M\frac{D}{a}\tilde{\boldsymbol{u}}, \quad p = \frac{\kappa\mathcal{J}}{a^2 D}\tilde{p}, \quad \bar{\boldsymbol{\tau}} = \frac{\kappa\mathcal{J}}{a^2 D}\tilde{\bar{\boldsymbol{\tau}}}, \quad c = \frac{\mathcal{J}}{Da}\tilde{c},$$

$$\mathbf{0} = -\tilde{\boldsymbol{\nabla}}\tilde{p} + \tilde{\boldsymbol{\nabla}}.\tilde{\bar{\boldsymbol{\tau}}}, \qquad M\ \tilde{\boldsymbol{u}}.\tilde{\boldsymbol{\nabla}}\tilde{c} = \tilde{\Delta}\tilde{c} + \tilde{\delta}(\tilde{\boldsymbol{r}}), \qquad \tilde{\bar{\tau}}.\boldsymbol{n} = -\boldsymbol{\nabla}_s\tilde{c}. \tag{4.12}$$

Even though such a non-dimensionlization may appear less natural, it is advantageous in the sense that the dimensionless viscous stress and surface gradient concentration keep the same order of magnitude, whereas for "$U = 1$" the factor between those two quantities can explode if $M \gg Pe$ [6]. Empirically, simulations implemented with this set converge more easily toward a solution.

4.1.3 Numerical implementation in *Comsol*

Before the idealized system described above can be simulated, several points need to be addressed. The first issue is to describe a moving object and therefore moving boundary in a fixed meshed system. A second issue is to mimic an infinitely large and deep pool with a simulated system of finite size. Finally, the third task is to adapt the mesh to the underlying physics: fine around the discontinuities and the singularities, and coarse in the region with a weak gradient. In this section, we detail how we implement the three basic components of a FEM calculation: the geometry, the physics and the mesh. While the main text describes only the overall approach, we add numerous footnotes indicating the tricks of the trade, for those who would want to reproduce those calculations with *Comsol* software.

a. System geometry for a semi-infinite domain

We work in the swimmer frame of reference, with the disk fixed at position $\{0, 0, 0\}$ and a mean flow $U\boldsymbol{e}_x$ at infinity[7]. The simulation box is a parallelepiped with a square base of dimension $L = 2l = 800$ and depth l. The boundary closest to the swimmer centre is thus at a distance l. Since the $y = 0$ plane is a symmetry plane, we limit our description to the positive y (see fig. 4.1).

b. Implementation of equations and boundary conditions

We implement the Stokes equations for an incompressible fluid and advection-diffusion for the surfactant [8]. For the transport, the equation $\boldsymbol{\nabla}\cdot(-D\boldsymbol{\nabla}c + \boldsymbol{u}c) = 0$ is used instead of the

[5] M can be seen as a Péclet number for Marangoni flow, therefore U^* is just the typical velocity for the Marangoni flow.

[6] *Comsol* proposes pre-implemented physics where the variables such as the density, the diffusion rate... have to be defined. To respect the dimensionless equations, we define those variables with a formula written with the dimensionless number Pe and M:

dimensionless equations	a	U	η	D	$\mathcal{J}$	κ
"$\mathbf{U = 1}$"	1	1	1	$1/Pe$	$1/Pe$	M/Pe
"$\kappa = \mathbf{1}$"	1	Pe/M	1	$1/M$	$1/M$	1

[7] The simulations are settled with an average flow toward positive x direction, which means that the simulations described a disk moving toward $-e_x$ in the laboratory frame of reference.

[8] Both default consistent stabilisation *streamline diffusion* and *crosswind stabilisation* are implemented. In FEM, when $Peh/a > 1$ with h the size of the local mesh, numerical instabilities appear. That is why the crosswind stabilisation *"Do Carmo & Galeao"* [8] is used.

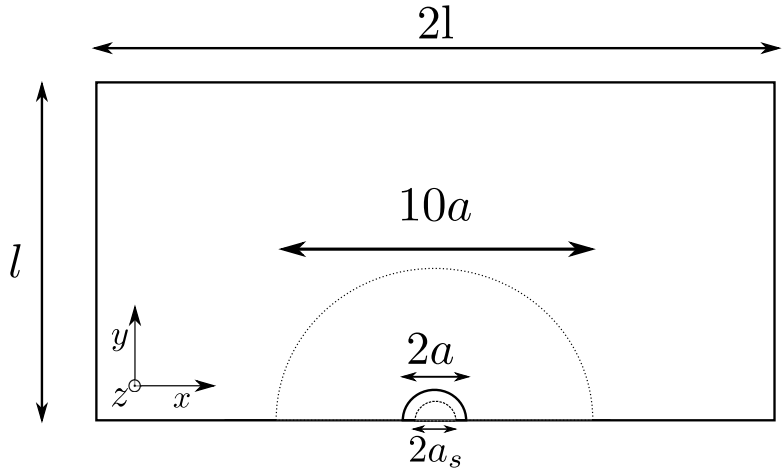

Figure 4.1: Top view of the simulated system (not to scale). The outer dashed circle is a helper for the mesh definition, the plain circle is the swimmer contour, and the inner dashed circle is the source boundary.

simplified form $-D\Delta c + \boldsymbol{u}\cdot\boldsymbol{\nabla}c = 0$ [9]. As regards boundary conditions, they have to be defined for only four faces: bottom, front, rear and side. For the transport part, the condition $c = 0$ is imposed on all those faces except the rear one, where the surfactant is evacuated by advection with a normal diffusive flux equal to zero. For the hydrodynamics, the speed $U\boldsymbol{e}_x$ is imposed on those three faces[10], the fourth rear face is an outlet with a pressure set to zero.

On the swimmer, the surfactant source is either implemented as a constant flux over a surface centred on the swimmer or as a central point source [11]. The normal flux is set to zero in the remaining surface. A no-slip boundary condition is implemented over the swimmer surface. Finally, the free surface is implemented with perfect slip, it remains perfectly flat with $\boldsymbol{u}\cdot\boldsymbol{e}_z = 0$ and a tangential Marangoni stress[12] given by (4.7).

c. Mesh

In FEM, the mesh can be locally adapted to local gradients: the faster the spatial variation, the finer the mesh. There are several places on the swimmer where the presence of physical discontinuities calls for a highly refined mesh. Those critical spots are grouped around the swimmer, more precisely they are located close to the physical discontinuities. For instance, the disk contour defines a sharp border between the no-slip and Marangoni stress boundary

[9] The transport equation simplified form assumes intrinsically an incompressible flow, which is true analytically, but if the incompressibility is not numerically verified, then it is equivalent to add a bulk source $c\boldsymbol{\nabla}\cdot\boldsymbol{u}$.

[10] More accurately the side and bottom are *sliding walls* moving at the speed $U\boldsymbol{e}_x$, the front is an *inlet* condition which imposes locally a normal speed U.

[11] In *Comsol* , the point source is not pre-implemented, a weak contribution has to be used instead. The right hand side expression of the weak expression for a point source at the origin can be written as $\int \mathcal{J}\delta(\boldsymbol{r})\ \mathrm{test(c)}\ \mathrm{d}\boldsymbol{r}$ with test(c) the test function. In our case, the formula to fill in is "$\mathcal{J}$/2*test(u)", the factor 2 comes from the position of the point source at the symmetry plane $y = 0$.

[12] There is no pre-implementation in *Comsol* for the Marangoni stress, we use a weak formulation instead. To understand how to implement it, we write a weak expression for the Stokes equation:

$$\int_{\mathcal{S}} (n_j\cdot\sigma_{ij})\ test(u_i)\ \mathrm{d}S - \int_{\mathcal{V}} \sigma_{ij}\ \partial_j test(u_i)\ \mathrm{d}V = 0.$$

with $\mathcal{V}$ and $\mathcal{S}$ respectively the bulk and the surface. The weak expression is composed of two integrals, the volume integration is already pre-implemented in *Comsol*, but the surface integral is by default null. However, the Marangoni stresses appear through this surface integral. Using the equation (4.7) in the surface integral we obtain the weak contribution of the Marangoni stress. Finally, the weak formulation formula to fill in is "$-\kappa\,(\partial_x c * \mathrm{test(u_x)} + \partial_y c * \mathrm{test(u_y)})$".

conditions. For an extended source, there is also the boundary separating a normal flux from a vanishing flux. Of course, for the point-source case, the point source location is also a special point, where the mesh must be sharp. Except for those specific spots, the remaining space does not need a particularly fine mesh, and a coarser mesh can be used without affecting the validity of the simulation results.

The mesh is composed of tetrahedrons, whose size can be adjusted. We define the following different areas where the mesh size is constrained:

- The swimmer contour with a typical size of 2.5 10^{-3}.
- Inside a disk centred on the swimmer and with radius 10, the mesh is defined by a maximal size of 5 10^{-2}, but the size is mostly controlled by an increasing rate[13] of 1.1.
- If a point source is present, the typical size around is 5 10^{-4}. If the source is extended, the constraints introduced above are sufficient.
- In the bulk, the maximal size is $l/20$. Again, the key parameter is the increasing rate of only 1.15, which ensures that the mesh refinements close to the swimmer "infuse" far from it.

The resulting mesh is shown on figure 4.2.

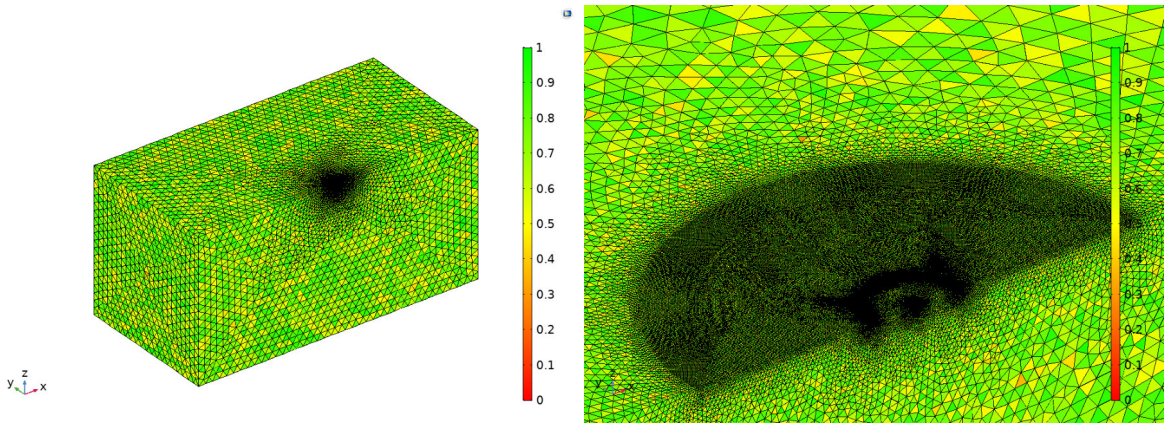

Figure 4.2: Typical mesh used in this work (Left) overall view. (Right) zoom on the swimmer area. The color bar indicates the quality of the tetrahedron composing the mesh, from 0 (=degenerate tetrahedron) to 1 (=regular tetrahedron). More accurately, the quality of a tetrahedron is given by the formula $1 - \max\left[\frac{\theta_{\max}-60°}{120°}, \frac{60°-\theta_{\min}}{60°}\right]$, with $\theta_{\max}$ and $\theta_{\min}$ respectively the maximal and minimum tetrahedron angle.

d. Finding the swimming point in practice

Two forces apply to the swimmer: the capillary force F_c and the viscous force F_v. Their definition is recalled in table 4.1, together with the various forces that we have discussed in the preceding chapter. As a reminder, the quantities with a hat "ˆ" refer to a dual problem whose solution is known analytically[14]. The viscous force has two expressions (4.16) and (4.17). The

[13]The two mains constraints governing the mesh generation are the continuity and the size. The former ensures a gradual transition in the tetrahedron size, which is controlled by a growth rate.

[14]By using the Lorentz's reciprocal theorem, the force exerted by the fluid flow can be expressed as a sum of two distinct contributions [7]. The formulas determined from the reciprocal theorem usually involve $\hat{\boldsymbol{u}}$ and $\hat{U}$ respectively the velocity field and the velocity of the swimmer in a dual system. The chosen dual system follows the same set of equations than capillary system without the Marangoni stress (4.7). Therefore, the flow of the dual system $\hat{\boldsymbol{u}}$ has an analytical solution [6, 4].

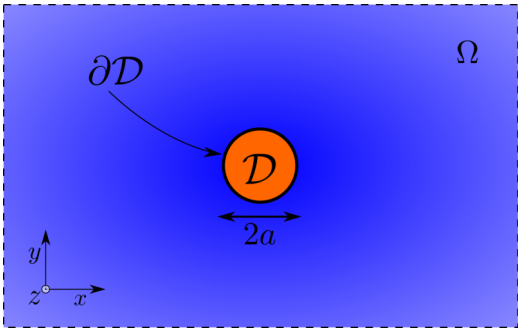

Figure 4.3: Notations used in the text: $\mathcal{D}$ the disk surface, $\partial\mathcal{D}$ the disk contour and Ω the free surface.

former is the classical expression for a body moving in a fluid: the integral of the stress over the swimmer surface. Evaluating such an expression in FEM simulations may be difficult: because the viscous stress diverges along the disk contour, we have observed that the presence of a singularity may prevent convergence of the flow force, even with mesh refinement[15]. Instead, we have found that the alternative expression of F_v, equation (4.17), which is based on Lorentz theorem, is generally easier to evaluate numerically, even with a coarser mesh. The reason for that is presumably that we avoid divergent quantities in the computation.

Force formula	Name & Description
$\boldsymbol{F}_\mathrm{c} = -\kappa \oint_{\partial\mathcal{D}} c\, \boldsymbol{n}\, \mathrm{d}l. \quad (4.13)$ with $\boldsymbol{n}$ normal to the swimmer contour $\partial\mathcal{D}$	*Capillary force:* surface tension force due to an asymmetric distribution of surfactant along the swimmer contour
$\hat{\boldsymbol{F}}_\mathrm{d} = -C\eta a U \boldsymbol{e}_x, \quad (4.14)$ with C a constant depending on the swimmer geometry, for the disk $C = 16/3$.	*Stokes drag*: drag force in Stokes regime without the Marangoni flows interaction.
$\boldsymbol{F}_{\mathrm{v}\mathcal{M}} = -\kappa \int_\Omega \boldsymbol{\nabla}_s c \cdot \frac{\hat{\boldsymbol{u}}}{\hat{U}}\, \mathrm{d}S\, \boldsymbol{e}_x, \quad (4.15)$ with Ω the free interface.	*Marangoni flow force*: specific hydrodynamic force from the Marangoni flow.
$\boldsymbol{F}_\mathrm{v} \equiv \iint_{\mathcal{D}} \boldsymbol{n} \cdot \bar{\boldsymbol{\tau}}\, \mathrm{d}S, \quad (4.16)$ $= \hat{\boldsymbol{F}}_\mathrm{d} + \boldsymbol{F}_{\mathrm{v}\mathcal{M}}, \quad (4.17)$ with $\boldsymbol{n}$ normal to the swimmer surface $\mathcal{D}$.	*Viscous force*: hydrodynamic force due to the flow interaction with the swimmer surface.
$\boldsymbol{F}_{\mathrm{m}\mathcal{M}} = \kappa \int_\Omega c \boldsymbol{\nabla}_s \cdot \frac{\hat{\boldsymbol{u}}}{\hat{U}}\, \mathrm{d}S\, \boldsymbol{e}_x, \quad (4.18)$ $= \boldsymbol{F}_\mathrm{c} + \boldsymbol{F}_{\mathrm{v}\mathcal{M}}. \quad (4.19)$	*Marangoni force*: sum of all the forces acting on the swimmer due to the capillary effects. Always a motor force, if there is motion.

Table 4.1: Force and contribution acting on the swimmer in Stokes flow regime

In contrast with experiments where it results from the forces at play, the swimmer velocity is fixed in simulations. Assuming steady-state motion at a constant speed, the swimming

[15]It seems that adding a boundary layer mesh (layers of thin parallelepiped) improves the flow force estimation.

velocity is thus reached when the resulting force on the swimmer vanishes:

$$\boldsymbol{F}_{\mathrm{v}} + \boldsymbol{F}_{\mathrm{c}} = \boldsymbol{0}. \qquad \textit{(First criterion)} \tag{4.20}$$

With the formula from table 4.1, this equality can be rewritten as

$$\hat{\boldsymbol{F}}_{\mathrm{d}} + \boldsymbol{F}_{\mathrm{m}\mathcal{M}} = \boldsymbol{0}. \qquad \textit{(Second criterion)} \tag{4.21}$$

This steady-state speed must also be associated with a stable state, which adds the constraint:

$$\left.\frac{\partial(\boldsymbol{F}_{\mathrm{v}} + \boldsymbol{F}_{\mathrm{c}}).\boldsymbol{e}_x}{\partial U}\right|_{\boldsymbol{F}_{\mathrm{c}}+\boldsymbol{F}_{\mathrm{v}}=\boldsymbol{0}} < 0 \quad \text{or} \quad \left.\frac{\partial(\hat{\boldsymbol{F}}_{\mathrm{d}} + \boldsymbol{F}_{\mathrm{m}\mathcal{M}}).\boldsymbol{e}_x}{\partial U}\right|_{\hat{\boldsymbol{F}}_{\mathrm{d}}+\boldsymbol{F}_{\mathrm{m}\mathcal{M}}=\boldsymbol{0}} < 0. \tag{4.22}$$

Depending on the context, the first or second criterion is used. The first criterion is more intuitive and closer to the classical representation of such systems. The second criterion involves a force evaluated with the simulation, $F_{\mathrm{m}\mathcal{M}}$, and an analytical force proportional to the speed, $\hat{F}_{\mathrm{d}}$. This second route has two advantages. The first is that the computation uncertainty is limited to one term only instead of two. The second advantage is that it may be easier to pinpoint the swimming velocity because $\hat{F}_{\mathrm{d}}$ is simply proportional to the imposed velocity. In practice, there are two methods to find the force balance. In the absence of Marangoni flows, when the surfactant distribution depends only on Pe, we conduct a series of simulations at different Pe and then compute the M value where the force balance, (4.20) or (4.21), is satisfied. In the presence of Marangoni flows, when the surfactant distribution depends also on M, we explore a range of Pe for each value of M. Using a linear interpolation of the force, we determine at which $Pe(M)$ the force balance is verified.

4.1.4 Reliability: convergence in mesh and finite size effect

To be confident in the results of our simulations, several conditions need to be checked. The first is the convergence in mesh. Because of the necessary discretization, the solution given by the FEM method is strongly correlated with the mesh employed. Thus, we must verify that if the mesh is sufficiently fine, the resulting solution becomes independent of the mesh details. A second condition is to check that finite-size effects become negligible, i.e. that our simulation box is large enough to mimic an effectively infinite system. Since our main goal is to find the swimming point (M, Pe) where the force balance is satisfied, we need convergence primarily for the forces (see tab. 4.1). In the following, we investigate convergence both in mesh and system size. Those tests are carried out on the fully coupled model including Marangoni flow. As a different, complementary check of our simulations, we also verify that we recover numerically the predictions of the basic and Lorentz toy models.

a. Mesh and size convergence

To check the convergence in mesh, we introduce two parameters: the inverse of the mesh factor $1/M_f$ and the size factor S_f. The mesh factor is proportional to the typical size of the mesh, the size factor is proportional to the size of the pool[16]. We computed all the forces with physical parameters Pe=3, M=230 [17]. All the computed forces seem well converged in size as shown by the mostly flat curves (see fig. 4.4). For the convergence in mesh, significant variations are seen in the viscous force computed with the formula (4.16). In that case, the slope at the highest M_f considered is not flat, meaning that the evaluated values would still

[16] $M_f = S_f = 1$ refers to the size defined in the detailed implementation part (see p.130).

[17] This configuration has been chosen because it is relatively close to the critical point presented later (see 4.2).

change for finer mesh[18]. However, F_{v} evaluated with the second formula (4.17) appears to have reached a constant value. Therefore, we use this route in the following. Overall, we see that forces have already converged for the reference configuration with size factor $S_f = 1$ and the mesh factor $M_f = 1$. Those are the conditions used in the following unless mentioned otherwise.

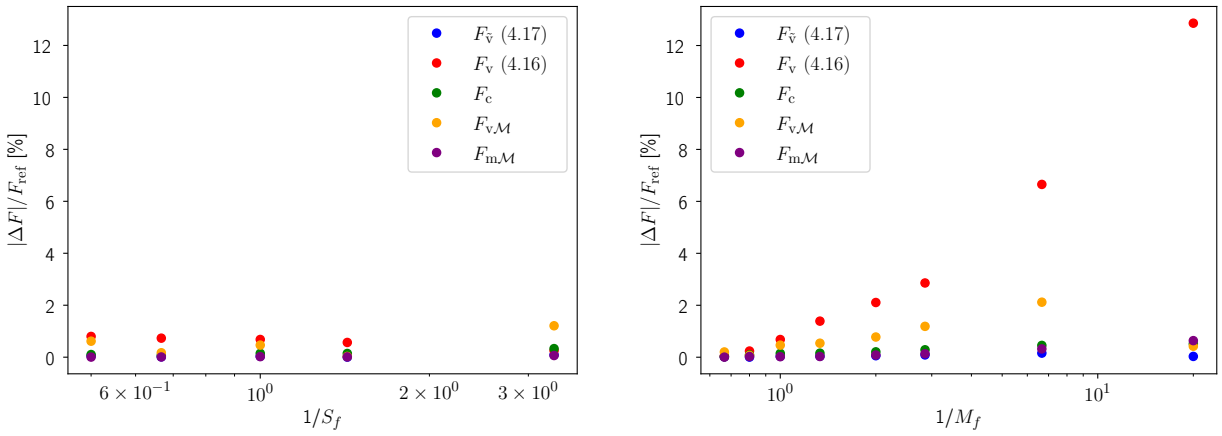

Figure 4.4: Size and mesh convergence (left and right) for $M = 230$ and $Pe = 3$. We show the absolute difference with a reference simulation with the largest box and finest mesh (S_f=2, M_f=1.5), as a function of $1/S_f$ or $1/M_f$. There are two ways to compute the total viscous force, (4.16) and (4.17), there are both considered. (Left) S_f varies from 0.1 to 2 and $M_f = 1$. (Right) M_f varies from 0.05 to 1.5 and $S_f = 1$.

b. Boundary layer and finite size effects

Rigorously, mesh and size convergence studies should be done for each couple of Pe and M tested. However, from the physics at play, we determine a range of validity for the proposed mesh and geometry. One important factor for the mesh size is the existence of boundary layers. As long as we assume a Stokes flow, there is no problem of hydrodynamic boundary layer below the swimmer: the typical size of the flow variations scales as the swimmer radius, this size being much larger than the typical mesh size, no problem is expected on this side. However, the advection-diffusion of surfactant released may lead to a diffusion boundary layer whose size is $L_{diff}/a = \sqrt{D/Ua} = 1/\sqrt{Pe}$. The range of Pe explored extends up to 60, which gives a minimum size of 10^{-1}. This is two orders of magnitude above the typical mesh size used in the vicinity of the swimmer, so we conclude that the mesh proposed is adapted for the range of Péclet considered. For $Pe > 60$ however, it is necessary to account for the surfactant boundary layer[19] at the surface, and to use a finer mesh around the swimmer volume for the flow. More information can be found in appendix 4.4.3.

We now turn to the finite size effects and discuss the size above which the effect of boundary on surfactant transport should become negligible. The boundary condition $c = 0$ assumes that before getting close to the side and bottom walls, the surfactant is swept by the average flow. The maximal extension of the surfactant distribution in the y-direction should then remain lower than the box size: $\sqrt{Dl/U} < l$, leading to $l/a > 1/Pe$. As regards the rear boundary,

[18] Though, the viscous stress diverges over the swimmer contour. A numerically expensive way to solve the problem is to lower the tetrahedron size with M_f.

[19] The boundary layer mesh is constituted of layers of parallelepipeds. Contrary to the tetrahedrons, their quality does not drop if they are much thinner than wide, which allows having a fine discretization in one direction and coarse in the perpendicular one.

the surfactant is evacuated by setting the normal diffusion flux to zero which assumes that the mean advection dominates the diffusion transport. Roughly, the typical diffusion flux is given by Dc_0/L_t with L_t the distance from the source and c_0 the typical concentration, whereas the typical advection flux is Uc_0. The two effects become of comparable magnitude when $l/a \sim 1/Pe$. As a result, we expect no difficulty in the diffusive transport as long as Pe is above $a/l(= 1/400)$.

As regards the Marangoni convection, the surfactant transport can also be confined by the pool border if M is too high compared to Pe. A tentative line of reasoning to understand this issue is to consider the Marangoni advection as a diffusive process with an effective diffusion rate, as discussed in [1]. Though the situation considered is somewhat different[20], it provides an estimates for an effective diffusion rate $D_{\mathrm{M}} = \gamma_1 a/\eta = \kappa\mathcal{J}/\eta D$, with $\gamma_1 = \kappa c_0$ and $c_0 = \mathcal{J}/Da$ a typical concentration. Treating the Marangoni advection as a diffusion process and proceeding as above, we can define a typical transport size given by $L_t/a \sim M/Pe$. Concretely, in a (M,Pe) diagram the Marangoni flow develops freely in the pool simulation as long as $Pe > Ma/l$. For $M < 1000$ and at low Pe, the effective diffusion argument allows to rationalize some unexpected observations. However, we will see below that at large M and Pe, close to the swimming point[21], the extension of the hydrodynamical and chemical wakes remains finite, with a typical width lower than the simulation box width (see 4.3 for more detail). Therefore for swimming points at large M, there is no need to extend the size of the box, even if $Pe > Ma/l$.

In conclusion, the default mesh and geometry proposed are reliable for most of the Pe and M tested. Attention should be paid at low Pe for the finite-size effects of the Marangoni flows.

c. Checking simulations by recovering the toy model predictions

The toy models constructed in chapter 3 (see tab. 4.3) have been solved analytically and their exact solution provides a reference case against which we can compare our simulations. This allows us to ensure that our implementation is correct before including additional physical ingredients. The simulations describe the concentration field around a point source with the surfactant transported by diffusion and advection via a uniform flow. In the toy models, the swimmer is a ghost shell, it does not have any influence on the flow or the concentration field, and we just need it to compute the capillary force (4.13) and the Marangoni force (4.18), for the basic and Lorentz toy model respectively. In both cases, the drag force is the Stokes force[22]. By verifying the swimming criterion, we obtain an equation for each toy model, indicating the swimming equilibrium point in (M,Pe) diagram (see table 4.2).

As we can see on figure 4.5, the swimming curves obtained in simulations agree very well with the predictions. However, the quality of the agreement gets lower for the low Pe. This is visible for the basic toy model where the transition around the critical point (i.e. the transition from zero to finite velocity) is smooth instead of sharp. This phenomenon may be ascribed to the finite-size effects and starts around $Pe \simeq a/l = 10^{-3}$ when diffusion transport is affected by the pool wall. Despite those deviations, the position of the critical point for the basic toy model is at the expected position with $M_c/C = 4.00 \pm 0.04$ [23]. The threshold obtained from simulation is only 1% away from the expected value. In conclusion, the simulations of the toy models give

[20] Experimentally in [11], it has been observed that a disk releasing a surfactant, laid on a surface seeded with floating particles, creates a depleted area around it. The evolution of this area evokes a diffusion transport process. To extract a typical distance from this process we set our reasoning on the analytic article [1]. Strictly speaking, this article considers a bidimensional problem involving insoluble surfactant released from a fixed source.

[21] We define a swimming point the couple (M,Pe), verifying the swimming equation for the analytical model, or associated to a simulation verifying swimming criteria for the simulation model.

[22] There is a distinction between the flow used for the surfactant transport, and the flow to compute the drag force. For the transport, it is the flow at order zero or the average flow. For the drag force, we consider the Stokes flows created by a moving disk at the interface.

[23] The position of the M_c is determined with a linear regression.

Toy model	$\underbrace{f(Pe)}_{motor} = \underbrace{C\frac{Pe}{M}}_{drag}$
basic	$e^{-Pe/2} I_1(Pe) = C\frac{Pe}{M}$, (4.23) with I_1 the modified Bessel function of the first kind.
Lorentz	$\frac{\sqrt{2}}{3\pi^{3/2}} \text{MeijerG}\left(\left\{ \left\{ \frac{1}{4}, \frac{3}{4} \right\}, \{\} \right\}, \left\{ \left\{ \frac{1}{2}, \frac{1}{2} \right\}, \left\{ -\frac{1}{2}, 0 \right\} \right\} \middle\| \frac{Pe^2}{4} \right) = C\frac{Pe}{M}$, (4.24) with MeijerG the Meiger G function.

Table 4.2: Swimming point equation in the (M,Pe) diagram

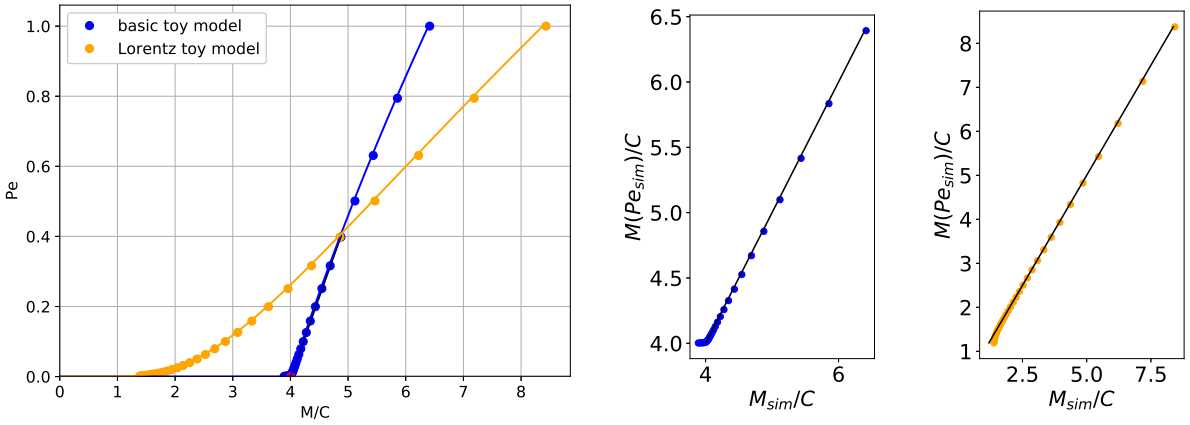

Figure 4.5: Toy models swimming diagram. (Left) swimming point in (M,Pe) diagram, $l \simeq 10^3$ a. The dots position is computed from the simulation results, while the continuous lines are toy model predictions. (Right) Expected M/C value (see tab 4.2) as a function of the value obtained from the simulation, the black line follows the equation $y = x$

results very close to analytical solutions. The potential difficulties, such as finite-size effects for diffusion transport at low Péclet number, are understood and with limited consequences.

4.2 Swimming diagram

To gain a better understanding of the physics at play in interfacial swimmers, we have not considered immediately the full idealized system. Rather, we have investigated a series of models, each including one additional physical ingredient compared to the previous one. The idea is to better assess the contribution of each ingredient. In this section, we focus on the swimming diagram. In the next section, we will extend our investigation to the concentration and flow fields.

The models considered are summarized in table 4.3. Starting from the toy models, model A includes the no-slip boundary condition on the swimmer. With this implementation, the swimmer disk has a "physical reality", it disturbs the flow around it and therefore the distribution of surfactant. Considering model A allows us to understand to what extent the no-slip

model name	hypothesis	dimensionless equations	motor contribution
basic toy models	• Point source • No capillary stress • Uniform flow but Stokes drag force	"$U = 1$"	$\frac{\lvert F_{\mathrm{c}}(Pe)\rvert}{M\eta D}$
model A	• Point source • No capillary stress • **No slip under the disk**	"$U = 1$"	$\frac{\lvert F_{\mathrm{c}}(Pe)\rvert}{M\eta D}$
model B	• Point source • **Capillary stress** • No slip under the disk	"$\kappa = 1$"	$\frac{\lvert F_{\mathrm{m}\mathcal{M}}(Pe\lvert M, a_{\mathrm{s}})\rvert}{M\eta D}$

Table 4.3: The three simulations models. The new elements are in bold

boundary affects the position of the swimming point. In model B, all the physics of the "idealized" system is implemented. The Marangoni stresses on the free surface are switched on. We will see that some features, such as the distribution of surfactant, are changed in a significant manner.

4.2.1 Incorporating no-slip and Marangoni flow effects

The main results of the toy models are the swimming equations (see tab. 4.2). The solutions of those equations can be displayed on a (M,Pe) diagram, the swimming diagram. A first approach to compare the analytical and the numerical model is to confront the resulting swimming diagrams. In particular, at low Pe, we note for the toy models a critical Marangoni number M_c, a threshold value below which there is no spontaneous motion. An interesting point is to see how the position of this critical value changes when accounting for the no-slip boundary condition and Marangoni stress. Also, we note at large Pe that the power-law $Pe \propto M^{2/3}$ is a feature common to all analytical models. Does this simple relation still apply in a more refined model?

a. Method and expectation

Before showing the results for model A and B, we should first explain which behaviour can be expected for the swimming diagram. To do so, we introduce a formulation of the swimming criterion based on a common formula for the drag contribution. Using intuitive physical arguments, we anticipate the shape for the motor contribution as a function of Pe and deduce the possible swimming diagrams.

Definition of the motor and drag contribution Both criteria ((4.20) or (4.21)) and set of dimensionless equations ("$U = 1$" or "$\kappa = 1$") are equivalent: for a given system they lead to the same swimming diagram. Yet, when dealing with numerical simulations, one approach can be easier to apply or be more reliable. For instance, the swimming diagram model A is

obtained with the first criterion (4.20) and the dimensionless equations "$U = 1$", while the swimming diagram model B is obtained with second criteria (4.21) and with the dimensionless equations "$\kappa = 1$". For the sake of convenience, the first criterion or second criterion can be rewritten as a similar dimensionless equation involving M and Pe:

$$\underbrace{f_{model}\left(c(Pe \mid a_{\mathrm{s}}, M)\right)}_{motor} = \underbrace{C\frac{Pe}{M}}_{drag}, \tag{4.25}$$

with f_{model} a positive dimensionless force based on the force scale $F^* = M\eta D$.

The motor contribution on the left-hand side balances the drag contribution on the right-hand side[24]. The important point is that the drag contribution is always linear in Pe/M, whatever the model considered. As a consequence, all the features of the swimming diagram are contained in the motor contribution. Such a motor contribution depends on the surface concentration only, itself a function of Pe and of M too if Marangoni stresses are present. Thus, the features of the swimming diagram can be always traced back to this balance between the motor and drag contributions.

Motor contribution: expectation From our investigation of toy models and physical intuition, we can expect some common behaviour for motor contributions as a function of Pe. At $Pe = 0$, the distribution of surfactant is isotropic, therefore the motor contribution is zero. Now, the Péclet number is correlated to the asymmetry of the surfactant distribution: the higher Pe, the more asymmetric the concentration, and the higher the motor force. We thus anticipate that the motor contribution increases with Pe at low values. On the other hand, if we consider a fixed flux rate J, the concentration around the swimmer must scale as $c^* = J/U$. Then, the average concentration around the swimmer decreases as a function of Pe[25]. Considering the formula of the two possible motor forces F_{c} (4.13) and $F_{\mathrm{m}\mathcal{M}}$ (4.18), lowering the global concentration around the swimmer leads to decrease those forces. A competition thus sets in between the two opposite effects of increasing Pe: an increase in asymmetry but a decrease in concentration. At large Pe, the asymmetry saturates, while the concentration tends toward zero, so the motor force eventually vanishes. To summarize, we expect the motor contribution to start at zero, to increase with Pe, to reach a maximum and finally to decrease asymptotically toward zero. This qualitative picture is corroborated by simulation, as shown in detail in appendix 4.4.5.

The type of swimming diagram depends on the concavity of the f_{model} function at the origin (see figure 4.6). Let us consider the concave case first. Because the drag is just linear in Pe/M, there is either one or two intersections, one being at the origin. This implies two different regions, separated by the critical value M_c, whose position is determined by the slope of the drag contribution tangent to the motor force. In region 1, which extends from 0 to M_c, there is only one stable branch at $Pe = 0$. In region 3, which extends from M_c to ∞, the solution at $Pe = 0$ becomes unstable and a rising stable branch starts from the point (M_c,0). Physically, this means that a swimmer in this region does not remain at rest but evolves spontaneously toward a moving state: there is a spontaneous symmetry breaking.

We consider now the second case where the function f_{model} is convex at the origin. Now there is a region (called 2) with three points of intersection. Two of them correspond to

[24]Those notions of drag and motor contribution help to understand more intuitively the idea of a stable or unstable point

$$\text{stable(resp. unstable):} \quad \left.\frac{\partial(motor - drag)}{\partial Pe}\right|_{motor=drag} < 0 \quad (\text{resp. } > 0).$$

[25]A simple analogy is the drawing of straight lines on a whiteboard at a different speed. If the line is drawn too fast the deposited ink quantity is lower than a line drawn slowly.

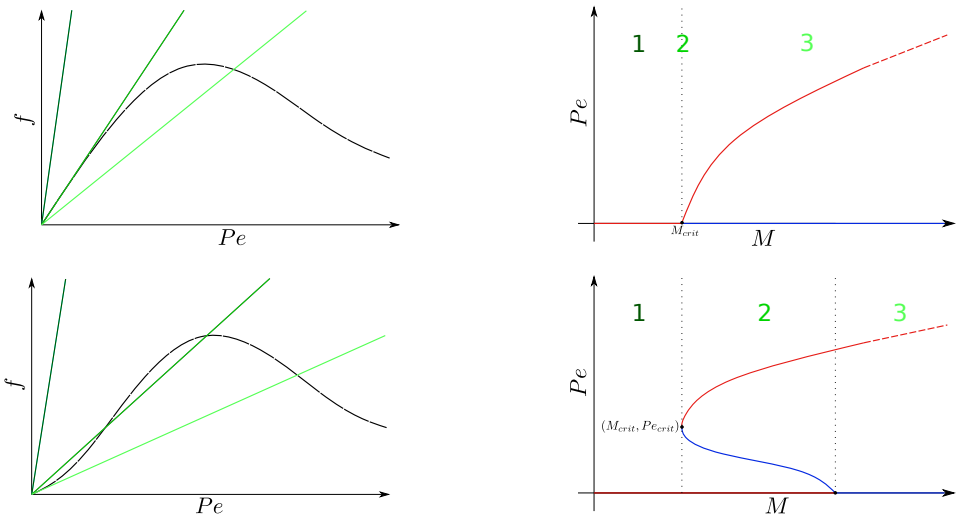

Figure 4.6: Schematic representation of a motor contribution dependence on Pe. The motor contribution is shown with the black curve while the drag contributions are the green lines, from dark green for low M to light green for high M. We consider two distinct behaviour for the motor force: (upper left) the increasing part is only concave, (lower left) the increasing part is convex then concave. They are associated with different swimming diagrams respectively (upper right) and (lower right). The blue lines are the unstable branches and the red lines are the stable branches.

stable branches, the last one to an unstable branch. Region 2 exists between the critical point and the merging point, where the unstable solution and the rest solution merge and disappear. Physically, a swimmer in region 2 is stable in the rest state. If a perturbation, however, increases its Péclet number above the unstable branch, it evolves spontaneously toward the moving state: the symmetry breaking is thus not spontaneous. To say it otherwise, a finite perturbation is required in region 2 to reach the swimming state. Note that this kind of bifurcation diagram is called a bistable behaviour. If one could control the M parameter – which is not obvious in experiments –, a hysteretic behaviour would be seen, with the transition between rest and swimming state occurring at different values of M.

In conclusion, the morphology of the swimming diagram is controlled by the concavity f_{model}. If it is concave at the origin, the transition from the rest state to a moving state is continuous. If however, it is convex, the transition is discontinuous, with a jump in Pe. For convenience, we call those two cases the continuous and the discontinuous phase diagram respectively.

b. Model A: incorporating no-slip

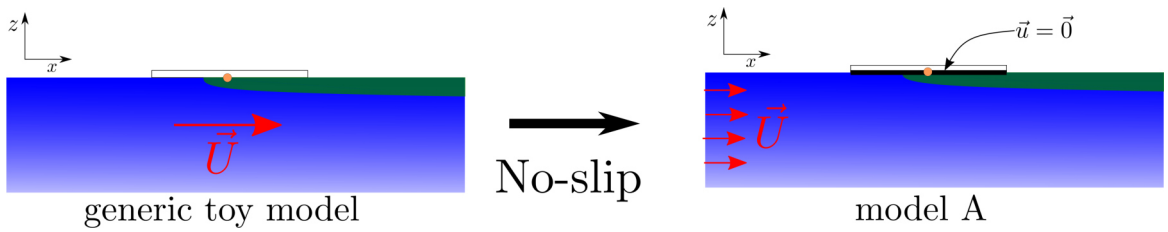

Figure 4.7: Sketch comparing the basic toy model to the model A.

As illustrated in figure 4.7, the model A differs from the basic toy model by the no-slip boundary condition on the swimmer surface, but the Marangoni stress is not yet implemented.

In the absence of Marangoni flow, M acts only on the computation of capillary force as a factor, while Pe controls the surfactant distribution. Then we can express the capillary force as $|\boldsymbol{F}_c| = M\eta D\ f_c\left(c(Pe)\right)$, f_c being the motor contribution in equation (4.25). This motor contribution depends only on surfactant distribution along the swimmer contour[26].

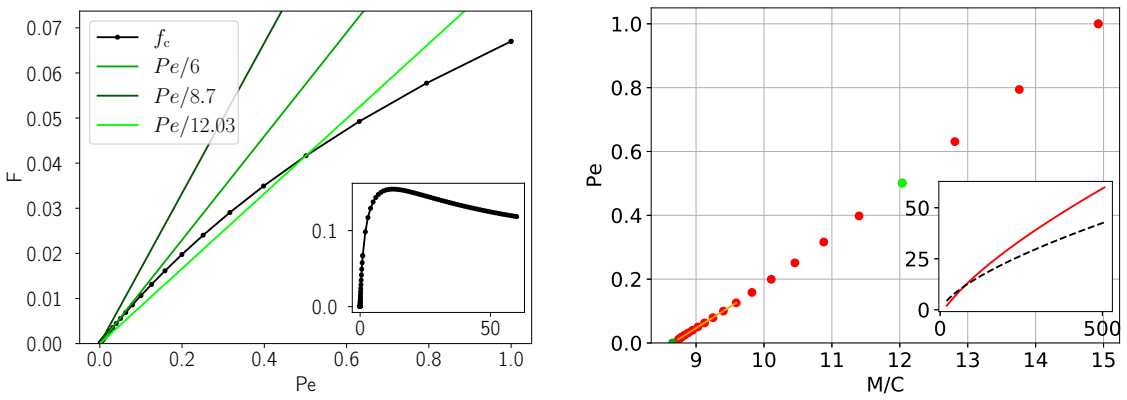

Figure 4.8: Swimming diagram for model A. (Left) $F_c(Pe)$, the lines are the drag contributions with $M/C \in \{6, 8.7, 12.03\}$, with $C = 16/3$ for a disk. The inset shows the large Pe regime. (Right) Stable branch for the model A, the position of the critical point (green) is estimated by using linear regression (orange line, $R^2 = 0.996$), the light green point corresponds to the crossing point between $f_{m\mathcal{M}}$ curve and the same line colour. For the inset, the continuous line is the stable branch of the model A, while the black dashed line is the stable branch for the basic toy model.

We find that with model A the swimming diagram is continuous. Indeed, as visible on figure 4.8, the motor function is concave up to a maximum. Compared to the toy model, there are thus only quantitative differences: the critical M is twice higher, the slope at the critical point is three times lower. At large M, the model A predicts faster swimming than the toy model[27]. To summarize, the changes in the swimming diagram from the toy model to model A are only quantitative.

c. Model B: incorporating no-slip and Marangoni flows

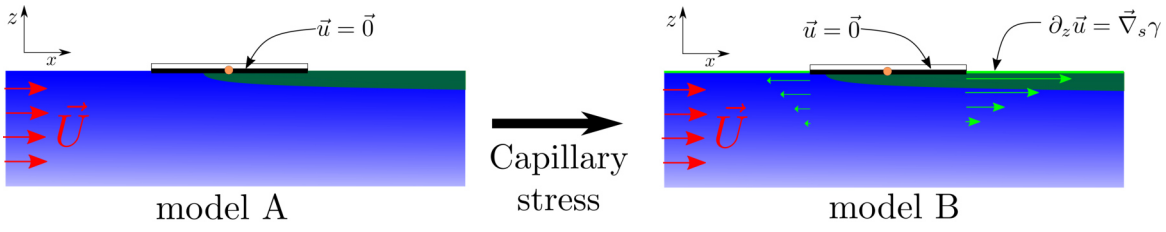

Figure 4.9: Sketch comparing the model A to the model B.

In model B, the Marangoni flows are now switched on. To delineate the swimming diagram, it is more convenient to use the second criterion.The key quantity is now the Marangoni force $F_{m\mathcal{M}}$. We find that the swimming diagram is of discontinuous type. Indeed, as can be seen in figure 4.10 the motor function can be convex at the origin. There is thus a region of bistability.

[26] A consequence is the no necessity to scan conjointly in Pe and M to find the swimming point, only a Pe scan is performed to obtain the different surfactant distribution. Since f_c is independent of M, finding the swimming M means scanning the curve of the motor force by changing the slope of the drag contribution.

[27] The crossing point is at $M = 75.0$ and $Pe = 11.6$.

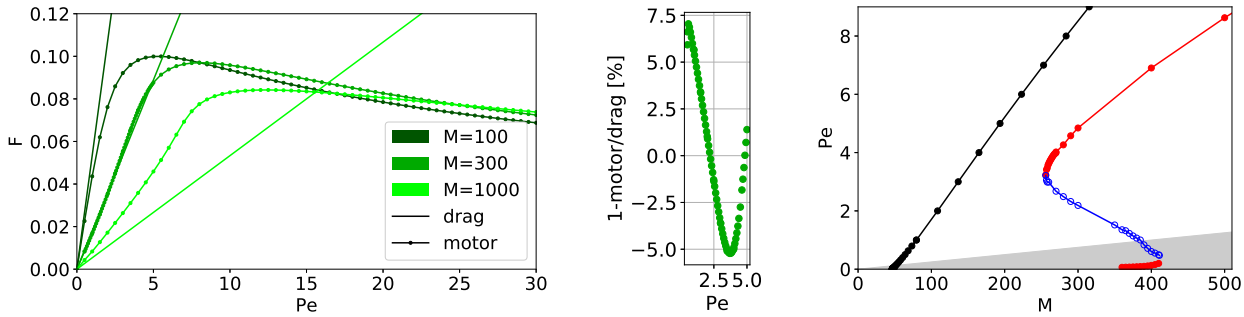

Figure 4.10: Swimming diagram for the model B. (Left) Motor and drag contribution for a point source at distinct M. (Middle) Evolution of the relative gap between the motor and drag contribution as a function of Pe for $M = 300$. (Right) Swimming diagram for model B, with filled and empty points showing stable and unstable state respectively. The swimming curve for model A (in black) is shown for comparison. The grey area covers the area where some finite-size effects might be expected [29].

To summarize the results so far, we have explored the swimming diagrams for three models. The inclusion of Marangoni stresses in model B modifies qualitatively the swimming diagram, from continuous to discontinuous. Quantitatively, $Pe_c = 3.23 \pm 0.05$, and the critical M is also much higher compared with the two previous models:

model	basic toy model	model A	model B
$\boldsymbol{M_c}$	$64/3 = 21.\underline{3}$	46.4 ± 0.5	255.5 ± 0.5

Note that there is a factor 5 between the model A and B critical Marangoni number, while between the toy model and the model A the factor is only 2. As regards the regime of intermediate Pe, we compare in figure 4.11 all models considered so far: toys models, models A and B. Here we see that the curves are qualitatively similar in shape. The curve of model B falls in between the two toys models, with the basic and Lorentz versions above and below respectively[30]. Since in the limit of large Pe, both follow the asymptotic dependence $Pe \sim M^{2/3}$, one can anticipate the same behaviour for model B. The data presented in figure 4.11 (right) is too limited in range to conclude unequivocally but do suggest that the 2/3 is at least a reasonable approximation. In any case, it is clear that the large-Pe regime involves much less difference than the low-Pe regime.

4.2.2 Relaxing additional simplifying assumptions

In our progression from toy model to a more realistic system, we have kept so far a number of assumptions: punctual release with fixed flux, Stokes flow and steady-state motion. In the following, we investigate how the swimming velocity is modified when such assumptions are relaxed. We will investigate in turn: an extended chemical source, a finite Reynolds regime and a time-dependent swimming. Finally, we will also reconsider the possibility of a concentration swimmer.

[29] As explained in the implementation section, for all the points in the light grey area we consider that the Marangoni flows are affected by the simulation boundaries. Knowing this delimitation, we assume that all the simulations done for (M,Pe) in this area give results out of our interest. Concretely, we ascribed the deviation from $Pe = 0$ to finite size effects.

[30] By the way, obtaining a higher velocity for model B than the Lorentz toy model is quite surprising since we were expecting that adding the Marangoni convection would decrease the speed. This slight underprediction of the Lorentz toy model tends to prove that the resistive contribution of Marangoni flow force is overestimated in the Lorentz toy model compared to the model B.

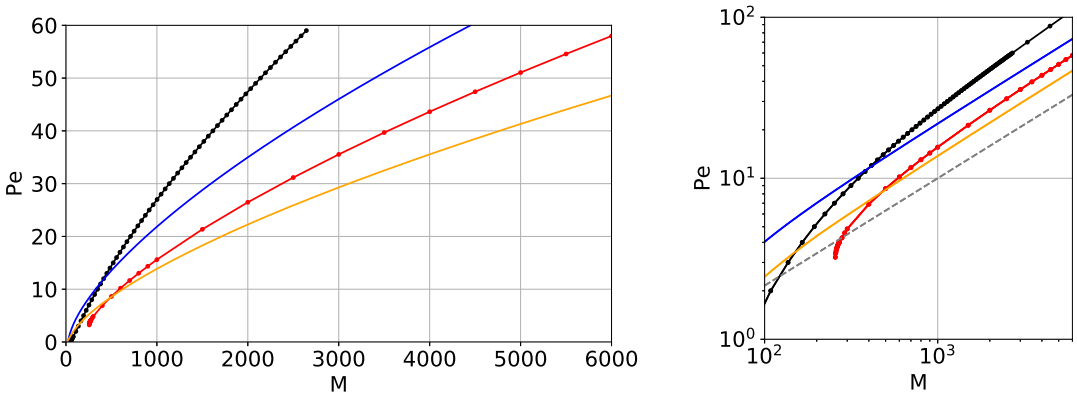

Figure 4.11: Swimming diagram of the stable branch for the model B (red dots), model A (black dot), the basic toy model (blue line) and the Lorentz toy model (orange line). Same data with linear scale (left) and log-log scale (right). The dashed line is a power law $Pe \sim M^{2/3}$.

a. Extended chemical source

Up to now, the surfactant is always released at point source centred on the swimmer. We now consider the extended chemical source: The surfactant is released over a disk of radius a_s with a local flux $J = \mathcal{J}/\pi a_s^2$, with $\mathcal{J}$ the total release rate as before. We now show that when implemented on model B, the extended chemical source can deeply alter the swimming diagram.

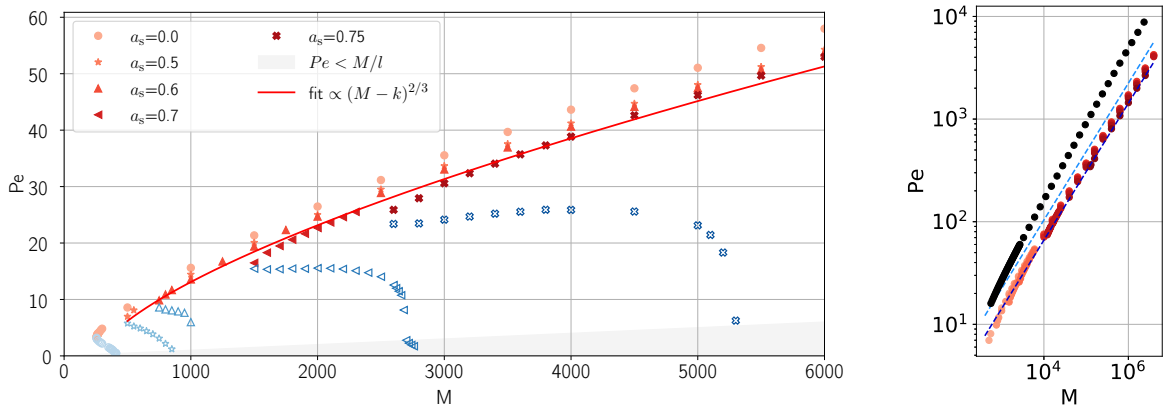

Figure 4.12: Swimming diagram for model B, with point and extended source. (Left) Bifurcation diagram for several source radii. The fit is drawn from the function $f(M) = a\,(M - M_o)^{2/3}$ with a and M_o the two fitting parameters. The fit gives $a = 0.17 \pm 0.005$ and $M_o = 200 \pm 200$. (Right) Log-log graph showing the stable branch for a_s varying from 0.5 to 0.9. The top and bottom blue dashed lines are the asymptotic $M^{2/3}$ power law for respectively the basic and the Lorentz toy model. The black dot is the stable branch for model A. Note that for all points above $M = 6000$ a specific mesh is used, more adapted to describe high Pe.

Surface source: swimming diagram When the surface source is implemented, the overall organisation remains the same as before (see fig. 4.12 left). We can see that the critical and the merging point are shifted to higher M when the source radius a_s increases. This trend is characterized in detail below. We also see that the unstable branch widens upon increasing the

source radius. Besides, the unstable branch does not decrease any more zero in a monotonous fashion. A plateau is clearly seen for $a_s = 0.7$, and an increasing portion for $a_s = 0.75$, suggesting that the early portion of the unstable branch tends to get closer the stable branch [31].

Now, there is a remarkable observation: for all source sizes, the stable branches end up collapsing on a master curve[32]. This collapse may be explained if the key quantity for determining the swimmer speed is not the source surface flux J but the total release rate $\mathcal{J}$. This master curve can be described with the power-law $Pe \propto (M - M_o)^{2/3}$, with M_o an offset around a hundred. At large Pe and M, the introduced offsets are negligible, and the master curve follows a $M^{2/3}$ power-law. As above, we observe on figure 4.12 right, that the model B swimming points are surrounded by those from the toy models; the basic toy model predicts consistently higher values while the Lorentz toy model gives results quite close to model B.

To summarize, replacing the point source by an extended source induces a shift in Pe and M for the critical and merging points. The overall shape is preserved. Remarkably, whatever the source size, the stable branch is close to a master curve that follows a 2/3 power law.

Evolution of $M_c(a_s)$ and $Pe_c(a_s)$ for the different models As the source radius approaches that of the swimmer, i.e. a release everywhere on the surface, the critical point is postponed to a higher value of M. A quantitative description of this trend is given in figure 4.13, where the position of the critical point is shown as a function of $\epsilon = 1 - a_s$. Both M_c and Pe_c appear to diverge as a power law of ϵ, with exponents around -3 and -2 respectively. This suggests that in the limit $\epsilon \to 0$, the critical point is pushed to infinity. Said otherwise, a swimmer with release all over its surface would not swim.

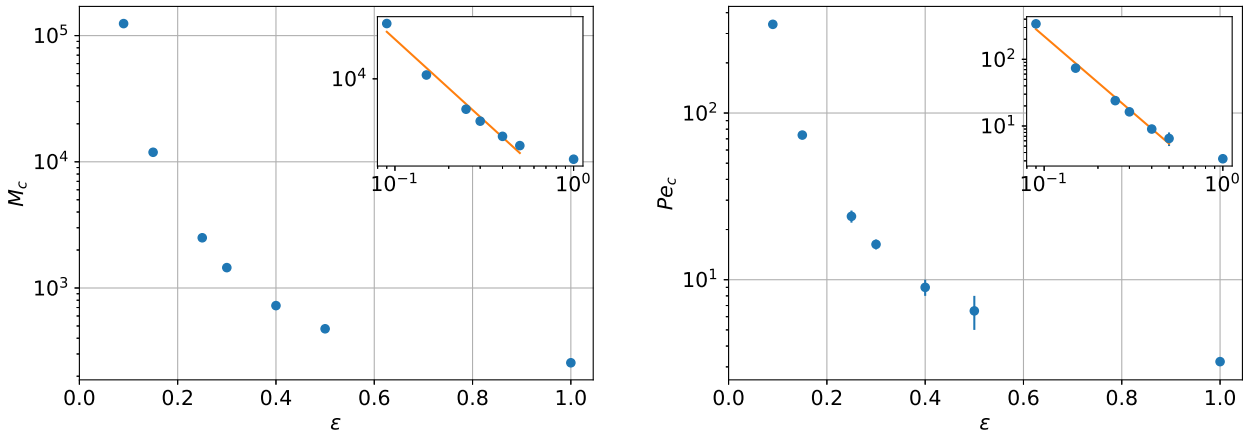

Figure 4.13: Effect of $\epsilon = 1 - a_s$ on the evolution of M_c (left) and Pe_c (right), the log-log graphs are the insets in the right corner, the slopes of the orange line are respectively -3.2 for M_c and -2.3 for Pe_c. We verify $2.3/3.2 \simeq 2/3$, which is consistent with the power describing the master curve. The error bar represents the step width of the scanning in M or in Pe.

To understand the origin of this observation, we reconsider previous models with an extended source. If the point source of the toy model and the model A is replaced by a surface

[31] Actually for a_s close enough to unity we observe a distinct increase (see fig. 4.29 in Appendix p. 162).

[32] The results of the point source study are displayed with the legend $a_s = 0$, however its stable branch does not seem to collapse on the master curve. The two sorts of source being distinct, we can expect two distinct results. Therefore the point source stable branch is not included in the two proposed fits.

source with a radius a_s, we can determine numerically[33] the evolution of the critical Marangoni number as a function of the source size. The figure 4.14 shows $M_c(a_s)$ for the basic toy model and the model A. In those cases, there is no divergence. More accurately, the critical Marangoni number is simply shifted by 17.5% in the basic toy model and by 10% in model A. This indicates that neither the diffusion transport nor the no-slip boundary condition alone can explain the divergence in M_c. Therefore it must be related to the presence of Marangoni flows.

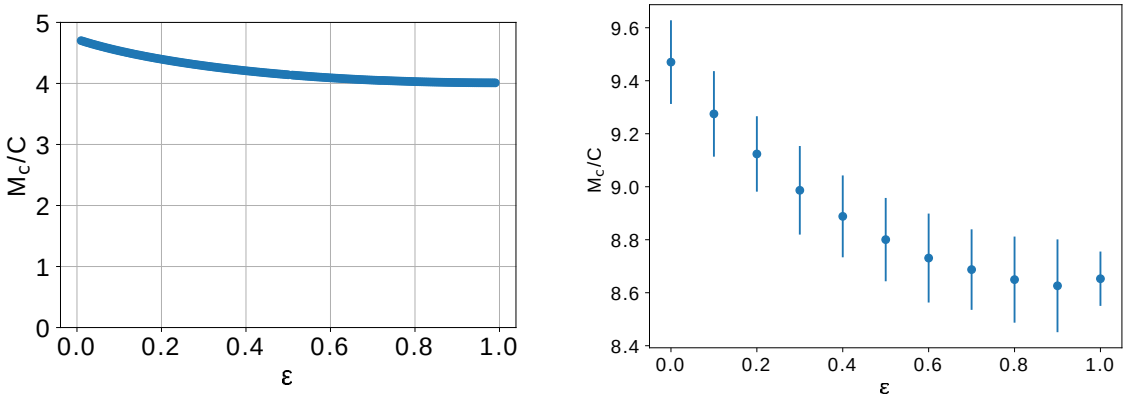

Figure 4.14: $M_c(\epsilon)/C$ with $\epsilon = 1 - a_s$ for the basic toy model (left) and the model A (right) by replacing the point source by a centred surface with the radius a_s. For both models, we determine either numerically or with simulation the M at low Pe, then the curve $Pe(M)$ is fitted with a straight. The line interception with abscissa gives the critical M.

b. Finite Reynolds

All the simulations done so far assume a Stokes flow ($Re = Ua\rho/\eta = 0$). However, our experiments are characterised by $Re \simeq 3 \times 10^2$. At this value, the inertia is no more negligible, and one should use the Navier-Stokes equation. We modify the model B simulation by adding the inertia term $\rho(\boldsymbol{u}\cdot\boldsymbol{\nabla})\boldsymbol{u}$ in the hydrodynamic equation (4.5). Using the dimensionless set of equation "$\kappa = 1$", the inertia term becomes $M/Sc\ (\tilde{\boldsymbol{u}}\cdot\tilde{\boldsymbol{\nabla}})\tilde{\boldsymbol{u}}$, with Sc the Schmidt number $Sc = \eta/D\rho = Pe/Re$. Note that with "$\kappa = 1$", the natural inertia number for the flow is Sc and not Re, that is why we use it instead to characterise our simulation. We designed a specific mesh adapted for such a system, with a finer mesh below the free surface and the swimmer. For more detail about the implementation and the mesh, we refer to appendix 4.4.3.

The effect of a finite Reynolds number is shown in figure 4.15. For Pe below 20, in the vicinity of the critical number, the swimming diagram obtained with finite Sc is very close to the one obtained at $Sc = \infty$, which is not surprising since the Reynolds number remains relatively low. The critical Péclet number is stable, while the critical Marangoni number is slightly lower, around 25% less for all the finite Sc simulation compared to the simulation results for $Sc = \infty$.

[33] For the basic toy model with a surface source of radius a_s, the swimming equation is

$$\frac{\tilde{F}_c(Pe)}{a_s^2} = C\pi^2\frac{Pe}{M},$$

$$\tilde{F}_c = -\int_{\theta'=0}^{\theta'=\pi}\int_{\mathcal{D}_{int}} \frac{\exp\left(-\frac{Pe}{2}(\cos\theta - x_p)\right)\exp\left(-\frac{Pe}{2}\sqrt{(\cos\theta - x_p)^2 + (\sin\theta - y_p)^2}\right)}{\sqrt{(\cos\theta - x_p)^2 + (\sin\theta - y_p)^2}}\,\mathrm{d}\theta\,\mathrm{d}x_p\,\mathrm{d}y_p,$$

with $\{x_p, y_p\} \in \mathcal{D}_{int}$, $\mathcal{D}_{int}$ being the surface source. The integral $\tilde{F}_c$ is computed numerically.

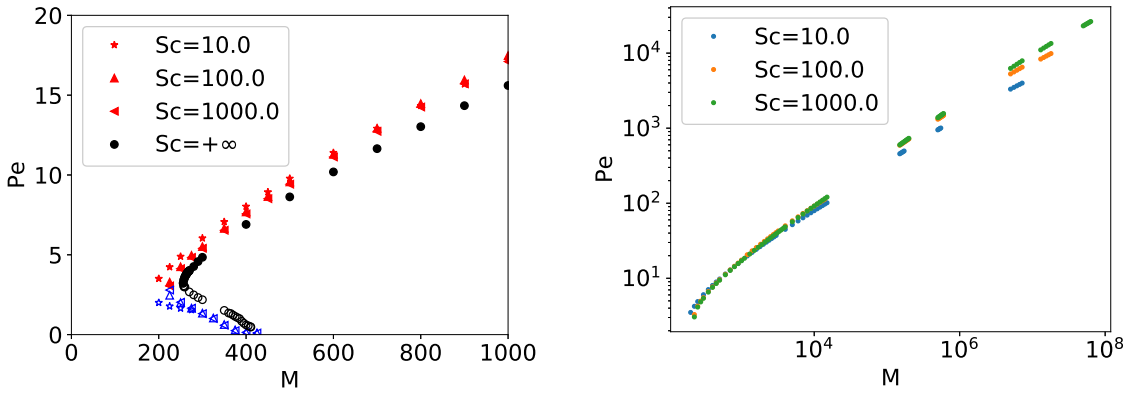

Figure 4.15: Swimming diagram with Navier-Stokes equations. (Left) the stable branch is in red and unstable branch in blue. For the Stoke flow simulation, $Sc = +\infty$ the results are in black with the stable branch represented by disks and the unstable branch by circles. (Right) stable branch in a log-log graph.

Sc	10	100	1000	∞
$\boldsymbol{M_c}$	190 ± 10	210 ± 10	210 ± 10	255.5 ± 0.5
$\boldsymbol{Pe_c}$	3.3 ± 0.6	3.0 ± 0.5	3.0 ± 0.5	3.23 ± 0.05

In the high Pe regime, the stable branches seem to verify a power-law $Pe \propto M^{\alpha}$. With a linear regression ($R^2 > 0.99$) for $M > 1 \times 10^4$, we determine the exponent and found $\alpha = 0.6,\ 0.62,\ 0.65$ for respectively $Sc = 10,\ 100,\ 1000$. Though this suggests a trend toward values lower than $2/3$, the deviation remains small.

In conclusion, the results obtained with the Navier-Stokes flow remain close to the ones obtained with a Stokes flow. However, we should mention that the maximal Re explored remains one order of magnitude below those relevant in experiments. We can not exclude a more pronounced effect in this range.

c. Relaxation toward steady-state

We saw previously that in the swimming diagram of model B, there is a bistability region, with two stable branches and one unstable branch. This suggests the possibility of a non-steady swimming that can not be described by a stationary study, hence the necessity to use time-dependent simulations, and to check whether the predictions from the swimming diagram are accurate.

We implemented time-dependent simulations whose details are given in appendix 4.4.2. A new dimensionless number is needed, N, which up to a geometric constant, is the ratio between the fluid density and the swimmer density. Since our main goal is just to check the swimming diagram prediction, we have considered only one couple of inertia number ($N = 1, Sc = 0.01$). While $N = 1$ is not so far from the experimental value associated to the gel swimmer (experimentally $N = 3$), the Schmidt number is five orders of magnitude below the experimental value ($Sc = 1000$), which corresponds to a dense fluid[34]. Time-dependent simulations are time-consuming, hence the choice of an inertia number leading to a monotonous behaviour easier to handle and faster to simulate. Because of the memory consumption, all the time-dependent simulations are implemented with a coarse mesh whose mesh factor is 0.1 instead of 1. Our simulation can not describe a swimmer at rest, as we explained in the section

[34] As a reminder, we use the time dependant Stoke flow equation.

devoted to the simulation reliability (see 4.1.4). In particular, for $Pe < Ma/l$ the results become unphysical. Therefore, we stop the simulation when this condition is reached.

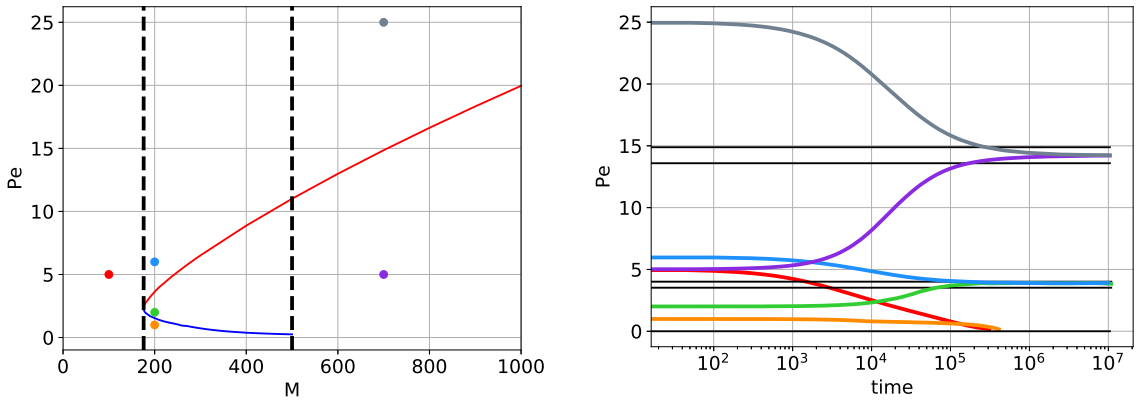

Figure 4.16: Time dependant simulation results. (Left) Swimming diagram for a mesh factor at 0.1, ten times lower than usual. The coloured dots represent the initial condition for the time dependency solution, one in each of the six areas. In each of them, we expect an evolution towards a stable speed, null for the areas below the critical Marangoni number (red dot/curve) and below the unstable branch (orange dot/curve) and a motion state for the others. (Right) time evolution of the Pe number for six different initial conditions (see the left figure for the colour legend). The black line surrounds the expected value at the steady-state. Note that the orange and red curves have been stopped prematurely at Pe close to zero since the simulation implementation is not adapted to describe the state $Pe = 0$.

As shown in figure 4.16 the simulations confirm the swimming diagram prediction with a relaxation towards the expected swimming point for the six initial states we considered, each in a different domain. When the predicted steady-state is associated with a non-zero speed, the velocity at a long time tends toward the expected velocity magnitude. A further interest of time-dependent simulations would be to reproduce the time-dependent behaviours I observed in some specific experiments, such as oscillations of the velocity for a stripe swimmer (see figure 4.17). This would though require further studies [35].

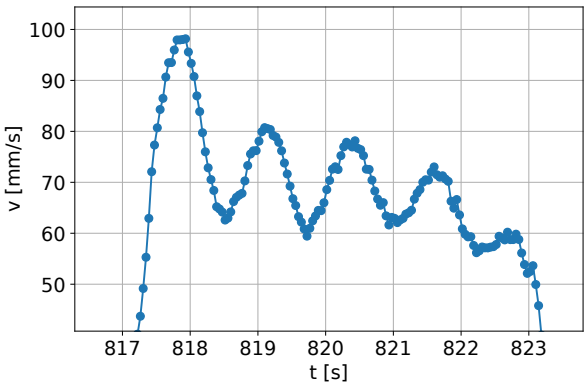

Figure 4.17: Non-steady motion in experiments: Oscillating velocity between interactions with pool walls for an interfacial strip swimmer of length L=20 mm and width l=2 mm.

[35] Actually in "pre-simulation" with a more degraded mesh, $M_f = 0.01$, we observed damped oscillations of the speed for N=30 and Sc=10

d. Concentration boundary condition

In chapter 3, we explored the possibility of an interfacial swimmer with a fixed concentration on its surface. Toys models predict that swimming is possible thanks to a motor Marangoni force. Using simulation to take into account, without approximations, all Marangoni effects, we reach the conclusion that the Marangoni flow force is indeed a motor force favouring motion, but we found no swimming point over the range of M and Pe tested since the drag force is larger in magnitude than the Marangoni force.

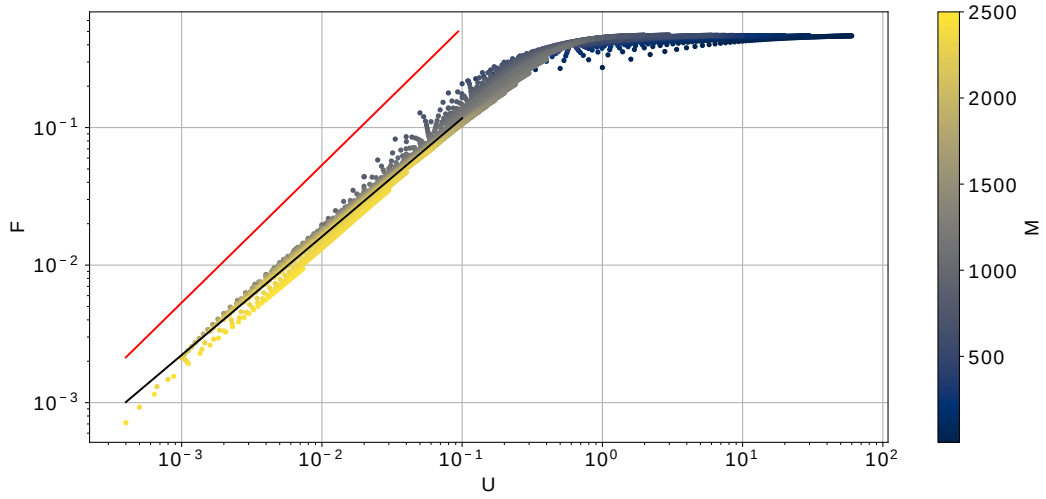

Figure 4.18: Evolution of the magnitude of the forces applying on the swimmer as a function of $U = Pe/M$ [37], in a log-log graph. The red line is the Stokes drag force (4.14), $\hat{F}_{\mathrm{d}} = CU$, and the coloured dots are the Marangoni force. Each dot is the computation of the Marangoni flow force from a simulation scan at different M and Pe, the colour of the dots indicates the value M of the simulation. The black line is a linear regression giving the slope $\alpha = 0.9$ ($R^2 = 0.99$) and the intercept $\beta = -0.2$. As a reminder, we use the set of dimensionless equation "$\kappa = 1$" then the force scale is $f^* = \eta MD$ and the speed scale is $u^* = MD/a$.

In practice, we keep the implementation of the model B, but the point source is replaced by a fixed concentration on the disk surface. The only change is that the definition of the Marangoni number is now given by $M = \kappa C_{sat} a/\eta D$.

We consider the Marangoni force $F_{\mathrm{m}\mathcal{M}}(U)$shown in figure 4.18 in a log-log scale. We choose to plot the data as a function of the velocity U, and not as a function of Pe, since it gives an overview of all the simulations performed in a simple graph. We first note that the Marangoni force is non-zero and would favour motion. In contrast with previous models, the Dirichlet condition over the swimmer surface changes the Marangoni force from resistive to motor. Surprisingly, when plotted as a function of the swimmer velocity U, the Marangoni force appears to collapse on a master curve, which may indicate that at first order it depends only on U. This master curve is characterised by two behaviours. For $U < 0.1$, the curve is very well described by a power-law with exponent 0.9. For $U > 1$, the Marangoni force reaches a plateau with magnitude $F_{\mathrm{m}\mathcal{M}} = 0.45 \pm 0.02$. This suggests that the surfactant field around the swimmer converges toward an asymptotic distribution at high speed U, or equivalently at high Pe and low M.

Given that the slope $\alpha < 1$ for $U < 0.1$, the possibility remains of a non-zero swimming velocity at very low $U = Pe/M \simeq 10^{-8}$. Experimentally, we have $Pe/M \simeq 10^{-3}$ for the pure camphor swimmer. While we can not conclude on the experimental side, now we have clear evidence that, in contrast to constant flux swimmers, a concentration swimmer can induce a

[37] By using the dimensionless set of equation "$\kappa = 1$".

Marangoni flow that favours the motion. Note that beyond the interfacial swimmers, this idea that the Marangoni flow can help to the motion has already been developed in [3]. It remains to see whether, as seems to be the case in the constant-flux swimmer, the absence of swimming is related to the fact that the whole surface participates to the surfactant release (including at the edge).

4.2.3 Discussion

As we just saw, using numerical simulations we have carried out a systematic approach whereby we introduced one by one physical ingredients to assess their impact on interfacial swimming. We now try to synthesize these different results in conjunction with experimental (chapter 2) and theoretical (chapter 3) investigations, focusing on the swimming diagram.

Symmetry breaking The first main feature of the swimming diagram is the detailed path by which achieving symmetry breaking and spontaneous swimming are achieved. Starting from the motionless reference state, this aspect thus corresponds to the low-Pe regime. Overall, we found that the exact transition scenario is quite sensitive to the degree of refinement of the model. Depending on it, we observed in the (M, Pe) plane either continuous transitions – at zero or a finite threshold M_c– or discontinuous transitions characterized by a critical point (M_c, $Pe_c > 0$).

This last regime is indeed novel as compared to earlier predictions and the near threshold regime might be dominated by residual, unavoidable asymmetries as pointed out in our analytical calculation. More importantly, the parameter range for our experimental swimmers (see table 4.4) falls in regimes very much above the low-Pe range and prevents a simple investigation of it. A possibility for future approaches could be to use an externally tunable power source with light-absorbing heat-driven swimmers. Alternatively, one may try to reduce the effective Marangoni number by changing the interfacial reference state with for instance a finite concentration of camphor introduced in the subphase. As for the problems of residual asymmetries, near-threshold regime will be extremely sensitive to additional spurious effects and both routes may for instance be confronted to uncontrolled residual contamination by surface pollutants.

Coming back to the novel discontinuous transition we report, let us stress that it predicts the existence of a bistable domain where stable motionless and swimming regimes coexist for a finite range of Marangoni number M above M_c is an interesting feature that is reminiscent of the intermittent or oscillatory swimming regimes reported in some experiments [10]. Yet, exploring a direct connection between our swimming diagram and those observations will require to go further with the stationary-state approach as practically the M parameter is a constant of the problem. Variation of its effective strength can only be imagined in time-varying scenarios as proposed for some experiments on interfacial boats [9]. Some time-dependent simulations have been conducted so far that confirm the attraction basins of each stable state, but further work is needed to be able to handle properly the motionless state to investigate possible stop-and-go regimes.

Finally, our numerical simulations have evidenced that the location of the swimming transition is very dependent on the details of the camphor release. Indeed, moving from the original point source considered in the toy model approach, toward an extended release over an inner surface of radius a_s have shown a drift of the critical swimming point (M_c, Pe_c) to higher values. Approaching the full surface active swimmer limit $a_s = 1$, this retardation is even found to diverge so that no swimming instability would occur in this case. This finding, which explicitly relates to the action of Marangoni flows over the camphor distribution, brings up questions as in experiments fully loaded swimmers do spontaneously swim. This apparent discrepancy

needs further investigations[38].

Let us note some other differences between experiments and numerics. Experimental observations on core and crown swimmers are not performed at a constant released rate, hence are more difficult to compare directly. Nevertheless, crown swimmers were measured to run faster than core swimmers (chapter 2). No numerical simulations have been done on crown configuration, but this is not the trend that arises naturally from our present results on core configuration. Are there fundamental reasons why swimming should disappear for full-area release? Can there be numerical artefacts due to singularities at the edge? These are some open questions that need to be addressed.

Similar interrogations arise when changing not the release area but the associated boundary condition: from fixed flux to fixed concentration. Again, no swimming is predicted when releasing camphor all over the swimmer with fixed concentration while experimental pure camphor swimmers do move. Whether this comes from numerical difficulties, some incorrect assumption of fixed concentration with pure camphor or from another source is a matter of future investigations.

High-Pe behaviour The second main feature of the swimming diagram is the $Pe(M)$ relationship once spontaneous swimming occurs, with a special attention to the high-Pe regime, far above threshold. Unlike the low-Pe regime, the striking feature of this high-Pe response is its robustness to the refinement level of the physical description. Indeed the $Pe \propto M^{2/3}$ power-law derived for analytical toy models is, with a very good approximation, maintained all over the tested models. This power-law resists considering the no-slip boundary condition on the disk (model A), but also the possibly key introduction of Marangoni effects (model B).

Moreover, the agreement between simple toy models and full numerics is found not only on the scaling but also quantitatively as can be seen in figures 4.11 and 4.12. These conclusions remain valid even when varying the chemical source extent that strongly affects the threshold location while preserving the high-Pe behaviour as an asymptotic master curve. This is a quite remarkable achievement for the crude toy models, which also raises a natural question: is there a fundamental argument that sets the high-Pe scaling irrespective of physical details?

For the toy models and the numerical models, we propose here a tentative explanation that exploits the fact that swimming indeed occurs at very large Péclet number. The basic assumption is that the flow between the release point and the swimmer periphery is dominated by advection. In those conditions, the chemical is found mostly behind the swimmer, in a thin wake of width $w \sim \sqrt{Dt_T}$, where $t_T \sim a/v$ is a transit time from the release point to the periphery. The balance between drag and surface tension forces yields $C\eta av = \phi w \kappa$, with $\phi \sim J/vw^{d-1}$ the typical value of concentration. In the 3D case that we consider here, this leads to $Pe \sim M^{2/3}$. The argument above implies only the flow between the release point and the periphery, in a very thin layer just below the swimmer. For the model B, the mechanism leading to the power-law is probably less straight forward. Indeed, as we point out in the next section, some hints lead to the hypothesises that the surface flow and concentration converge toward an asymptotic structure at high M probably related to an equilibrium between mean and Marangoni flows. However, if the extension of the chemical wake is thin enough, the relation $Pe \propto M^{2/3}$ should remain verified despite the Marangoni flow. The precise characterization of the flows in high-Pe regime in the various models remains to be done and should allow concluding on the validity of this simple picture.

Coming back to the experiments, unlike the swimming threshold, we have gathered quantitative elements to confront to predictions. As regards the scaling, it is indirectly probed by

[38] A possible way to rationalize this gap between experiment and simulation would be to consider the gel depletion layer put in evidence in chapter 2. Knowing that this layer gets thicker along the swimmer contour we may expect a lower camphor flux along this border.

Dimensionless number	Pe	M	Re	Sc	N
Value for agarose gel swimmer	4×10^5	6×10^{10}	3×10^2	1×10^3	2

Table 4.4: Typical dimensionless numbers for experimental agarose gel swimmers.

the swimming velocity dependence on the disk radius with $M \sim a^2$. Consistently with the above findings, the experimental velocity can be described by a sub-linear growth $U \sim a^{1/3}$. Beyond the scaling, it is also possible to interrogate the absolute value of the velocity, knowing experimental estimate for M. Even if toy models quantitatively agree with simulations including Marangoni effects, it does not with the experimental velocity which differs by a factor of 5 from the predictions.

To begin with, let us note that although we expect numerical simulations to have incorporated all relevant contributions, the explored parameter range still falls short as compared to experimental ones, with Pe and M numbers one or two decades higher. From the various effects explored, let us nonetheless point the effect of finite inertia as measured by Re. Looking at the results presented in figure 4.15 ($Pe(M)$ for different Sc), we found that inertia reduces the swimming velocity with a slight change in the scaling law exponent from about 2/3 to about 0.60 for the experimental Schmidt number. When applied to experimental values of the Marangoni number, such a tiny shift in the exponent of the scaling law actually translates into velocity reduction by a factor of 5, yielding agreement with experimental values.

4.3 Local features: flow and concentration fields

In contrast to our experiments, simulation gives access not only to the swimming diagram but also to local features such as the flow and the concentration fields. Here we examine to what extent those fields give insight on the Marangoni propulsion and swimming diagrams presented above. We investigate in particular the properties of hydrodynamical and chemical wakes.

Three preliminary remarks are in order. (i) We first need to recall the orientation convention The simulations are conducted in the swimmer frame of reference. Our conventions are illustrated in figure 4.19. In particular, the definition of θ is such that 0° corresponds to the rear and 180° to the front of the swimmer (ii) For model A, the concentration and velocity fields are independent of the Marangoni number, but we still associate them to a M such that the force balance on the swimmer is verified. (iii) For model B, we consider only the simulations close to the stable branch in the swimming diagram.

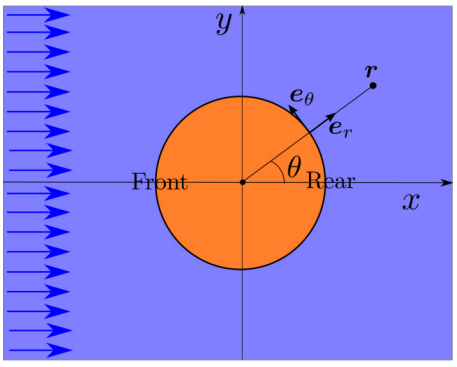

Figure 4.19: Schematics of the swimmer, showing notations and convention used in the simulations.

4.3.1 Evolution from the toy model to model B

In our series of models, we introduce first the no-slip on the swimmer and then Marangoni flows (see tab. 4.3 p.138). As above, we discuss the influence of each ingredient in turn.

a. No-slip boundary condition

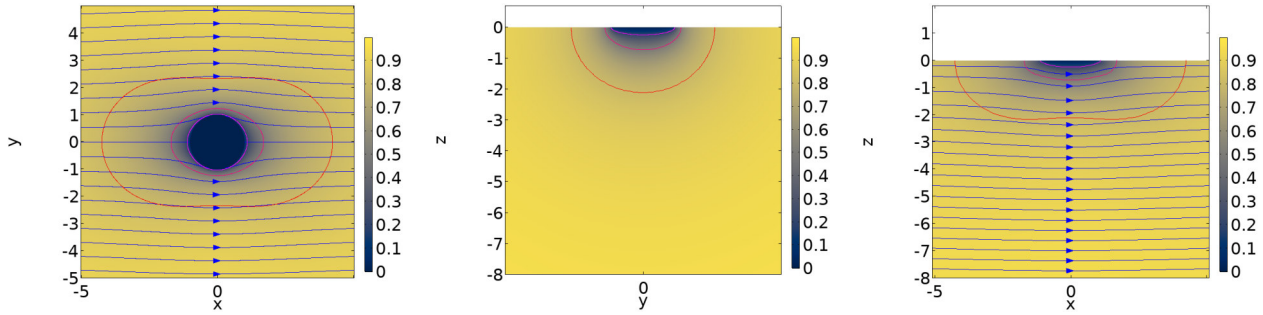

Figure 4.20: Velocity field in model A. This is the Stokes flow generated by a moving disk, as seen in the swimmer frame. The magnitude of velocity is indicated by the colour, streamlines are in blue. Three iso-velocity curves are also shown $[0.2, 0.5, 0.8]$. From left to right, top view ($z = 0$), rear view (x=0), side view (y=0). Note, for the plane $x = 0$ there are no streamlines since the flow is normal.

Compared to the uniform flow of the toy model, the velocity field[39] in model A is different, as illustrated in fig. 4.20. The no-slip boundary condition on the swimmer induces a deviation of the streamlines at the surface. There is a moderate bent of streamlines below the swimmer but still, the velocity magnitude is very different close to the swimmer as it now goes to zero[40].

The comparison of concentration fields does not reveal striking differences between toy model and model A. We show in figure 4.21 the field for the latter only (for the former, the result is quite similar in this representation). For the surface concentration field at low Pe, characterising the asymmetry just by seeing the surfactant field is not obvious. At low velocity (Pe=0.01), it is barely visible, with iso-concentration curves very close to circles. At higher velocity (Pe=1), the asymmetry develops, with iso-curves that have an egg-like shape. As expected, the surfactant distribution affects the capillary force, with a factor 60 between $Pe = 0.01$ and $Pe = 1$.

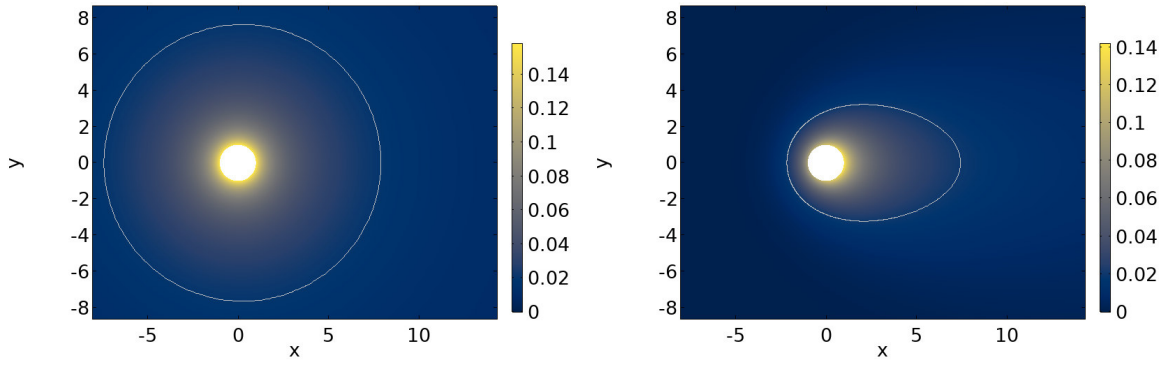

Figure 4.21: Surface concentration, model A point source, surfactant distribution for distinct Pe, respectively 0.01 for (left) and 1 for (right), the white line is the iso-concentration $c = 0.02$.

[39] We recall that the velocity field is the analytical solution of a fixed disk in a Stokes flow [4] (see figures 4.20).

[40] Note that the fore-aft symmetry of our swimmer, combined with the Stokes flow, ensures anti-symmetry of the flow concerning the $y = 0$ plane.

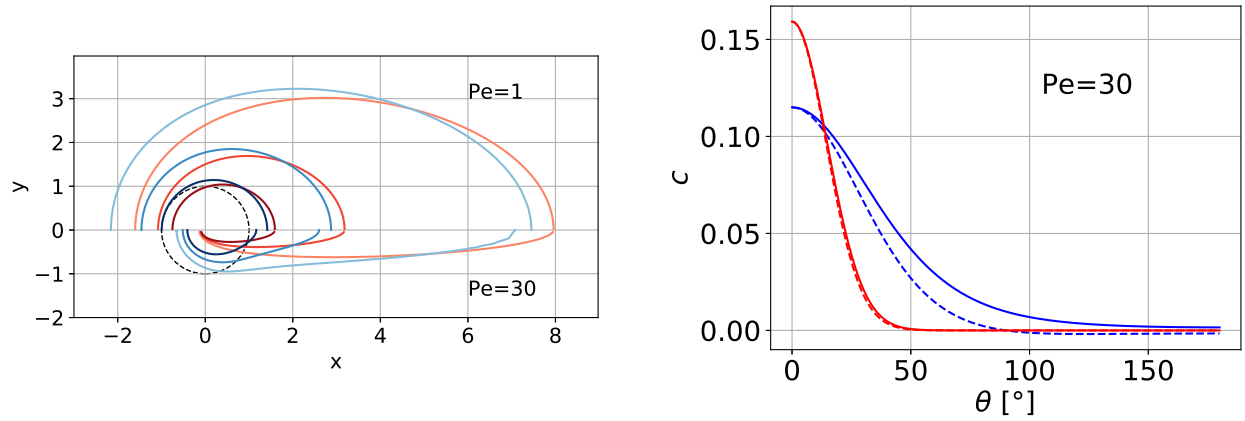

Figure 4.22: Comparison of iso-concentration curves in toy models (red) and model A (blue). (Left) Iso-concentration for values c=[0.1, 0.05, 0.02] (from dark to light). The dashed lined is the swimmer disk. (Right) Concentration profile along the disk contour for Pe=30. The local contribution to capillary force $c\cos\theta$ is also shown (dashed lines).

It is often far from obvious to relate the concentration field to the force applying on the swimmer. For instance, for $Pe > 11.6$, the swimming diagram 4.8 indicates that model A yields a capillary force higher than in the toy model, whereas the surfactant distribution appears less polarized (see fig. 4.22). Some insight is given when considering the concentration c and the quantity $c\cos\theta$ along the swimmer contour whose integral determines the capillary force[41]. As visible in figure 4.22, the contour concentration profile has a lower maximum but is wider for the model A, leading to a force 40% larger. We may explain this phenomenon by the slight rising flow behind the swimmer. The surfactant which has diffused into the bulk is advected back to the surface by this fluid movement, yielding a higher concentration of surfactant near the swimmer rear.

b. Marangoni stresses

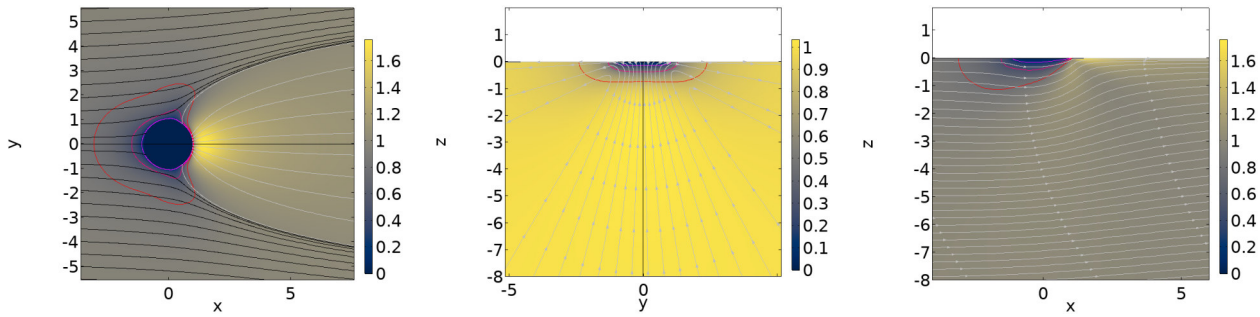

Figure 4.23: Velocity field in model B ($M = 2500$, $Pe = 35.6$). This is the Stokes flow generated by a moving disk, as seen in the swimmer frame. The magnitude of velocity is indicated by the colour. Three iso-velocity curves are also shown $[0.2, 0.5, 0.8]$. From left to right, top view ($z = 0$), rear view (x=0), side view (y=0). Note for the surface flow we use two colours to distinguish the lines starting from the infinite in front of the swimmer (black) from the streamlines starting from the swimmer (grey).

[41] As a reminder, the capillary force (4.13) projection along the x-axis is the integral of $c\cos\theta$ times the constant $-a\kappa$.

Accounting for Marangoni stresses deeply alters the velocity field. This is visible when comparing figure 4.23 for model B with figure 4.20 for model A. In particular, a new feature is the wake, illustrated by white streamlines on figure 4.23. The origin of the wake appears to be a divergent flow at the swimmer rear characterised by a flow velocity almost twice higher than the swimmer velocity. This observation matches results observed for asymmetric swimmers [12]. This divergent flow is generated by the Marangoni stresses which drive the mean flow away, as reflected by the accumulation of initially evenly spaced streamlines along the wake boundary. We characterize more thoroughly this hydrodynamic wake in the next part. Another new feature is the recirculation taking place in the whole pool. This is visible in a rear view ($x = 0$ plane, fig. 4.23 middle), where one sees the flow rising from the depth of the fluid before moving away from the swimmer on each side. The side view (plane $y = 0$) gives another indication of the divergent flow and recirculation, with the flow slightly rising behind the swimmer.

This strong divergent flow at the swimmer rear is at the origin of the Marangoni flow force resistive contribution (see appendix 4.4.5). Indeed, the flow tends to transport the swimmer in a direction opposite to its own motion, hence a viscous force. For this Marangoni flow, considering the symmetry, the total contribution is along $+\boldsymbol{e}_x$, which is indeed the opposite direction than the swimmer motion $-\boldsymbol{e}_x$, hence the resistive contribution.

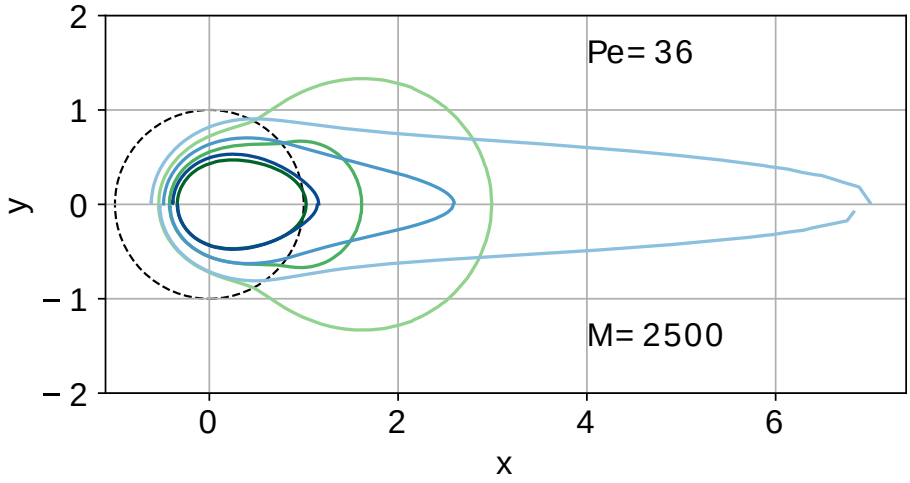

Figure 4.24: Comparison of concentration fields in model A (blue) and model B (green). The continuous color lines are the iso-concentrations $[0.1, 0.05, 0.02]$, with a gradient of color from dark to light with $Pe = 36$ for $y > 0$ and $M = 2500$ for $y < 0$. Note the upper and low results for the model B are the same and extracted from a simulation ($Pe = 36, M = 2500$), close to the swimming branch.

As can be anticipated from the flow, the presence of Marangoni stresses has significant consequences on the concentration field. The comparison between model A and model B (fig. 4.24) can be done either at the same Pe (upper part of the figure) or the same M (lower part of the figure) [42]. We see a similar feature in both cases: a clear widening of the iso-concentration lines. This is very different from what happens in model A, where iso-concentration lines get closer the x-axis, an effect already expected in a simple Stokes flow. The wide spreading of the surfactant reflects the homogenising effect associated to the Marangoni convection.

To summarize, the Marangoni stresses of model B induce two new phenomena. First, the high concentration gradient at the swimmer rear generates a divergent high-speed flow at the origin of a resistive force. Second, this Marangoni flow transports the surfactant toward the low concentration area, whence a homogenising effect that reduces the motor forces. Those

[42] For the model B, M influences the surfactant and velocity field, it is no more an adjustable variable used to equalise the drag and the motor contribution, contrary to the toy models or the model A.

two phenomena may explain why for the same Marangoni number, model A leads to a higher velocity[43].

4.3.2 Hydrodynamic and chemical wakes

By moving and releasing a surfactant, the swimmer generates a hydrodynamic and a chemical wake. To better understand the fluid flow and surfactant distribution, we now investigate those wakes in detail.

a. The hydrodynamic wake

The hydrodynamic wake is visible from the streamlines at the surface (see fig. 4.23). It can be defined as the domain where the streamlines do not reach $x = -\infty$, and is limited by two separatrix curves [44].

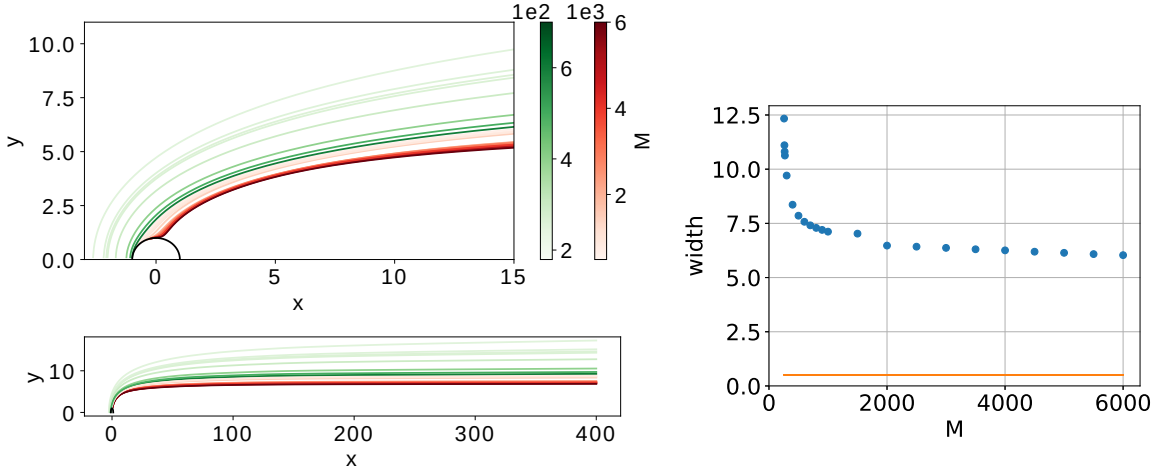

Figure 4.25: Hydrodynamic wake at different Marangoni numbers. (Left) Representation of the hydrodynamic wake for the model B point source at different Marangoni number, the upper figure represents the evolution close to the swimmer, while the lower figure shows their evolution for a wider x range. There are two colour bars, the green gradient one goes up to M=700, and the red gradient one goes from 800 to 6000. (Right) Evolution of the wake width at $x = 400$ as a function of the Marangoni number. Note that the model B results are the blue dots, the orange line is the result for the model A Stokes flow.

As visible in Figure 4.25, and whatever M, one can observe two regimes in the hydrodynamic wake: close or far from the swimmer. We first focus on the vicinity of the swimmer. There the wake expands rapidly, approximately as a square root[45] (see upper-left figure). Another feature is the stagnation point that may exist in front of the swimmer. For instance, at the critical point $M_c = 256$, the stagnation point is 1.6 radius away from the swimmer surface. This distance decreases upon increasing M until the stagnation point reaches the swimmer contour[46]. The separatrix then emerges from the swimmer contour, at an angular position

[43]There is no supplementary resistive force and the capillary force is higher since the surfactant exhibit a sharper distribution on the swimmer contour.

[44]To determine the streamline position we use two methods which change according to the separatrix starting point. If the separatrix appears in front of the swimmer, then we determine it as a streamline arbitrarily close to the line $y = 0$ for x negative far from the swimmer, more accurately the streamlines passing by the point ($x = -20$, $y = 0.001$, $z = 0$). If the separatrix appears on the swimmer contour, we plot a set of streamlines starting from the swimmer contour and we select the most external one.

[45]Deduced by linear regression.

[46]This event appears between M=600 and M=700 (green gradient curve).

that varies from 180° to 100° for $M = 6000$. This latter value seems to be the limiting value, suggesting that the angular position 90° would no be reached even for larger M [47]. This is one indication that the hydrodynamic wake flow seems to converge at large M towards a stable flow structure.

Far from the swimmer, the width of the wake becomes constant or expands more slowly: the lower M, the weaker the expansion, as illustrated by figure 4.25. We note again that in the limit of high Marangoni numbers, all curves approach an asymptotic curve. A similar observation holds for the width of the wake: after a drop near M_c, it approaches a limit value around 6.

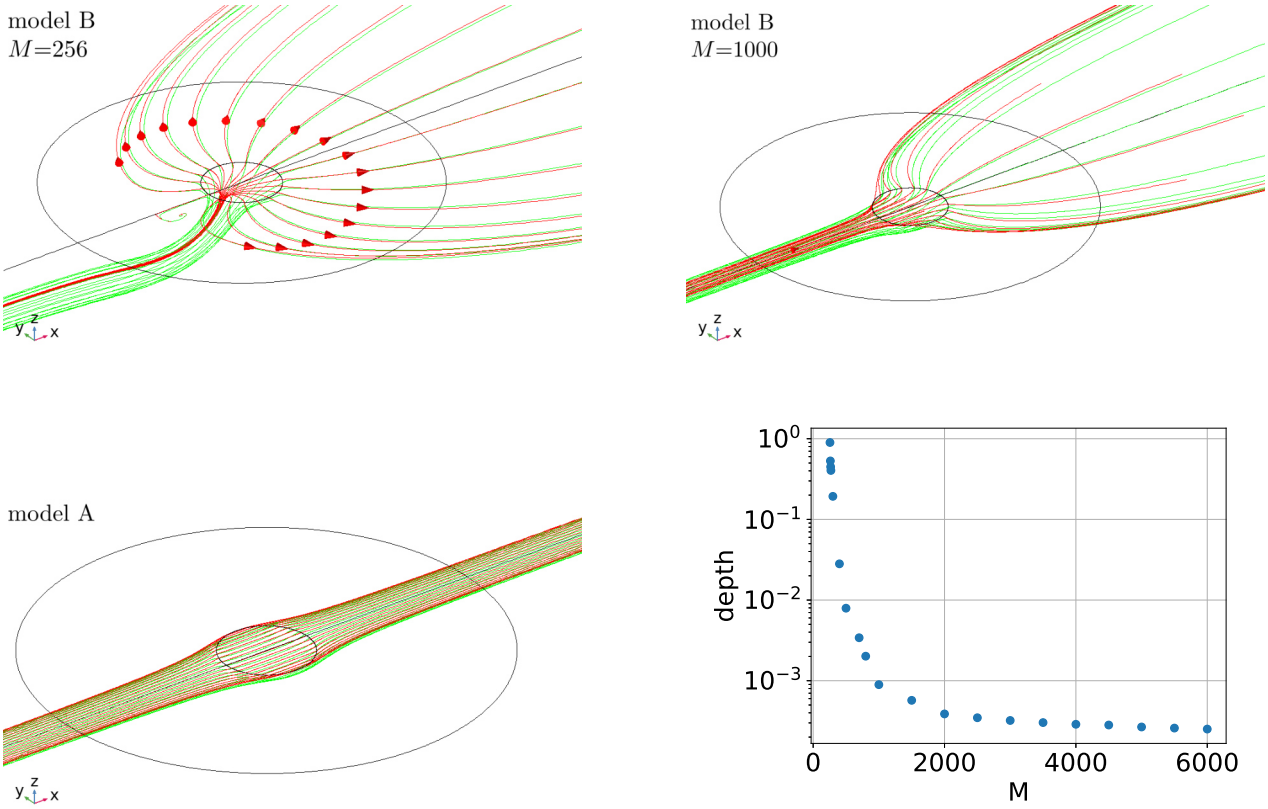

Figure 4.26: 3D Streamlines for model B and A. (up & low-left) streamlines for the simulations (M=256, Pe=3.2, model B) closest simulation to the critical point, (M=1000, Pe=15.5, model B) and (model A) valid for all the M and Pe. The red lines pass below the swimmer disk contour at the depth z=-0.001 and z=-0.1 for the green lines. Two circles are represented at the surface $z = 0$, the inner circle represents the swimmer while the outer circle is just a support to help the mesh implementation. The black straight line at the surface is the x-axis. (Right) Depth of the tube formed by the red streamlines as a function of the Marangoni number M at the position $x = -400$ for the model B.

Where does the fluid of the surface wake come from? To answer this question we consider the streamlines passing close to the swimmer contour. They define a tube of streamlines in the x-negative half-space (see figure 4.26). The tube remains at a constant depth until it approaches the swimmer, it dives slightly before going up under the swimmer; the streamlines splay at the surface forming the hydrodynamic wake previously described. Contrary to what we may expect, those streamlines do not describe recirculation loops in the swimmer frame of reference. Instead, liquid from the bulk rises to the surface, supplying in fluid the divergent

[47] For a flow dominated by the mean flow, the expected angular position for the start of the wake frontier is 90°.

flow. On the contrary for the model A (figure 4.26 lower-left), there is no such characteristic divergent flow at the swimmer rear and the global structure is flatter than the one observed in model B. Finally, for large M, in model A, the tube structure gets very close to the surface (figure 4.26 top-right). This suggests that the flow advecting the surfactant remains close to the surface.

b. Chemical wake

Because of finite diffusion, the chemical wake does not have a clear boundary but we can define the characteristic width W of the wake as

$$W(x) = \sqrt{\frac{\int_{-\infty}^{\infty} y^2 c(x,y)\ \mathrm{d}y}{\int_{-\infty}^{\infty} c(x,y)\ \mathrm{d}y}}. \tag{4.26}$$

$W(x)$ is thus the standard deviation of the surfactant distribution along y for a fixed x. In practice we can evaluate the width only up to $x = 50$, so our analysis is limited to this range[48].

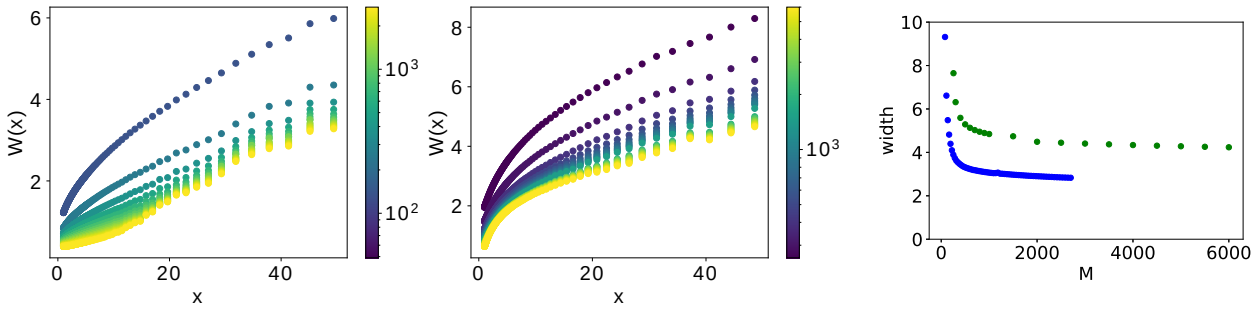

Figure 4.27: Width of the chemical wake. (Left & Middle) Width along the x-axis for model A and model B, the color bar represents the Marangoni number, for $M \in [80, 2600]$ and $M \in [256, 6000]$ respectively. (Right) Width of the wake at position $x = 40$, as a function of the Marangoni number M for model A (blue dots) and model B (green dots).

We observe some differences between the wake in model A and model B. In the latter, the width grows sub-linearly with x at moderate M, but exhibits a convex shape for large M and $x < 20$. In model B, the wake width keeps everywhere a sublinear shape in the whole range of tested $M = 256 - 6000$, being close to power-law with an exponent around $\alpha \sim 0.4$. Now, a surprising feature is that in contrast to the velocity fields, the difference in wake is much smaller than could be expected. The advection by Marangoni flow widens the chemical wake, but the effect is only moderate. For instance, if one considers the width $W(x) = 40$, the value in models A and B differ by only 40%. Finally, we saw above that the hydrodynamic flow seems to approach a limit as M increases. This observation holds for the width of the wake, which reaches a plateau at large M. This seems natural given that the hydrodynamic and transport problems are fully coupled.

4.3.3 Conclusion

The complete access to concentration fields and velocity fields given by simulation should provide rich information on the behaviour of interfacial swimmers. However, the results presented here have to be further explored. We have observed that the presence of Marangoni effects significantly alters the velocity field. By comparison, a surprising finding that emerges

[48]Far from it the mesh is too rough to have an accurate description of the low surface concentration distribution.

from our analysis is the fact that the chemical wake is much less sensitive. One would naively expect these Marangoni effects to have a stronger influence on the surfactant redistribution but the widening away from the swimmer is quite similar in the presence or in the absence of Marangoni flows. It is clear however from the simulations that near the swimmer the concentration fields are quite different. This suggests that the surfactant distribution in the vicinity of the swimmer plays a key role that needs to be better described. On a different note, we should also seek a complete understanding of the large-Pe regime with a $M^{2/3}$ power law observed for all models considered. Further analysis of the concentration and velocity fields are required to ascertain the origin and the robustness of this scaling law.

There are several additional directions that are worth exploring. First, it would be interesting to compare our numerical concentration profiles with those obtained by [5] for the asymmetric swimmer, and to characterize the speed and concentration decay profiles along the swimmer axis, to study the possibility of a power-law decay. Second, it remains essential to compare our numerical results to experimental observations, such as those obtained recently on asymmetric swimmers [12]. If having access to the camphor concentration profile is a challenge experimentally, measuring the velocity flow around and below the swimmer is less difficult. Some preliminary comparisons will be discussed in the last part (perspectives) of this manuscript.

4.4 Appendices

4.4.1 Demonstration: from the laboratory to the swimmer frame of reference

In this appendix, we explain how the governing equations are modified when switching from the laboratory frame of reference to the swimmer frame. The case of time-dependent swimming is included. Let us call R the laboratory frame and R' the swimmer frame. With natural notations, we have $\boldsymbol{u} = \boldsymbol{u}' + U(t)\boldsymbol{e}_x$ where $U(t)$ is the swimmer speed. Then

$$\left.\frac{\partial c}{\partial t}\right|_R = \left.\frac{\partial c}{\partial t}\right|_{R'} - U(t)\left.\frac{\partial c}{\partial x'}\right|_{R'}, \tag{4.27}$$

$$\boldsymbol{\nabla}\cdot\boldsymbol{u}c|_R = \boldsymbol{\nabla}\cdot\boldsymbol{u}c|_{R'} \quad \Rightarrow \quad \boldsymbol{\nabla}\cdot(\boldsymbol{u}c)|_R = \boldsymbol{\nabla}\cdot(\boldsymbol{u}'c)|_{R'} + U(t)\left.\frac{\partial c}{\partial x}\right|_{R'}, \tag{4.28}$$

$$\boldsymbol{\nabla}c|_R = \boldsymbol{\nabla}c|_{R'}, \tag{4.29}$$

Note that the change of frame induces a new advection term in the temporal derivation. It appears also when developing the general advection term. By exploiting equations (4.27), (4.28) and (4.29) we obtain:

- Transport equation :

$$\begin{aligned}
&\left.\frac{\partial c}{\partial t} + \boldsymbol{\nabla}\cdot(\boldsymbol{u}c) - D\Delta c\right|_R = \left.\mathcal{J}\delta\left(\boldsymbol{r} - \int_{-\infty}^{t} V(t')\,\mathrm{d}t'\boldsymbol{e}_x\right)\right|_R \\
\Leftrightarrow\ &\left.\frac{\partial c}{\partial t} - V\frac{\partial c}{\partial x} + \boldsymbol{\nabla}\cdot(\boldsymbol{u}c) + V\frac{\partial c}{\partial x} - D\Delta c\right|_{R'} = \left.\mathcal{J}\delta(\boldsymbol{r}')\right|_{R'} \\
\Leftrightarrow\ &\left.\frac{\partial c}{\partial t} + \boldsymbol{\nabla}\cdot(\boldsymbol{u}'c) - D\Delta c\right|_{R'} = \left.\mathcal{J}\delta(\boldsymbol{r}')\right|_{R'}
\end{aligned}$$

- Navier-Stokes equation :
  for $i = y$ or z:

$$\begin{aligned}
&\rho\left(\partial_t u_i + \boldsymbol{u}\cdot\boldsymbol{\nabla}u_i\right)|_R = \eta\Delta u_i + \partial_i p|_R \\
\Leftrightarrow\ &\rho\left(\partial_t u_i - V\partial_x u_i + \boldsymbol{u}'\cdot\boldsymbol{\nabla}u_i + V\partial_x u_i\right)|_{R'} = \eta\Delta u_i + \partial_i p|_{R'} \\
\Leftrightarrow\ &\rho\left(\partial_t u_i + \boldsymbol{u}'\cdot\boldsymbol{\nabla}u_i\right)|_{R'} = \eta\Delta u_i + \partial_i p|_{R'}
\end{aligned}$$

  for x : $u_x = u'_x + U(t)$

$$\begin{aligned}
&\rho\left(\partial_t u_x + \boldsymbol{u}\cdot\boldsymbol{\nabla}u_x\right)|_R = \eta\Delta u_x + \partial_x p|_R \\
\Leftrightarrow\ &\rho\left(\partial_t u_x + \partial_t U + \boldsymbol{u}\cdot\boldsymbol{\nabla}u_x\right)|_R = \eta\Delta u_x + \partial_x p|_R \\
\Leftrightarrow\ &\rho\left(\partial_t u'_x - U\partial_x u'_x + \boldsymbol{u}'\cdot\boldsymbol{\nabla}u'_x + U\partial_x u'_x\right)|_{R'} = \eta\Delta u'_x + \partial_x p - \rho\partial_t U|_{R'} \\
\Leftrightarrow\ &\rho\left(\partial_t u'_x + \boldsymbol{u}'\cdot\boldsymbol{\nabla}u'_x\right)|_{R'} = \eta\Delta u'_x + \partial_x p - \rho\partial_t U|_{R'}
\end{aligned}$$

  In conclusion :

$$\rho\left(\partial_t\boldsymbol{u} + (\boldsymbol{u}\cdot\boldsymbol{\nabla})\boldsymbol{u}\right)|_R = \eta\Delta\boldsymbol{u} + \boldsymbol{\nabla}p|_R \quad \text{or} \quad \rho\left(\partial_t\boldsymbol{u}' + (\boldsymbol{u}'\cdot\boldsymbol{\nabla})\boldsymbol{u}'\right)|_{R'} = \Delta\boldsymbol{u}' + \boldsymbol{\nabla}p - \rho\partial_t U|_{R'}.$$

  Note that if we apply directly the same method for the Stokes equation we see an advection term $U\partial_x\boldsymbol{u}|_{R'}$ that appears. It is not an issue if we consider that the Stokes equation is a simplification of the Navier-Stokes equation. Then the good method is to reintroduce the inertia terms, changing the reference frame and finally going back to the Stokes equation by neglecting the inertia terms.

4.4.2 Implementation of time-dependent simulation

In this appendix, we present the implementation of the time-dependent simulation. The simulation results are presented in 4.2.2 p.146. The geometry and the mesh are the same as the initial implementation already presented (see 4.1.3). Because of the time dependence, the equations driving the system are modified, with in particular a new an inertial force (see the demonstration in the appendix 4.4.1). The boundary conditions which apply on the box need also some changes.

a. Dimensionless equations and numbers

Because of the inertia of the fluid and the swimmer dynamics, we have to introduce two new dimensionless numbers:

$$Sc = \frac{\eta}{D\rho}, \qquad N = \frac{R^3\rho}{m}. \tag{4.30}$$

The Schmidt number Sc is the ratio between the surfactant diffusivity and the momentum diffusivity. The number N is up to a geometric constant the ratio between the fluid density and the swimmer density. We complete the set of dimensionless equation "$\kappa = 1$" with the inertia terms and the volume force, by taking: $t = \frac{R^2}{MD}\tilde{t}$ and $F_T = \eta M D \tilde{F}_T$, the inertia force due to unsteady motion of the swimmer.

$$\frac{M}{Sc}\frac{\partial \tilde{\boldsymbol{u}}}{\partial \tilde{t}} = -\tilde{\boldsymbol{\nabla}}\tilde{p} + \tilde{\boldsymbol{\nabla}}.\tilde{\bar{\boldsymbol{\tau}}} - N\tilde{F}_T\boldsymbol{e}_x, \qquad M\left(\frac{\partial \tilde{\boldsymbol{u}}}{\partial \tilde{t}} + \ \tilde{\boldsymbol{u}}.\tilde{\boldsymbol{\nabla}}\tilde{c}\right) = \tilde{\Delta}\tilde{c} + \tilde{\delta}(\tilde{\boldsymbol{r}}), \qquad \tilde{\bar{\tau}}.\boldsymbol{n} = -\boldsymbol{\nabla}_s\tilde{c}. \tag{4.31}$$

In *Comsol* we implement:

dimensionless equations	a	U	η	D	$\mathcal{J}$	κ	ρ	m
"$\kappa = \mathbf{1}$"	1	Pe/M	1	$1/M$	$1/M$	1	M/Sc	$\frac{M}{Sc\ N}$

b. Boundary conditions

We just mention the differences with the steady problem implementation.

- Bulk : changing the frame of reference adds an inertia force on the fluid $\boldsymbol{F}_T = -\rho\partial_t U\boldsymbol{e}_x$. The first Newton law of motion gives, $\partial_t U\boldsymbol{e}_x = (\boldsymbol{F}_\mathrm{v} + \boldsymbol{F}_\mathrm{c})/m$, we deduce

$$\boldsymbol{F}_T = -\boldsymbol{F}_\mathrm{c} - \boldsymbol{F}_\mathrm{v}. \tag{4.32}$$

- Front side (previously: *Inlet*, normal flow V): We impose a normal flow with the pressure fixed at zero, the speed norm can vary in time and in space. The previous boundary condition is too strict to be kept.

- Bottom and lateral side (previously: *sliding wall with the speed* V), we keep the impenetrability condition but impose a perfect slip.

This implementation has more degrees of freedom than the spontaneous intuitive implementation where the velocity is computed and directly injected from the external boundary condition.

c. New definition of $U(t)$

$U(t)$ is the swimmer velocity in the laboratory frame of reference or the average speed flow in the swimmer frame of reference. In the stationary simulations, U is implemented through the inlet flow and the sliding walls. Similarly, we define an effective $U(t)$ in the time depending simulation as the average speed along the inlet boundary (front side). We also compute the standard deviation σ_U to check that this speed is uniform enough along this side, typically the criterion is $\sigma_U/U < 0.01$.

$$U(t) = \frac{1}{HL_y} \iint_{\text{front side}} \boldsymbol{u}(t) \cdot \boldsymbol{e}_x \, \mathrm{d}S, \qquad \sigma_U = \sqrt{\frac{1}{HL_y} \iint_{\text{front side}} (\boldsymbol{u}(t).\boldsymbol{e}_x - U(t))^2 \, \mathrm{d}S}. \tag{4.33}$$

From $U(t)$ we compute the Péclet number $Pe(t) = U(t)\ M$.

4.4.3 Implementation of the Navier-Stoke flow simulation: the high-Pe mesh

In this appendix, we present the implementation used for the simulation at finite Reynolds number. This situation requires a refinement of the mesh that can handle the concentration boundary layers that appear at large Pe. The results from those simulation are presented in 4.2.2 p.145.

a. Mesh

To describe the velocity and concentration boundary layer, the external circle defined in figure 4.1 is replaced with a 3D structure characterised by three lengths: $a = 10$, $b = 5$ and $c = 2$. The front part is the quarter of an oblate of radius b and thickness c, the rear is an ellipsoid in the continuity of the oblate with the length a. This 3D structure surrounds the swimmer as shown in the left figure 4.28. The purpose of the oblate is the same as the external circle of the basic geometry, helping to generate the mesh (see fig. 4.28).

To simplify the description, we only present the differences compared to the basic implementation (if not mentioned otherwise, the swimmer contour, the point source and the mesh in the bulk are subject to the same constraints than in the previous implementation):

- The volume and inner area delimited by the new structure are characterised by a growth rate 1.05.
- For the entire upper face, a boundary layer mesh (thin layers of parallelepiped) is added at the surface. We impose that between the free surface and the surface where $c(x, y, z)/c(x, y, z = 0) = 0.1$, there are at least 10 elements of mesh in depth, so as to resolve the high gradients present there with sufficient resolution.

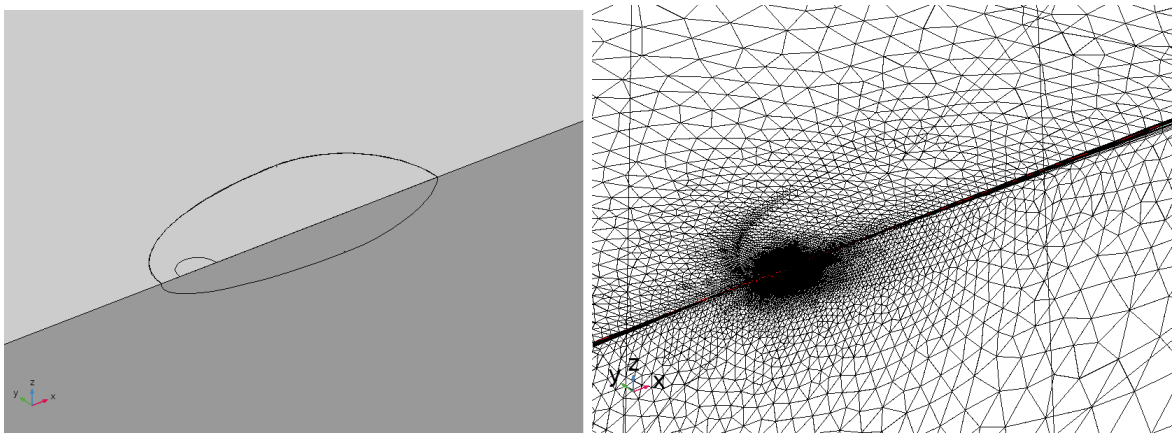

Figure 4.28: Geometry and mesh. (Left) geometry of the simulation close to the swimmer. (Right) Mesh around the swimmer.

4.4.4 Complementary figures

a. Swimming diagram: $a_s = 0.88$, see 4.2.2 p.143

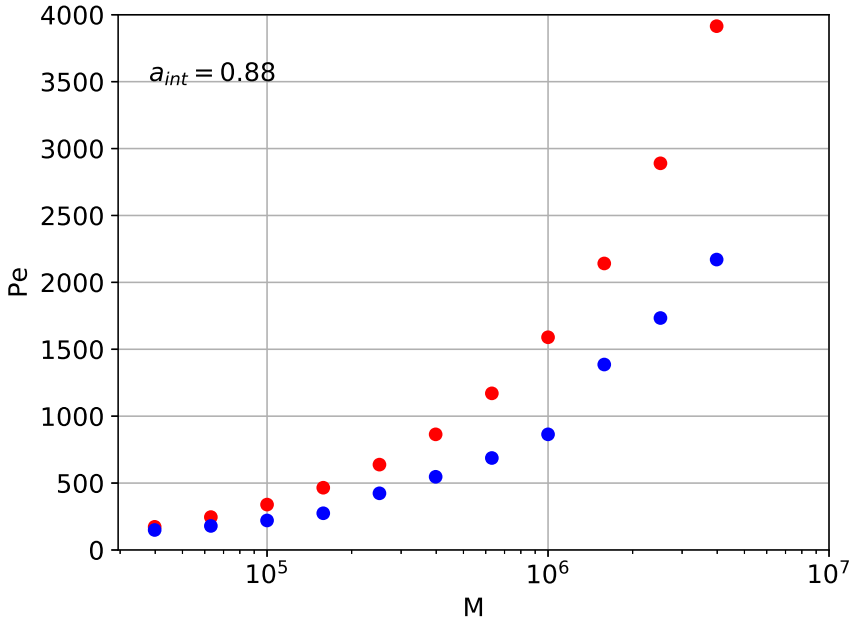

Figure 4.29: Swimming diagram for $a_s = 0.88$. The red dots belong to the stable branch while the blue dots belong to the unstable branch.

b. Concentration field: model A & model B, see 4.3.1 p. 152

For all the figures, the colours express the velocity field normalised by $\mathcal{J}a/D$, from c_{max} to zero, with c_{max} the maximum concentration over the swimmer contour. The coloured lines going from magenta to red are the iso-concentration $[0.1, 0.05, 0.02]$. Since the model considers a point source the colour bar would be dominated by the concentration around this point. To avoid this issue, we only plot the concentration below the maximum concentration along the swimmer contour, hence a white space corresponding to the local concentration which does not

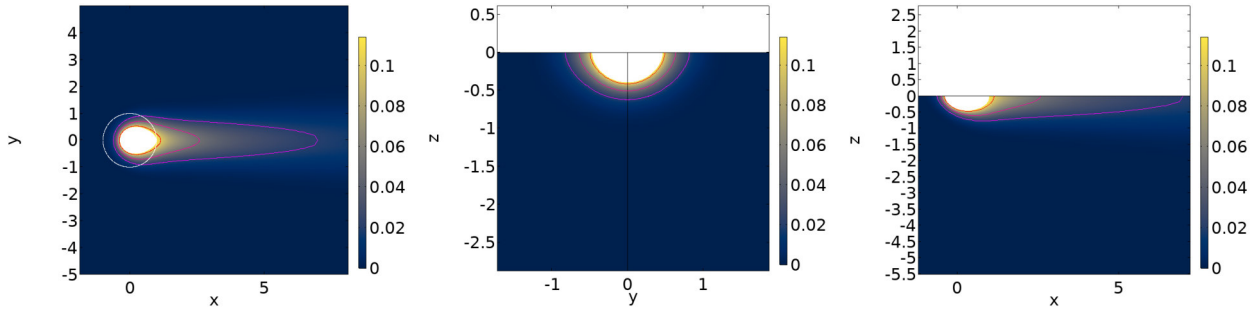

Figure 4.30: Concentration field model A. From left to right, top view ($z = 0$), rear view (x=0), side view (y=0).

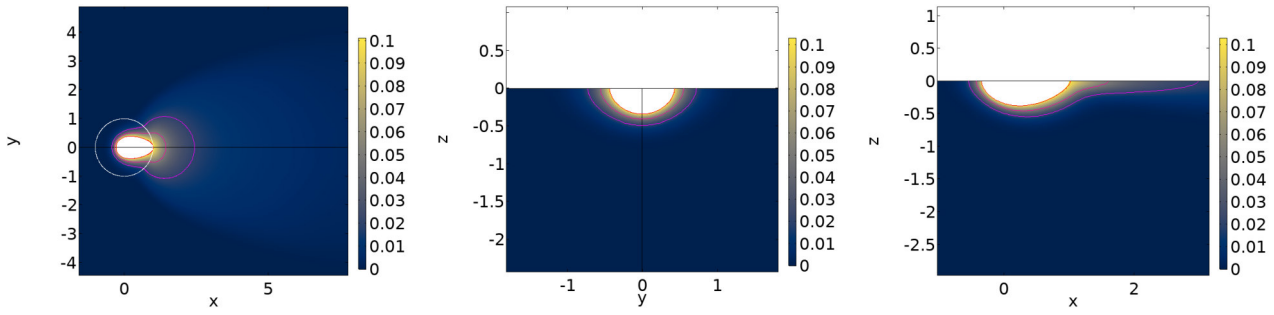

Figure 4.31: Concentration field model B ($M = 2500$, $Pe = 35.6$). From left to right, top view ($z = 0$), rear view (x=0), side view (y=0).

verify this criterion. For the plane $z = 0$, the white line represents the swimmer contour.

4.4.5 Forces evolution in model B

We investigated in this chapter the forces applying on the swimmer (see tab. 4.1). Here we display the evolutions of those forces as a function of the Péclet number Pe at three Marangoni numbers, 100, 300 and 1000, that is one value for each of the three different ranges put in evidence in the swimming diagram of fig. 4.6. All those results are obtained with model B simulations, such that reference force is $f^* = M\eta D$. We apply the convention that negative value corresponds to a resistive contribution for the swimmer motion, while positive value corresponds to a motor contribution.

The main goal is to display some interesting features put in evidence in chapter 3 with the toys models and remaining valid for the model B, in particular, the motor contribution of the Marangoni flow force at low Pe (see 4.2.1 p.139). Moreover, we had discussed in that chapter the qualitative variation of the driving force (F_c and $F_{m\mathcal{M}}$). With simple physical arguments, we predicted that those forces vanish at $Pe = 0$ then increase with Pe reaching a maximum and then decrease asymptotically toward zero (4.3.1 p.153), and indeed we verify this prediction as shown in figure 4.32.

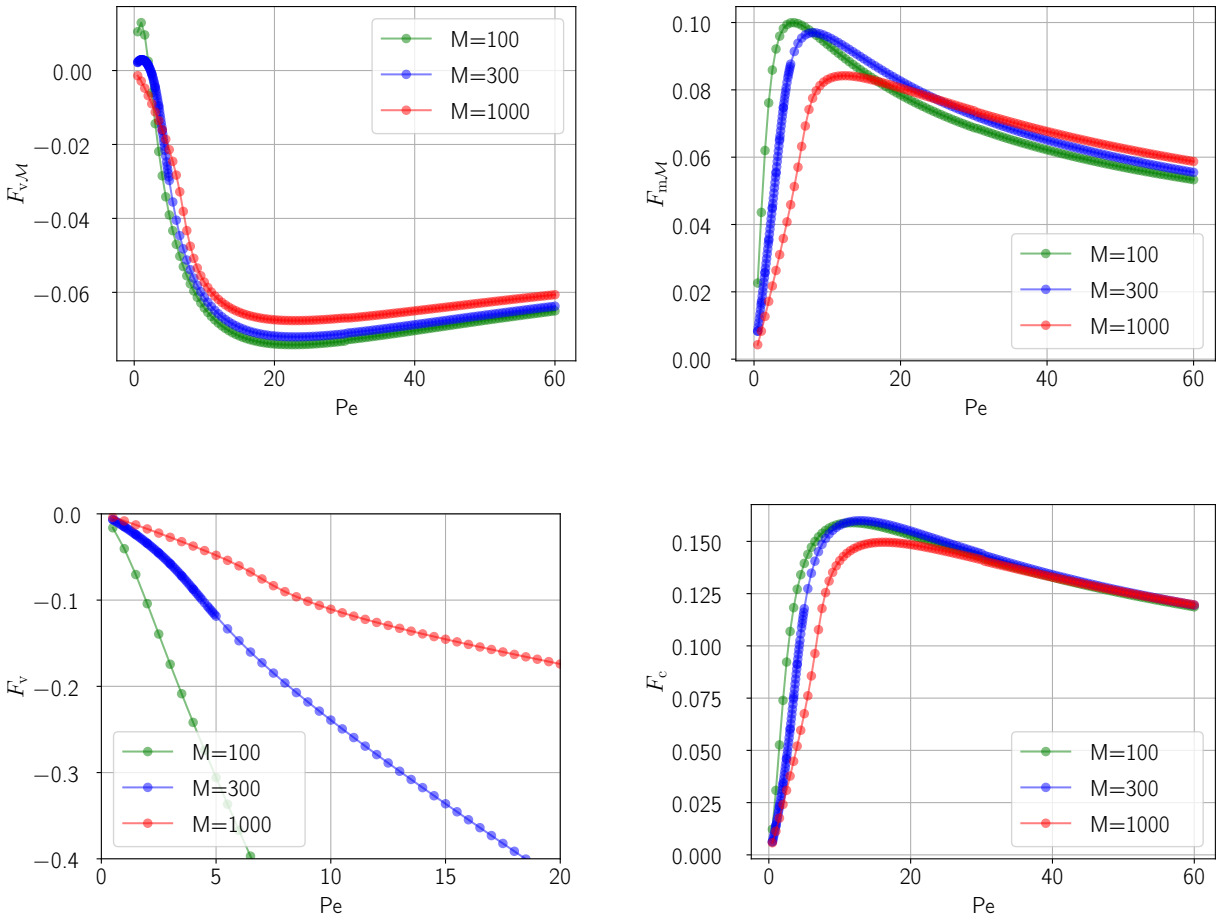

Figure 4.32: Evolution of the force as a function of Pe: (upper-left) Marangoni flow force (4.15), (upper-right) Marangoni force (4.18), (low-left) flow force (4.16) and (low-right) capillary force (4.13).

Bibliography

[1] Thomas Bickel. Spreading dynamics of reactive surfactants driven by Marangoni convection. *Soft Matter*, 15(18):3644–3648, 2019.

[2] R. Courant. Variational methods for the solution of problems of equilibrium and vibrations, 1943.

[3] Harinadha Gidituri, Mahesh V. Panchagnula, and Andrey Pototsky. Dynamics of a fully wetted Marangoni surfer at the fluid-fluid interface. *Soft Matter*, 15(10):2284–2291, 2019.

[4] J. Happel and H. Brenner. 1983_Book_LowReynoldsNumberHydrodynamics. 1963.

[5] Eric Lauga and Anthony M.J. Davis. Viscous Marangoni propulsion. *Journal of Fluid Mechanics*, 705:120–133, 2012.

[6] Hassan Masoud and Howard A. Stone. A reciprocal theorem for Marangoni propulsion. *Journal of Fluid Mechanics*, 741:1–7, 2014.

[7] Hassan Masoud and Howard A. Stone. The reciprocal theorem in fluid dynamics and transport phenomena. *Journal of Fluid Mechanics*, 879:P1, nov 2019.

[8] Augusto Cesar Gale O. Approximate upwind petrov-galerkin. *Computer Methods in Applied Mechanics and Engineering*, 68:83–95, 1988.

[9] Nobuhiko J. Suematsu, Yumihiko Ikura, Masaharu Nagayama, Hiroyuki Kitahata, Nao Kawagishi, Mai Murakami, and Satoshi Nakata. Mode-switching of the self-motion of a camphor boat depending on the diffusion distance of camphor molecules. *Journal of Physical Chemistry C*, 114(21):9876–9882, 2010.

[10] Nobuhiko J. Suematsu and Satoshi Nakata. Evolution of Self-Propelled Objects: From the Viewpoint of Nonlinear Science. *Chemistry - A European Journal*, 24(24):6308–6324, 2018.

[11] Nobuhiko J. Suematsu, Tomohiro Sasaki, Satoshi Nakata, and Hiroyuki Kitahata. Quantitative estimation of the parameters for self-motion driven by difference in surface tension. *Langmuir*, 30(27):8101–8108, 2014.

[12] Samrat Sur, Hassan Masoud, and Jonathan P. Rothstein. Translational and rotational motion of disk-shaped Marangoni surfers. *Physics of Fluids*, 31(10):102101, 2019.

[13] Alla Vilk, Irina Legchenkova, Mark Frenkel, and Edward Bormashenko. Spiral Thermal Waves Generated by Self-Propelled Camphor Boats, 2020.

je me flatte d'en avoir donné une juste explication
I pride myself on having given a fair explanation

D. J. Carradori de Prato (1801)[1]
about the motion of camphor upon water

Chapter 5

Conclusions and perspectives

This PhD work has been devoted to the study of individual motion of symmetric interfacial swimmers and in particular to the understanding of their self-propulsion mechanism. Experiments with millimetre-sized camphor disks evolving upon water provided a detailed characterization of the parameters controlling swimming. This experimental approach has been complemented by analytical developments on toy models based on a moving point source. Although crude, they provide a basic understanding of the symmetry-breaking mechanism and the overall swimming response. A third line of attack was a full numerical treatment of the problem using the Finite Element Method simulation in *Comsol*. This allows for the first time to assess potentially key phenomena such as Marangoni effects.

Main Results

On the experimental side, we have shown that camphor-loaded agarose disks have a spontaneous motion characterised by a steady velocity with a typical velocity of several centimetres per second (from 30 mm/s for 1 mm radius to 110 mm/s for 15 mm radius). Among various parameters, we investigated in particular the velocity dependence on swimmer radius and found a sublinear increase consistent with a power-law $a^{1/3}$. We also investigated experimentally how the camphor is released from the swimmer, and proposed a model based on diffusion a growing layer surrounding the core of precipitated camphor. The decrease in swimmer velocity observed in long times is then consistent with the reduction expected in global flux.

Despite being symmetric objects, camphor disks move upon water, suggesting that their propulsion mechanism involves a spontaneous instability breaking the rotational invariance. Following this idea, we developed a toy model which aims at capturing the swimming behaviour while circumventing the complexity intrinsic to the fully coupled non-linear problem. To do so, the key idea is to assume a complete decoupling between the surfactant transport and the hydrodynamic problem. The disk in steady motion is thus represented by a chemical point source in a uniform flow. At low Péclet number, it is indeed found that a symmetry breaking occurs above a critical Marangoni number. At large Péclet number, the model predicts that Pe increases with Marangoni number as power-law with exponent 2/3. This is compatible with the velocity-radius relation measured in experiments. Besides, the toy model also predicts that a small asymmetry should not change significantly the velocity, which is indeed what we found experimentally.

The key simplification of the basic toy model is to neglect the Marangoni flows, a step which appears as unavoidable to decouple the transport and hydrodynamic problems. This assumption can not be rationalized as a well-posed perturbative scheme because the neglected Marangoni flows and the capillary forces considered to evaluate the swimmer motion derive from the same underlying physical phenomenon. We show that it is nonetheless possible to

partially account for those Marangoni effects by using the Lorentz reciprocal theorem to express the viscous force they generate on the interfacial swimmer. Taking into account this new contribution, we obtain a more advanced version: the Lorentz toy model. At low Pe, the threshold in M now disappears, meaning that a spontaneous symmetry breaking always occurs and suggesting that the contribution of Marangoni flow favours the swimmer motion. At large Pe, the 2/3 power law is preserved and only the magnitude of the velocity is modified. The predicted values are 60% lower than with the basic toy model, coming closer to the experimental values,

Even if our theoretical framework gives some insight into the spontaneous swimming of our camphor disks, it requires gross simplifications, in particular in the treatment of hydrodynamics and Marangoni effects. It was therefore interesting to go one step further, and to approach the problem with a complete numerical model that includes all coupling at work in the swimmer propulsion (advection and Marangoni stress). The swimming diagram so obtained is notably different from those found with toy models: It is discontinuous. There is a critical point defined by a critical Péclet number and a critical Marangoni number, where the velocity jumps to a finite value, and from which emerges both a stable and an unstable branch. The M range where two stable branches exist thus corresponds to a bistability regime possibly inducing hysteretic behaviour between rest and moving states. In this region, the system evolves toward a swimming state only if the perturbation is sufficiently large, otherwise, it falls back to rest. We check this behaviour explicitly using time-dependent simulations. In the regime of large Pe, the swimming curve predicted by simulations remains close to the $M^{2/3}$ power law, with a prefactor not far from that in the Lorentz toy model. By considering swimmers with extended source, we also found that as the source radius approaches that of the swimmer, the critical point is pushed toward infinity, implying that a swimmer with a release all over its surface would not swim. As we discuss, this is not necessarily in contradiction with experiments, but there is a lack of understanding here that calls for further investigation.

The $M^{2/3}$ power law in the large Pe regime seems to be a robust property and remains approximately verified even in the most realistic simulations we carried on. This recurrent feature is quite surprising. Indeed, it is clear from numerical simulations that local features such as the velocity and concentration fields are quite different in the absence or presence of Marangoni flows, as seen in the quantitative characterization of the hydrodynamic and chemical wakes. Further analysis would now require additional theoretical work on Marangoni flows, and some comparisons with experimental measurement by PIV and/or local probes of the concentration.

Throughout our analytical model and numerical investigations, we made ample use of the Lorentz reciprocal theorem to disentangle the different forces acting on the swimmer. Capillary effects appear in two ways: a direct triple line contribution, and an indirect flow-mediated contribution occurring through the viscous stress acting over the swimmer surface and which is governed by Marangoni flows. Unexpectedly, such indirect contribution can be either motor or resistive depending on the parameters, respectively for a fixed concentration or a fixed flux over the swimmer surface. This brought us to introduce the concept of a concentration swimmer, with a fixed concentration all over its surface. That such an object could swim is quite counter-intuitive, because the capillary force vanishes, whereas so far it was always seen as the force driving motion. We show in the full numerical model that the flow-mediated contribution could be a motor one. However, we found no spontaneous motion over the range of M and Pe tested. Meanwhile, at a much higher M regime, the concentration swimmer may be realized experimentally with pure camphor disks, that do swim and with velocities higher than the gel swimmers. Therefore a gap remains between modelling and experimental evidence on the "concentration swimmer", which will require further investigation. It is already clear though

that the effect of Marangoni flow can be hard to anticipate.

New directions and perspectives

In addition to the perspectives that naturally arise from the results summarized above, there are some further directions that we partially explored during this PhD. These works are all related to interfacial swimmers and Marangoni propulsion, but either did not fit simply in the present corpus of investigation or remained too preliminary for a thorough presentation. We briefly present the new directions that we consider the most promising in terms of questions or perspectives.

Wall interaction Initially motivated by questions from active matter, an initial part of this PhD sought to characterize the interaction of an interfacial swimmer with a wall. We thus developed a hung aluminium barrier (see right fig. 5.1), which behaves as an overdamped oscillator, and give access to the force acting on the barrier (see left fig. 5.1) by measuring its displacement with a sensor. We also recorded the motion of the swimmer to characterize the motion before and after the collision.

We could infer from our measurements that the capillary force induced by the surfactant field around the swimmer probably has an impact on the barrier much stronger than the direct contact interaction. This is illustrated in figure 5.1 (right) which shows the force on the barrier as a function of time. We observe an asymmetric evolution with respect to the impact (red dot). Whereas five seconds after the collision the swimmer is already far away from the barrier, a force is detected, which may be explained by the capillary force induced by the chemical wake left behind the swimmer and/or the hydrodynamic interaction with the barrier.

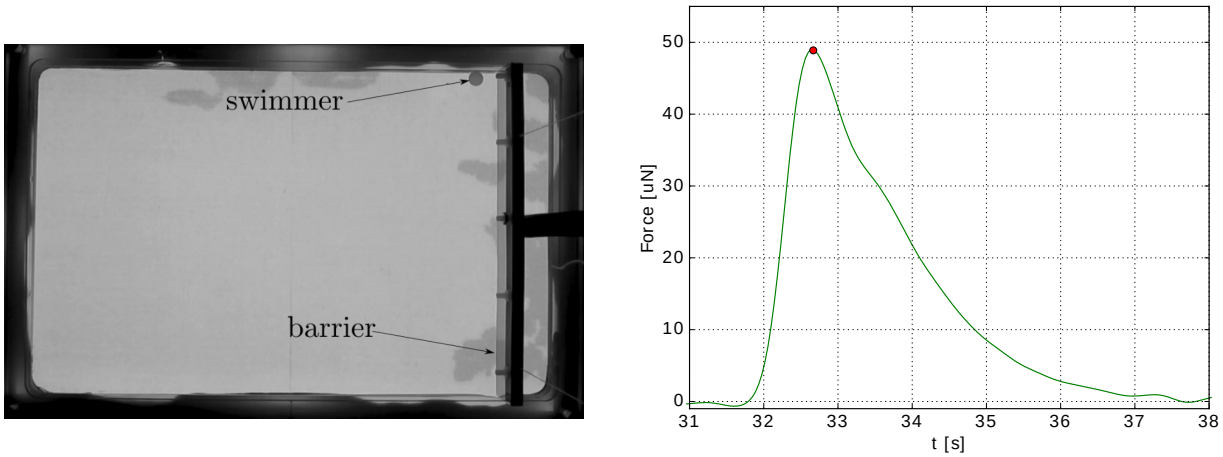

Figure 5.1: Interaction of a swimmer with a wall. (Left) Experimental set-up: a 4-mm radius agarose-camphor disk evolves in the $17 \times 27 \times 1$ cm pool filled with water. The disk interacts with a hung aluminium barrier positioned at the right of the pool. (Right) Force applying on the barrier as a function of time. The red dot indicates the time of contact as seen in the video recording.

We also studied the trajectory of the swimmer after the impact. We observed that after hitting the barrier the swimmer bends its trajectory that tends to run parallel to the wall (fig. 5.2). The bent trajectory after the collision may be attributed to the chemical wake left behind the swimmer. The wall forces the swimmer to interact back with the surfactant normally left behind. Because of the low surface tension in this wake, the swimmer is repelled from it, hence a repulsion bending the swimmer trajectory toward the wall.

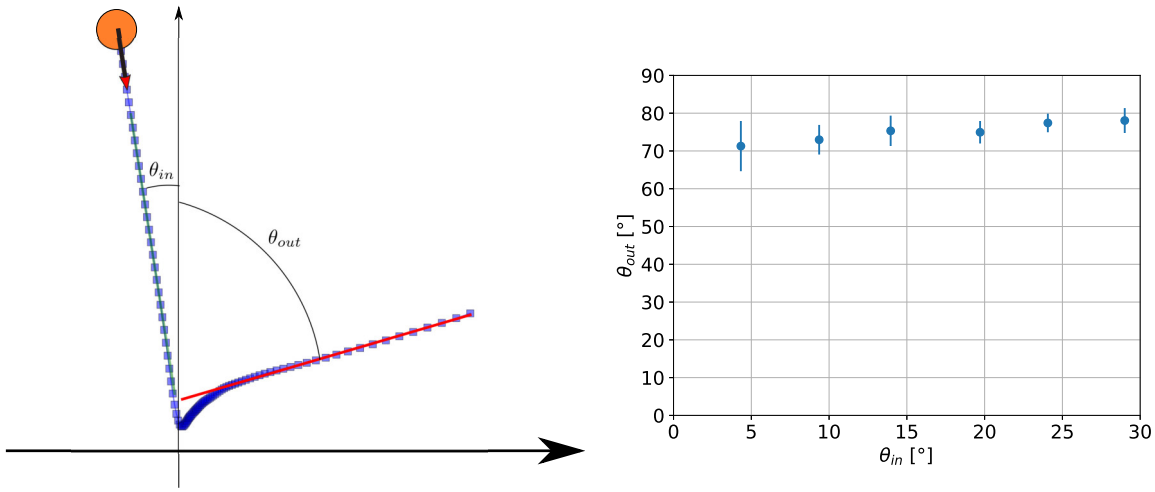

Figure 5.2: Interaction angle. (Left) trajectory example for a 4mm radius swimmer interacting with the barrier, represented here by the abscissa arrow. The angle θ_{in} and θ_{out} are determined by linear regression with the point representing the trajectory. (Right) Evolution of θ_{out} as a function of θ_{in}.the error bars correspond to a 95% confidence interval obtained from Student's t-distribution.

One of the advantages of devising a simplistic toy model that reasonably accounts for the main features of swimming is that it can be used to investigate more complex situations. We used the method of the image to account for the interaction with the wall[1] and solved the resulting model numerically. The preliminary results are consistent with the observations made above, but would still require further work and investigations. Simulating the fully coupled problem with the FEM method to take into account the chemical wake and Marangoni flows is possible in principle, but it is certainly a difficult task since the mesh would have to change at each time iteration. On the experimental side, an interesting perspective is to consider the wall interaction of pure camphor swimmers. Qualitative observations suggest that the bending of trajectories after a collision is weaker. Finally, another topic for future work is to study the interaction between two swimmers, as was recently considered theoretically for a head-on collision with 3D Marangoni droplets [2]. The understanding of the interaction between the swimmer and its surrounding is crucial if we want to use them as elementary objects in the field of active matter.

Visualising the surfactant and flow field A key element missing in the understanding of Marangoni propulsion is an experimental characterisation of the swimmer environment, including concentration and flow fields. As regards the later, a recent article used the PIV method [4] to measure the flow generated by asymmetric swimmers. However, the type of swimmer used does not last long, – less than one minute –and the flow measured may be transient rather than steady. PhD student Clément Gouiller is now carrying out PIV experiments to characterize the flow induced by an agarose gel camphor swimmer. From those experimental data, one can extract the two-dimensional divergence of velocity ($=\boldsymbol{\nabla}_{2D} \cdot \boldsymbol{u}$), [2]. It is compared with the simulation results obtained for a model B simulation in figure 5.3). Even if the simulations are done in a different range of Re and Pe, we note a similar organisation for the flow in the experiments and the simulation. In both cases, there are precursors of the surface hydrodynamic wake [3].

[1] The idea is to use a virtual image swimmer to satisfy the barrier impermeability condition for the surfactant.

[2] The advantage of the surface divergent flow is to display easily all the hydrodynamic structures evidenced during the simulation chapter, in particular the hydrodynamic wake, while the flow fields are harder to interpret.

[3] While it was defined in chapter 3 from the streamlines, the wake also corresponds to the region of positive surface divergence (expanding Marangoni flow), and is surrounded by a region of negative surface divergence (contracting flow),

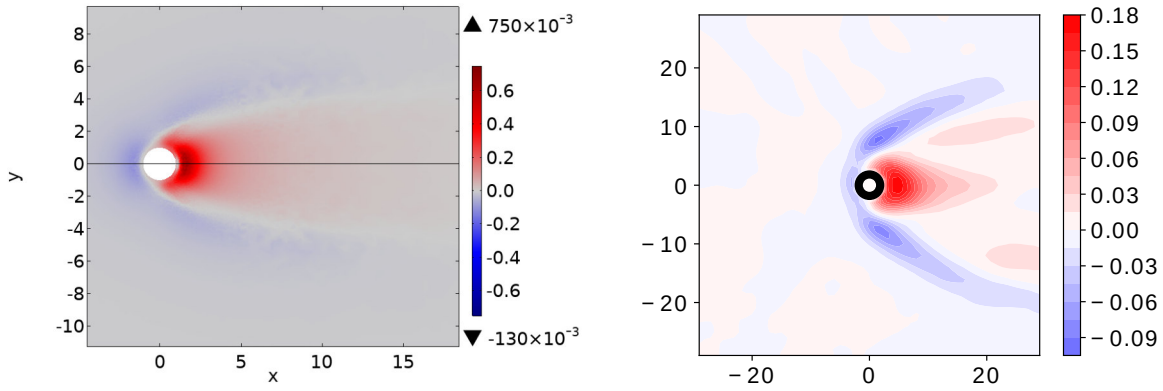

Figure 5.3: 2D surface divergence ($\boldsymbol{\nabla}_{2D} \cdot \boldsymbol{u}$) for the plan z=-0.4. All the lengths are normalized by the swimmer radius and the speeds by the swimmer speed. (Left) result from the simulation M=2500, $Pe = 36$ and $Re = 0$. (Right) PIV result made with a 2.5mm radius and 0.5mm thickness agarose gel - camphor disk, $M \sim 10^{11}$, $Pe \sim 10^5$ and $Re \sim 10^2$. The white circle is the swimmer position and the black circle is a mask hiding unphysical data around the swimmer neighbourhood inherent to PIV experiment. This experimental figure has been made by Clément Gouiller.

We observe the same high divergent spot behind the swimmer. We also note that the extension of the hydrodynamic wake is more important in the experiment than in the simulations. Those differences may come from the different regimes (Pe,Re) probed in experiments and simulations, but those preliminary results are very encouraging. A further step would be to engage in some theoretical analysis to build a comprehensive framework for the phenomena at stake. The hope is to build on the observation to help in this difficult task.

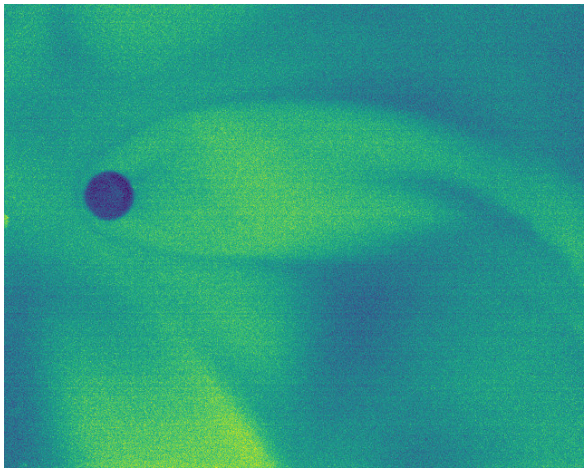

Figure 5.4: Image from the thermic camera recording the motion of a 4 mm radius agarose-camphor swimmer (darker disk) at the air-water interface. Between the lightest (hot) and the darkest (cold) colours there is less than 1 °C gap.

To have additional information regarding the flow/wake around the interfacial swimmer we have also used a thermic camera to measure the eventual thermal gap around the swimmer. The preliminary results are very encouraging. The method has already been used very recently with the same purpose but for spinning camphor boat [6]. For camphor swimmers, the water surrounding the camphor disk seems to be slightly hotter than the free surface. We attribute this phenomenon to the water evaporation. Because of it, the surface of the pool is slightly colder than the water in the bulk. Then when the swimmer passes, it pumps the bulk water toward

with the limit given by $\boldsymbol{\nabla}_{2D} \cdot \boldsymbol{u}(z = 0) = 0$.

the surface which allows recognising the hydrodynamic wake despite the low-temperature gap (see fig. 5.4). Further investigation may yield some valuable and novel information about the dynamical processes involved in the swimmers dynamics.

Dynamic pattern in shallow water During most of this thesis, the effects due to the finite depth of water were either neglected or discarded in the simulations and models that assume an infinite half-space. However, it seems that the most interesting collective effect as swarming or pattern formation occurs mostly in shallow water [3]. In prospective experiments in low depth water involving agarose camphor disk, we observed pattern formation reminiscent of those described in [3]. However, the pattern in our case is not static but dynamic with a pair of swimmers oscillating around their stable position, (see fig. 5.5). The oscillations motion are seen with a number up to five swimmers beyond which the pattern becomes static. Numerous

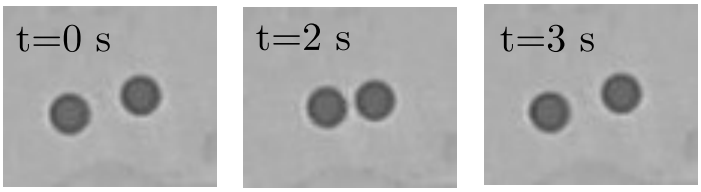

Figure 5.5: Series of images illustrating the oscillation motion of two 2.5-mm radius disk of agarose - camphor in shallow water $h_w = 1.4$ mm.

aspects of this observation would need to be clarified. First, the attractive force leading to the formation is probably related to the "reverse Marangoni surfing" [5], by which the swimmer move opposite to the direction of the capillary force. By extension, the proximity between two swimmers may lead to a lower surface tension area between them inducing this attractive force. This hypothesis would require further experimental investigation but also simulation in a shallow water environment. A second aspect which needs clarification is the oscillatory motion. A hypothesis to explain it is the competition between the attractive force, probably related to the “"reverse Marangoni surfing"” [5] and the capillary force. When the swimmers are far enough, the attractive force dominates but as soon as they get too close, the capillary force repels them and then the cycle restarts, generating the oscillating dynamic. Those observations and the origin of the oscillations would certainly deserve further investigations.

To conclude, more than two centuries after the “fair explanation” from the Italian physicist Carradorri, the interfacial swimmers remain a very interesting system displaying a variety of behaviours from spinning to swarming. However, most of those phenomena still require a characterisation. Even for the simple translation of a camphor disk, some aspects remain unclear and the path is still long before the complete understanding.

Bibliography

[1] D.J. Carradori de Prato. Sur les expériences de cit. Prevost de Genève sur la force expansible des émanations odoriférantes, et du citoyen Venturi de Modène sur les mouvemens du camphre sur l'eau. *Annales de Chimie*, 37, 1801.

[2] K. Lippera, M. Morozov, M. Benzaquen, and S. Michelin. Collisions and rebounds of chemically active droplets. *Journal of Fluid Mechanics*, 2020.

[3] Siowling Soh, Kyle J M Bishop, and Bartosz A. Grzybowski. Dynamic self-assembly in ensembles of camphor boats. *Journal of Physical Chemistry B*, 2008.

[4] Samrat Sur, Hassan Masoud, and Jonathan P. Rothstein. Translational and rotational motion of disk-shaped Marangoni surfers. *Physics of Fluids*, 31(10):102101, 2019.

[5] Vahid Vandadi, Saeed Jafari Kang, and Hassan Masoud. Reverse Marangoni surfing. *Journal of Fluid Mechanics*, 811:612–621, 2017.

[6] Alla Vilk, Irina Legchenkova, Mark Frenkel, and Edward Bormashenko. Spiral Thermal Waves Generated by Self-Propelled Camphor Boats, 2020.